Structural and kinetic studies of surfactant and phospholipid monolayers at the air/liquid interface using sum-frequency generation spectroscopy

Sami Goussous

September 2018

Churchill College

University of Cambridge

This dissertation is submitted for the degree of Doctor of Philosophy

Declaration

This thesis is the result of my own work and includes nothing which is the outcome of work done in collaboration, except where specified in the text. No part of this dissertation has been, or is being, submitted at this or any other University for a degree or equivalent qualification.

This thesis is not substantially the same as any that I have submitted, or, is being concurrently submitted for a degree or diploma or other qualification at the University of Cambridge or any other University or similar institution except as declared in the Preface and specified in the text. I further state that no substantial part of my dissertation has already been submitted, or, is being concurrently submitted for any such degree, diploma or other qualification at the University of Cambridge or any other University or similar institution, except as declared in the Preface and specified in the text.

This thesis does not exceed the prescribed limit of 60,000 words

Sami Goussous

Acknowledgements

I would like to express my sincerest gratitude to Dr Mike Casford and Prof Paul Davies for their invaluable guidance during the past four years. My research has been more productive, my writing a little more coherent, and my enthusiasm bolstered, because of their interventions and advice. Thanks must also go to Dr Simon Johnson, for his advice and for his friendship during my secondment at Unilever, and to Dr Annabel Murphy who obtained the deuterated surfactin from *Bacillus Subtilis*. For their financial support and for allowing me to undertake this research, I am also grateful to Unilever and the EPSRC.

Of course I would not have made it this far without my amazing family, and their ever-present support. Thank you so much, for everything.

Abstract

In this work, the non-linear optical technique of sum-frequency spectroscopy (SFG) has been used to investigate a variety of surfactant and phospholipid systems at different interfaces.

Firstly, the effects of temperature and ionic strength on the adsorption of cationic and non-ionic surfactants were investigated. The binary surfactant system used here is a simplified hair conditioner model, consisting of a fatty alcohol and a long chain quaternary ammonium salt, self-assembled from solution onto a silica surface (which serves as a very approximate model of the hair surface). SFG was used to investigate and the effects of temperature and ionic strength on the conformational ordering of the adsorbed monolayer.

The structure of a tethered bilayer lipid membrane (tBLM) produced by different methods was investigated. The tBLM is a bilayer of phospholipids, which are tethered to a gold substrate by a self-assembled monolayer (SAM). The SAM is a mixture of disulfide tether molecules and disulfide spacer molecules, which form covalent bonds to the gold surface. Ideally, the tether molecules should inter-digitate into the phospholipid membrane and hold it to the gold surface. This type of system is often used as a robust model for a cell membrane. Here, SFG was used to investigate the structure of the SAM, and of the membrane when formed either by rapid solvent exchange, or by a combination of Langmuir-Blodgett and Langmuir-Schaefer deposition. Significant differences in the resulting spectra of the tBLM were observed, as a result of the fabrication technique. SFG was also used to confirm that the polar orientation of the phospholipid in the tethered membrane systems was as expected for a bilayer.

Two versions of the quaternary ammonium surfactant used previously were also investigated at the air/water interface. The only difference between the two surfactants was their counterion. The slow collapse of the compressed monolayer was monitored using SFG and by surface pressure measurements. Langmuir-Blodgett deposition onto glass and mica was used at different stages of the monolayer collapse; the resulting air/solid systems were investigated using SFG and atomic force microscopy. Two different methods of obtaining sum-frequency intensity data over time were evaluated, and the effect of the counterions on the kinetics of the slow collapse mechanism was discussed.

The structure of surfactin, a surface-active lipopeptide, was investigated at the air/water interface. Deuterated analogues of the bio-surfactant were produced from *Bacillus Subtilis* by feeding the bacteria with deuterated glucose and/or deuterated leucine. These analogues were used to confirm spectroscopic assignments and make conclusions of the structure of surfactin at the air/water interface. The effect of the surfactin concentration, the pH of the subphase, and the addition of calcium ions to the subphase was also investigated.

The acquired knowledge of the structure of surfactin was then used to investigate the interaction of surfactin with a phospholipid monolayer. The surface pressure and sum-frequency spectra were monitored over time after the injection of surfactin into the subphase beneath a phospholipid monolayer compressed at the air/water interface. The surface pressure rose, indicating that surfactin penetrated into the monolayer, but it was found that sum-frequency signals arising from surfactin disappear in the final equilibrium system. Mechanisms and possible structures which are compatible with the data are discussed.

Contents

1. Introduction

The work in this thesis can be divided into two broad categories. The first is the study of two synthetic surfactants; a long chain quaternary ammonium surfactant, and a long chain alcohol. In this case, the performance of hair conditioner models were the primary focus, but these types of surfactants are significant components of a vast array of cosmetic products. A binary surfactant system containing both the quaternary ammonium and the alcohol surfactants are the subject of Chapter 4. Chapter 5 deals with the behaviour of just the quaternary ammonium surfactant at the air/water interface. The second category is the study of a surface active lipopetide named surfactin, and its interaction with phospholipid membranes. Surfactin is produced by some strains of *Bacillus Subtilis*, a ubiquitous bacterium which is found in the soil and the gastrointestinal tract of some mammals, including humans. Chapter 6 describes the production and characterisation of a type of solid-supported cell membrane to potentially be used for future work. The investigation of surfactin and its interaction with a phospholipid monolayer at the air/water interface is the focus of Chapters 7 and 8.

1.0.1 Publications

Parts of the work in Chapter 5 have been published in the Journal of Colloid and Interface Science [1], and parts of the work in Chapter 7 have been published in the Journal of Physical Chemistry B [2].

1.1 The binary surfactant system

Adsorption of surfactants onto a solid surface can greatly modify the properties of the surface such as its hydrophobicity, charge, and wettability, and affect interfacial processes such as corrosion and lubrication [3]. This makes them an important field in industrial research, where the relatively small amount of material needed to cover a surface makes modification in this manner desirable. In almost all applications, mixtures of one or more surfactants are used. Partly this is for economic reasons, but often mixtures will display properties that are more desirable than either of the pure surfactants; this phenomenon is referred to as synergism. In this report, a surfactant mixture of cetyl alcohol (CetOH, Figure 1.1a) and behenyl trimethylammonium chloride (BTAC, Figure 1.1b) are investigated on a silica surface as a simple model of hair conditioner.

Two forms of this mixture are investigated - one prepared by Unilever, using their proprietary method, which involves carefully heating the mixture to precise temperatures while stirring; and one prepared by hand in Cambridge, by grinding together using a mortar and pestle (both surfactants are solid at room-temperature). Both mixtures contain a 2:1 mass ratio of CetOH/BTAC.

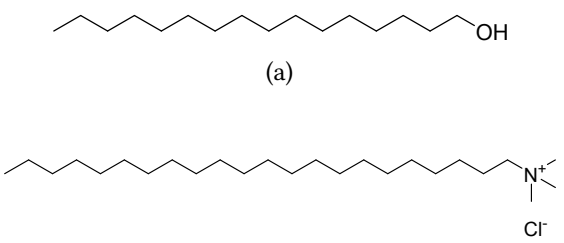

Figure 1.1: The structures of the surfactants used in this work.
(a) Hexadecan-1-ol (also known as cetyl alcohol, abbreviated in this thesis as CetOH).
(b) N,N,N-trimethyldocosan-1-aminium chloride (Behenyl trimethylammonium chloride, BTAC)

1.1.1 Mechanism of surfactant adsorption

BTAC is a cationic surfactant and has a positively charged head-group. Figure 1.2 shows the various regimes of adsorption of cationic surfactants onto solid surfaces. At low concentrations, cationic surfactants adsorb onto a negatively charged surface (such as silica) mainly via electrostatic attraction (top panel of Figure 1.2). Hydrophobic effects do not play a significant role at this low concentration, due to the distance between adsorbed molecules [4]. At slightly higher concentrations, more surfactants join those initially attracted, and hydrophobic interactions favour the formation of "islands" on the surface, rather than an even distribution of surfactant molecules. At concentrations just below the critical micelle concentration (CMC), micelles can form on the surface, seeded by the islands already present. Above the CMC, micelles adsorb directly from solution onto the surface [4]. When a cationic and non-ionic surfactant are combined in a mixture, the CMC is synergistically reduced [5, 6]. This is thought to be due to the shielding of the charge-charge repulsion between the head-groups of the cationic surfactant by the non-ionic surfactant.

The concentrations used here are above the theoretical CMC for BTAC, approximately 0.024 mM, which has been predicted here from the CMC values of shorter chain quaternary ammonium salts [7, 8]. There are no literature values for the CMC of BTAC; the solubility limit of BTAC is below the predicted CMC. CetOH is entirely insoluble, and does not form micelles spontaneously. Since the CMC of the CetOH/BTAC mixture is expected to be lower than that of the cationic component alone, the adsorption mechanism is likely to be in the hydrophobic region above the CMC, as depicted in the bottom panel of Figure 1.2, with micelles, comprised of a mixture of CetOH and BTAC, adsorbing directly onto the surface.

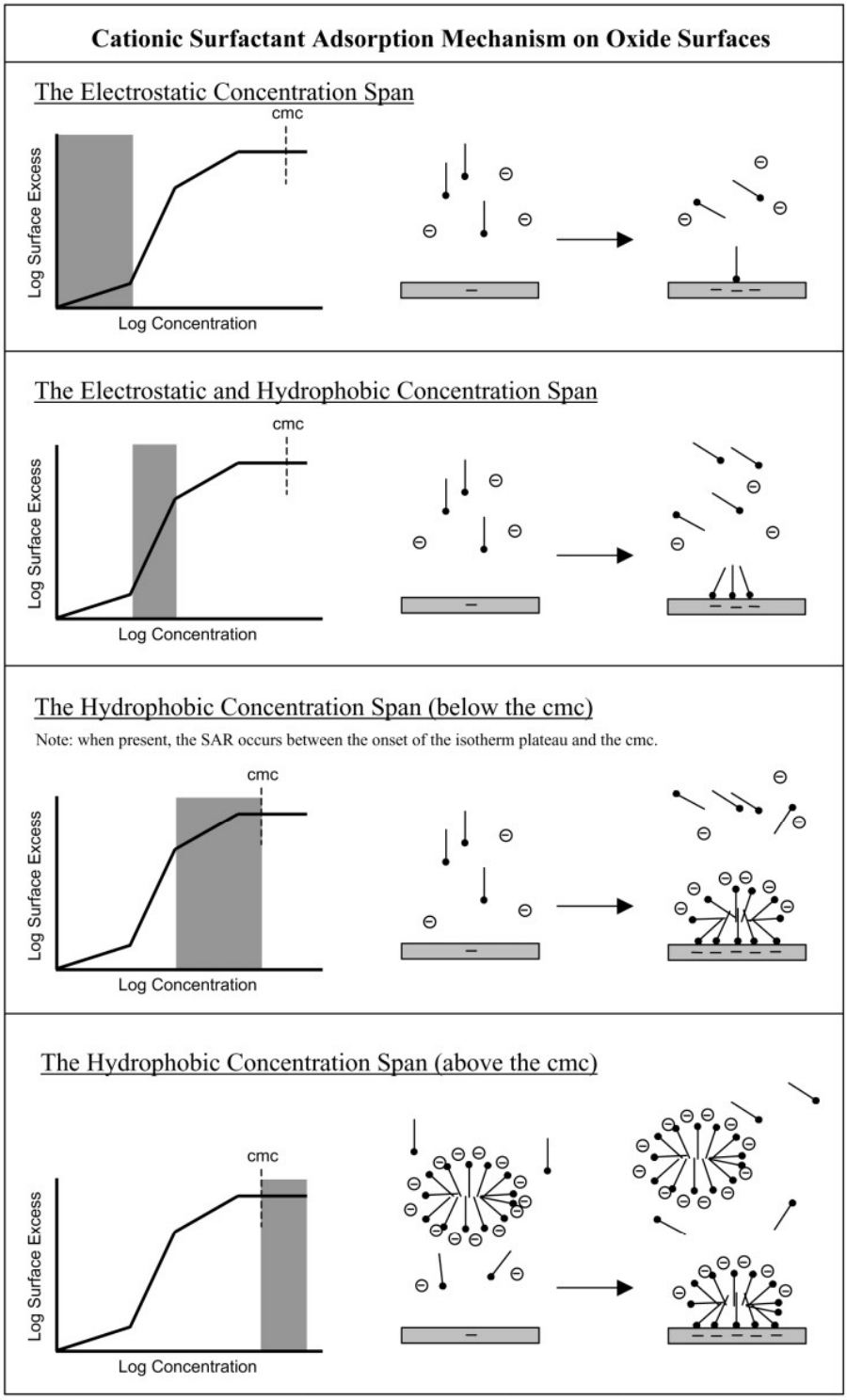

Figure 1.2: The different regimes of cationic surfactant absorption. Reproduced with permission from [4]. In each panel, the shaded region of the graph shows the concentration range (referred to as concentration span in the figure) in which each regime occurs. The adsorption experiments in Chapter 4 are expected to operate in the regime above the CMC.

1.1.2 Effect of increasing temperature

At higher temperatures, cationic surfactants show a reduced adsorption density at the surface. Higher temperatures favour higher entropy systems, and therefore promote desorption and reduced aggregate organisation on the surface [5, 9, 10]. However, for non-ionic surfactants, the opposite trend is observed [5, 11, 12]. It has been suggested that this is because of desolvation of the head-group at higher temperatures, making the surfactant less hydrophilic and more compact, and therefore more surface active [12].

1.1.3 Effect of increasing ionic strength

For non-ionic surfactants, the effect of ionic strength varies, depending on the specific surfactant and surface. The maximum adsorption amount has been observed to decrease if the ions adsorb strongly to the charged surface, displacing the surfactant [13]; or to increase due to improved lateral interactions between chains [11, 14]; or to be unaffected [13] by increasing the ionic strength.

For cationic surfactants adsorbing onto a negatively charged surface, increasing the ionic strength of the solution shields the charges, diminishing the attractive forces [5, 15], and reducing the rate of adsorption in the electrostatic concentration range. However, in the hydrophobic concentration range below the CMC, the adsorption amount increases [5]. In this region, the charge-charge repulsion between the head-groups is reduced by the shielding effect of the ions in the solution, and the aggregate on the surface becomes more stable. At higher concentrations of surfactant, in the hydrophobic range above the CMC, the total amount adsorbed is not greatly affected by ionic strength [5, 16]. For the mixed micelles of CetOH:BTAC investigated , the cations are already separated by the CetOH, and therefore the ions' effect of reducing charge-charge repulsion should be muted.

1.1.4 Prior art

Previous work on this system was carried out in an undergraduate study by Ben Caller. The focus of his work was to determine whether the BTAC/CetOH mixture was "draped" from the air/liquid interface onto the surface of the substrate - as the water recedes from

beneath the surfactant, the surfactant is laid onto the substrate. He concluded that this draping mechanism is not significantly responsible for the formation of the surfactant layer based on two main points. Firstly, he found that self-assembly occurs irreversibly before the water is removed. Secondly, he found that the ratio of CetOH/BTAC was different at the air/water interface compared to the silica/water interface, and that both were different from the bulk ratio. (Note that the second point was only confirmed for a hand-made mixture, not the mixture provided by Unilever.)

Since he concluded that self assembly is the primary mechanism by which the monolayers form, this work will investigate the effect of temperature and ionic strength on the self assembly of the mixtures onto silica surfaces.

1.2 Surfactants at the air/water interface

Amphiphilic molecules in water will be adsorbed to the air-water interface with hydrophobic sections in the air, and hydrophilic groups towards the water so as to reduce the free energy of the surface. When these molecules are insoluble, the monolayer must be cast onto the air-water interface from a volatile solvent which is immiscible with water, such as chloroform. Physical properties of films at the air/water interface are routinely investigated by the use of the Langmuir trough. The trough also enables the compression and study of these monolayers above their equilibrium spreading pressures (the surface pressure achieved when an amount of solid surfactant is placed at the surface and allowed to spread). Additionally, casting onto the air/water interface is the first step in the production of monolayer, bilayer and multilayer assemblies at solid/air and solid/water interfaces - important for cell membrane models (see section 1.3).

Since there is no solid support, the air/water interface itself can be experimentally challenging. However it is possible to use most spectroscopic techniques (such as IR, Raman, etc) by reflection or transmission through the air/water interface. Understanding surfactant behaviour at the air/water interface is important for atmospheric modelling [17, 18], oil-spill clean up processes (aquifer remediation) [19], and for any processes which involve liquid foams, including cosmetics, detergents, food products, and fire-fighting materials, as well as any processes in which foams are undesirable, such as wine fermentation, and glass and paper manufacturing [20, 21].

1.3 Cell membrane models

Biological cell membranes are incredibly complex molecular assemblies, serving multiple functions. Apart from forming a selectively permeable container, and protecting the contents of the cell, they also provide a scaffold for a vast array of biomolecules. (Figure 1.3). These are primarily comprised of proteins, and, amongst other activities, regulate cell signalling, cell adhesion, and the active transport of materials in and out of the cell.

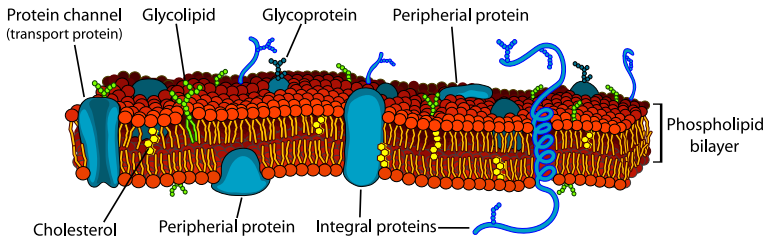

Figure 1.3: A depiction of a cell membrane, with various biomolecules embedded or attached. Adapted from [22].

This complexity makes investigation of the cell membrane very difficult. Therefore simplified models, which are more accessible to available experimental techniques, are often used. The cell membrane is comprised chiefly of the phospholipid bilayer; the most basic models are systems containing only phospholipids.

One of the earliest such models is the black lipid membrane, a phospholipid bilayer painted across the hole of a substrate [23, 24]. Since the membrane is in contact with aqueous solution on both sides, electrical conductivity tests are simple to do, and investigation of ion channel formation by proteins and other pore-forming biomolecules has been successfully carried out this way [24–26]. This also means that this system could be used as an electronic biosensor - a membrane protein could bind to a specific molecule and change the conductivity of the membrane, allowing electronic detection of that molecule [27–30].

However black lipid membranes have no solid support and are therefore extremely fragile. This makes surface-sensitive detection techniques, such as infrared or sum-frequency spectroscopy, very difficult. Forming a bilayer on a solid support is therefore desirable, and if the solid support is conductive, electrochemical impedance studies can still be carried out. Many variations of solid-supported bilayer systems exist, and a selection

are depicted in Figure 1.4. Reviews of the advantages and disadvantages of each are available in the literature [31–33], but briefly: the most basic solid-supported phospholipid bilayer system (Figure 1.4a) displays the most similar flexibility and lateral mobility of the phospholipid compared to a biological cell membrane; the hybrid phospholipid membrane (Figure 1.4b) combines a self-assembled monolayer (SAM) of thioalkanes and phospholipids - it sacrifices the lateral mobility and biological relevance of the proximal leaflet for greater resilience, longevity and a very straightforward synthesis; the fully tethered phospholipid bilayer membrane (Figure 1.4c) is somewhat more difficult to synthesise [34], but provides a better representation of a biological membrane. The sparsely tethered phospholipid bilayer membrane (Figure 1.4d) seeks to produce as relevant a model as possible while retaining some of the longevity of the fully tethered systems. This compromise can be affected by changing the tether/spacer ratio. Also, by selecting the correct tether and spacer, it is possible to introduce an ionic reservoir beneath the proximal leaflet, and thus make the model more similar to a biological membrane. This is especially important when investigating, for example, trans-membrane proteins [32, 33]. The system used in (Section 1.3.1) is of this type.

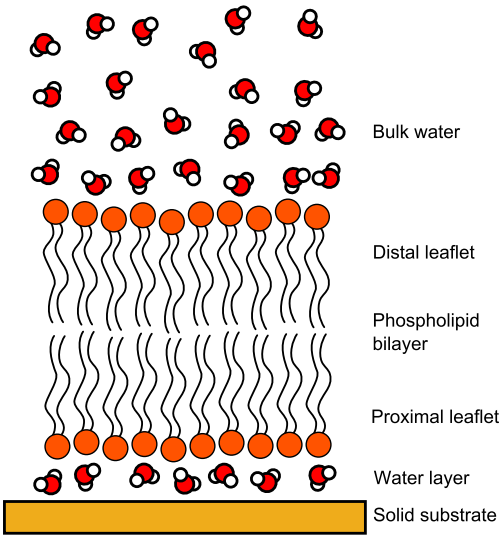

(a) A basic solid-supported phospholipid bilayer membrane

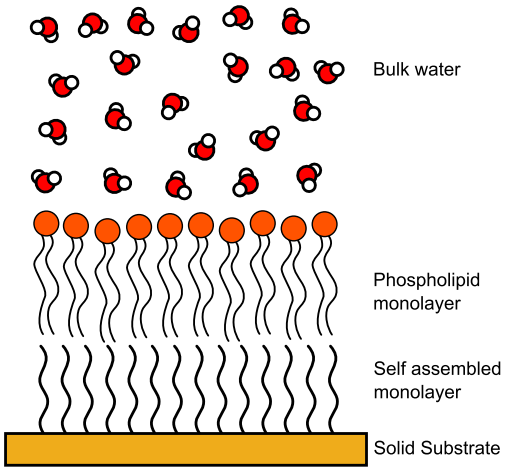

(b) A hybrid SAM phospholipid membrane.

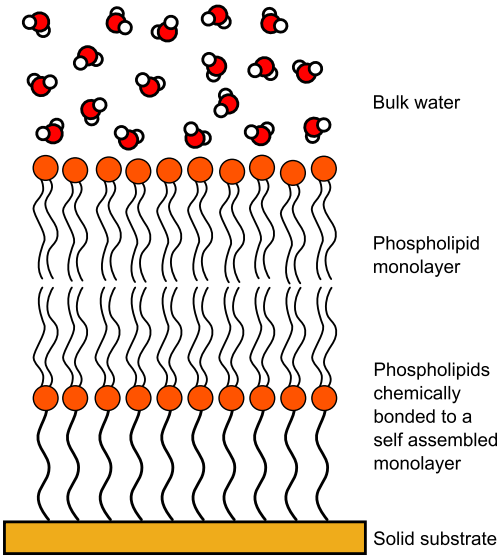

(c) A fully tethered phospholipid bilayer membrane.

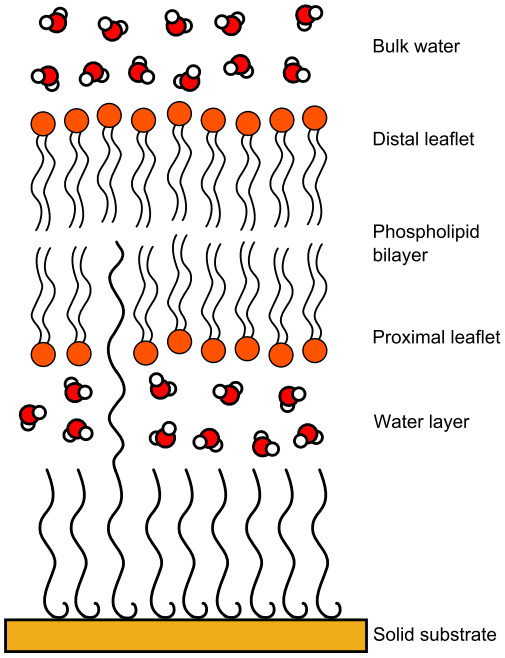

(d) A sparesly tethered phospholipid bilayer membrane.

Figure 1.4: Diagrams of four types of solid-supported model membranes. Many other variations exist. The type used in Chapter 6 is a sparsely tethered bilayer membrane, which is shown in (d).

1.3.1 The T10 self-assembled monolayer (SAM)

The initial T10 SAM (supplied by SDx Tethered Membranes) is prepared by self assembly of the disulfide tethers and spacers (Figure 1.5) onto a gold substrate from an ethanolic solution, to produce a monolayer of mixed disulfides on gold (Figure 1.6). The phytanyl acts as a half membrane spanning tether, and the OH-terminated spacer and polyethylene glycol chain together form an ionic reservoir beneath the proximal phospholipid leaflet. The T10 SAM and other tethered membrane SAMs of this type are in widespread use as the basis for cell membrane models [28, 30, 35–39].

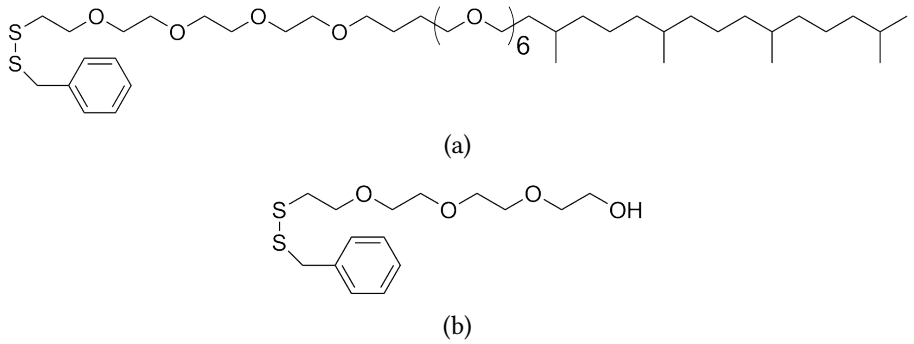

Figure 1.5: The structures of the disulfides used for self assembly to produce the T10 SAM: (a) the tether, benzyl disulfide PEG phytanyl, and (b) the spacer, benzyl disulfide tetraethylene glycol

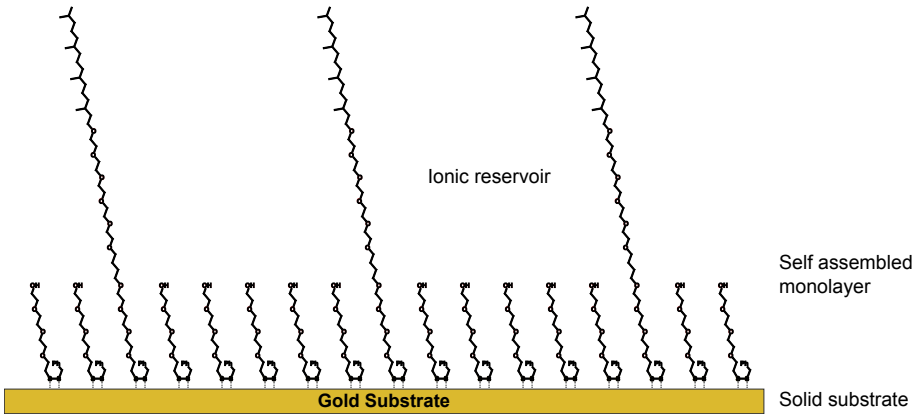

Figure 1.6: The structure of the T10 SAM as supplied by SDx Tethered Membranes. The spacer/tether ratio is 9:1.

1.3.2 Completing the tethered bilayer lipid membrane (tBLM)

A phospholipid must be incorporated between the tethers of the T10 SAM to produce a tBLM. The phospholipid in use here, dipalmitoyl phosphatidylethanolamine (DPPE), is shown in Figure 1.7 in the deuterated form.

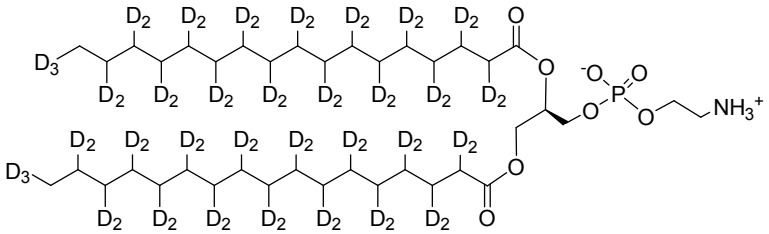

Figure 1.7: The structure of the deuterated phospholipid, d-DPPE, used in this work.

A common method of producing the phospholipid bilayer on the SAM tether is rapid solvent exchange (RSE) [27, 40–42]. The SAM is placed into a solution of phospholipid in ethanol. This is then flushed with a large amount of water or buffer, and this causes the precipitation of the phospholipid onto the SAM, forming a bilayer under water.

The RSE technique has been shown to produce complete bilayers, with the tethers incorporated (as shown in Figure 1.8), by both electrical impedance studies and by neutron reflectivity experiments [40, 42, 43]. However, because the bilayer is produced in one step, RSE alone cannot be used to form a bilayer in which only one leaflet is perdeuterated. This isotopic distinction of the leaflets is required for sum-frequency generation spectroscopy (SFG) due to the symmetry requirements of SFG, as discussed in Section 2.2).

Langmuir-Blodgett (LB) deposition, followed by Langmuir-Schaefer (LS) deposition, is capable of producing such a bilayer. In this technique, the SAM is submerged beneath the surface of the water in the Langmuir trough. The phospholipid is cast onto the surface, and compressed by barriers to a constant pressure, forming a monolayer on the surface. The SAM is then drawn up into air, whilst keeping the phospholipid at constant pressure, depositing this onto the SAM. However, since the monolayer of phospholipid is formed first, it is possible that once this has been deposited onto the SAM

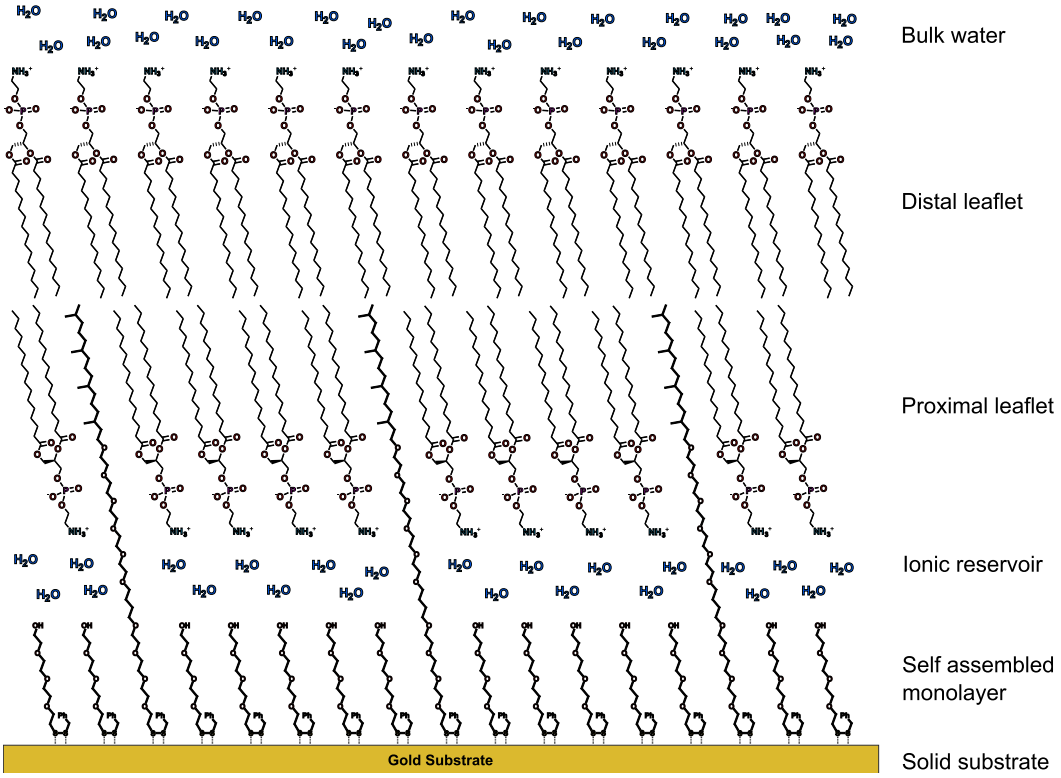

Figure 1.8: The structure of the T10 SAM, with an incorporated phospholipid lipid bilayer.

that the tethers are not incorporated in the proximal leaflet. The SAM starts under water, so the hydrophobic phytanyl tethers should be in random coils. Once the monolayer has been deposited onto the SAM, it presents a solid face of hydrophilic headgroups. This represents an energy barrier to the incorporation of the tethers - for the tether to penetrate the monolayer, the hydrogen bonds and electrostatic interactions between the headgroups of the phospholipid must be broken.

In any case, the bilayer can be completed by Langmuir-Schaefer deposition - the SAM, with the first half of the membrane already in place, is held face down above another monolayer of phospholipid cast onto the surface of the water in the LB trough. The SAM is lowered onto this monolayer, completing the bilayer, and then further lowered into the water (as the bilayer is not stable in air). Now the completed membrane, with isotopically distinguishable leaflets, has been formed on the SAM.

1.4 Phospholipid monolayers at the air/water interface

Another example of a phospholipid membrane is a simple monolayer at the air/water interface. Whilst the tethered bilayer is in most aspects a much better model for the cell membrane, the monolayer at the air/water interface has some useful advantages. Firstly, the structure and behaviour of the phospholipid monolayer at the air/water interface is relatively well studied and understood by infrared spectroscopy [44, 45], Brewster angle [46] and fluorescence microscopy [47], and surface pressure - area isotherms [48]. The lateral pressure (surface pressure) of the air/water interface can be monitored and controlled throughout experiments so that the molecular area matches that of cell membranes. This is especially useful if the goal of the experiment is to monitor a change in monolayer properties due to membrane-penetrating molecules (such as described in Section 1.6). Secondly, being a monolayer, no isotopic distinction is required to observe the monolayer using SFG spectroscopy. This enables the use of deuteration to observe a different molecule in the monolayer, whilst also monitoring the phospholipid signals.

1.5 Antimicrobial peptides (AMPs)

Antimicrobial peptides (AMPs) are produced by various organisms as part of their immune response to microbial infection. Their mode of action is often by permeating the cell membrane, disrupting their function by causing leakage, reducing ion gradients, or in some cases by lysis of the cell (essentially dissolving the membrane), all resulting in cell death. AMPs were first identified as early as 1922 [49] and then sporadically [50–53] until the 1980s, at which point discoveries were made more rapidly [54–56]. There are now more than 2000 known AMPs in multiple online databases [57–68] The vast majority of natural AMPs are cationic (the bacterial membranes which they target are usually overall negatively charged) and 30-65 amino acid residues in length [69].

There are many models explaining the mode of action of AMPs on the cell membrane, as shown in Figure 1.9 [70]. These include the carpet-like and detergent models, which cause membrane instability or solubilisation by affecting mechanical properties such as membrane curvature, and pore-forming models such as the toroidal-pore and the barrel-

stave models, which have more well-defined structures, whereby the AMP stabilises the formation of a pore in the membrane. Additionally, AMPs may simply aggregate within the membrane without forming well-defined structures, as in the toroidal-pore and barrel-stave models. There is overlap between these models - that is, they share certain characteristics with each other. Firstly, they all begin with adsorption of the AMP to the membrane. In the toroidal-pore, barrel-stave, and carpet mechanisms, a critical threshold of adsorbed AMP at the membrane is reached. In the barrel-stave and toroidal-pore model, this results in insertion of the AMPs into the membrane, whereby multiple AMP molecules insert simultaneously in a concerted manner. In the carpet mechanism, reaching the critical threshold of adsorbed AMPs results in micellisation and solubilisation of the membrane. The detergent model is sometimes distinguished by including an insertion step, and then later solubilisation, as the number of AMP molecules within the bilayer increases.

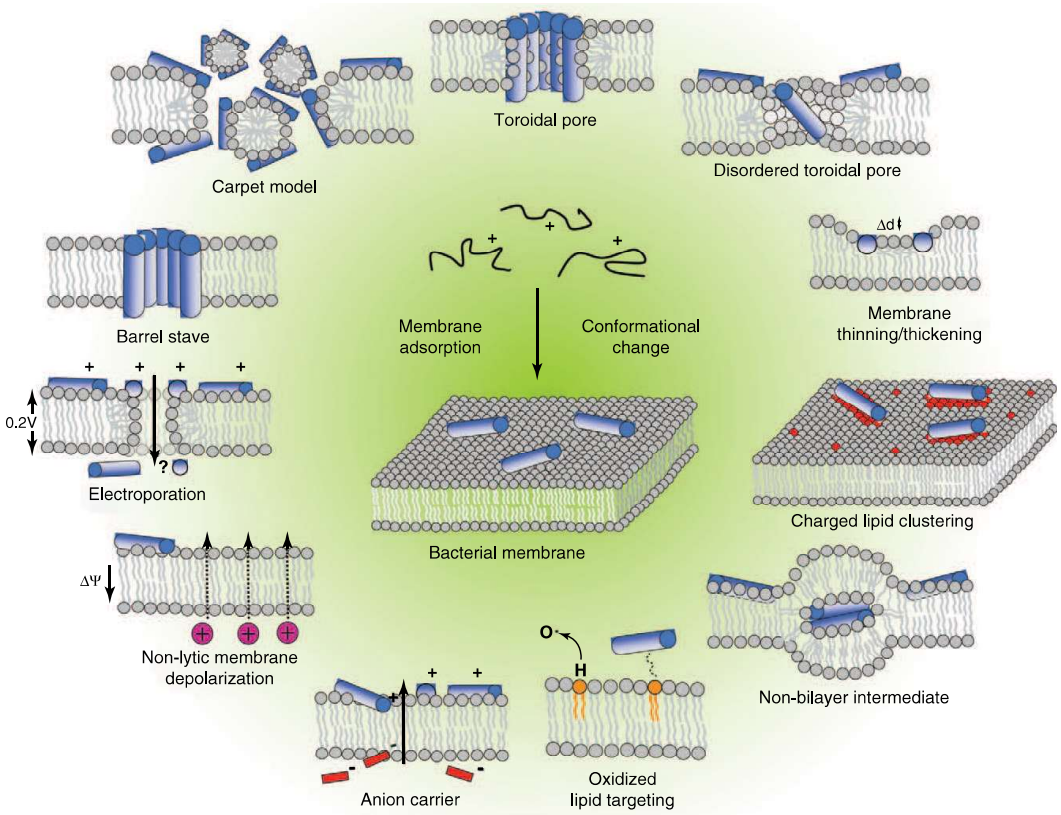

Figure 1.9: Shown are different models of AMP-membrane interactions. All begin with an adsorption step, shown in the central feature of this diagram. Reproduced with permission from [70].

1.6 Surfactin

Surfactin (Figure 1.10) is a microbial lipopeptide that was first isolated in 1968 from a culture of *Bacillis Subtilis*, and aptly named for its very high surface activity [71]. Much research has been conducted on its physical properties, chemical structure, and biological activity. It can reduce the surface tension of water from 72 mN/m to 27 mN/m at concentrations as low as 6×10^{-6} M, its critical micelle concentration (cmc) [72, 73], making it much more potent than sodium dodecyl sulfate, a common commercial surfactant that reduces surface tension to 34 mN/m at 8.1 $\times 10^{-3}$ M [74]. Surfactin also displays strong antibacterial, antiviral, and haemolytic properties.

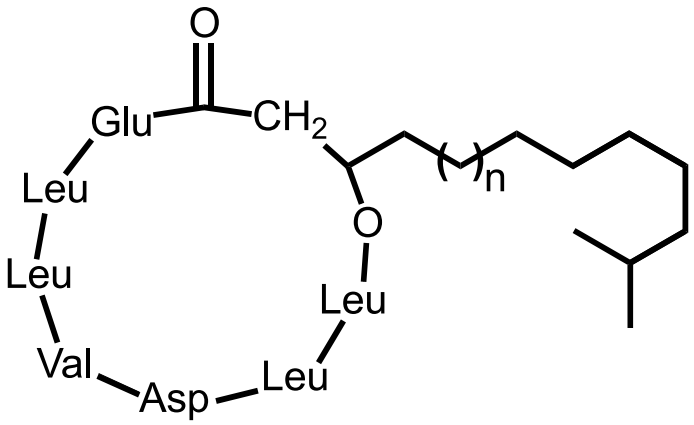

Figure 1.10: The structure(s) of surfactin A (n=1), surfactin B (n=2) and surfactin C (n=3), as produced by Bacillus Subtilis. Amino acid residues are represented by their three letter codes. The full explicit structure is shown in Chapter 7, Figure 7.1.

Surface pressure studies of surfactin have found that its behaviour at the air/water interface depends strongly on the pH of the subphase and the presence of metal cations [75]. Maget-Dana and Ptak concluded that these observations were due to a change in ionisation of the surfactin - the acid groups were neutralised by the low pH and metal cations, and this affected the compressibility of the surfactin monolayer. Ishigami et al. used compression isotherms to infer that the surfactin molecules form dimers on the surface so that alkyl tails share a hydrophobic contact [76]. Computer simulation of surfactin at the air-water interface by Iglesiaz-Fernández concluded that tail groups should interact strongly with the hydrophobic leucine groups of the heptapeptide ring, both within a single molecule and with the leucine groups of neighbouring molecules [77].

Like other antibacterial lipopeptides, surfactin is known to act as an antibacterial agent via interaction with bacterial cell membranes [78]. At low concentrations, it causes leakage of the cell contents, and at concentrations above the CMC, it is capable of entirely solubilising the membrane. Surfactin's interaction with cell membranes has been studied by NMR [79, 80], atomic force microscopy (AFM) and surface pressure studies [81–85], neutron reflectivity (NR) and small-angle neutron scattering (SANS) [86, 87], and computer modelling [83, 88]. The exact mechanism by which surfactin penetrates into the membrane, or by which it solubilises the cell membrane, is not clear. However, a detergent-like model [79, 88–90] and a mechanism with characteristics of a barrel-stave and aggregation model [86, 87] have both been proposed.

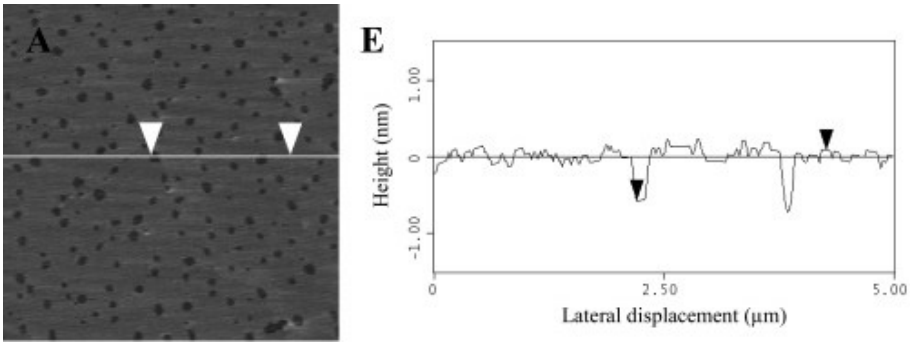

Figure 1.11: AFM image of a surfactin-DPPC monolayer (left). Reproduced with permission from [84]. Copyright © 2006 American Chemical Society. Surfactin-rich domains are darkly coloured, and are lower than the DPPC region, as shown in the cross section (right).

The interaction of surfactins of different fatty acid chain lengths with monolayers of different phospholipids was investigated by Deleu and co-workers using Atomic Force Microscopy (AFM) in combination with surface pressure - area isotherms recorded on a Langmuir trough. They found that surfactin-rich domains formed in the phospholipid monolayers, and that the size and shape of these domains was strongly influenced by the type of phospholipid used (due to chain length, and headgroup charge). The AFM image (reproduced from [84]) for the surfactin and 1,2-dipalmitoyl-sn-glycero-3-phosphocholine (DPPC) combination is shown in Figure 1.11. Computer simulation by the same group indicated that surfactin solubilises phospholipid bilayers via a detergent mechanism in two distinct steps: "In the first step, a low concentration of surfactin penetrates into the erythrocyte membrane by interacting via its fatty acid chain. In a

second step, approaching the CMC, surfactin molecules self-associate to form micelles involving membrane phospholipids and leading to membrane rupture." [88]

NMR studies conducted by Heerklotz, Wieprecht and Seelig on multilamellar vesicles of 1-palmitoyl-2-oleoyl-sn-glycero-3-phosphocholine (POPC) incorporating surfactin indicated that surfactin embeds deeply into the hydrophobic region of the bilayer [79], which they concluded on the basis of the phospholipid structure inferred from their data. This is in agreement with the computer-modelling results for uncharged membranes by Deleu et al [83, 88]. However, when the membrane was charged, computer modelling indicated that the centre of mass of the surfactin was located in the headgroup region of the phospholipid membrane. The modelling results also indicated that, when the surfactin was incorporated into the phospholipid membrane, extending the alkyl tail to interact with the phospholipid hydrophobic region was favourable. However, neutron reflectivity (NR) and SANS studies by Shen et al [73, 86, 87] showed that surfactin was localized closer to the headgroup rather than the chain of the phospholipid, and that in general surfactin maintained a compact ball-like structure and that "surfactin is more like a mainly hydrophobic ball than a conventional surfactant" [87].

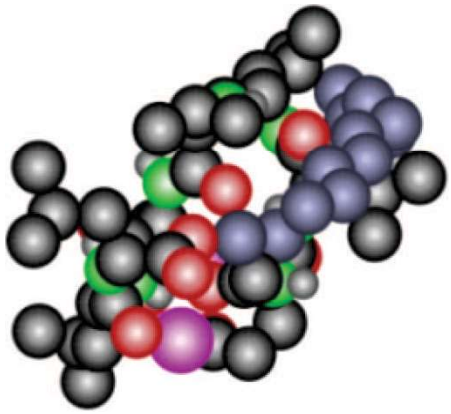

Figure 1.12: The "hydrophobic ball" structure proposed by Shen et al on the basis of their NR results. Reproduced with permission from [73]. Copyright ©2009 American Chemical Society. The alkyl tail (shown with blue-grey carbon atoms) is folded over the top of the ring structure, to interact with the leucine isopropyl groups (peptide carbons are rendered in black). Nitrogen atoms are green, oxygen atoms are red, and the O^- of the acid groups are magenta.

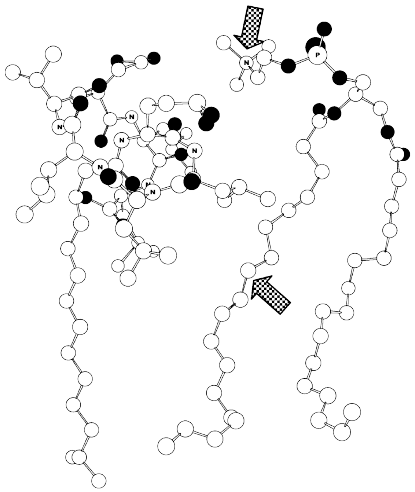

(a) The structure of the phospholipid and surfactin interaction proposed by Heerklotz et al on the basis of their NMR data. Reproduced with permission from [79]. Copyright ©2004 American Chemical Society. Surfactin (left molecule) is fairly deeply embedded into the phospholipid (right molecule). Arrows indicate the structural changes of the lipid induced by the surfactin.

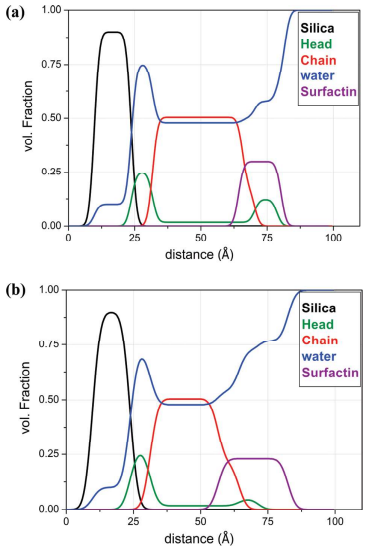

(b) The distribution profile of surfactin in a solid-supported phospholipid bilayer. Reproduced with permission from [86]. Copyright ©2010 American Chemical Society. "Head" and "Chain" refer to the phospholipid. The top distribution profile was obtained when the bilayer was formed on the solid support with surfactin already present, and the lower profile was obtained when surfactin was injected into the solution after the DPPC bilayer had been formed.

Figure 1.13: Two proposed structures of the surfactin-phospholipid systems

Shen et al used their NR data to infer a barrel-stave mechanism for the penetration of surfactin into the outer leaflet of the bilayer membrane [86]. They also showed that solubilisation required a threshold concentration of surfactin in the bilayer to be reached, in agreement with the modelling results of Deleu et al [88]. Their SANS data indicated that surfactin-DPPC vesicles had surfactin aggregates with an aggregation number of around 50 in the bilayer structure. They concluded that significant rearrangement would be required after the penetration step for this aggregation number to be reached, and that this rearrangement resulted in the immediate desorption of the surfactin and the DPPC in proximity with the aggregate [87].

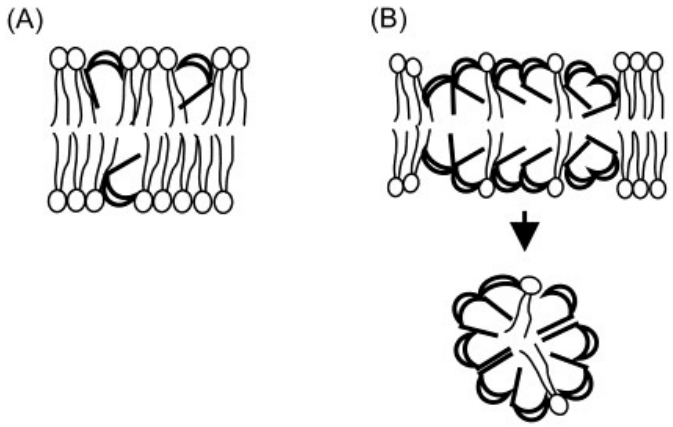

Figure 1.14: The two-step detergent mechanism proposed by Deleu et al [88], on the basis of their AFM data and computer simulation. Quoting directly: "(A) At low concentration, penetration of surfactin in the bilayer (B) at concentrations closer to the CMC, formation of micelles including membrane phospholipids, leading to the solubilisation of the bilayer." Reproduced with permission from [88]. Copyright ©2003 American Society.

1.7 Sum-frequency generation spectroscopy of lipid membranes

Although surfactin has not previously been studied using sum-frequency generation spectroscopy (SFG), the clear utility of this interface-specific technique in studying the phospholipid membranes and the various molecules and processes associated with them has been widely realised. The earliest SFG studies of phospholipid membranes was in 1997 by the Richmond group [91]. In this case, a DPPC monolayer was established at the CCl_4/water interface. In 1999, two more groups used SFG to study phospholipids. Löbau et al [92] used SFG to observe the temperature-dependent phase transition in a selection of phospholipids cast onto a solid/air interface. Petralli-Mallow et al [93] used SFG to monitor the formation of a hybrid bilayer membrane by vesicle fusion of DPPC onto a self-assembled alkanethiol monolayer on gold. Since then, a wide variety of model membranes have been studied, including Langmuir monolayers [94, 95], solid-supported bilayers [96–99] and tethered bilayer membranes [34]. Model membranes with adsorbed or embedded biomolecules have been investigated using SFG by various groups, and include studies of cholesterol [100], membrane proteins [101–104], and both natural and synthetic AMPs [105–112].

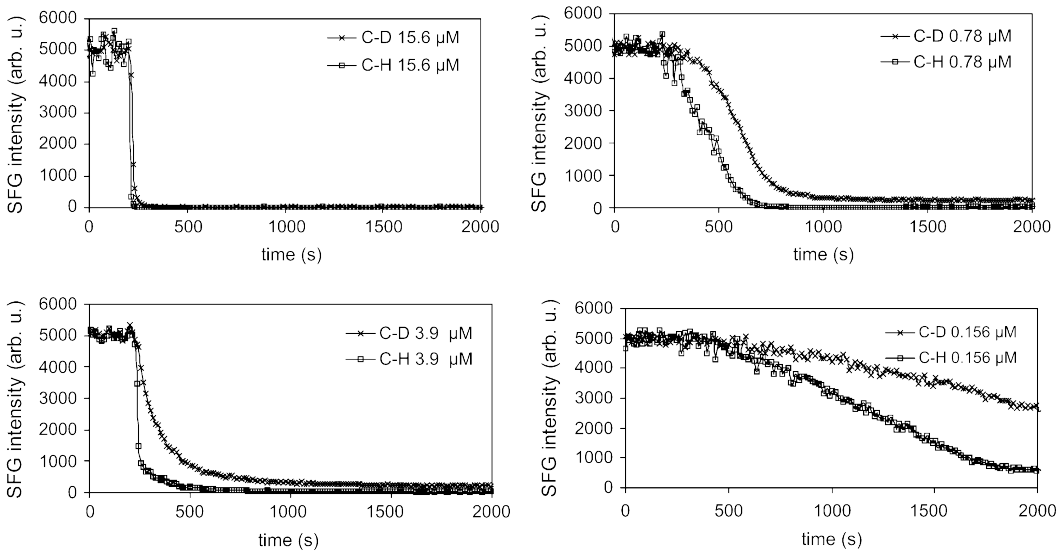

Figure 1.15: SFG was used to monitor the effect of melettin, an AMP, on a solid-supported d-DPPG/DPPG bilayer at 4 different concentrations. Both the CH methyl and CD methyl resonances reduce in intensity during the interaction with the membrane-penetrating AMP, representing the increasing disordering caused by melettin. Reproduced with permission from [107]. Copyright ©2007 American Chemical Society.

The Chen group, in a series of publications, was able to use SFG to observe the destruction of solid-supported membranes due to AMPs such as melettin [106, 107], alamethicin [110], and a synthetic AMP [111], as well as one planar molecule designed to have amphiphilic properties that mimic natural AMPs, such as magainin [108]. MSI-78 (the synthetic AMP), melettin, and alamethicin were monitored primarily through the amide I band in the spectral region 1630-1680 cm^{-1}. All three comprise a well-defined α-helix structure, and by measuring the polarisation ratio of χ_{SSP}/χ_{PPP} (discussed later in Section 2.2), they were able calculate the average tilt angle of the amide bond, and therefore the orientation of the peptide in the membranes. In the case of the planar synthetic antimicrobial compound, tilt angle calculations were conducted on CH and CO stretches. Additionally, by monitoring CH and CD signals arising from the phospholipid bilayers, they were able to monitor the disruption of each layer as the AMP of interest penetrated the membrane.

References

[1] S. A. Goussous, M. T. L. Casford, S. A. Johnson, and P. B. Davies, "A structural and temporal study of the surfactants behenyltrimethylammonium methosulfate and behenyltrimethylammonium chloride adsorbed at air/water and air/glass interfaces using sum frequency generation spectroscopy," *Journal of Colloid and Interface Science*, vol. 488, pp. 365–372, Feb. 2017.

[2] S. A. Goussous, M. T. L. Casford, A. C. Murphy, G. P. C. Salmond, F. J. Leeper, and P. B. Davies, "Structure of the fundamental lipopeptide surfactin at the air/water interface investigated by sum frequency generation spectroscopy," *The Journal of Physical Chemistry B*, vol. 121, pp. 5072–5077, May 2017.

[3] R. Zhang and P. Somasundaran, "Advances in adsorption of surfactants and their mixtures at solid/solution interfaces," *Advances in Colloid and Interface Science*, vol. 123-126, pp. 213–229, Nov. 2006.

[4] R. Atkin, V. Craig, E. Wanless, and S. Biggs, "The influence of chain length and electrolyte on the adsorption kinetics of cationic surfactants at the silica–aqueous solution interface," *Journal of Colloid and Interface Science*, vol. 266, pp. 236–244, Oct. 2003.

[5] S. Paria and K. C. Khilar, "A review on experimental studies of surfactant adsorption at the hydrophilic solid–water interface," *Advances in Colloid and Interface Science*, vol. 110, pp. 75–95, Aug. 2004.

[6] P. Somasundaran and L. Huang, "Adsorption/aggregation of surfactants and their mixtures at solid–liquid interfaces," *Advances in Colloid and Interface Science*, vol. 88, pp. 179–208, Dec. 2000.

[7] J. A. Cella, D. N. Eggenberger, D. R. Noel, L. A. Harriman, and H. J. Harwood, "The relation of structure and critical concentration to the bactericidal activity of quaternary ammonium salts," *Journal of the American Chemical Society*, vol. 74, pp. 2061–2062, Apr. 1952.

[8] M. J. Rosen and J. T. Kunjappu, *Surfactants and Interfacial Phenomena.* Hoboken, NJ, USA: John Wiley & Sons, Inc., Mar. 2012.

[9] A. L. Meader and B. A. Fries, "Adsorption in the detergent process," *Industrial & Engineering Chemistry*, vol. 44, pp. 1636–1648, July 1952.

[10] P. C. Pavan, E. L. Crepaldi, G. de A. Gomes, and J. B. Valim, "Adsorption of sodium dodecylsulfate on a hydrotalcite-like compound. Effect of temperature, pH and ionic strength," *Colloids and Surfaces A: Physicochemical and Engineering Aspects*, vol. 154, pp. 399–410, Aug. 1999.

[11] S. Partyka, S. Zaini, M. Lindheimer, and B. Brun, "The adsorption of non-ionic surfactants on a silica gel," *Colloids and Surfaces*, vol. 12, pp. 255–270, Jan. 1984.

[12] J. M. Corkill, J. F. Goodman, and J. R. Tate, "Adsorption of non-ionic surface-active agents at the graphon/solution interface," *Transactions of the Faraday Society*, vol. 62, p. 979, Jan. 1966.

[13] D. Nevskaia, A. Guerrero-Ruíz, and J. de D. López-González, "Adsorption of polyoxyethylenic nonionic and anionic surfactants from aqueous solution: effects induced by the addition of NaCl and $CaCl_2$," *Journal of Colloid and Interface Science*, vol. 205, pp. 97–105, Sept. 1998.

[14] S. Partyka, M. Lindheimer, and B. Faucompre, "Aggregate formation at the solid-liquid interface: the calorimetric evidence," *Colloids and Surfaces A: Physicochemical and Engineering Aspects*, vol. 76, pp. 267–281, Sept. 1993.

[15] A. W. Adamson and A. P. Gast, *The Physical Chemistry of Surfaces.* Wiley, 6th ed., 1997.

[16] L. K. Koopal, E. M. Lee, and M. R. Böhmer, "Adsorption of cationic and anionic surfactants on charged metal oxide surfaces," *Journal of Colloid and Interface Science*, vol. 170, pp. 85–97, Mar. 1995.

[17] W.-t. Tsai, "An assessment of the effect of sea surface surfactant on global atmosphere-ocean CO_2 flux," *Journal of Geophysical Research*, vol. 108, p. 3127, Apr. 2003.

[18] R. Pereira, I. Ashton, B. Sabbaghzadeh, J. D. Shutler, and R. C. Upstill-Goddard, "Reduced air–sea CO_2 exchange in the Atlantic Ocean due to biological surfactants," *Nature Geoscience*, vol. 11, pp. 492–496, July 2018.

[19] G. Hirasaki, C. Miller, R. Szafranski, J. Lawson, and N. Akiya, "Surfactant/foam process for aquifer remediation," in *International Symposium on Oilfield Chemistry*, pp. 471–480, Society of Petroleum Engineers, Apr. 1997.

[20] P. Stevenson, *Foam Engineering: Fundamentals and Applications*. Chichester, UK: John Wiley & Sons, Ltd, Feb. 2012.

[21] I. Cantat, S. Cohen-Addad, F. Elias, F. Graner, R. Höhler, O. Pitois, F. Rouyer, A. Saint-Jalmes, and R. Flatman, *Foams: Structure and Dynamics*. Oxford University Press, July 2013.

[22] M. Ruiz, "commons.wikimedia.org/wiki/File:Cell_membrane_detailed_diagram_en.svg," 2007.

[23] P. Mueller, D. O. Rudin, H. T. Tien, and W. C. Wescott, "Methods for the formation of single biomolecular lipid membranes in aqueous solution," *The Journal of Physical Chemistry*, vol. 67, pp. 534–535, Feb. 1963.

[24] P. Mueller, D. O. Rudin, H. T. Tien, and W. C. Wescott, "Reconstitution of cell membrane structure in vitro and its transformation into an excitable system," *Nature*, vol. 194, pp. 979–980, June 1962.

[25] E. Bamberg, H. Alpes, H. J. Apell, R. Bradley, B. Härter, M. J. Quelle, and D. W. Urry, "Formation of ionic channels in black lipid membranes by succinic derivatives of Gramicidin A," *The Journal of Membrane Biology*, vol. 50, pp. 257–270, Sept. 1979.

[26] F. Gómez-Lagunas, A. Peña, A. Liévano, and A. Darszon, "Incorporation of ionic channels from yeast plasma membranes into black lipid membranes," *Biophysical Journal*, vol. 56, pp. 115–119, July 1989.

[27] B. A. Cornell, V. L. Braach-Maksvytis, L. G. King, P. D. Osman, B. Raguse, L. Wieczorek, and R. J. Pace, "A biosensor that uses ion-channel switches.," *Nature*, vol. 387, pp. 580–583, June 1997.

[28] V. Atanasov, N. Knorr, R. S. Duran, S. Ingebrandt, A. Offenhäusser, W. Knoll, and I. Köper, "Membrane on a chip: a functional tethered lipid bilayer membrane on silicon oxide surfaces," *Biophysical Journal*, vol. 89, pp. 1780–1788, Sept. 2005.

[29] H. Z. Goh, *Solid-Supported Lipid Membranes : Formation , Stability and Applications*. PhD thesis, Carnegie Mellon University, 2013.

[30] J. Prashar, P. Sharp, M. Scarffe, and B. Cornell, "Making lipid membranes even tougher," *Journal of Materials Research*, vol. 22, pp. 2189–2194, Jan. 2007.

[31] F. Giess, M. G. Friedrich, J. Heberle, R. L. Naumann, and W. Knoll, "The protein-tethered lipid bilayer: a novel mimic of the biological membrane," *Biophysical Journal*, vol. 87, pp. 3213–3220, Nov. 2004.

[32] M. Tanaka and E. Sackmann, "Polymer-supported membranes as models of the cell surface.," *Nature*, vol. 437, pp. 656–63, Sept. 2005.

[33] E. T. Castellana and P. S. Cremer, "Solid supported lipid bilayers: from biophysical studies to sensor design," *Surface Science Reports*, vol. 61, pp. 429–444, June 2006.

[34] M. T. L. Casford, A. Ge, P. J. N. Kett, S. Ye, and P. B. Davies, "The structure of lipid bilayers adsorbed on activated carboxy-terminated monolayers investigated by sum frequency generation spectroscopy," *The Journal of Physical Chemistry B*, vol. 118, pp. 3335–3345, Mar. 2014.

[35] B. Raguse, V. Braach-Maksvytis, B. A. Cornell, L. G. King, P. D. J. Osman, R. J. Pace, and L. Wieczorek, "Tethered lipid bilayer membranes: formation and ionic reservoir characterization," *Langmuir*, vol. 14, pp. 648–659, Feb. 1998.

[36] G. Krishna, J. Schulte, B. A. Cornell, R. J. Pace, and P. D. Osman, "Tethered bilayer membranes containing ionic reservoirs: selectivity and conductance," *Langmuir*, vol. 19, pp. 2294–2305, Mar. 2003.

[37] E. Petrov, P. R. Rohde, B. Cornell, and B. Martinac, "The protective effect of osmoprotectant TMAO on bacterial mechanosensitive channels of small conductance MscS/MscK under high hydrostatic pressure," *Channels*, vol. 6, pp. 262–271, Oct. 2014.

[38] W. Hoiles, V. Krishnamurthy, C. G. Cranfield, and B. Cornell, "An engineered membrane to measure electroporation: effect of tethers and bioelectronic interface," *Biophysical Journal*, vol. 107, pp. 1339–1351, Sept. 2014.

[39] C. G. Cranfield, B. A. Cornell, S. L. Grage, P. Duckworth, S. Carne, A. S. Ulrich, and B. Martinac, "Transient potential gradients and impedance measures of tethered bilayer lipid membranes: pore-forming peptide insertion and the effect of electroporation," *Biophysical Journal*, vol. 106, pp. 182–189, Jan. 2014.

[40] D. J. McGillivray, G. Valincius, D. J. Vanderah, W. Febo-Ayala, J. T. Woodward, F. Heinrich, J. J. Kasianowicz, and M. Lösche, "Molecular-scale structural and functional characterization of sparsely tethered bilayer lipid membranes.," *Biointerphases*, vol. 2, pp. 21–33, Mar. 2007.

[41] D. J. McGillivray, G. Valincius, F. Heinrich, J. W. Robertson, D. J. Vanderah, W. Febo-Ayala, I. Ignatjev, M. Lösche, and J. J. Kasianowicz, "Structure of functional staphylococcus aureus α-hemolysin channels in tethered bilayer lipid membranes," *Biophysical Journal*, vol. 96, pp. 1547–1553, Feb. 2009.

[42] R. Budvytyte, M. Mickevicius, D. J. Vanderah, F. Heinrich, and G. Valincius, "Modification of tethered bilayers by phospholipid exchange with vesicles," *Langmuir*, vol. 29, pp. 4320–4327, Apr. 2013.

[43] S. Shenoy, R. Moldovan, J. Fitzpatrick, D. J. Vanderah, M. Deserno, and M. Lösche, "In-plane homogeneity and lipid dynamics in tethered bilayer lipid membranes (tBLMs)," *Soft Matter*, vol. 6, p. 1263, Jan. 2010.

[44] R. Mendelsohn, G. Mao, and C. R. Flach, "Infrared reflection-absorption spectroscopy: principles and applications to lipid-protein interaction in Langmuir films," *Biochimica et Biophysica Acta - Biomembranes*, vol. 1798, pp. 788–800, Jan. 2010.

[45] T. E. Goto and L. Caseli, "Understanding the collapse mechanism in Langmuir monolayers through polarization modulation-infrared reflection absorption spectroscopy," *Langmuir*, vol. 29, pp. 9063–9071, July 2013.

[46] R. Volinsky, F. Gaboriaud, A. Berman, and R. Jelinek, "Morphology and organization of phospholipid/diacetylene Langmuir films studied by Brewster angle microscopy and fluorescence microscopy," *The Journal of Physical Chemistry B*, vol. 106, pp. 9231–9236, Sept. 2002.

[47] H. Mohwald, "Phospholipid and phospholipid-protein monolayers at the air/water interface," *Annual Review of Physical Chemistry*, vol. 41, pp. 441–476, Oct. 1990.

[48] A. Saint-Jalmes, M. Assenheimer, and F. Gallet, "Surface tension and compression modulus anisotropies of a phospholipid monolayer spread on water and on formamide," *The Journal of Physical Chemistry B*, vol. 102, pp. 5810–5815, July 1998.

[49] A. Fleming and V. D. Allison, "Further observations on a bacteriolytic element found in tissues and secretions," *Proceedings of the Royal Society B: Biological Sciences*, vol. 94, pp. 142–151, Nov. 1922.

[50] R. D. Hotchkiss and R. J. Dubos, "Fractionation of the bactericidal agent from cultures of a soil Bacillus," *Journal of Biological Chemistry*, vol. 132, pp. 791–792, Feb. 1940.

[51] G. F. Gause and M. G. Braznhikova, "Gramicidin S and its use in the treatment of infected wounds," *Nature*, vol. 154, pp. 703–703, Dec. 1944.

[52] P. G. Stansly, R. G. Shepherd, and H. J. White, "Polymyxin: a new chemotherapeutic agent.," *Bulletin of the Johns Hopkins Hospital*, vol. 81, pp. 43–54, July 1947.

[53] J. F. Fennell, W. H. Shipman, and L. J. Cole, "Antibacterial action of a bee venom fraction (melittin) against a penicillin-resistant staphylococcus and other microorganisms," *Research and development technical report. United States. Naval Radiological Defense Laboratory, San Francisco*, pp. 1–13, Dec. 1967.

[54] H. Steiner, D. Hultmark, Å. Engström, H. Bennich, and H. G. Boman, "Sequence and specificity of two antibacterial proteins involved in insect immunity," *Nature*, vol. 292, pp. 246–248, July 1981.

[55] M. E. Selsted, S. S. Harwig, T. Ganz, J. W. Schilling, and R. I. Lehrer, "Primary structures of three human neutrophil defensins," *Journal of Clinical Investigation*, vol. 76, pp. 1436–1439, Oct. 1985.

[56] M. Zasloff, "Magainins, a class of antimicrobial peptides from Xenopus skin: isolation, characterization of two active forms, and partial cDNA sequence of a precursor," *Proceedings of the National Academy of Sciences of the United States of America*, vol. 84, pp. 5449–53, Aug. 1987.

[57] Z. Wang, "APD: the antimicrobial peptide database," *Nucleic Acids Research*, vol. 32, pp. 590D–592, Jan. 2004.

[58] G. Wang, X. Li, and Z. Wang, "APD2: the updated antimicrobial peptide database and its application in peptide design," *Nucleic Acids Research*, vol. 37, pp. D933–D937, Jan. 2009.

[59] V. Seshadri Sundararajan, M. N. Gabere, A. Pretorius, S. Adam, A. Christoffels, M. Lehväslaiho, J. A. C. Archer, and V. B. Bajic, "DAMPD: a manually curated antimicrobial peptide database," *Nucleic Acids Research*, vol. 40, pp. D1108–D1112, Jan. 2012.

[60] S. Thomas, S. Karnik, R. S. Barai, V. K. Jayaraman, and S. Idicula-Thomas, "CAMP: a useful resource for research on antimicrobial peptides," *Nucleic Acids Research*, vol. 38, pp. D774–D780, Jan. 2010.

[61] M. Brahmachary, "ANTIMIC: a database of antimicrobial sequences," *Nucleic Acids Research*, vol. 32, pp. 586D–589, Jan. 2004.

[62] L. Whitmore, "The Peptaibol Database: a database for sequences and structures of naturally occurring peptaibols," *Nucleic Acids Research*, vol. 32, pp. 593D–594, Jan. 2004.

[63] R. Hammami, J. Ben Hamida, G. Vergoten, and I. Fliss, "PhytAMP: a database dedicated to antimicrobial plant peptides," *Nucleic Acids Research*, vol. 37, pp. D963–D968, Jan. 2009.

[64] Y. Gueguen, J. Garnier, L. Robert, M. Lefranc, I. Mougenot, J. de Lorgeril, M. Janech, P. Gross, G. Warr, B. Cuthbertson, A. B. Margherita, P. Bulet, A. Aumelas, Y. Yang, D. Bo, J. Xiang, A. Tassanakajon, D. Piquemal, and E. Bachère, "PenBase, the shrimp antimicrobial peptide penaeidin database: sequence-based classification and recommended nomenclature," *Developmental & Comparative Immunology*, vol. 30, pp. 283–288, May 2006.

[65] M. Novković, J. Simunić, V. Bojović, A. Tossi, and D. Juretić, "DADP: the database of anuran defense peptides," *Bioinformatics*, vol. 28, pp. 1406–1407, Mar. 2012.

[66] A. de Jong, A. J. van Heel, J. Kok, and O. P. Kuipers, "BAGEL2: mining for bacteriocins in genomic data," *Nucleic Acids Research*, vol. 38, pp. W647–W651, July 2010.

[67] R. Hammami, A. Zouhir, C. Le Lay, J. Ben Hamida, and I. Fliss, "BACTIBASE second release: a database and tool platform for bacteriocin characterization," *BMC Microbiology*, vol. 10, p. 22, Oct. 2010.

[68] S. Seebah, A. Suresh, S. Zhuo, Y. H. Choong, H. Chua, D. Chuon, R. Beuerman, and C. Verma, "Defensins knowledgebase: a manually curated database and information source focused on the defensins family of antimicrobial peptides," *Nucleic Acids Research*, vol. 35, pp. D265–D268, Jan. 2007.

[69] G. Wang, "Database-guided discovery of potent peptides to combat HIV-1 or superbugs," *Pharmaceuticals*, vol. 6, pp. 728–758, May 2013.

[70] L. T. Nguyen, E. F. Haney, and H. J. Vogel, "The expanding scope of antimicrobial peptide structures and their modes of action," *Trends in Biotechnology*, vol. 29, pp. 464–472, Sept. 2011.

[71] K. Arima, A. Kakinuma, and G. Tamura, "Surfactin, a crystalline peptidelipid surfactant produced by Bacillus subtilis: isolation, characterization and its inhibition of fibrin clot formation.," *Biochemical and Biophysical Research Communications*, vol. 31, pp. 488–94, May 1968.

[72] M.-S. Yeh, Y.-H. Wei, and J.-S. Chang, "Enhanced production of surfactin from Bacillus subtilis by addition of solid carriers," *Biotechnology Progress*, vol. 21, pp. 1329–1334, Sept. 2008.

[73] H.-H. Shen, R. K. Thomas, C.-y. Chen, R. C. Darton, S. C. Baker, and J. Penfold, "Aggregation of the naturally occurring lipopeptide, surfactin, at interfaces and in solution: an unusual type of surfactant?," *Langmuir*, vol. 25, pp. 4211–4218, Apr. 2009.

[74] K. J. Mysels, "Surface tension of solutions of pure sodium dodecyl sulfate," *Langmuir*, vol. 2, pp. 423–428, July 1986.

[75] R. Maget-Dana and M. Ptak, "Interfacial properties of surfactin," *Journal of Colloid and Interface Science*, vol. 153, pp. 285–291, Oct. 1992.

[76] Y. Ishigami, M. Osman, H. Nakahara, Y. Sano, R. Ishiguro, and M. Matsumoto, "Significance of β-sheet formation for micellization and surface adsorption of surfactin," *Colloids and Surfaces B: Biointerfaces*, vol. 4, pp. 341–348, July 1995.

[77] J. Iglesias-Fernández, L. Darré, A. Kohlmeyer, R. K. Thomas, H.-H. Shen, and C. Domene, "Surfactin at the water/air interface and in solution," *Langmuir*, vol. 31, pp. 11097–11104, Oct. 2015.

[78] N. Tsukagoshi, G. Tamura, and K. Arima, "A novel protoplast-bursting factor (surfactin) obtained from Bacillus subtilis IAM 1213," *Biochimica et Biophysica Acta (BBA) - Biomembranes*, vol. 196, pp. 204–210, Feb. 1970.

[79] H. Heerklotz, T. Wieprecht, and J. Seelig, "Membrane perturbation by the lipopeptide surfactin and detergents as studied by deuterium NMR," *The Journal of Physical Chemistry B*, vol. 108, pp. 4909–4915, Apr. 2004.

[80] H. Heerklotz and J. Seelig, "Leakage and lysis of lipid membranes induced by the lipopeptide surfactin," *European Biophysics Journal*, vol. 36, pp. 305–314, Apr. 2007.

[81] M. Deleu, M. Paquot, P. Jacques, P. Thonart, Y. Adriaensen, and Y. F. Dufrêne, "Nanometer scale organization of mixed surfactin/phosphatidylcholine monolayers," *Biophysical Journal*, vol. 77, pp. 2304–2310, Oct. 1999.

[82] M. Deleu, K. Nott, R. Brasseur, P. Jacques, P. Thonart, and Y. F. Dufrêne, "Imaging mixed lipid monolayers by dynamic atomic force microscopy," *Biochimica et Biophysica Acta (BBA) - Biomembranes*, vol. 1513, pp. 55–62, July 2001.

[83] O. Bouffioux, A. Berquand, M. Eeman, M. Paquot, Y. Dufrêne, R. Brasseur, and M. Deleu, "Molecular organization of surfactin–phospholipid monolayers: Effect of phospholipid chain length and polar head," *Biochimica et Biophysica Acta (BBA) - Biomembranes*, vol. 1768, pp. 1758–1768, July 2007.

[84] M. Eeman, A. Berquand, Y. F. Dufrêne, M. Paquot, S. Dufour, and M. Deleu, "Penetration of surfactin into phospholipid monolayers: nanoscale interfacial organization," *Langmuir*, vol. 22, pp. 11337–11345, Dec. 2006.

[85] G. Francius, S. Dufour, M. Deleu, M. Paquot, M. P. Mingeot-Leclercq, and Y. F. Dufrêne, "Nanoscale membrane activity of surfactins: influence of geometry, charge and hydrophobicity," *Biochimica et Biophysica Acta - Biomembranes*, vol. 1778, pp. 2058–2068, Apr. 2008.

[86] H.-H. Shen, R. K. Thomas, and P. Taylor, "The location of the biosurfactant surfactin in phospholipid bilayers supported on silica using neutron reflectometry," *Langmuir*, vol. 26, pp. 320–327, Jan. 2010.

[87] H.-H. Shen, R. K. Thomas, J. Penfold, and G. Fragneto, "Destruction and solubilization of supported phospholipid bilayers on silica by the biosurfactant surfactin," *Langmuir*, vol. 26, pp. 7334–7342, May 2010.

[88] M. Deleu, O. Bouffioux, H. Razafindralambo, M. Paquot, C. Hbid, P. Thonart, P. Jacques, and R. Brasseur, "Interaction of surfactin with membranes: a computational approach," *Langmuir*, vol. 19, pp. 3377–3385, Apr. 2003.

[89] H. Heerklotz, "Interactions of surfactants with lipid membranes," *Quarterly Reviews of Biophysics*, vol. 41, p. 205, Nov. 2008.

[90] H. Heerklotz and J. Seelig, "Detergent-like action of the antibiotic peptide surfactin on lipid membranes," *Biophysical Journal*, vol. 81, pp. 1547–1554, Sept. 2001.

[91] R. A. Walker, J. C. Conboy, and G. L. Richmond, "Molecular structure and ordering of phospholipids at a liquid-liquid interface," *Langmuir*, vol. 13, pp. 3070–3073, June 1997.

[92] J. Löbau, M. Sass, W. Pohle, C. Selle, M. Koch, and K. Wolfrum, "Chain fluidity and phase behaviour of phospholipids as revealed by FTIR and sum-frequency spectroscopy," *Journal of Molecular Structure*, vol. 480-481, pp. 407–411, May 1999.

[93] T. P. Petralli-Mallow, K. A. Briggman, L. J. Richter, J. C. Stephenson, and A. L. Plant, "Nonlinear optics as a detection scheme for biomimetic sensors: SFG spectroscopy of hybrid bilayer membrane formation," in *Proc. SPIE* (M. Fallahi and B. I. Swanson, eds.), vol. 25, p. 25, Dec. 1999.

[94] S. Roke, J. Schins, M. Müller, and M. Bonn, "Vibrational spectroscopic investigation of the phase diagram of a biomimetic lipid monolayer," *Physical Review Letters*, vol. 90, p. 128101, Mar. 2003.

[95] L. Fu, G. Ma, and E. C. Y. Yan, "In situ misfolding of human islet amyloid polypeptide at interfaces probed by vibrational sum frequency generation," *Journal of the American Chemical Society*, vol. 132, pp. 5405–5412, Apr. 2010.

[96] J. Liu and J. C. Conboy, "Direct measurement of the transbilayer movement of phospholipids by sum-frequency vibrational spectroscopy," *Journal of the American Chemical Society*, vol. 126, pp. 8376–8377, June 2004.

[97] J. Liu and J. C. Conboy, "Phase transition of a single lipid bilayer measured by sum-frequency vibrational spectroscopy," *Journal of the American Chemical Society*, vol. 126, pp. 8894–8895, June 2004.

[98] J. Liu and J. C. Conboy, "Structure of a gel phase lipid bilayer prepared by the Langmuir-Blodgett/ Langmuir-Schaefer method characterized by sum-frequency vibrational spectroscopy," *Langmuir*, vol. 21, pp. 9091–9097, Aug. 2005.

[99] J. Liu and J. C. Conboy, "Asymmetric distribution of lipids in a phase segregated phospholipid bilayer observed by sum-frequency vibrational spectroscopy," *Journal of Physical Chemistry C*, vol. 111, pp. 8988–8999, Mar. 2007.

[100] P. J. N. Kett, M. T. L. Casford, and P. B. Davies, "Structure of mixed phosphatidylethanolamine and cholesterol monolayers in a supported hybrid bilayer membrane studied by sum frequency generation vibrational spectroscopy," *The Journal of Physical Chemistry B*, vol. 115, pp. 6465–6473, May 2011.

[101] K. T. Nguyen, R. Soong, S.-C. Lm, L. Waskell, A. Ramamoorthy, and Z. Chen, "Probing the spontaneous membrane insertion of a tail-anchored membrane protein by sum frequency generation spectroscopy," *Journal of the American Chemical Society*, vol. 132, pp. 15112–15115, Nov. 2010.

[102] K. T. Nguyen, J. T. King, and Z. Chen, "Orientation determination of interfacial β-sheet structures in situ," *The Journal of Physical Chemistry B*, vol. 114, pp. 8291–8300, July 2010.

[103] X. Chen, A. P. Boughton, J. J. G. Tesmer, and Z. Chen, "In situ investigation of heterotrimeric G protein $\beta\gamma$ subunit binding and orientation on membrane bilayers," *Journal of the American Chemical Society*, vol. 129, pp. 12658–12659, Oct. 2007.

[104] P. Yang, A. Boughton, K. T. Homan, J. J. G. Tesmer, and Z. Chen, "Membrane orientation of Gα(i)β(1)γ(2) and Gβ(1)γ(2) determined via combined vibrational spectroscopic studies.," *Journal of the American Chemical Society*, vol. 135, pp. 5044–51, Apr. 2013.

[105] T. C. Anglin, J. Liu, and J. C. Conboy, "Facile lipid flip-flop in a phospholipid bilayer induced by gramicidin a measured by sum-frequency vibrational spectroscopy," *Biophysical Journal*, vol. 92, pp. L01–L03, Jan. 2007.

[106] X. Chen, J. Wang, A. P. Boughton, C. B. Kristalyn, and Z. Chen, "Multiple orientation of melittin inside a single lipid bilayer determined by combined vibrational spectroscopic studies," *Journal of the American Chemical Society*, vol. 129, pp. 1420–7, Feb. 2007.

[107] X. Chen, J. Wang, C. B. Kristalyn, and Z. Chen, "Real-time structural investigation of a lipid bilayer during its interaction with melittin using sum frequency generation vibrational spectroscopy," *Biophysical journal*, vol. 93, pp. 866–75, Aug. 2007.

[108] X. Chen, H. Tang, M. A. Even, J. Wang, G. N. Tew, and Z. Chen, "Observing a molecular knife at work," *Journal of the American Chemical Society*, vol. 128, pp. 2711–4, Mar. 2006.

[109] C. W. Avery, A. Som, Y. Xu, G. N. Tew, and Z. Chen, "Dependence of antimicrobial selectivity and potency on oligomer structure investigated using substrate supported lipid bilayers and sum frequency generation vibrational spectroscopy," *Analytical Chemistry*, vol. 81, pp. 8365–72, Oct. 2009.

[110] S. Ye, K. T. Nguyen, and Z. Chen, "Interactions of alamethicin with model cell membranes investigated using sum frequency generation vibrational spectroscopy in real time in situ.," *The Journal of Physical Chemistry B*, vol. 114, pp. 3334–40, Mar. 2010.

[111] P. Yang, A. Ramamoorthy, and Z. Chen, "Membrane orientation of MSI-78 measured by sum frequency generation vibrational spectroscopy.," *Langmuir*, vol. 27, pp. 7760–7, June 2011.

[112] Y. Liu, J. Jasensky, and Z. Chen, "Molecular interactions of proteins and peptides at interfaces studied by sum frequency generation vibrational spectroscopy," *Langmuir*, vol. 28, pp. 2113–2121, Jan. 2012.

2. Theory

2.1 The Langmuir trough

The Langmuir trough is extensively used when studying monolayers and bilayers, either in their preparation onto solid substrates, or for studying directly by surface pressure - area isotherms or by spectroscopy at the air/water interface. Therefore, a brief description of the theory is warranted.

2.1.1 Surface tension and surface pressure

Surface tension is a measure of the forces that cause a liquid to maintain the smallest surface area it can (the reason why water droplets at zero gravity are spherical). It is most easily explained using an argument of balancing energy - water molecules are in a lower energy state when maximising the number of hydrogen bonds. Minimising the surface area for a given volume of water maximises the number of hydrogen bonds formed, and results in a lower free energy state. An explanation from examining the balance of forces is also often used, as shown in figure 2.1. However, the imbalance observed here is only in the perpendicular direction, whilst empirically surface tension is observed as a force in the surface plane. Perhaps because of this, the idea that an actual tensile force is present in the plane and pulling on molecules has been questioned. It has been said that understanding surface tension in this way is "a useful fiction" [1], and that "surface tension does not exist as a physical reality, and is only the mathematical equivalent of free surface energy" [2]. However, an explanation for the origin of such a force has been presented [3, 4]. An in-depth review of this explanation is beyond the scope of this document, but by examining how the pressure and density of the liquid changed during the transition from bulk liquid to the vapour phase, the author [3, 4] concluded that the tensile force is real, and therefore force arrows drawn in the plane of the surface are physically valid.

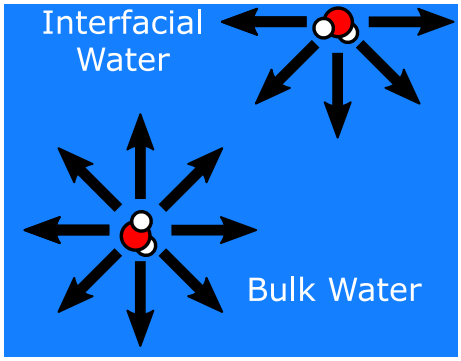

Figure 2.1: The imbalanced attractive forces acting on the water molecules at the interface are often used to explain surface tension.

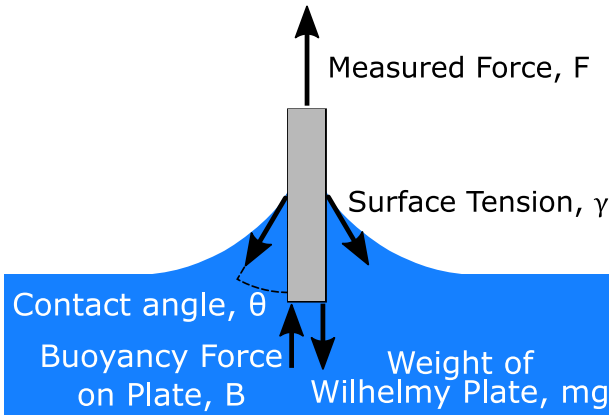

Figure 2.2: A cross-sectional image of a Wilhelmy plate in contact with the water surface, showing the forces involved in measuring the surface pressure. An arbitrary contact angle has been shown here; in practice, the plate is roughened so that it is completely wetted, so that this angle is zero.

In any case, if one were to dip an object into the water surface, it would be pulled by the surface tension. Using a Wilhelmy Plate in a Langmuir trough (see Figure 2.2), the pulling force on the plate can be measured to deduce the surface tension:

$$F = 2(t + w)\gamma cos\theta + mg - B \tag{2.1}$$

where F is the measured force, γ is the surface tension, t and w are the thickness and width of the paper plate, θ is the contact angle of the meniscus with the plate, m is the mass of the plate, g is the gravitational constant, and B is the upward force of buoyancy. If the electrobalance is zeroed with the plate just off the surface (where $\gamma = 0$), when the

plate is lowered to barely contact the water surface (so that buoyancy doesn't contribute), the measured force represents only the first term. With knowledge of the thickness and width of the plate, and contact angle of the water, the absolute value of the surface tension of the liquid can be calculated. In practice, when studying surfactants, the absolute surface tension is often not of interest. In this case, the electrobalance is zeroed after the plate is in contact with the water and has equilibrated, but before any surfactant is added. The change in the force being measured after this point is given by:

$$F_0 - F = \left[2(t + w)\gamma_0 cos\theta + mg - B\right] - \left[2(t + w)\gamma cos\theta + mg - B\right] \tag{2.2}$$

$$\Delta F = 2(t + w)(\gamma_0 - \gamma)cos\theta \tag{2.3}$$

where γ_0 is the original surface tension of the pure liquid and γ is the surface tension of the liquid with any impurities added (generally a negative value, as the surface tension drops when impurities are added). For the commonly assumed case of complete wetting of the Wilhelmy plate, the contact angle θ is equal to zero, and therefore the equation can be simplified and rearranged:

$$\frac{\Delta F}{2(t + w)} = \gamma_0 - \gamma \tag{2.4}$$

$\frac{\Delta F}{2(t+w)}$ is known as the surface pressure, Π. Just as in-plane forces are valid for surface tension, the surface pressure can be thought of as in-plane lateral repulsive forces exerted by surfactants at the interface.

In order to measure this, the surfactants must be applied to the surface. The surfactant of interest is dissolved in a suitable volatile solvent, and a small drop of this surfactant solution is allowed to fall from a syringe held a few millimetres above the surface. This drop spreads across the surface of the water, and the solvent is allowed to evaporate, leaving behind just the surfactant at the air/water interface. If the solvent used is soluble in water, it may also dissolve into the subphase, carrying the surfactant with it - hence water-miscible solvents are avoided where possible. After the solvent has evaporated, the monolayer can be compressed by use of barriers on the water surface, which are moved to reduce the available water surface area. The surface pressure is measured as the monolayer is compressed, and is plotted against the molecular area (which is calculated by dividing the available surface area by the number of molecules applied to the surface). This produces the isotherm shown in figure 2.3.

The packing and organisation of the monolayer depend strongly on the lateral pressure and on the molecular area available. At high molecular areas, the surfactants have room

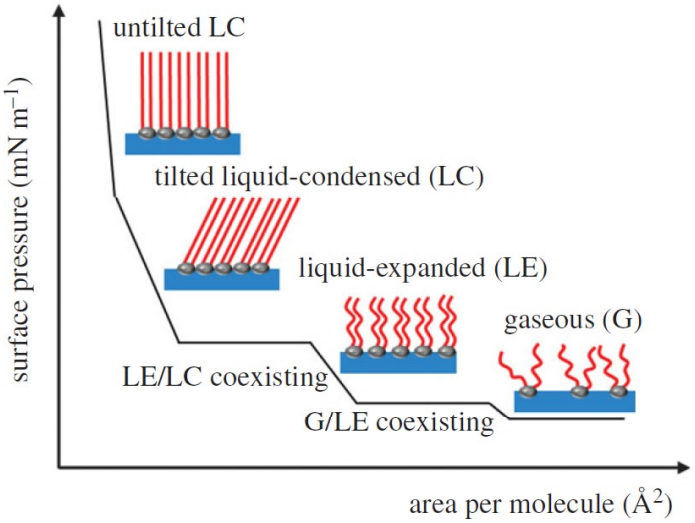

Figure 2.3: An illustration of a surface pressure - molecular area (Π-*A*) isotherm with cartoons of the phase state. Flat regions represent the coexistence of two phases. Adapted from [5].

to form gauche defects and become disordered on the surface. As the monolayer is compressed, these molecules must fit into a smaller area, and therefore gauche defects disappear, and the molecules become less tilted, reducing their molecular area. The formation of these gauche defects and the degree of tilting can be measured by sum-frequency spectroscopy, as explained in the next section.

2.2 Sum-frequency generation (SFG) spectroscopy

SFG spectroscopy is a surface-specific non-linear optical technique. To produce a SFG signal, a fixed-frequency visible laser beam and a variable-frequency infrared (IR) laser beam are temporally and spatially overlapped on a surface or interface (figure 2.4). In addition to reflection and transmission of the visible and IR lasers, the non-linear process of SFG results in light being emitted at the sum of their frequencies:

$$\omega_{SFG} = \omega_{VIS} + \omega_{IR} \tag{2.5}$$

where ω is the frequency of the relevant beam. By varying the frequency of the IR beam and measuring the output SFG beam intensity, the SFG response of the molecules at the surface can be obtained through a range of frequencies, producing a vibrational spectrum analogous to that produced by conventional IR spectroscopy. SFG spectroscopy has been used to gain information on the polar orientation [6, 7], tilt angle [8–10], and degree of conformational ordering of alkyl chains [11–13] adsorbed at an interface or surface since first being observed from an alkane monolayer in the mid to late 1980s [7, 14].

Full theoretical descriptions of SFG are available in the literature [15–19], as well as recent developments in its application [10], but a brief summary of SFG theory and analysis is presented in this section, following closely the method and conventions used in the review by Lambert et al [20].

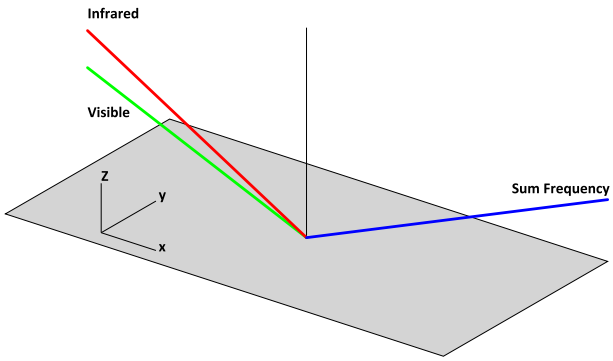

Figure 2.4: An example of an SFG stage with the co-propagating beam geometry used in this work. All beams propagate in the positive x direction, and the reflected IR and visible beams have been omitted for clarity.

2.2.1 Origin of the sum-frequency signal

When light is incident on an isolated molecule in the gas phase, the electric field of the light exerts a force on the valence electrons of the molecule [21]. A first approximation for the induced dipole moment, $\boldsymbol{\mu}$ is given by,

$$\boldsymbol{\mu} = \boldsymbol{\mu}_0 + \alpha \mathbf{E} \tag{2.6}$$

where $\boldsymbol{\mu}_0$ is the permanent dipole of the molecule, α is the polarisability of the molecule, and $\mathbf{E}$ is the electric field component of the incident light.

In a bulk material, the sum over the induced dipole moments of the individual molecules gives the bulk polarisation, $\mathbf{P}$. For low-intensity light, this is given by,

$$\mathbf{P} = \mathbf{P}_0 + \epsilon_0 \chi^{(1)} \mathbf{E} \tag{2.7}$$

where $\mathbf{P}_0$ is the permanent bulk polarisation of the material, ϵ_0 is the vacuum permittivity, $\chi^{(1)}$ is the first-order bulk susceptibility, and $\mathbf{E}$ is the electric field component of the incident light, as before.

The majority of materials do not have a permanent bulk polarisation, and therefore $\mathbf{P}_0$ may be set to zero to give,

$$\mathbf{P} = \epsilon_0 \chi^{(1)} \mathbf{E} \tag{2.8}$$

Equation (2.8) is a valid approximation when the intensity of the incident light is low. For higher intensities, higher-order terms of the electric field strength, along with higher-order terms for the susceptibilities and polarisabilities, must also be considered. Equations (2.6) and (2.8) then become:

$$\boldsymbol{\mu} = \boldsymbol{\mu}_0 + \alpha \mathbf{E} + \beta \mathbf{E}^2 + \gamma \mathbf{E}^3 + \ldots \tag{2.9}$$

$$\mathbf{P} = \epsilon_0 (\chi^{(1)} \mathbf{E} + \chi^{(2)} \mathbf{E}^2 + \chi^{(3)} \mathbf{E}^3 + \ldots) \tag{2.10}$$

where β and γ are the second- and third-order molecular polarisabilities, and $\chi^{(2)}$ and $\chi^{(3)}$ are the second- and third-order bulk susceptibilities, respectively. $\chi^{(2)}$ is the macroscopic average of β, and $\chi^{(3)}$ is the macroscopic average of γ. [1]

[1] The form of equation (2.10) as written is a common (and possibly confusing) shorthand. Strictly speaking, the polarisation is a vector field, and the i^{th} component of $\mathbf{P}$ is expressed as

$$\mathbf{P}_i = \epsilon_0 \Big[\sum_j \chi^{(1)}_{ij} \mathbf{E}_j + \sum_{jk} \chi^{(2)}_{ijk} \mathbf{E}_j \mathbf{E}_k + \sum_{jkl} \chi^{(3)}_{ijkl} \mathbf{E}_j \mathbf{E}_k \mathbf{E}_l + \ldots \Big] \tag{2.11}$$

Non-linear optical effects, such as SFG, arise from the second-order polarisability, $\chi^{(2)}$, which is much smaller in magnitude than $\chi^{(1)}$. To observe significant non-linear optical effects, $\mathbf{E}$ must be sufficiently large to compensate for the fact that $\chi^{(2)}$ is much smaller than $\chi^{(1)}$. Therefore, pulsed lasers, which are capable of producing these large field strengths, are used to probe $\chi^{(2)}$.

In the SFG experiment, the IR and visible lasers are temporally and spatially overlapped at the surface, so the total $\mathbf{E}$ is given by summing over the two oscillating electric fields of the two incident beams. The instantaneous electric field at the surface at time, t is given by,

$$\mathbf{E} = \mathbf{E}_{IR} \cos \omega_{IR} t + \mathbf{E}_{vis} \cos \omega_{vis} t \tag{2.12}$$

Substituting this equation for $\mathbf{E}$ into the equation for the bulk polarisation, equation (2.10), gives:

$$\begin{aligned} \mathbf{P} = \epsilon_0 [\chi^{(1)} &(\mathbf{E}_{IR} \cos \omega_{IR} t + \mathbf{E}_{vis} \cos \omega_{vis} t) \\ &+ \chi^{(2)} (\mathbf{E}_{IR} \cos \omega_{IR} t + \mathbf{E}_{vis} \cos \omega_{vis} t)^2 \\ &+ \chi^{(3)} (\mathbf{E}_{IR} \cos \omega_{IR} t + \mathbf{E}_{vis} \cos \omega_{vis} t)^3 + \ldots] \end{aligned} \tag{2.13}$$

Considering only the second-order term (from which the SFG signal arises), and multiplying out the brackets:

$$\mathbf{P}^{(2)} = \epsilon_0 \chi^{(2)} (\mathbf{E}_{IR}^2 \cos^2 \omega_{IR} t + \mathbf{E}_{vis}^2 \cos^2 \omega_{vis} t + 2\mathbf{E}_{IR} \cos \omega_{IR} t \mathbf{E}_{vis} \cos \omega_{vis} t) \tag{2.14}$$

and then applying trigonometric identities:

$$\begin{aligned} \mathbf{P}^{(2)} = \epsilon_0 \chi^{(2)} [\frac{1}{2} &(\mathbf{E}_{IR}^2 + \mathbf{E}_{vis}^2) + (\mathbf{E}_{IR}^2 \cos 2\omega_{IR} t + \mathbf{E}_{vis}^2 \cos 2\omega_{vis} t) \\ &+ \mathbf{E}_{IR} \mathbf{E}_{vis} \cos(\omega_{vis} - \omega_{IR}) t + \mathbf{E}_{IR} \mathbf{E}_{vis} \cos(\omega_{vis} + \omega_{IR}) t \ ] \end{aligned} \tag{2.15}$$

The first term of equation (2.15) is $\epsilon_0 \chi^{(2)} [\frac{1}{2} (\mathbf{E}_{IR}^2 + \frac{1}{2} \mathbf{E}_{vis}^2)]$, and gives rise to a direct current (DC) field with no frequency dependence.

The second term, $\epsilon_0 \chi^{(2)} [\mathbf{E}_{IR}^2 \cos 2\omega_{IR} t + \mathbf{E}_{vis}^2 \cos 2\omega_{vis} t]$, gives rise to a second-harmonic generation (SHG) field for each of the IR and visible inputs, at twice their input frequency.

Equation (2.11) is harder to follow, and not necessary for understanding the origin of SFG spectra. Therefore the convention of equation (2.10) will be used throughout the rest of this section.

The third term, $\epsilon_0 \chi^{(2)}[\mathbf{E}_{IR}\mathbf{E}_{vis}\cos(\omega_{vis} - \omega_{IR})t]$, gives rise to difference-frequency generation (DFG) where light is emitted at the difference of the input IR and visible frequencies.

Finally, the fourth term, $\epsilon_0 \chi^{(2)}[\mathbf{E}_{IR}\mathbf{E}_{vis}\cos(\omega_{vis} + \omega_{IR})t]$, gives rise to SFG, where light is emitted at the sum of the two input frequencies.

This simple electromagnetic approach demonstrates the origin of SFG; a more thorough description of SFG requires quantum-mechanical calculation and can be found in the literature [17, 22, 23].

2.2.2 Second-order susceptibility

The intensity of sum-frequency light that is generated is proportional to the square of the induced polarisation, **P**, and therefore to the square of the second-order non-linear bulk susceptibility, $\chi^{(2)}$,

$$I_{SF} \propto |\chi^{(2)}|^2 \tag{2.16}$$

Since $\chi^{(2)}$ is the macroscopic average of the molecular second-order polarisabilities β of the molecules at the surface, probing $\chi^{(2)}$ by scanning through infrared wavenumbers gives us insight into the molecular vibrations at the surface. $\chi^{(2)}$ is a third-rank tensor, and has 27 components that fully describe the non-linear response of the surface to incident and emitted **E**. For all third-rank tensors, a change in sign of all three axes (i.e. reversing the axis system) must produce a sign change in the physical phenomenon that it describes:

$$\chi^{(2)}_{ijk} = -\chi^{(2)}_{-i-j-k} \tag{2.17}$$

where i, j, and k are unit vectors along the x, y and z axes, respectively. However, for a centrosymmetric environment, all directions are equivalent, and therefore the value of $\chi^{(2)}_{ijk}$ in opposite directions must be the same:

$$\chi^{(2)}_{ijk} = \chi^{(2)}_{-i-j-k} \tag{2.18}$$

To satisfy both of these requirements, the value of $\chi^{(2)}_{ijk}$ must be 0; hence SFG is forbidden in a centrosymmetric environment, which is the case for the majority of bulk matter. However, an isotropic planar surface is not centrosymmetric along the z axis. The result

is that only the terms of $\chi^{(2)}_{ijk}$ which are quadratic in x or in y, or which do not contain x and y, may contribute to the intensity. This leaves 7 possible terms, and since x and y are indistinguishable for an isotropic surface, only 4 are unique:

$$\begin{aligned} &\chi^{(2)}_{zxx}(\equiv \chi^{(2)}_{zyy}) \\ &\chi^{(2)}_{xzx}(\equiv \chi^{(2)}_{yzy}) \\ &\chi^{(2)}_{xxz}(\equiv \chi^{(2)}_{yyz}) \\ &\chi^{(2)}_{zzz} \end{aligned} \tag{2.19}$$

The SFG response to unpolarised light would have a contribution from all four possible components of $\chi^{(2)}$. However, it is possible to selectively probe the different components of $\chi^{(2)}$ by using polarised light, such as in figure 2.5.

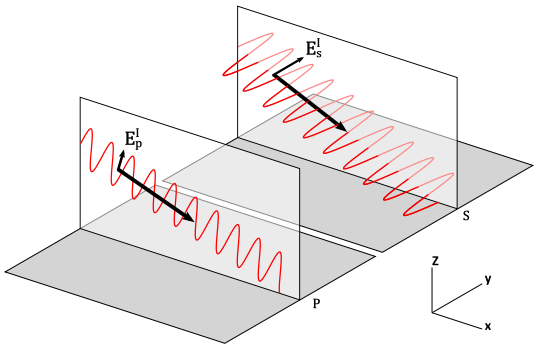

Figure 2.5: The S and P polarised light, labelled with the direction of propagation of the beam, and with $\mathbf{E^I_p}$ & $\mathbf{E^I_s}$, the electric field in the p and s polarisations. $\mathbf{E^I_p}$ lies in the xz plane, and $\mathbf{E^I_s}$ lies parallel to the y axis.

Incident light is polarised so that the electric field vector is parallel (P-polarised) or perpendicular (S-polarised) to the plane of incidence (the xz plane, which is rendered translucent in figure 2.5). The components of $\chi^{(2)}$ that are probed by the 4 possible combinations of S- and P-polarised visible and infrared light are presented in table 2.1. The sum-frequency polarisation that is generated is determined by the response of the components of $\chi^{(2)}$ to the incident infrared and visible light. For dielectric surfaces, all of these polarisation combinations are experimentally accessible. However S-polarised infrared light reflecting from a metallic surface produces a very weak electric field, due to a phase reversal on reflection at the metal surface, causing destructive interference. Hence, only the SSP and PPP combinations are accessible on metals such as gold.

Table 2.1: The combinations of S- and P- polarised light in SFG (listed in order SF, visible, IR), and the terms of $\chi^{(2)}$ probed.

Polarisation combination	Contributing elements of $\chi^{(2)}$
PSS	$\chi^{(2)}_{zyy}$
SPS	$\chi^{(2)}_{yzy}$
SSP	$\chi^{(2)}_{yyz}$
PPP	$\chi^{(2)}_{zzz}$ $\chi^{(2)}_{zyy}$ $\chi^{(2)}_{yzy}$ $\chi^{(2)}_{yyz}$

Gold and other metal surfaces do have some advantages in SFG. The previous equations involving $\chi^{(2)}$ have assumed that the molecules are adsorbed onto a substrate which is SF inactive. This is valid for dielectric substrates such as silica, but not for metals. Generally, $\chi^{(2)}$ can be split into two terms to give

$$\chi^{(2)} = \chi^{(2)}_R + \chi^{(2)}_{NR} \tag{2.20}$$

so that the intensity now becomes:

$$I_{SF} \propto |\chi^{(2)}_R + \chi^{(2)}_{NR}|^2 \tag{2.21}$$

$\chi^{(2)}_R$ is the resonant susceptibility, arising from molecular vibrations, and varies strongly with infrared frequency. $\chi^{(2)}_{NR}$ is the non-resonant susceptibility, which arises from the surface, and it is largely independent of frequency. In dielectrics such as silica, $\chi^{(2)}_{NR}$ is very small. For metallic surfaces, $\chi^{(2)}_{NR}$ is much larger, due to surface-plasmon resonance of the conduction electrons. Because of the squared dependence of I_{SF} on $\chi^{(2)}$, the effect is an enhancement of the absolute signal strength, and of the signal-to-noise ratio.

Equations (2.17) and (2.21) also imply that the polarisation of the molecule will affect the phase of the signal. Reversing the axis system is equivalent to reversing the polarisation of the molecule, so the polarisation of the molecule will affect the sign of $\chi^{(2)}_R$, and therefore will determine whether dips or peaks are observed (figure 2.6). This is only the case when $\chi^{(2)}_{NR}$ is relatively large; for dielectrics, only peaks will be observed (although overlapping resonances from different vibrational modes may still interfere destructively with each other).

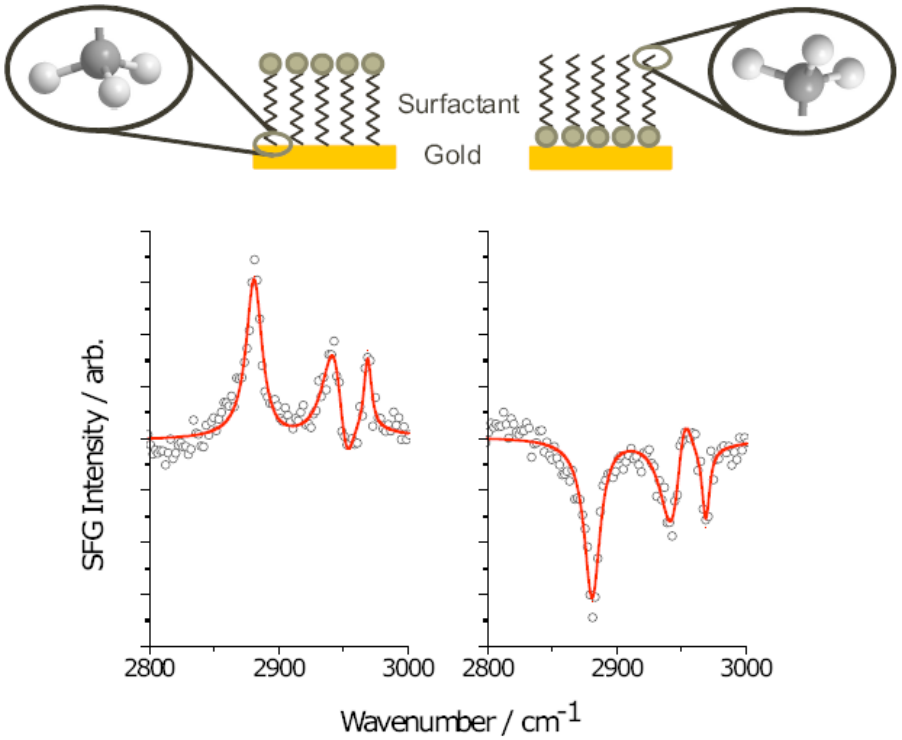

Figure 2.6: Spectra of a surfactant on a gold substrate, adapted from [24]. When the methyl points toward the substrate, peaks appear in the spectrum. When pointed away from the surface, dips appear. Note that this applies to the co-propagating beam geometry shown in Figure 2.4 - it is reversed for a counter-propagating geometry.

2.2.3 Molecular susceptibility

$\chi^{(2)}_{ijk}$ is the macroscopic average of the molecular second-order non-linear susceptibility, $\beta_{\alpha\beta\gamma}$ (sometimes called the first *hyper*polarisability), $\beta_{\alpha\beta\gamma}$ can be derived by perturbation theory [25]. A simple form of the equation for $\beta_{\alpha\beta\gamma}$, which is applicable when ω_{IR} is near a vibrational transition (ω_υ) of the molecule and ω_{vis} is not near an electronic transition, is presented here:

$$\beta_{\alpha\beta\gamma} = \frac{1}{2\hbar}\frac{M_{\alpha\beta}A_\gamma}{(\omega_\upsilon - \omega_{IR} - i\Gamma)} \tag{2.22}$$

where $M_{\alpha\beta}$ and A_γ are the Raman and IR transition moments respectively, ω_υ is the frequency of a vibrational mode (not to be confused with ω_{vis}, the frequency of the visible laser), and Γ is the relaxation time of the vibrationally excited state. Note that the coordinates $\alpha\beta\gamma$ refer to the molecular frame, and are not the same as ijk which refer to

the lab frame. By inspecting Equation (2.22), it is clear that $\beta_{\alpha\beta\gamma}$ is only non-zero when $M_{\alpha\beta}$ and A_γ are both also non-zero. This gives rise to the selection rule that a resonance must be both infrared and Raman active to be SFG active. Therefore, by the rule of mutual exclusion (which states that a centrosymmetric molecule cannot be both infrared and Raman active), any molecule or functional group that has a centre of symmetry, will be SFG-inactive.

Expressing $\chi_R^{(2)}$ in terms of $\beta_{\alpha\beta\gamma}$ gives:

$$\chi_{ijk}^{(2)} = \frac{N}{\varepsilon_0} \sum_{\alpha\beta\gamma} \langle R(\psi)R(\theta)R(\phi)\beta_{\alpha\beta\gamma} \rangle \tag{2.23}$$

where N is the number of molecules per volume, $R(\psi)R(\theta)R(\phi)$ are the rotation matrices that convert the molecular coordinates $\alpha\beta\gamma$ to the lab frame ijk, and $\langle\rangle$ denotes that the orientational average of $\beta_{\alpha\beta\gamma}$ is taken.

For a single resonant susceptibility, $\chi_R^{(2)}$ may also be re-expressed as:

$$\chi_R^{(2)} = \frac{B}{\omega_\upsilon - \omega_{IR} - i\Gamma} \tag{2.24}$$

where B the strength of the resonance, and includes all the appropriate terms of the previous Equation (2.23). This expression is useful when considering how $\chi_R^{(2)}$ varies with infrared wavenumber. First, it is separated into real and imaginary components:

$$\begin{aligned}
\chi_R^{(2)} &= \frac{B}{\omega_\upsilon - \omega_{IR} - i\Gamma} \\
\chi_R^{(2)} &= \frac{B}{\omega_\upsilon - \omega_{IR} - i\Gamma} \cdot \frac{\omega_\upsilon - \omega_{IR} + i\Gamma}{\omega_\upsilon - \omega_{IR} + i\Gamma} \\
\chi_R^{(2)} &= \frac{\omega_\upsilon - \omega_{IR} + i\Gamma}{(\omega_\upsilon - \omega_{IR})^2 + \Gamma^2} \\
\chi_R^{(2)} &= \frac{\omega_\upsilon - \omega_{IR}}{(\omega_\upsilon - \omega_{IR})^2 + \Gamma^2} + i\frac{\Gamma}{(\omega_\upsilon - \omega_{IR})^2 + \Gamma^2}
\end{aligned} \tag{2.25}$$

and these terms can be plotted against wavenumber to produce the graph shown in Figure 2.7.

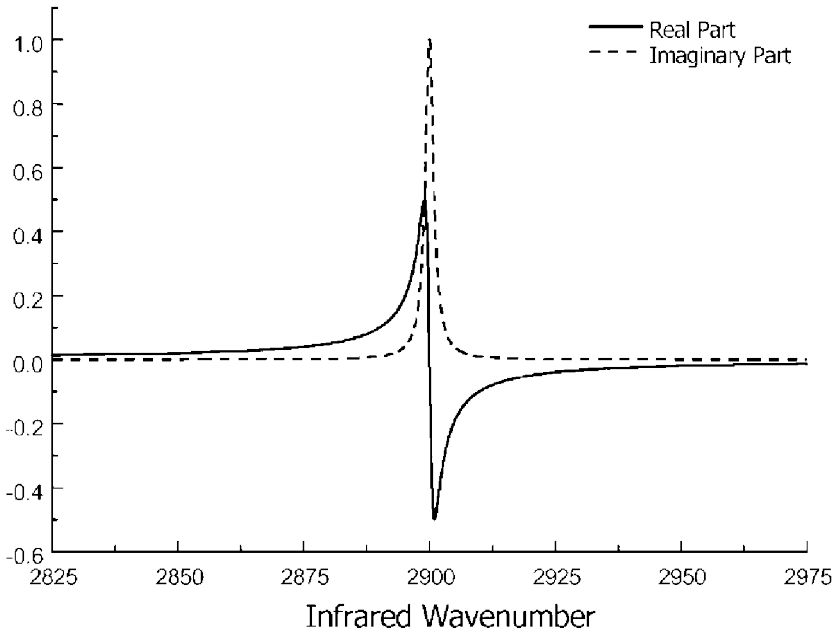

Figure 2.7: The real and imaginary components of $\chi_R^{(2)}$ for a resonance centred at 2900 cm^{-1} (i.e. ω_v= 2900 cm^{-1}). Γ has been arbitrarily set to 1. Reproduced with permission from [20].

2.2.4 Interpreting sum-frequency spectra of CH & CD vibrational modes

β, the molecular property from which $\chi_R^{(2)}$ arises, depends on both the infrared and Raman transition moments. Therefore, observing an SFG signal requires that a molecular vibration is both infrared and Raman active. C-H vibrational modes fulfil this requirement, and are therefore good candidates for SFG spectroscopy. The majority of the spectra in this report are taken in the range 2800-3000 cm^{-1}, where the C-H resonances occur. A list of common C-H and C-D assignments are given in Table 2.2. SFG spectra of the C-H modes are normally assigned by comparison to infrared and Raman spectra [26]. This is assisted by examining the phase and intensity in different polarisation modes and applying the polarisation selection rules derived by Lu et al. [12, 27]. For the CH_3 group, the selection rules relevant to the SSP and PPP polarisations are:

- For the symmetric mode, the SSP intensity is always many times that for PPP.
- For the antisymmetric mode, the PPP is always many times that for SSP, and both peak when the tilt angle of the group is 54.7°

- In SSP spectra, the antisymmetric and symmetric modes will negatively interefere where their frequencies overlap

For the CH_2, the relevant selection rules are very similar:

- For the symmetric mode, the SSP intensity is always many times that of PPP.
- For the antisymmetric mode, the PPP is always many times that for SSP. That is to say, if there is any peak which is stronger in the SSP than the PPP spectra, it cannot be from the antisymmetric mode.
- In SSP spectra, the antisymmetric and symmetric modes will negatively interefere where their frequencies overlap when their orientations are similar.

Table 2.2: SFG peak assignments in the CH [8] and CD [28] stretching regions

Mode	Description	CH /cm^{-1}	CD /cm^{-1}
d^+	Methylene symmetric stretch	2846-2850	2103
r^+	Methyl symmetric stretch	2868-2878	2073
d^-	Methylene antisymmetric stretch	2890-2915	2200
r^-	Methyl antisymmetric stretch	2960-2966	2220
d^+_{FR}	Methylene symmetric stretch Fermi resonance	2904-2954	2145-2167
r^+_{FR}	Methyl symmetric stretch Fermi resonance	2926-2938	2130

The ability to probe specific elements of the second-order susceptibility, as shown in Table 2.1, also has implications for the observable modes for each polarisation combination, which can give rise to selection rules. For a vibrational mode to give rise to an SFG response, it must have some component of $\beta_{\alpha\beta\gamma}$ that contributes to the elements of the macroscopic second-order susceptibility, $\chi^{(2)}_{ijk}$, that are being probed. In the PPP polarisation, the combined elements of $\chi^{(2)}_{ijk}$ being probed means that this effect does not limit the orientation of modes being probed. However, in the SSP polarisation, χ_{yyz} is the only element being probed, and in this case only modes that have a component of their transition moment parallel to the surface normal can contribute to the spectrum.

The fact that $\chi_R^{(2)}$ is zero in a centrosymmetric environment, as described in Section 2.2.3 also has significant implications for the interpretation of SFG spectra. In a monolayer of surfactant containing an all-trans polymethylene chain, the methylene (-CH_2) groups are locally centrosymmetric, and so are SFG inactive. Therefore, the spectrum will only contain r resonances which arise from methyl (-CH_3) groups, as shown in figure 2.8a. If some gauche defects are introduced, the local centrosymmetry is broken, and therefore SFG is no longer forbidden. The spectrum will now also contain d resonances (figure 2.8b) arising from methylene groups adjacent to the defect. As further disorder is introduced, the orientation of the alkyl chains becomes essentially random, and SFG intensity decreases due to polar orientational averaging (figure 2.8d). Therefore, as the number of gauche defects increases, the intensity of the d resonances will increase to a maximum and then decrease, while the r resonances will decrease monotonically.

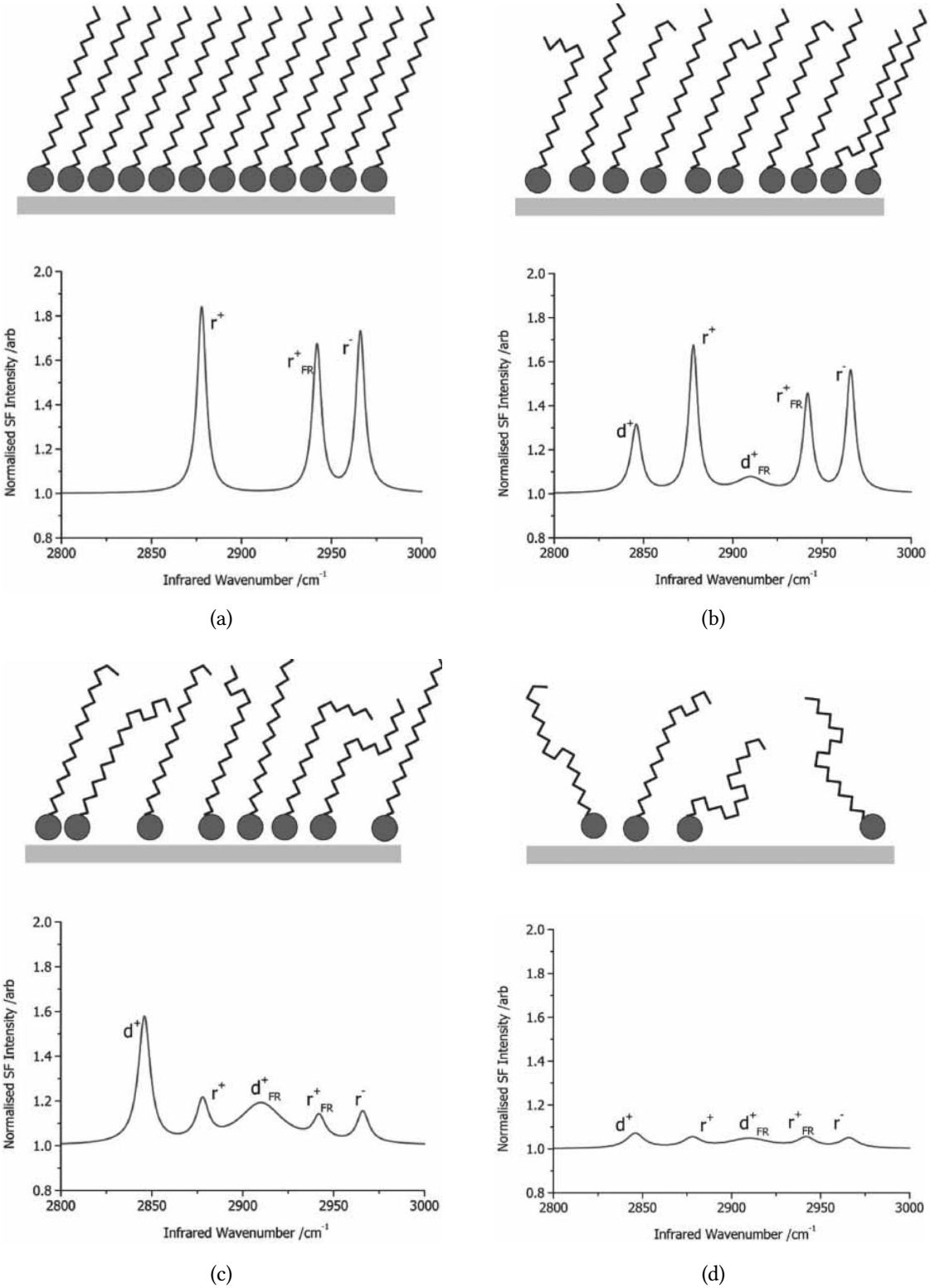

Figure 2.8: Simulated sum-frequency spectra of monolayers which are fully ordered (a) to completely disordered (d). Reproduced from [20]

2.2.5 Modelling sum-frequency spectra

As stated above, a single resonant susceptibility may be expressed as:

$$\chi_R^{(2)} = \frac{B}{\omega_v - \omega_{IR} - i\Gamma} \tag{2.24}$$

where ω_v is the frequency of the vibrational mode, and ω_{IR} is the infrared frequency, Γ is the relaxation time of the vibrationally excited state, and B is the strength of the resonance, as defined in Equation (2.22). The magnitude of $\chi_R^{(2)}$ is given by:

$$\begin{aligned} |\chi_R^{(2)}| &= \sqrt{\frac{B}{\omega_v - \omega_{IR} - i\Gamma} \cdot \frac{B}{\omega_v - \omega_{IR} + i\Gamma}} \\ |\chi_R^{(2)}| &= \sqrt{\frac{B^2}{(\omega_v - \omega_{IR})^2 + \Gamma^2}} \end{aligned} \tag{2.26}$$

This has a similar form to the equation for a Lorentzian curve:

$$y = \frac{HW^2}{(\omega_v - \omega_{IR})^2 + W^2} \tag{2.27}$$

where H is the height of the resonance, and W is the half width at half the maximum height (HWHM). The infrared wavenumber, ω_{IR}, is used as the x coordinate. By comparing Equations (2.26) and (2.27), $\chi_R^{(2)}$ can be expressed as:

$$|\chi_R^{(2)}| = \sqrt{\frac{HW^2}{(\omega_v - \omega_{IR})^2 + W^2}} \tag{2.28}$$

so that $B = \sqrt{H}W$, and $\Gamma = W$. However, Equation (2.28) does not account for the phase of the resonant signal. Given that $\chi_R^{(2)}$ is complex in nature, it may also be expressed in polar coordinates,

$$\chi_R^{(2)} = |\chi_R^{(2)}| e^{i\delta} \tag{2.29}$$

where $|\chi_R^{(2)}|$ is the absolute magnitude and δ is the phase of the resonant susceptibility. Expressing Equation (2.21) in polar coordinates and expanding gives:

$$\begin{aligned} I_{SF} &\propto |\chi_R^{(2)} + \chi_{NR}^{(2)}|^2 \\ I_{SF} &\propto ||\chi_R^{(2)}| e^{i\delta} + |\chi_{NR}^{(2)}| e^{i\varepsilon}|^2 \\ I_{SF} &\propto ||\chi_R^{(2)}|^2 + |\chi_{NR}^{(2)}|^2 + 2|\chi_R^{(2)}||\chi_{NR}^{(2)}| \cos(\varepsilon - \delta) \end{aligned} \tag{2.30}$$

where δ and ε are the phases of the resonant and non-resonant terms, respectively.

Substituting in Equation (2.28) gives:

$$I_{SF} \propto \frac{HW^2}{(\omega_v - \omega_{IR})^2 + W^2} + |\chi^{(2)}_{NR}|^2 + 2|\chi^{(2)}_{NR}|\sqrt{\frac{HW^2}{(\omega_v - \omega_{IR})^2 + W^2}}\cos(\varepsilon - \delta) \tag{2.31}$$

The term $\cos(\varepsilon - \delta)$ can be analysed further. By plotting Equation (2.29) on an Argand diagram (Figure 2.9), trigonometry can be used to express δ as:

$$\begin{aligned} \delta &= \tan^{-1}\left(\frac{Im[\chi^{(2)}_R]}{Re[\chi^{(2)}_R]}\right) \\ \delta &= \tan^{-1}\left(\frac{-\Gamma}{\omega_v - \omega_{IR}}\right) \end{aligned} \tag{2.32}$$

Substituting this into Equation (2.31), with the Lorentzian parameter $W = \Gamma$, gives:

$$\begin{aligned} I_{SF} \propto \frac{HW^2}{(\omega_v - \omega_{IR})^2 + W^2} &+ |\chi^{(2)}_{NR}|^2 \\ &+ 2|\chi^{(2)}_{NR}|\sqrt{\frac{HW^2}{(\omega_v - \omega_{IR})^2 + W^2}}\cos\left[\varepsilon - \tan^{-1}\left(\frac{-W}{\omega_v - \omega_{IR}}\right)\right] \end{aligned} \tag{2.33}$$

This is the equation which is used to fully fit SFG spectra which include non-resonant backgrounds, such as those taken on metal. H, W, and ω_v are initially estimated by inspection, and then H, W, ω_v, $\chi^{(2)}_{NR}$ and ε are fitted by using the Levenburg-Marquardt least-squares algorithm to minimise the error between the modelled and recorded spectra.

The constant of proportionality is difficult to determine accurately, as it depends on the overlap of the infrared and linear beams, the linear and non-linear Fresnel factors,[2] and the efficiency of the detector. Additionally, the line-shape of a spectrum produced in an actual SFG experiment depends on other experimental factors, such as the line widths of the laser beams. These factors are often modelled by convolution of the Lorentzian description of $\chi^{(2)}_R$ with a Gaussian distribution of vibrational frequencies [30].

[2]Fresnel factors describe the strength of the emitted **E** fields generated by the incident **E** fields. The Fresnel factors depend on the polarisation of the light, the angle of incidence, and the refractive indices of the transmission medium (often air) and the reflection medium (the bulk material, such as water or gold substrate). However, they do not normally change significantly with wavenumber, and consequently do not affect the interpretation of spectra (although there are exceptions [29]). Fresnel factors are discussed in detail in the literature [17, 20, 23].

For much of this thesis, spectra are obtained on dielectric materials. In these cases, $\chi^{(2)}_{NR}$ is small enough to be negligible, and then only the first term of Equation (2.33) remains. In fact, these spectra can be fit very satisfactorily using just simple Lorentzian peaks.

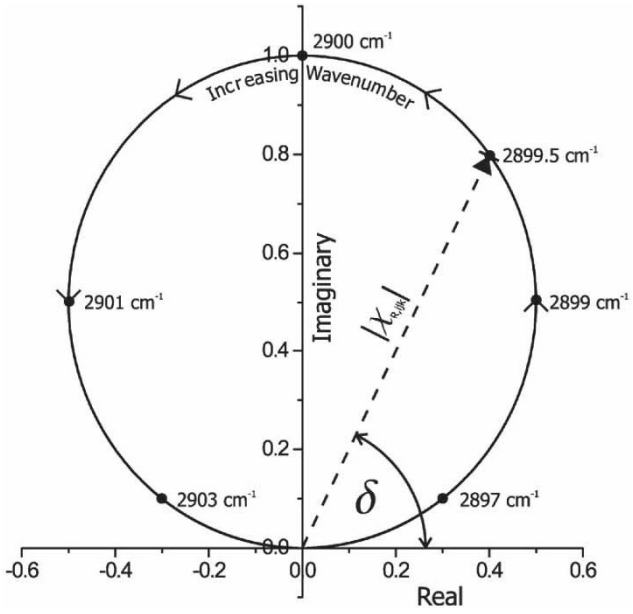

Figure 2.9: An Argand diagram showing $|\chi^{(2)}_R|$ and δ varying with wavenumber. The real and imaginary components of $\chi^{(2)}_R$ from Figure 2.7 are plotted on the x and y axes, respectively. Reproduced from [20].

References

[1] C. F. Champion and N. Davy, *Properties of Matter*. 1936.

[2] N. K. Adam, *The Physics and Chemistry of Surfaces*. Oxford, 2 ed., 1938.

[3] M. V. Berry, "The molecular mechanism of surface tension," *Physics Education*, vol. 7, pp. 60–61, Jan. 1972.

[4] A. Marchand, J. H. Weijs, J. H. Snoeijer, and B. Andreotti, "Why is surface tension a force parallel to the interface?," *American Journal of Physics*, vol. 79, pp. 999–1008, Oct. 2011.

[5] A.-C. Schöne, T. Roch, B. Schulz, and A. Lendlein, "Evaluating polymeric biomaterial–environment interfaces by Langmuir monolayer techniques," *Journal of The Royal Society Interface*, vol. 14, p. 20161028, May 2017.

[6] R. N. Ward, P. B. Davies, and C. D. Bain, "Orientation of surfactants adsorbed on a hydrophobic surface," *The Journal of Physical Chemistry*, vol. 97, pp. 7141–7143, July 1993.

[7] P. Guyot-Sionnest, J. H. Hunt, and Y. R. Shen, "Sum-frequency vibrational spectroscopy of a Langmuir film: study of molecular orientation of a two-dimensional system," *Physical Review Letters*, vol. 59, pp. 1597–1600, Oct. 1987.

[8] H.-F. Wang, W. Gan, R. Lu, Y. Rao, and B.-H. Wu, "Quantitative spectral and orientational analysis in surface sum frequency generation vibrational spectroscopy (SFG-VS)," *International Reviews in Physical Chemistry*, vol. 24, pp. 191–256, Apr. 2005.

[9] L. Velarde and H.-F. Wang, "Unique determination of the –CN group tilt angle in Langmuir monolayers using sum-frequency polarization null angle and phase," *Chemical Physics Letters*, vol. 585, pp. 42–48, Oct. 2013.

[10] H.-F. Wang, L. Velarde, W. Gan, and L. Fu, "Quantitative sum-frequency generation vibrational spectroscopy of molecular surfaces and interfaces: lineshape, polarization, and orientation," *Annual Review of Physical Chemistry*, vol. 66, pp. 189–216, Apr. 2015.

[11] M. T. L. Casford, A. Ge, P. J. N. Kett, S. Ye, and P. B. Davies, "The structure of lipid bilayers adsorbed on activated carboxy-terminated monolayers investigated by sum frequency generation spectroscopy," *The Journal of Physical Chemistry B*, vol. 118, pp. 3335–3345, Mar. 2014.

[12] R. Lu, W. Gan, B.-h. Wu, H. Chen, and H.-F. Wang, "Vibrational polarization spectroscopy of CH stretching modes of the methylene group at the vapor/liquid interfaces with sum frequency generation," *The Journal of Physical Chemistry B*, vol. 108, pp. 7297–7306, June 2004.

[13] P. J. N. Kett, M. T. L. Casford, and P. B. Davies, "Sum frequency generation (SFG) vibrational spectroscopy of planar phosphatidylethanolamine hybrid bilayer membranes under water," *Langmuir*, vol. 26, pp. 9710–9719, June 2010.

[14] X. D. Zhu, H. Suhr, and Y. R. Shen, "Surface vibrational spectroscopy by infrared-visible sum frequency generation," *Physical Review B*, vol. 35, pp. 3047–3050, Feb. 1987.

[15] C. D. Bain, "Sum-frequency vibrational spectroscopy of the solid/liquid interface," *Journal of the Chemical Society, Faraday Transactions*, vol. 91, pp. 1281–1296, Jan. 1995.

[16] Y. R. Shen, "Basic theory of surface sum-frequency generation," *The Journal of Physical Chemistry C*, vol. 116, pp. 15505–15509, July 2012.

[17] Y. R. Shen, *The Principles of Nonlinear Optics.* Wiley, 2002.

[18] P. Guyot-Sionnest, W. Chen, and Y. R. Shen, "General considerations on optical second-harmonic generation from surfaces and interfaces," *Physical Review B*, vol. 33, pp. 8254–8263, June 1986.

[19] C. K. Lin, L. Yang, M. Hayashi, C. Y. Zhu, Y. Fujimura, Y. R. Shen, and S. H. Lin, "Theory and applications of sum-frequency generations," *Journal of the Chinese Chemical Society*, vol. 61, pp. 77–92, Jan. 2014.

[20] A. G. Lambert, P. B. Davies, and D. J. Neivandt, "Implementing the theory of sum frequency generation vibrational spectroscopy: a tutorial review," *Applied Spectroscopy Reviews*, vol. 40, pp. 103–145, May 2005.

[21] E. Hecht, *Optics.* Addison-Wesley, 4th ed., 2002.

[22] R. W. Boyd, *Nonlinear Optics.* Elsevier, 3rd ed., 2008.

[23] Y. R. Shen, *Fundamentals of sum-frequency spectroscopy*. Cambridge: Cambridge University Press, 2016.

[24] P. J. N. Kett, *The structure of multilayer films studied by sum frequency generation spectroscopy*. PhD thesis, University of Cambridge, 2011.

[25] J. Hunt, P. Guyot-Sionnest, and Y. Shen, "Observation of C-H stretch vibrations of monolayers of molecules optical sum-frequency generation," *Chemical Physics Letters*, vol. 133, pp. 189–192, Jan. 1987.

[26] R. N. Ward, *Sum-frequency spectroscopy of molecules at interfaces*. PhD thesis, University of Cambridge, 1993.

[27] R. Lu, W. Gan, B.-h. Wu, Z. Zhang, Y. Guo, and H.-F. Wang, "C-H stretching vibrations of methyl, methylene and methine groups at the vapor/alcohol (N = 1-8) interfaces," *The Journal of Physical Chemistry B*, vol. 109, pp. 14118–14129, July 2005.

[28] C. S. Yang, L. J. Richter, J. C. Stephenson, and K. A. Briggman, "In situ, vibrationally resonant sum frequency spectroscopy study of the self-assembly of dioctadecyl disulfide on gold," *Langmuir*, vol. 18, pp. 7549–7556, Oct. 2002.

[29] E. H. Backus, N. Garcia-Araez, M. Bonn, and H. J. Bakker, "On the role of Fresnel factors in sum-frequency generation spectroscopy of metal-water and metal-oxide-water interfaces," *Journal of Physical Chemistry C*, vol. 116, pp. 23351–23361, Oct. 2012.

[30] C. D. Bain, P. B. Davies, T. Hui Ong, R. N. Ward, and M. A. Brown, "Quantitative analysis of monolayer composition by sum-frequency vibrational spectroscopy," *Langmuir*, vol. 7, pp. 1563–1566, May 1991.

3. Materials and methods

3.1 Chemicals used

Constituents of the binary surfactant system

- Genamin BTLF (Unilever), consisting of ~70% docosyltrimethylammonium chloride (BTAC), ~30% dipropylene glycol (DPG, itself a mixture of isomers).
- Lanette S3 (Unilever), principally cetostearyl alcohol (CetOH), with some stearyl alcohol.
- A hand-made model hair conditioner made by manually grinding the Lanette S3 and Genamin BTLF in a mortar and pestle in a 2:1 mass ratio. Hereafter referred to as “hand-made mixture”.
- A model hair conditioner provided by Unilever, produced by heating an aqueous emulsion containing 2% Genamin BTLF and 4% Lanette S3 (by mass). Hereafter referred to as “Unilever mixture”.
- A model hair conditioner provided by Unilever, produced by extruding an aqueous mixture containing 2% Genamin BTLF and 4% Lanette S3 (by mass) back and forth between two syringes at 63℃. Hereafter referred to as "RR63".
- A model hair conditioner provided by Unilever, produced by extruding an aqueous mixture containing 2% Genamin BTLF and 4% Lanette S3 (by mass) back and forth between two syringes at 80℃. Hereafter referred to as "RR80".

Behenyltrimethylammonium surfactants at the air/water and air/glass interfaces

- Genamin BTLF (Unilever), consisting of ~70% docosyltrimethylammonium chloride (BTAC), ~30% dipropylene glycol (DPG, itself a mixture of isomers).

- Genamin BTMS (Clariant) consisting of ~80% docosyltrimethylammonium methyl sulfate (BTMS), ~20% isopropyl alcohol (IPA). This was ground to a powder in a pestle and mortar and placed in a vacuum desiccator for 72 h for facile removal of the IPA impurity. The removal of IPA was confirmed by Raman, IR, and mass spectrometry. NMR and mass spectrometry recordings showed no other significant impurities.

- Deuterated hexadecyl-d33-trimethylammonium bromide (d-CTAB), >99.5%, Sigma-Aldrich

- Sodium methyl sulfate, >92% (<3% methanol, <5% water are the primary impurities), Sigma-Aldrich

Cell membrane model substrates

- Gold slide (made in-house) - a glass slide with a gold surface produced by thermal evaporation of gold onto a clean glass slide.

- T10 slide (provided by SDx Tethered Membranes) - a glass slide with a gold surface, upon which a 9:1 mixture of benzyldisulphide TEG-OH (the spacer) and benzyldisulphide PEG phytanyl (the tether) had been self-assembled (see Section 1.3.1 for details).

Phospholipids

- 1,2-dipalmitoyl-sn-glycero-3-phosphoethanolamine (DPPE), >99%, Avanti Polar Lipids

- Deuterated 1,2-dipalmitoyl-d62-sn-glycero-3-phosphoethanolamine (d-DPPE), >99%, Avanti Polar Lipids

- 1,2-dipalmitoyl-sn-glycero-3-phosphocholine (DPPC), >99%, Avanti Polar Lipids

- Deuterated 1,2-dipalmitoyl-d62-sn-glycero-3-phosphocholine (d-DPPC), >99%, Avanti Polar Lipids

- Deuterated 1,2-dipalmitoyl-d75-sn-glycero-3-phosphocholine-1,1,2,2-d4-N,N,N-trimethyl-d9 (d75-DPPC), >99%, Avanti Polar Lipids

Surfactin

- Surfactin from *Bacillus Subtilis*, $C_{53}H_{93}N_7O_{13}$, >98%, Sigma-Aldrich
- Surfactin with deuterated leucine residues, from *Bacillus Subtilis* (made in-house - see Section 3.9 for details).

3.2 Cleaning

Glass

Glassware and glass slide substrates were cleaned by soaking in DECON 90 for a minimum of 24 hours, and then rinsed with ultrapure water (>18.2 MΩcm) 20 times. Glass slides were also cleaned by UV ozone for 30 minutes.

Gold substrates

Gold-coated glass slides were cleaned by UV ozone for 30 minutes.

T10 slides

T10 slides, which have organic materials bound to the gold surface, could not be cleaned by UV ozone. Instead, they were cleaned by repeated rinsing with both ultrapure water (>18.2 MΩcm) and ethanol (≥99.9% HPLC grade, Sigma)

Langmuir-Blodgett (LB) trough

The cleaning procedure was largely the same for both the NIMA and custom troughs, both of which are described in the next section, 3.5. The troughs were cleaned with tissue soaked in water, followed by tissue soaked in chloroform. For the custom trough, the injection ports were also cleaned by flushing water and ethanol through them using an aspirator. Ultrapure water was placed into the trough, and a surface pressure/area isotherm taken using a paper Wilhelmy plate to measure the surface pressure. The water surface was cleaned of surface contamination with an aspirator, and another isotherm was taken. This was repeated until the isotherm showed a <0.1 mN/m increase in surface pressure over a full barrier compression. The clean water sub-phase was then used for deposition procedures, as described in Section 3.5).

3.3 Sum-frequency spectroscopy

SFG spectra were recorded in SSP and PPP polarization combinations (sum-frequency, visible, infrared) using a picosecond spectrometer (EKSPLA, Vilnius, Lithuania). The second harmonic of a mode-locked Nd:YAG laser (Ekspla PL4431B) provided the visible beam at 532 nm (30 ps pulses at 50 Hz). Tunable infrared beams in the 1000-1800 and 2700-4000 cm^{-1} regions were produced by an optical parametric generator (Ekspla PG401). The input IR and visible laser beams were overlapped in a copropagating geometry at angles of 53° and 60°, respectively, to the surface normal.

Heated stage

For spectra taken at temperatures greater than room temperature, a metal stage, containing a cartridge heater controlled thermostatically by a Eurotherm PID controller, was used, with the sample placed atop this (Figure 3.1).

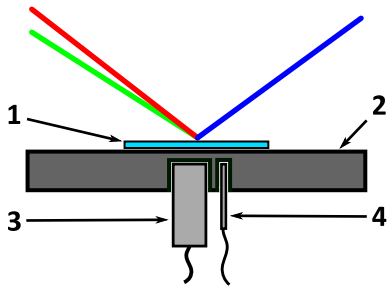

Figure 3.1: A cross-sectional diagram of the heated stage used for SFG experiments of samples at high temperatures. The sample (1) is placed on the metal SFG stage (2). A cartridge heater (3) controlled by a PID controller (not shown) is inserted into the stage. A thermostat (4) also connected to the PID controller is inserted alongside the heater. This allows the stage and sample to be heated, and maintained at the desired temperature.

Liquid cell

Sum-frequency spectra of samples under liquids were taken using a liquid cell constructed in-house, a diagram of which is shown in Figure 3.2.

Spectroscopy at the air/water interface

SFG spectra of surfactants at the air/water interface were initially conducted using a small PTFE trough (dimensions 2.2 by 9.5 cm), with a small PTFE-coated steel bar atop this, which could be moved by hand to compress the monolayer at the interface. This was the method used for the spectra in Chapters 5 and 7. Later, spectra at the air/water interface were conducted using a custom-built PTFE trough with a computer-controlled barrier (a schematic of the trough is shown in Figure 3.3). This was the method used for the spectra in Chapter 8.

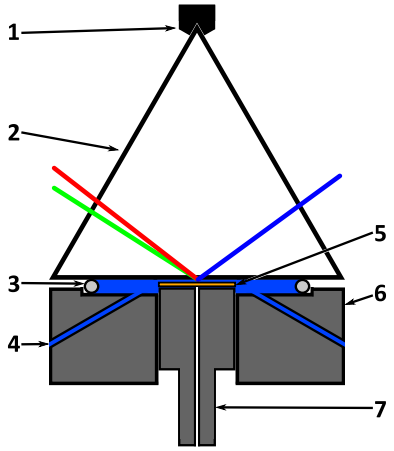

Figure 3.2: A cross-sectional diagram of the liquid cell used for SFG experiments on substrates under liquids. A clamp (1) holds the prism (2) down against a teflon seal (3). Liquid can be introduced or flushed through via inlet/outlet tubes (4). The sample (5) is held within the cell body (6) against the prism, by a plunger (7) which can also be connected to a vacuum line in order to function as the dipper in the Langmuir-Schaefer setup.

3.4 Infrared spectroscopy

All spectroscopy experiments were conducted using an FT-IR spectrometer (Perkin-Elmer 100) fitted with a liquid-nitrogen-cooled mercury-cadmium-telluride (MCT) detector, with different accessories for Attenuated Total Reflection (ATR) and Reflection Absorption Infrared Spectroscopy (RAIRS). ATR spectra were recorded using a diamond ATR accessory (Specac Heated Golden Gate™ Type IIIA). RAIRS spectra of phospholipid/surfactin systems were recorded using a grazing-angle reflectance accessory (Specac Monolayer/Grazing Angle Specular Reflectance Accessory) with a polariser and a custom-built PTFE trough (described in 3.5). The mirrors were adjustable, enabling a range of angles of incidence to be used.

3.5 Langmuir-Blodgett (LB) trough techniques

Standard surface pressure - area (π-A) isotherms and experiments involving monolayer/bilayer on substrates were recorded using a commercial trough (NIMA 611) with two symmetrical computer-controlled barriers and a central well for dipping substrates (which was also computer-controlled). Due to the space limitations of the SFG sample stage, sum-frequency spectroscopy experiments with simultaneous surface pressure measurement of the air/water interface could not be done with the larger NIMA trough, so a custom-built PTFE trough was used (see Figure 3.3). This trough had only one barrier, the speed of which was controlled by a manually operated potentiometer and motor, and multiple ports for injection into the subphase without disturbing the interfacial layer. Reflection adsorption experiments were conducted with a second custom-built PTFE trough, which allowed for surface pressure measurements but did not have a barrier, again due to space constraints of the RAIRS stage.

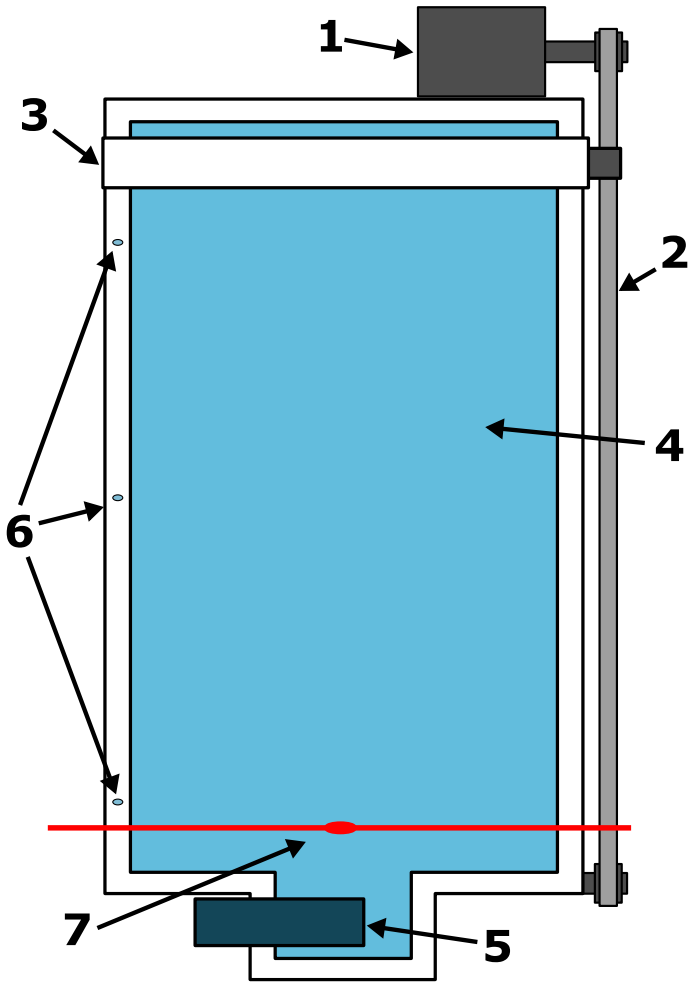

Figure 3.3: A schematic diagram of the Langmuir trough setup used for SFG experiments of liquid/air interfaces with simultaneous surface pressure measurements. A variable-speed motor (1) drives a belt (2) to which a moveable teflon barrier (3) is attached, allowing compression of monolayers on the water surface (4). Surface pressure changes are recorded by a surface pressure sensor (5) which is clamped to the back of the SFG laser box. Injection ports (6) are placed at 3 points in the wall of the trough, so that injections into the subphase can be behind or in front of the barrier, and at different distances from the beam spot (7) and from the Wilhelmy plate (beneath the surface pressure sensor)

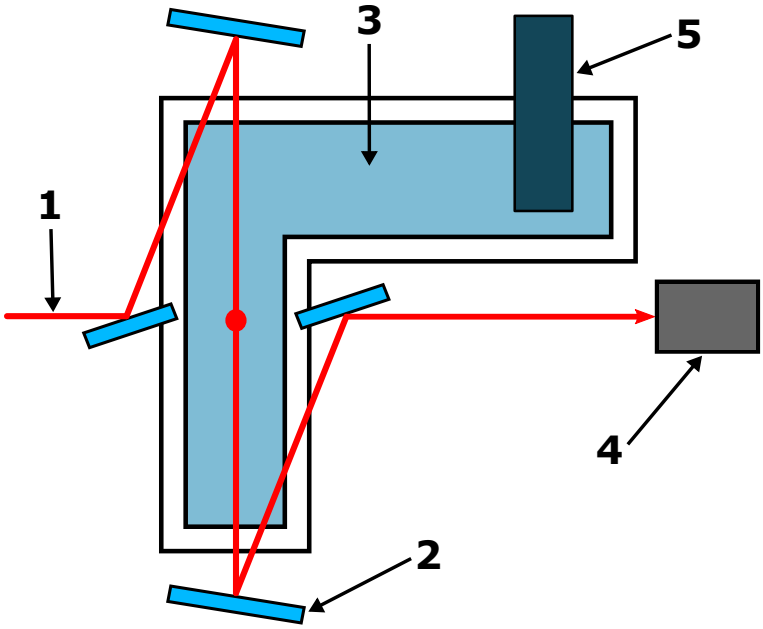

Figure 3.4: A schematic diagram of the Langmuir trough and optical path used for RAIRS experiments of liquid/air interfaces with simultaneous surface pressure measurements. The infrared beam (1) is reflected by adjustable mirrors (2) onto the water surface (3) at the desired incident angle, and then through to the MCT detector (4). Surface pressure changes are recorded by a surface pressure sensor (5) which is clamped to a baseplate.

3.6 Preparation and spectroscopy of the binary surfactant system

Solutions of hand-made mixtures (0.008 g/ml) and Unilever samples (25 ml in 180 ml of water, approximately equivalent to 0.008 g/ml of the hand-made solution) were prepared with stirring. The solution was raised to a specific temperature, and a clean glass slide (section 3.2) was placed into this mixture for 15 minutes. The glass slides were then rinsed with ultrapure water to remove remaining bulk solution, and spectra were taken on a temperature-controlled stage. This was repeated at the solution and stage temperatures listed in the "Cold Stage" and "Hot Stage" experiments of Table 3.1.

For the ionic strength experiments, a sample was prepared as above, at 18℃, and then excess calcium carbonate was added to the solution, and a second sample prepared. Spectra were taken of these at the four temperatures shown in Table 3.1. The solubility of $CaCO_3$ varies markedly with temperature, and therefore only one solution temperature was used.

3.7 Preparation of model cell membranes

Rapid solvent exchange (RSE)

A T10 slide was placed in a solution of d-DPPE in ethanol (1 mg/ml) for one hour, and then copious water was added rapidly, diluting the ethanol and causing the d-DPPE to come out of solution and deposit on the slide [1–3].

Langmuir-Blodgett (LB) deposition - producing a monolayer on a substrate

A T10 slide, cleaned as described above, was placed into the clean water sub-phase, clamped to a computer-controlled dipper. The DPPE was dissolved in chloroform (1mg/ml) and slowly added drop-wise to the surface of the clean water sub-phase,

Table 3.1: A list of the temperatures used in the binary surfactant system experiments

Experiment Series	Temperature (℃) Solution	Stage
	18	18
Cold Stage	35	18
Experiments	40	18
	45	18
	18	18
Hot Stage	35	35
Experiments	40	40
	45	45
	18	18
Ionic Strength	18	35
Experiments	18	40
	18	45

with the barriers fully open. The chloroform was allowed to evaporate for 30 minutes (much longer than required), and the computer-controlled barriers were compressed at 15 cm^2/min to a surface pressure of 40 mN/m^2. The T10 slide was then withdrawn at 10 mm/min, whilst the surface pressure was maintained by the computer-controlled barriers.

Langmuir-Schaefer (LS) deposition - producing a bilayer on a substrate

The DPPE was solvent cast as above, and the barriers were compressed to a fixed surface pressure of 40 mN/m^2, as for LB deposition. The substrate, held parallel to the surface of the water by a vacuum to a computer-controlled dipper, was lowered at 10 mm/min into the water, into an open liquid cell, the details of which can be found in section 3.3.

3.8 Preparation and spectroscopy of behenyltrimethylammonium surfactants

All experiments were conducted at room temperature (19℃). BTMS and BTAC are almost completely insoluble under these conditions - the solubility of these surfactants is less than their critical micelle concentration (CMC) (estimated to be 0.024 mM by extrapolation from the available CMC data for shorter-chain trimethylammonium cationics [4]). For isotherm measurements, BTMS and BTAC were spread from 4.2 mM chloroform solutions (Fisher HPLC grade) onto Millipore water (>18.0 MΩcm) at pH 7, in an LB trough (Nima 611, Coventry, U.K.). For SFG spectroscopy at the air/water interface, the same surfactant concentration in chloroform solution was spread on Millipore water in a bespoke Teflon trough (dimensions 2.2 cm by 9.5 cm). Compression of the surfactant layer on this trough was achieved by moving a Teflon barrier manually. To record SFG spectra of BTMS films at the air/glass interface, the surfactant was LB-deposited onto a clean glass slide from the surface of Millipore water at pH 7. The dipper was raised at 20 mm/min while computer-controlled barriers kept the surface pressure constant. To record corresponding AFM images of BTMS at the air/solid interface, the surfactant was LB-deposited onto a freshly cleaved mica substrate from the surface of Millipore water at pH 7, as above. AFM images were recorded on an Agilent 5500 microscope in tapping mode using a silicon cantilever (NSC15, MikroMasch, Russia) at 325 kHz with a spring constant of 46 N/m.

3.9 Preparation of surfactin from *Bacillus Subtilis*

The following paragraph is reproduced from the account written by Dr Annabel Murphy [5], who prepared the deuterated surfactin for the experiments described in Chapter 7: "Production of partially deuterated surfactin was carried out following protocol described by Shen et al [6]. Bacillus subtillus BBK006 was inoculated into lysogeny broth (LB) medium and incubated at 30℃ for 16 hours. A 1% subculture was inoculated in 20mL of M9 minimal medium (glucose, 0.2% w/v; $Na_2HPO_4 \cdot 2\,H_2O$, 34 mM; KH_2PO_4, 22 mM; NaCl, 8.6 mM; NH_4Cl, , 9.4 mM; $MgSO_4$, 1 mM; $CaCl_2$, 0.3 mM; biotin, 1 µg/L.; thiamin, 1 µg/L; EDTA, 0.13 mM; $FeCl_3$, 31 µM; $ZnCl_2$, 6.2 µM; $CuCl_2$, 0.76 µM; $CoCl_2$, 0.42 µM; H_3BO_3, 1.6 µM, $MnCl_2$, 0.08 µM) and the culture was incubated at 30℃ for 48 hours with

shaking at 250 rpm. This seed culture was used to inoculate (10%) 2 × 100 ml of M9 medium containing 0.04% (w/v) deuterated D/L-leucine (D_{10}), in 500 ml unbaffled shake flasks. The culture was incubated at 30℃ for 48 hours with shaking at 250 rpm. Cells were removed by centrifugation and the supernatant subjected to sterile filtration then acidified to pH 2 with 1M HCl, whereupon a fine precipitate was formed. The precipitate was extracted using CH_2Cl_2, and after drying over $MgSO_4$, the solvent was removed *in vacuo*. Further purification was achieved following the protocol described by Cooper et al [7]. Production of partially deuterated surfactin was confirmed by proton NMR (Bruker 400 MHz Avance III HD Spectrometer) and high resolution mass spectrometry using positive ion electrospray ionization (Waters Xevo G2-S QTOF). These spectra are available in the supporting information of [5]. Labelled surfactins A, B, and C were identified, with masses indicating that the deuterium atoms located at the alpha-carbons of the leucine residues had been replaced by protons during the course of fermentation, such that 9 deuterium atoms were incorporated per leucine residue. In addition, surfactins A and C featuring D_9 labelling of the fatty acid side-chain were observed, presumably via the conversion of leucine-D_{10} into isovaleryl-CoA and its subsequent use as a starter unit for fatty acid biosynthesis. "

3.10 Sum-frequency spectroscopy of the phospholipid/surfactin system

Sum-frequency spectroscopy of the phospholipid monolayer on water was conducted using the custom trough described earlier (and shown in Figure 3.3). When placed in the SFG sample area, this trough allowed for simultaneous measurement of the surface pressure and sum-frequency intensity, and therefore all spectra recorded in this manner have an associated surface pressure measurement. The trough was cleaned as described in section 3.2, and filled with ultrapure water so that a positive meniscus was present. The Wilhelmy plate was given time to absorb water until the surface pressure reading had reached a constant value, which was set as the zero point. After this point, the surface pressure sensor data were recorded until the end of the experiment. The barrier was opened and approximately 30 µl of 1 mM phospholipid in chloroform solution was added to the surface, dropwise, from a 250 µl syringe. The chloroform was allowed to evaporate (for at least 20 minutes), and then the barriers were compressed until the

surface pressure reached the required value. Following this, the monolayer undergoes some relaxation, and a reduction in surface pressure of approximately 3-6 mN/m was observed. The monolayer was allowed to reach equilibrium (about 15-20 minutes) and spectra were taken of this initial system. At this point, the spectrometer was set to continuously record the intensities at two wavelengths (e.g. 2076 cm^{-1} and 2878 cm^{-1} in order to monitor the C-H and C-D r^{+} signals). It does this by recording at each wavelength for 400 acquisitions, and repeating until the end of the experiment. This number of acquisitions corresponds to a time resolution of roughly 20 seconds. After approximately 5 minutes to establish the initial intensity of these signals, 25 µl of a surfactin solution (1.88 mM) in DMSO was injected through the port nearest the surface pressure sensor, and the surface pressure and SFG intensities were monitored until the experiment reached its conclusion, whereupon further spectra were recorded of the system in its final state.

3.11 Reflection absorption infrared spectroscopy of the phospholipid/surfactin system

As for the sum-frequency experimental arrangement, a custom trough allowed for the simultaneous collection of surface pressure data and infrared spectra. Due to the limitations of the RAIRS sample stage, the experimental method was similar except for two things. Firstly, due to the lack of a compressible barrier, the monolayer was prepared by addition of extra solution until the surface pressure sensor read 15 mN/m. Secondly, the surfactin solution was injected directly through the surface monolayer. The syringe needle was wiped clean before injection, with a small amount of air in the needle to ensure that no surfactin contaminated the surface. To confirm that this did not affect the results, this methodology was validated by using it in the sum-frequency experiment and compared to the method described previously (in 3.10), and found to be satisfactory. For time-dependent results, the spectrometer was set to continuously recorded spectra of 150 acquisitions each, giving a time resolution of roughly 7 minutes 20 seconds. In these experiments, spectra were recorded in P-polarisation with the angle of incidence set to 28°.

References

[1] C. Miller, P. Cuendet, and M. Grätzel, "K^+sensitive bilayer supporting electrodes," *Journal of Electroanalytical Chemistry*, vol. 278, pp. 175–192, Aug. 1990.

[2] D. J. McGillivray, G. Valincius, D. J. Vanderah, W. Febo-Ayala, J. T. Woodward, F. Heinrich, J. J. Kasianowicz, and M. Lösche, "Molecular-scale structural and functional characterization of sparsely tethered bilayer lipid membranes.," *Biointerphases*, vol. 2, pp. 21–33, Mar. 2007.

[3] F. Heinrich, T. Ng, D. J. Vanderah, P. Shekhar, M. Mihailescu, H. Nanda, and M. Lösche, "A new lipid anchor for sparsely tethered bilayer lipid membranes.," *Langmuir : the ACS journal of surfaces and colloids*, vol. 25, pp. 4219–29, Apr. 2009.

[4] R. Zieliński, "Effect of temperature on micelle formation in aqueous NaBr solutions of octyltrimethylammonium bromide," *Journal of Colloid and Interface Science*, vol. 235, pp. 201–209, Mar. 2001.

[5] S. A. Goussous, M. T. L. Casford, A. C. Murphy, G. P. C. Salmond, F. J. Leeper, and P. B. Davies, "Structure of the fundamental lipopeptide surfactin at the air/water interface investigated by sum frequency generation spectroscopy," *The Journal of Physical Chemistry B*, vol. 121, pp. 5072–5077, May 2017.

[6] Y. R. Shen, "Surface properties probed by second-harmonic and sum-frequency generation," *Nature*, vol. 337, pp. 519–525, Feb. 1989.

[7] D. G. Cooper, C. R. Macdonald, S. J. Duff, and N. Kosaric, "Enhanced production of surfactin from Bacillus subtilis by continuous product removal and metal cation additions.," *Applied and Environmental Microbiology*, vol. 42, pp. 408–12, Sept. 1981.

4. The effects of ionic strength and temperature on the adsorption of surfactant mixtures

The following chapter will present spectra of monolayers self-assembled from solutions of Unilever and hand-made mixtures (both of which are mixtures of CetOH and BTAC, see Figure 4.1), at various temperatures as described in Section 3.6. These studies focus on their adsorption behaviour from solution. The monolayer self-assembles on the glass with a molecular area determined by the solution conditions. This molecular area determines the range of tilt angles available to the molecules in the monolayer. A smaller molecular area requires that the molecules have a smaller tilt angle. A large molecular area will either cause the surfactants to tilt over in order to maintain favourable van der Waals interactions, or cause gauche defects to form in order to increase the cross-sectional area of the alkyl tail, again to maintain the favourable van der Waals forces [1, 2]. In the "cold-stage" experiments, monolayers were produced by self-assembly from heated solutions onto glass slides, and spectra were recorded at room-temperature. In the "hot-stage" experiments, monolayers were again produced by self-assembly from heated solutions onto glass slides, but the spectra were recorded at the same temperature as the solution. For experiments examining the effect of ionic strength, monolayers were first produced from a room-temperature solution without calcium carbonate, and a spectrum was taken on the heated SFG sample stage. This was then repeated with a second sample after adding excess calcium carbonate to the solution. Calcium carbonate was used in order to replicate the effect of "hard" water.

In all spectra taken in the SSP polarisation in this chapter, three resonances can be modelled. These are the r^+ (at 2878 cm^{-1}) and r^+_{FR} (at 2940 cm^{-1}), arising from the methyl symmetric stretch and its Fermi resonance, and the d^+ (at 2855 cm^{-1}, which corresponds to the methylene symmetric stretching mode. In the SSP polarisation, the ratio of the r^+/d^+ resonances is often used to evaluate monolayer packing and ordering, and these are given in Table 3.1 for all the SSP spectra presented. One issue here is that because these monolayers are very well ordered, the size of the d^+ resonance becomes very small,

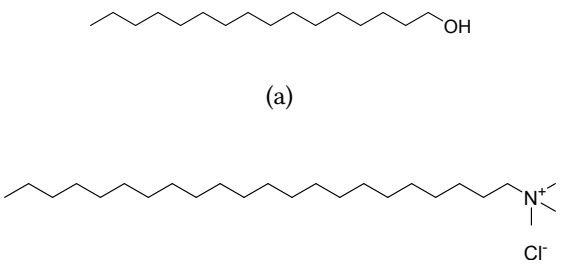

Figure 4.1: (a) Hexadecan-1-ol (also known as cetyl alcohol, CetOH). (b) N,N,N-trimethyldocosan-1-aminium chloride (Behenyl trimethylammonium chloride, BTAC)

and errors in fitting can be very large. The reported error of the r^+/d^+ ratio arises mostly due to the error in the fitting of the d^+ peak, whereas the r^+ peak is easily fitted. This is the reason that the standard error tends to be smaller for lower r^+/d^+ ratios - the d^+ resonance has become larger and therefore easier to fit accurately. In fact, the standard errors from the fitting procedure are probably underestimated; small changes in peak centres or in the baseline correction can produce a large change in the calculated d^+ area, and this is not accounted for in the error calculation.

In the spectra taken in the PPP polarisation, a clear resonance appears in all spectra at 2966 cm^{-1} (corresponding to r^-, the methyl antisymmetric stretch). The r^+ (at 2878 cm^{-1}), d^- (at 2915 cm^{-1}) and r^+_{FR} (at 2940 cm^{-1}) are also present in some of the spectra, although in others they barely rise above the noise level, or are absent completely.

4.1 "Cold-stage" experiments

The spectra in Figure 4.2 were all taken at room-temperatures (18℃, on the unheated SFG sample stage) after assembly at the solution temperatures indicated on the plots. Neither the PPP nor the SSP spectra of either of the mixtures display any systematic trends upon increasing the temperature of self-assembly. This indicates that the quality of the monolayers is not significantly disturbed by varying the self-assembly temperature in the range explored. It is certainly possible that the ratio of CetOH:BTAC changes

at different temperatures, but since they have similar alkane tails, this is not directly discernible by SFG since no isotopic enrichment was used.

Comparing the Unilever to the hand-made samples; the SSP spectra show no differences, except perhaps slightly larger d^+ resonances (at 2855 cm^{-1}) from the hand-made samples. The spectra of both the Unilever and hand-made mixtures (Figures 4.2a and 4.2c) have r^+/d^+ ratios consistent with a well-ordered monolayer [3]. In the PPP, the r^+ (at 2878 cm^{-1}) is very slightly larger in the Unilever sample, but otherwise all of these spectra are essentially those of a well-ordered alkane monolayer.

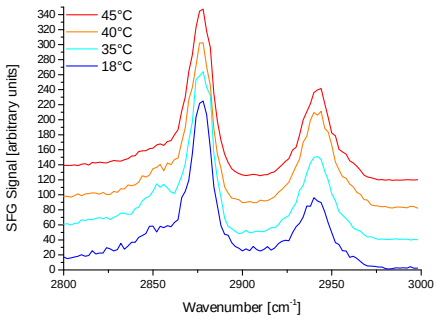

(a) SSP polarisation spectra of hand-made sample. Scaled so that the peak at 2878 cm^{-1} is the same height in all samples.

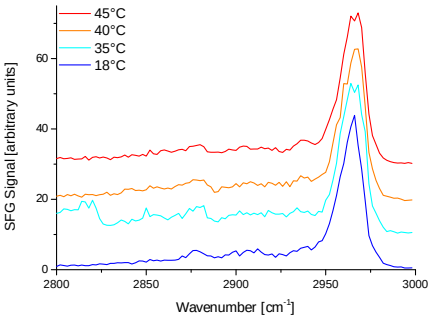

(b) PPP polarisation spectra of hand-made sample. Scaled so that the peak at 2966 cm^{-1} is the same height in all samples.

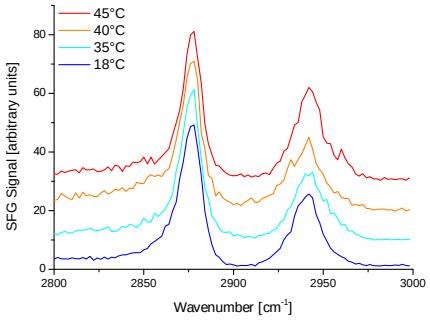

(c) SSP polarisation spectra of Unilever sample. Scaled so that the peak at 2878 cm^{-1} is the same height in all samples.

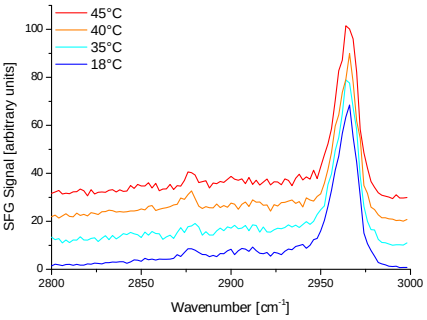

(d) PPP polarisation spectra of Unilever sample. Scaled so that the peak at 2966 cm^{-1} is the same height in all samples.

Figure 4.2: Sum-frequency spectra obtained on a room-temperature stage. Samples were prepared by self-assembly onto glass slides from a solution at the temperature indicated on the graphs.

4.2 "Hot-stage" experiments

The spectra in Figure 4.3 were taken at the same temperature as the solution temperature used for self-assembly. In the SSP spectra (Figures 4.3a and 4.3c), the r^+/d^+ ratio is consistent with a good monolayer at all temperatures. However- in this case, the ratio decreases as the stage temperature increases, as quantified in Table 4.1, indicating that more gauche defects are present at higher temperatures. This trend is clearer in the Unilever mixture (Figure 4.3c). In addition, a slight peak shift to higher wavenumbers can be observed at higher temperatures, similar to the shifts seen in infrared spectroscopy. This type of peak shift is often difficult to detect, and in fact it is hardly noticeable in Figure 4.3a. One of the advantages of SFG over some other spectroscopic techniques such as RAIRS is that it is much easier to see the increasing intensity of the d^+ peaks than the small peak shifts as the monolayer order decreases [4].

In the PPP spectra (Figures 4.3b and 4.3d), a clear difference is seen between the two mixtures. For the Unilever samples, as the self-assembly and stage temperature increases, the r^+, d^-, and r^+_{FR} peaks become stronger, and the r^- peak becomes weaker. A new peak also appears at 2855 cm^{-1}, assigned to the d^+ resonances. This trend is not present in the hand-made samples.

While the Unilever and hand-made mixture appear very similar to each other in the cold-stage experiments, the hot-stage experiments reveal a marked difference in their response to temperature. The Unilever mixture has preservative additives included which may affect the structure; however, the surface-active constituents of the Unilever and hand-made mixtures are the same. In dilute solutions, these constituents, the surfactants BTAC and CetOH, will dominate the surface activity of the mixture. If the observed difference in temperature response is not due to the constituents, it could be due to the microstructure of the material (for example a lamellar sheet structure or a spherical micelle structure). This might affect the proportions of CetOH/BTAC which adsorb onto the glass, or the packing density of the monolayer as it adsorbs onto the glass slide. These factors are related; the ratio of CetOH/BTAC affects the proportion of positively charged molecules in the monolayer. For example, a very low proportion of BTAC would encourage a higher density monolayer, to neutralise the negatively charged glass surface, and also because charge-charge repulsion would not be as great a factor. The density of the monolayer dictates the molecular area of each surfactant chain and therefore

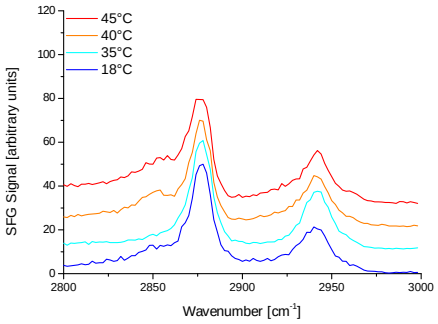

(a) SSP polarisation spectra of hand-made sample. Scaled so that the peak at 2878 cm^{-1} is the same height.

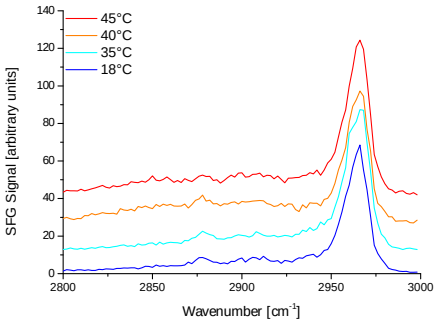

(b) PPP polarisation spectra of hand-made sample. Scaled so that the peak at 2966 cm^{-1} is the same height.

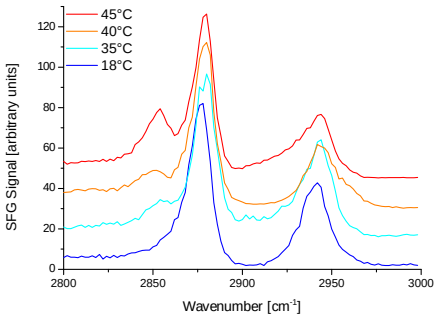

(c) SSP polarisation spectra of Unilever sample. Scaled so that the peak at 2878 cm^{-1} is the same height.

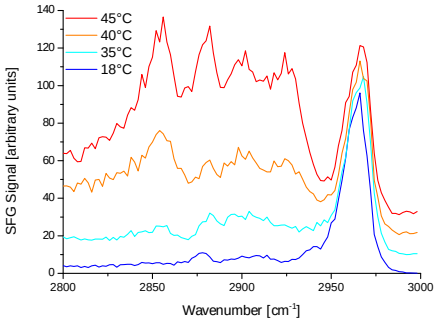

(d) PPP polarisation spectra of Unilever sample. Scaled so that the peak at 2966 cm^{-1} is the same height.

Figure 4.3: Sum-frequency spectra, acquired on a heated stage, of samples prepared by self-assembly from solution onto glass slides. The stage temperature, equal to the solution temperature in each case, is indicated by the legend on each graph.

their tilt angle - a high molecular area should cause them to be more tilted to maintain favourable van der Waals interactions [1, 2].

The data suggest that this could be the case for the Unilever samples. At higher solution temperatures, a less densely packed monolayer is formed, resulting in a larger tilt angle. At higher stage temperatures, the alkane-chain tilt angles decrease, allowing more room for gauche defects to occur. The spectra of the Unilever sample hot-stage experiments support this; at higher stage/solution temperatures, the SSP spectra show decreasing r^+/d^+ ratios indicating a greater proportion of gauche defects, as do the d^+ and d^- resonances in the PPP spectra. Additionally, the PPP spectra show an increasing r^+/r^- ratio at higher

temperatures. According to the polarisation selection rules [5], this suggests that the tilt-angle of the monolayer is decreasing (see Figure 4.4) as the temperature increases.

In contrast, the spectra of the hand-made samples indicate that these monolayers are more resilient to increasing temperature. Although the PPP spectra of the Unilever and hand-made spectra look close to identical at 18℃, implying that the tilt angles are initially similar, the PPP spectra of the hand-made sample show little or no evidence of decreasing tilt angle at higher temperatures. Additionally, the SSP spectra r^+/d^+ ratios indicate a more muted decrease in monolayer order with increasing temperature compared to the SSP spectra of the Unilever sample. Therefore, the preparation method appears to be important for the temperature susceptibility.

On reviewing these results, Unilever R&D suggested that this might be due to the microstructure that is formed by different preparation methods. The samples prepared at Unilever are thought to have a lamellar sheet microstructure, whereas the mixture prepared by hand has an unknown microstructure.

Table 4.1: r^+/d^+ ratios (from the area of fitted peaks) for the SSP spectra.

	Temperature (℃)	Cold-stage, Hot-Solution r^+/d^+ ratio	Hot-stage, Hot-Solution r^+/d^+ ratio
Handmade Mixture	18	3.4 ±0.5	3.4 ±0.5
	35	2.4 ±0.4	5.0 ±0.7
	40	2.1 ±0.3	1.6 ±0.3
	45	3.0 ±0.5	1.1 ±0.4
Unilever Mixture	18	3.7 ±0.6	3.7 ±0.6
	35	4.5 ±0.7	4.8 ±0.2
	40	2.4 ±0.6	2.1 ±0.3
	45	3.3 ±0.4	1.5 ±0.2

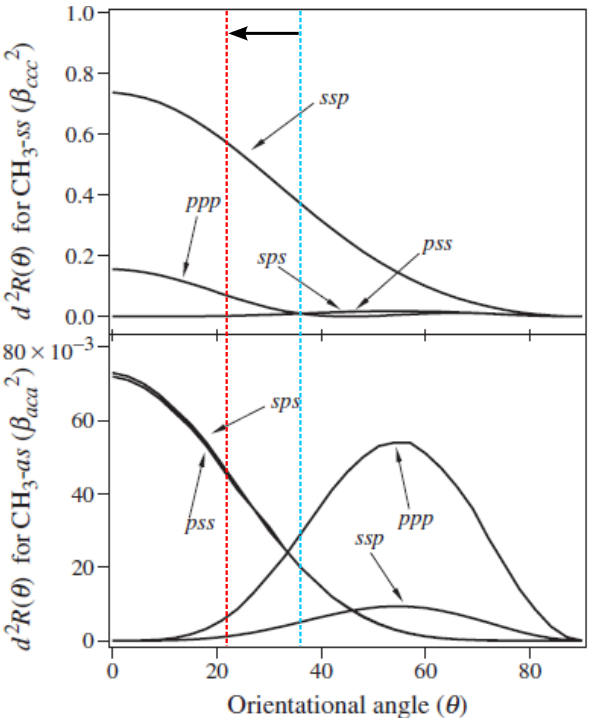

Figure 4.4: Calculated SFG intensities as a function of tilt angle, plotted for each of the different polarisation combinations. Reproduced from [5]. Copyright 2005 American Chemical Society. The top graph shows the variation of the methyl symmetric stretch (r^+) resonances, and the bottom graph shows the variation of methyl antisymmetric stretch (r^-) resonances. Superimposed onto this is an example of a tilt angle change (blue to red) that would cause the r^+/r^- ratio to increase.

4.3 Effect of ionic strength on the temperature properties

In general, increasing ionic strength would be expected to improve the quality of the self-assembled monolayers by shielding charge-charge repulsion of the BTAC [6], so that a greater density of surfactant adsorbs onto the surface. Divalent counter-ions (such $[CO_3]^{2-}$) generally increase the aggregation number of oppositely charged surfactants, and preferentially interact with the surfactants, expelling monovalent cations in competition [7]. This would reduce the number of gaps in the monolayer on the substrate, resulting in a more dense, more stable monolayer. Since the monolayers produced were

already of good quality, the effect of ionic strength was not expected to be large. Figure 4.5 shows the spectra obtained when the surfactant solution was saturated with $CaCO_3$. The SSP and PPP spectra of the handmade solutions indicate that the monolayer quality decreased slightly when formed from a solution containing $CaCO_3$. For the Unilever mixture, the SSP spectra are identical within their signal-to-noise ratios, and the PPP spectra indicate a very slight increase in monolayer quality at higher temperatures when $CaCO_3$ was present.

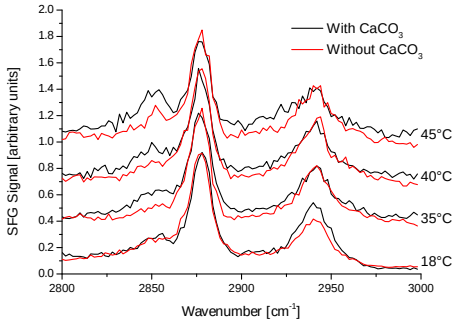

(a) SSP polarisation spectra of hand-made sample.Scaled so that the peak at 2878 cm^{-1} is the same height.

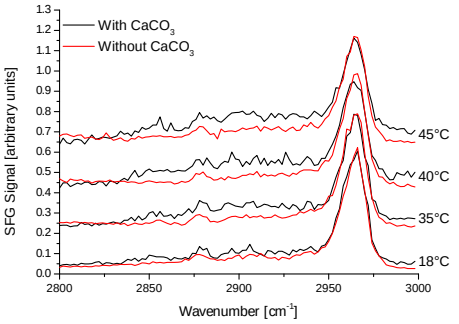

(b) PPP polarisation spectra of hand-made sample. Scaled so that the peak at 2966 cm^{-1} is the same height.

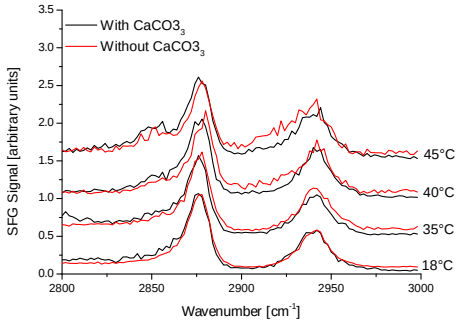

(c) SSP polarisation spectra of Unilever sample. Scaled so that the peak at 2878 cm^{-1} is the same height.

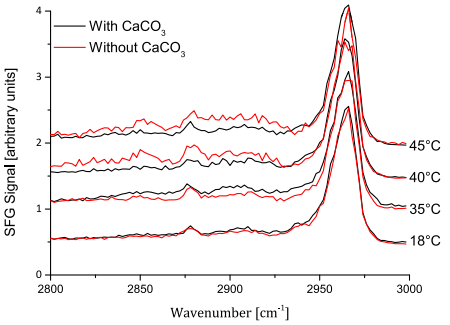

(d) PPP polarisation spectra of Unilever sample. Scaled so that the peak at 2966 cm^{-1} is the same height.

Figure 4.5: Comparison of sum-frequency spectra obtained on a stage heated to the indicated temperature, of samples that were were prepared from room-temperature solutions with $CaCO_3$ (red lines) and without $CaCO_3$ (black lines).

In the case of the Unilever mixture, the PPP spectra (Figure 4.5d) do indicate that the monolayer is less susceptible to temperature increase, supporting the idea that the carbonate has increased the monolayer quality. Conversely the monolayers produced

from the hand-made samples become more susceptible to temperature increases when $CaCO_3$ was present in the solution, and evidence of this is seen in both the SSP and the PPP spectra (Figures 4.5a and 4.5b). This implies a less well-packed monolayer was formed. If there are fewer BTAC molecules in the monolayer, replacing chloride ions with carbonate ions might have a destabilising effect. This might be because the carbonate is larger than the chloride ion, increasing the distance between alkane chains further, but does not return as much stabilisation from favourable interactions with the positively charged head-groups of the BTAC molecules. In general, the solubility of $CaCO_3$ is very low (approximately 0.00013M at 18℃ [8]), and the slight increase in ionic strength has not made much difference to the monolayer quality, which was already good to begin with.

There is another point to be made about these data, focusing on the red spectra in Figures 4.5c and 4.5d (i.e. ignoring those with $CaCO_3$). Although the stage temperatures are increasing in these experiments, the spectra of the Unilever mixture do not show the same trend as seen in the previous section, in Figures 4.3c and 4.3d. The difference between these two sets of experiments is the temperature of the solution that was used during the self-assembly of the monolayer. For example, in Figures 4.5c and 4.5d, the red 45℃ spectrum represents a sample that was produced from solution at 18℃. Although this sample was heated to 45℃ on the SFG stage, there is little evidence of gauche defects. In contrast, the 45℃ spectra of Figures 4.3c and 4.3d represent a sample that was produced from a solution at 45℃, and when heated to 45℃ on the SFG stage large d^+ resonances are observed, indicating the presence of gauche defects. This supports the idea that at low solution temperature, a high-density monolayer is produced with a low tilt angle, whereas at a high solution temperature, a lower-density monolayer is produced with a greater tilt angle. When heated on the SFG sample stage, the tilt angle of the high-density monolayer cannot change significantly, whereas the tilt angle of the lower-density monolayer can be reduced to create room for gauche defects to form.

4.4 Effect of formulation temperature on the deposition behaviour of model hair conditioners

Two further samples were supplied by Unilever, which were formulated at two different temperatures. One involved the mixing of the ingredients at 63℃, and the other at 80℃, labelled RR63 and RR80, respectively. Both include CetOH and BTAC as before, and experiments to evaluate the behaviour of the two model hair conditioners followed a similar pattern as previously - monolayers were deposited onto glass and spectra were taken at the various temperatures shown in Table 3.1.

The cold-stage, hot-solution experiments indicate that at low temperature, the monolayers are well packed, since regardless of the density on the substrate, the molecular tilt angle increases enough that packing is good regardless, and therefore it is not possible to observe the effects of solution temperature on the monolayer quality by SFG. In order to reveal these effects, the monolayer must be heated, so that the tilt angle of less dense monolayers is reduced and room is made for gauche defects to occur, resulting in a change in SFG response. To separate the effects of stage temperature from the effect of the solution temperature, a third set of experiments was conducted where the stage was heated but the solution temperature remained fixed.

As before, these spectra are all typical of good monolayers. Fitting the spectra results in the r^+/d^+ ratios presented in Table 4.2. Comparing RR63 to RR80 indicates that RR63 produced monolayers with a slightly better ordering, especially at low temperature.

Table 4.2 reveals some strong similarities in how the performance of the model conditioners changes at higher stage and solution temperatures. In all cases when the SFG stage is not heated, it is difficult to spot any trend in the r^+/d^+ ratios of any of the mixtures. However, the r^+/d^+ ratios drop when both the solution and stage temperatures are increased. The extent to which this trend is still true when only the stage is heated is different for each of the samples. For the homemade and Unilever samples, this trend is much reduced, if it is present at all. However for RR63 and RR80, this trend is still present to a similar extent when only the stage is heated.

Therefore, in the case of the Unilever and homemade samples, the solution temperature has a strong effect on the density of the self-assembled monolayer. However, to observe

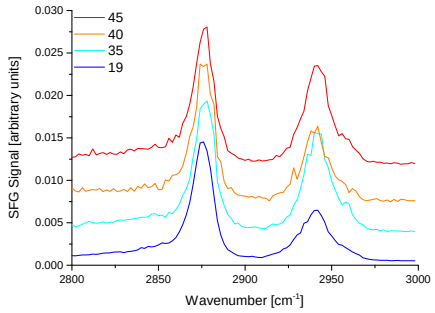

(a) SSP polarisation spectra of the RR63 sample. Scaled so that the peak at 2878 cm^{-1} is the same height in all samples.

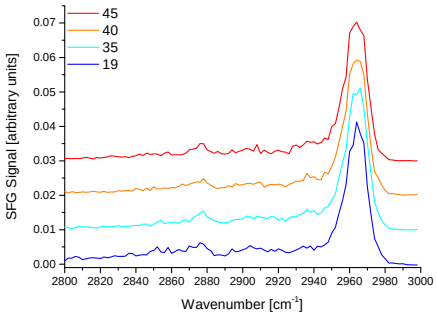

(b) PPP polarisation spectra of the RR63 sample. Scaled so that the peak at 2966 cm^{-1} is the same height in all samples.

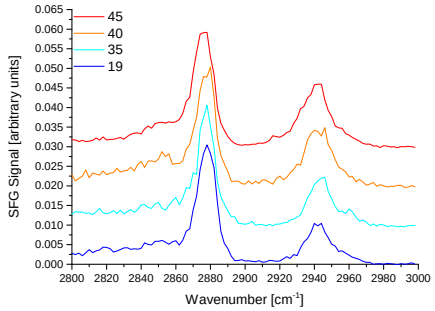

(c) SSP polarisation spectra of the RR80 sample. Scaled so that the peak at 2878 cm^{-1} is the same height in all samples.

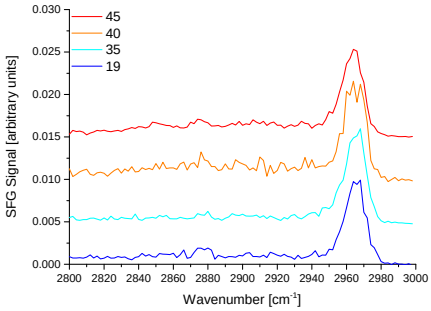

(d) PPP polarisation spectra of the RR80 sample. Scaled so that the peak at 2966 cm^{-1} is the same height in all samples.

Figure 4.6: Sum-frequency spectra obtained on a room-temperature stage. Samples were prepared by self-assembly onto glass slides from a solution at the temperature indicated on the graphs.

this, the stage temperature must also be heated. The explanation for this behaviour is as follows - at low solution temperature, the Unilever and homemade samples deposit fairly densely on the surface, giving a close-packed monolayer with a small tilt angle. When this dense self-assembled monolayer is heated, only a slight reduction in tilt angle is possible, and as a result little room for gauche defects to appear. At higher solution temperature, these samples deposit less densely, but with a higher tilt angle so that the packing is still close. When this less dense monolayer is heated, a larger reduction in tilt angle is possible, creating more room for gauche defects to appear.

For RR63 and RR80, the stage temperature alone is enough to account for the observed change in r^+/d^+ ratios - the solution temperature does not appear to be strongly affecting

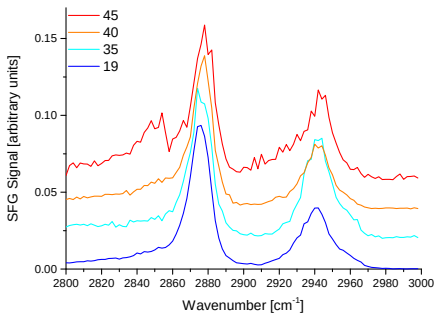

(a) SSP polarisation spectra of the RR63 sample. Scaled so that the peak at 2878 cm^{-1} is the same height.

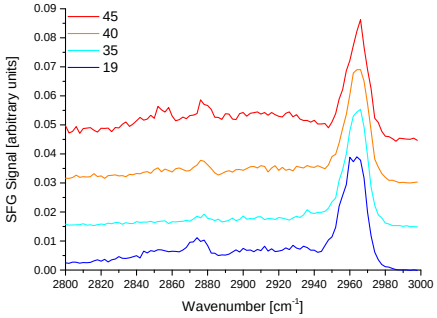

(b) PPP polarisation spectra of the RR63 sample. Scaled so that the peak at 2966 cm^{-1} is the same height.

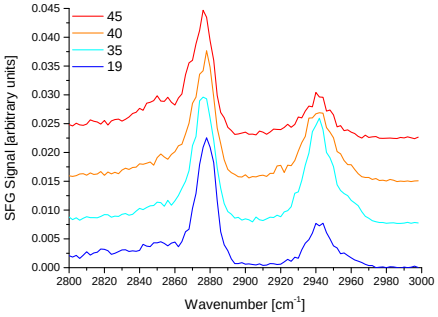

(c) SSP polarisation spectra of the RR80 sample. Scaled so that the peak at 2878 cm^{-1} is the same height.

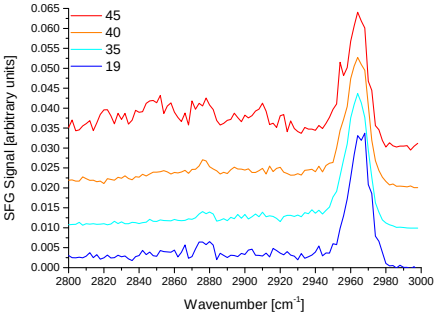

(d) PPP polarisation spectra of the RR80 sample. Scaled so that the peak at 2966 cm^{-1} is the same height.

Figure 4.7: Sum-frequency spectra, acquired on a heated stage, of samples prepared by self-assembly from solution onto glass slides. The stage temperature, equal to the solution temperature in each case, is indicated by the legend on each graph.

the deposition of the monolayer. The fact that the stage temperature affects the r^+/d^+ ratio at all solution temperatures means that the monolayers are never as densely packed as for the Unilever/homemade samples at low solution temperature. A cartoon depicting these ideas is presented in Figure 4.9.

It has been found that cationic surfactant adsorption is decreased at higher temperatures. This can be explained by entropy arguments - at higher temperatures, aggregation and organisation on the surface is dis-favoured for the higher entropy systems of dissolved surfactants and micelles [9–12]. Non-ionic surfactants, on the other hand, show the opposite temperature-dependent behaviour. The authors proposed that the species that are adsorbing onto the surface are in fact the solvated surfactant. At higher temperatures

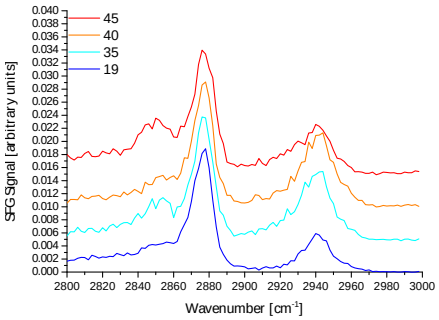

(a) SSP polarisation spectra of the RR63 sample. Scaled so that the peak at 2878 cm^{-1} is the same height.

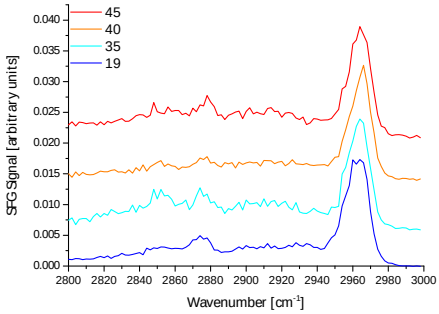

(b) PPP polarisation spectra of the RR63 sample. Scaled so that the peak at 2966 cm^{-1} is the same height.

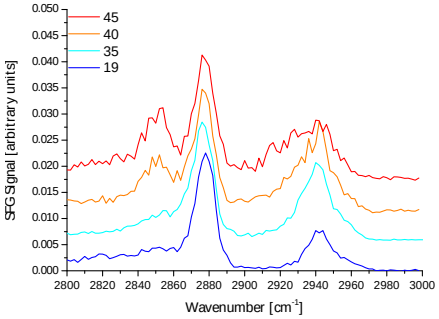

(c) SSP polarisation spectra of the RR80 sample. Scaled so that the peak at 2878 cm^{-1} is the same height.

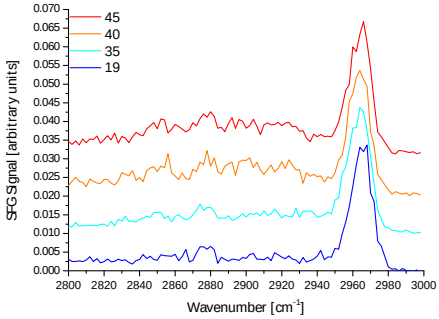

(d) PPP polarisation spectra of the RR80 sample. Scaled so that the peak at 2966 cm^{-1} is the same height.

Figure 4.8: Sum-frequency spectra, acquired on a heated stage, of samples prepared by self-assembly from room-temperature solutions onto glass slides. The stage temperature is indicated by the legend on each graph.

the head group solvation is reduced, making it more hydrophobic, compact, and this increases the surface activity so that a greater amount of surfactant is adsorbed [9, 13, 14]. The Unilever mixture displays a cationic-like behaviour, where the monolayer adsorption is reduced at higher solution temperature. The RR63 and RR80 mixtures do not show this trend, behaving more like non-ionic surfactants.

Table 4.2: r^+/d^+ ratios (from the area of fitted peaks) for the SSP spectra.
This table includes the results in table 4.1 for comparison

	Temperature (℃)	Cold-stage, Hot Soln r^+/d^+ ratio	Hot-stage, Hot Soln r^+/d^+ ratio	Hot-stage, Cold Soln r^+/d^+ ratio
Handmade Mixture	18	3.4 ±0.5	3.4 ±0.5	3.4±0.5
	35	2.4 ±0.4	5.0 ±0.7	3.6±0.4
	40	2.1 ±0.3	1.6 ±0.3	2.4±0.3
	45	3.0 ±0.5	1.1 ±0.4	2.3±0.2
Unilever Mixture	18	3.7 ±0.6	3.7 ±0.6	3.7±0.6
	35	4.5 ±0.7	4.8 ±0.2	3.1±0.5
	40	2.4 ±0.6	2.1 ±0.3	4.3±0.4
	45	3.3 ±0.4	1.5 ±0.2	2.3±0.4
RR63	18	4.6 ±0.7	4.7 ±0.4	4.6±0.7
	35	4.8 ±0.7	5.3 ±0.7	1.8±0.3
	40	6.7 ±0.9	2.4 ±0.5	1.8±0.3
	45	3.4 ±0.8	1.9 ±0.5	1.3±0.2
RR80	18	3.3 ±0.4	3.3 ±0.4	2.9±0.4
	35	1.8 ±0.6	3.9 ±0.5	2.0±0.4
	40	2.1 ±0.4	2.1 ±0.5	1.3±0.2
	45	2.7 ±0.4	1.3 ±0.3	1.5±0.2

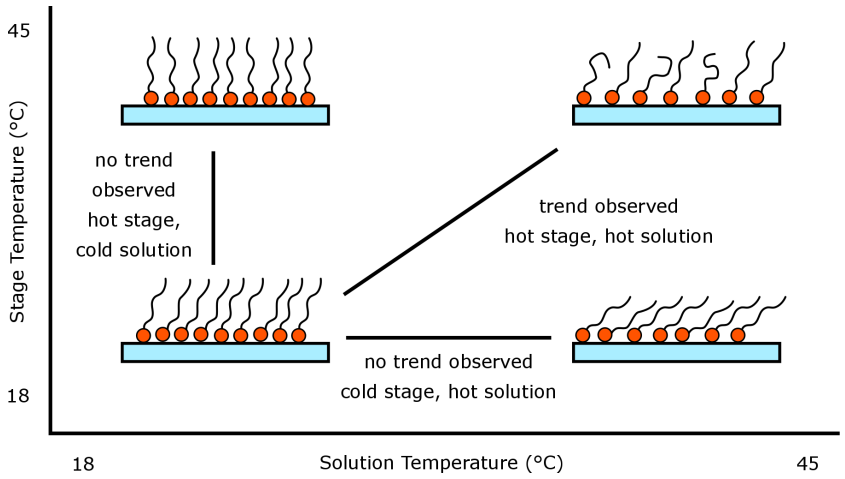

(a) Cartoons depicting the proposed monolayer structure for the Unilever and homemade samples at different stage/solution temperatures. As the solution temperature is increased, the monolayer density decreases, although this cannot be observed in the SFG experiments at low stage temperature (the cold-stage, hot-solution experiments along the bottom). When the stage is heated, the different density of monolayers becomes apparent as the tilt angle decreases. Monolayers produced from low-temperature solutions are so well packed that the small reduction in tilt angle is not enough to make room for gauche defects at high stage temperatures (the hot-stage, cold-solution experiments going up the left side). Monolayers produced from high-temperature solutions are less well packed, and therefore gauche defects appear at higher stage temperatures (as revealed in the hot-stage, hot-solution experiments).

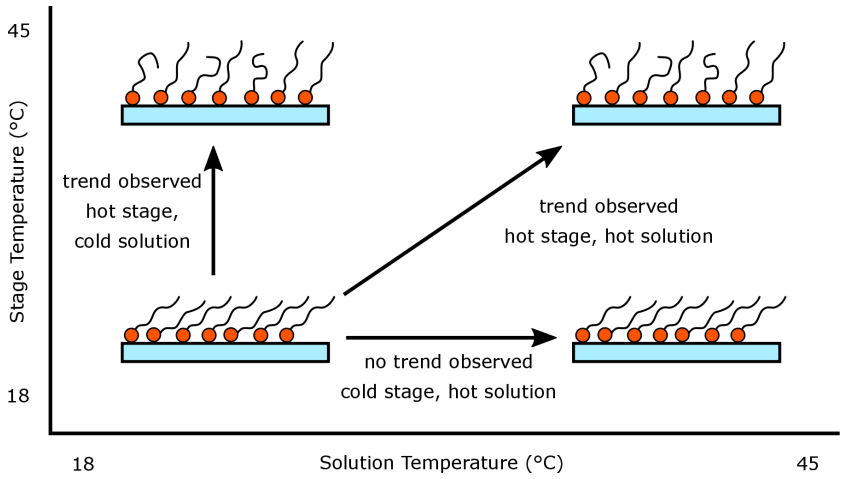

(b) Cartoons depicting the proposed monolayer stucture for the RR63 and RR80 samples at different temperatures. In this case, the monolayer density is not significantly affected by the solution temperature, so that heating the stage produces a similar change in monolayer packing, regardless of solution temperature.

Figure 4.9: Diagrams to explain the observed trends in r^+/d^+ ratios of the SFG spectra presented in this chapter. Arrows show how the solution and stage temperatures were changed in each set of experiments.

References

[1] K. Kjaer, J. Als-Nielsen, C. A. Helm, P. Tippman-Krayer, and H. Moehwald, "Synchrotron x-ray diffraction and reflection studies of arachidic acid monolayers at the air-water interface," *The Journal of Physical Chemistry*, vol. 93, pp. 3200–3206, Apr. 1989.

[2] J. P. Bareman, G. Cardini, and M. L. Klein, "Characterization of structural and dynamical behavior in monolayers of long-chain molecules using molecular-dynamics calculations," *Physical Review Letters*, vol. 60, pp. 2152–2155, May 1988.

[3] S. Roke, J. Schins, M. Müller, and M. Bonn, "Vibrational spectroscopic investigation of the phase diagram of a biomimetic lipid monolayer," *Physical Review Letters*, vol. 90, p. 128101, Mar. 2003.

[4] A. N. Bordenyuk, C. Weeraman, A. Yatawara, H. D. Jayathilake, I. Stiopkin, Y. Liu, and A. V. Benderskii, "Vibrational sum frequency generation spectroscopy of dodecanethiol on metal nanoparticles," *The Journal of Physical Chemistry C*, vol. 111, pp. 8925–8933, June 2007.

[5] R. Lu, W. Gan, B.-h. Wu, Z. Zhang, Y. Guo, and H.-F. Wang, "C-H stretching vibrations of methyl, methylene and methine groups at the vapor/alcohol (N = 1-8) interfaces," *The Journal of Physical Chemistry B*, vol. 109, pp. 14118–14129, July 2005.

[6] A. W. Adamson and A. P. Gast, *The Physical Chemistry of Surfaces.* Wiley, 6th ed., 1997.

[7] H. H. Wennerstrom, A. Khan, and B. B. Lindman, "Ionic surfactants with divalent counterions," *Advances in Colloid and Interface Science*, vol. 34, pp. 433–449, Jan. 1991.

[8] G. Aylward and T. Findlay, *SI Chemical Data.* New York: Wiley, 3 ed., 1994.

[9] S. Paria and K. C. Khilar, "A review on experimental studies of surfactant adsorption at the hydrophilic solid–water interface," *Advances in Colloid and Interface Science*, vol. 110, pp. 75–95, Aug. 2004.

[10] A. Fava and H. Eyring, "Equilibrium and kinetics of detergent adsorption - a generalized equilibration theory," *Journal of Physical Chemistry*, vol. 60, pp. 890–898, July 1956.

[11] A. L. Meader and B. A. Fries, "Adsorption in the detergent process," *Industrial & Engineering Chemistry*, vol. 44, pp. 1636–1648, July 1952.

[12] P. C. Pavan, E. L. Crepaldi, G. de A. Gomes, and J. B. Valim, "Adsorption of sodium dodecylsulfate on a hydrotalcite-like compound. Effect of temperature, pH and ionic strength," *Colloids and Surfaces A: Physicochemical and Engineering Aspects*, vol. 154, pp. 399–410, Aug. 1999.

[13] S. Partyka, S. Zaini, M. Lindheimer, and B. Brun, "The adsorption of non-ionic surfactants on a silica gel," *Colloids and Surfaces*, vol. 12, pp. 255–270, Jan. 1984.

[14] J. M. Corkill, J. F. Goodman, and J. R. Tate, "Adsorption of non-ionic surface-active agents at the graphon/solution interface," *Transactions of the Faraday Society*, vol. 62, p. 979, Jan. 1966.

5. Behenyltrimethylammonium surfactants at the air/water and air/glass interfaces

Quaternary ammonium cationic surfactants, or 'quats', are widely used in cosmetic products such as hair conditioners and shampoos. Behenyltrimethylammonium methyl sulfate (BTMS) and behenyltrimethylammonium chloride (BTAC) are two of the longest chain quats in regular use (22 carbons long, as shown in Figure 5.1). Predicting the performance of such a product requires an understanding of the behaviour and microstructure of the ingredients in the environment that they would be used. In hair conditioners, the product begins as a solution and ends up as a film on the hair. Therefore, the behaviour of the ingredients at both the air/water and air/solid interfaces is important.

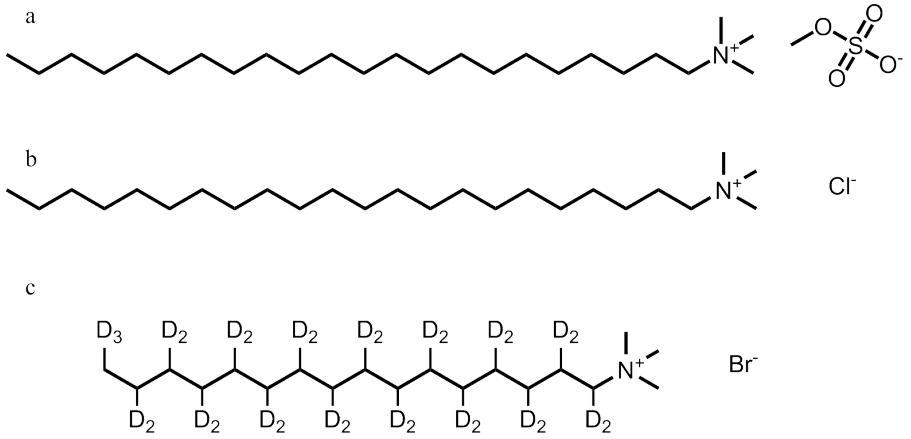

Figure 5.1: Molecular structure of: (a) behenyltrimethylammonium methyl sulfate (BTMS); (b) behenyltrimethylammonium chloride (BTAC); and (c) partially deuterated cetyltrimethylammonium bromide (d-CTAB).

In this chapter, BTMS and BTAC monolayers at the air/water interface were investigated by surface pressure measurements, and sum-frequency generation spectroscopy (SFG). A slow-collapse mechanism was observed following compression of the monolayer on

the LB trough. Atomic force microscopy (AFM) and SFG were also used to investigate BTMS and BTAC cast on mica or glass slides. LB deposition of the monolayers onto glass can capture the state of the film during the slow-collapse period. Deuterated cetyltrimethylammonium bromide (d-CTAB) and D_2O were used to confirm assignments of the resonances of the behenyl surfactants on water. Sum-frequency spectra presented in this chapter include SFG signals arising from CH bonds (2800-3000 cm^{-1}), and signals from OH bonds of water (above 3000 cm^{-1}). Signals in the region 2000-2300 cm^{-1} arise from the CD bonds of deuterated materials, and in the region 2300-2800 cm^{-1} arise from D_2O.

5.1 Surface pressure - area behaviour of BTMS and BTAC

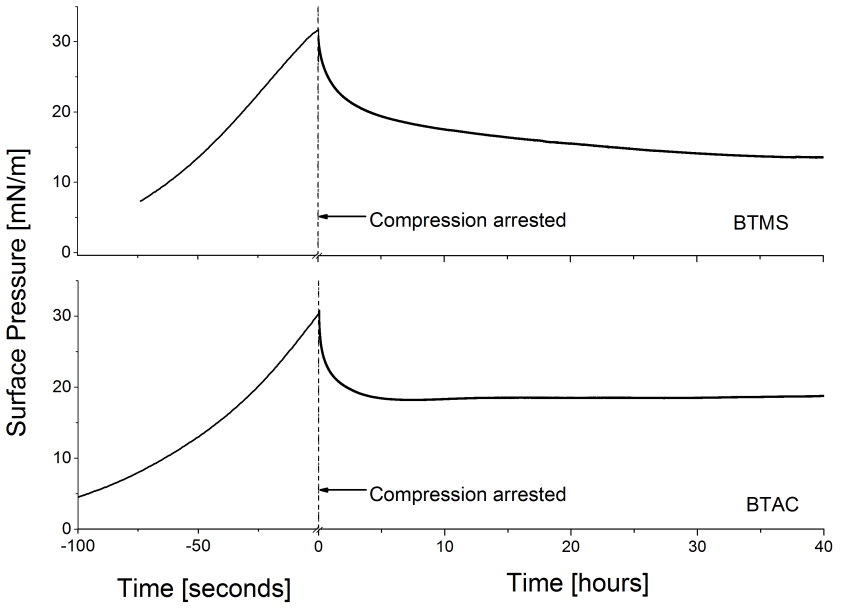

Figure 5.2: Plot of surface pressure against time following compression. BTMS and BTAC films were compressed on the Langmuir trough at a rate of 50 cm^2/min, the barrier arrested and the films allowed to relax over a period of 2 days. Note that the time scale changes from seconds to hours after the compression is arrested.

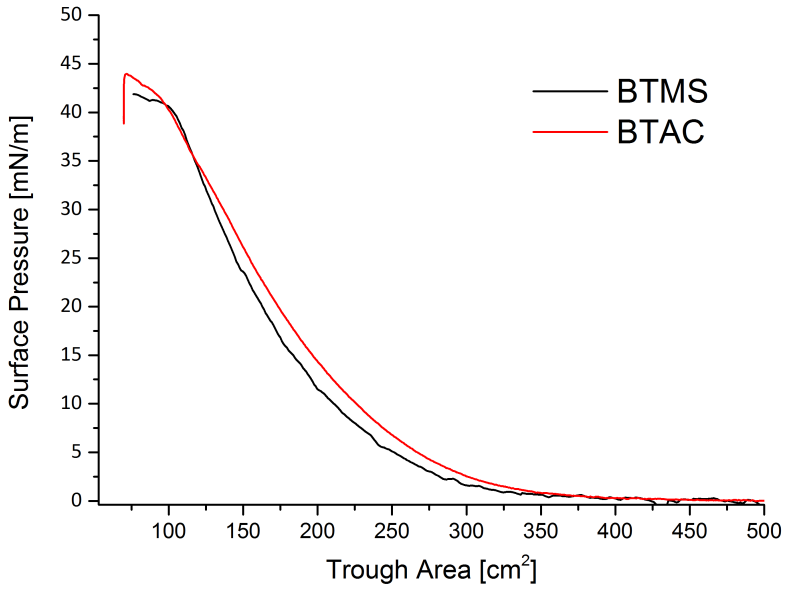

Figure 5.3: Surface pressure - area (π-A) isotherms of BTMS and BTAC. Collapse of the monolayers occurs above 40 mN/m.

Figure 5.2 shows the surface pressure - time (π-t) plot of BTMS and BTAC during and after compression of the monolayer on the Langmuir trough. Compression was arrested when the surface pressure reached 30 mN/m, below the pressure at which rapid film collapse occurs (approximately 40 mN/m for both molecules, as shown in the conventional surface pressure - area (π-A) isotherm Figure 5.3). The plots show that the surface pressure drops after this compression is halted. BTMS and BTAC are both highly insoluble in water, and dissolution into the sub-phase can be ruled out on that basis. The drop in surface pressure must therefore arise from a rearrangement of the film on water. To investigate this behaviour, SFG spectra of the monolayers of uncompressed BTMS/BTAC were recorded.

5.2 SFG spectra of uncompressed BTMS and BTAC

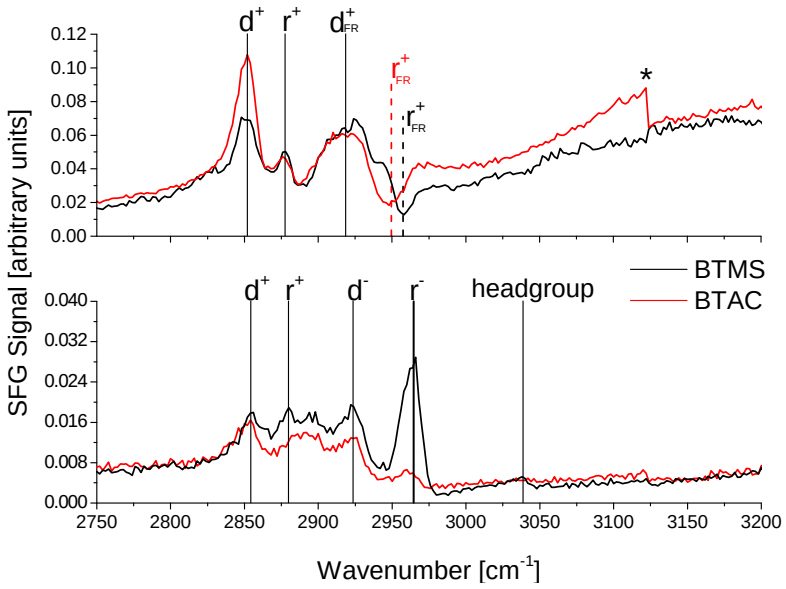

Figure 5.4: SFG spectra in the SSP (top) and PPP (bottom) polarisations of BTAC and BTMS cast onto water without compression. The discontinuity (*) at 3125 cm^{-1} is due to a power step in the output of the infrared laser, which can interfere with the normalisation of the SFG signal. The effect is usually not as large as seen in the spectrum of BTAC in the SSP here.

Figure 5.4 shows the SSP and PPP spectra of uncompressed BTMS and BTAC monolayers at the air/H_2O interface. The spectra of both compounds are similar to each other in most respects, and also similar to other, shorter chain quats, such as cetyltrimethylammonium bromide (CTAB) [1]. The assignment of the prominent CH resonances in the two compounds are d^+, 2853 cm^{-1}; r^+, 2878 cm^{-1}; d^+_{FR}, 2922 cm^{-1} (SSP); d^-, 2924 cm^{-1};and r^-, 2960 cm^{-1}. These features all appear as peaks, except for the dips in SSP spectra at 2945 cm^{-1} and 2960 cm^{-1} for BTMS and BTAC, respectively. These dips appear due to destructive interference with the broad OH resonances of hydrogen bonded water that occur centred at 3200 cm^{-1} and 3400 cm^{-1} [2, 3]. The SFG resonance at 2922 cm^{-1} in the SSP spectrum of CTAB has previously been assigned to the d^- resonance [4]; however antisymmetric resonances are typically weak in the SSP polarisation [5]. Additionally, the spectra of these quats on D_2O (Figure 5.5) make our assignment of the d^+_{FR} unambiguous and in agreement with other published assignments [1].

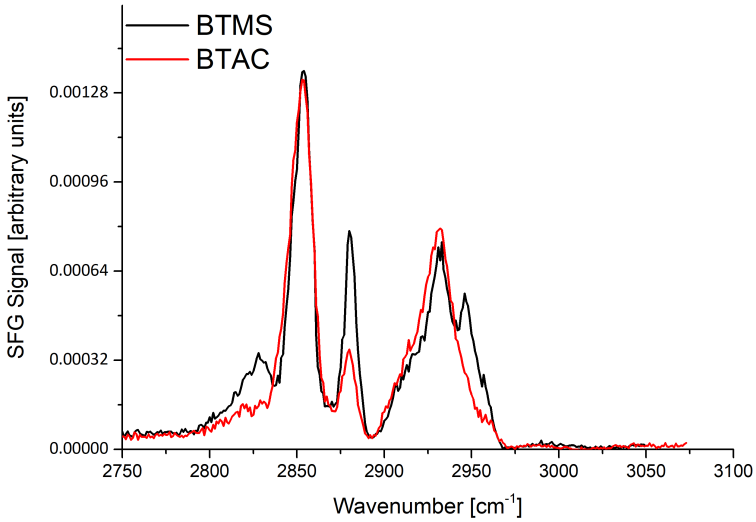

Figure 5.5: SFG spectra in the SSP polarisation of BTMS (black) and BTAC (red) cast onto D_2O without compression, normalised to the d^+ resonance at 2852 cm^{-1}.

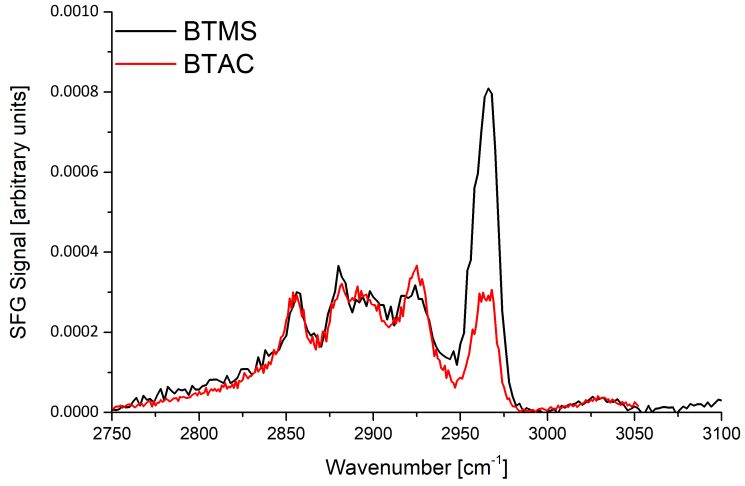

Figure 5.6: SFG spectra in the PPP polarisation of BTMS (black) and BTAC (red) cast onto D_2O without compression, normalised to the d^+ resonance at 2852 cm^{-1}.

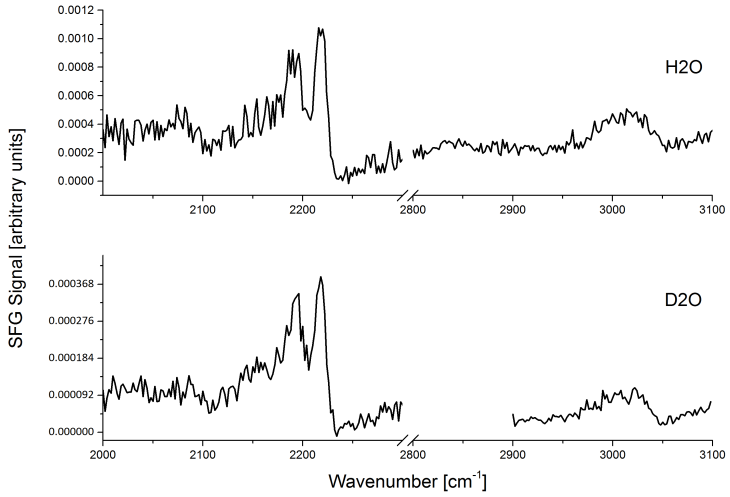

Figure 5.7: SFG spectra in the PPP polarisation of dCTAB cast onto H_2O (top) and D_2O (bottom) without compression. Signals in the CH region can only arise from the CH bonds of the headgroup.

The PPP spectrum of BTMS shows a small resonance at 3040 cm^{-1}. BTMS and BTAC both contain 3 methyl groups in their cationic headgroups. To confirm whether these were responsible for this resonance, partially deuterated cetyltrimethylammonium bromide (d-CTAB, Figure 5.1)), in which only the methyl groups of the headgroup were protonated, was obtained. The PPP spectra of d-CTAB on H_2O and D_2O are shown in Figure 5.7. The only visible resonances in the CH region are centred on 3025 cm^{-1}. This is typical of a methyl anti-symmetric stretch (r^-) when adjacent to an electronegative atom [6], and given the selective deuteration of the compound, it is reasonable to assume that it must arise from the methyl headgroups. Similar features appear in approximately the same region of the linear infrared ATR spectra of BTMS and BTAC at 3034 cm^{-1} and 3022 cm^{-1} respectively (Figure 5.8), and also in the SFG PPP spectra of both at 3025 cm^{-1} when recorded at the air/D_2O interface (Figure 5.6). Therefore, this resonance can be confidently assigned to the r^- mode of the methyl head groups of these molecules. The methyl sulfate counter ion of BTMS also contains methyl groups. To confirm that these did not contribute to the spectrum of BTMS, SFG spectra of sodium methyl sulfate solutions were recorded at various concentrations. No resonances in the CH or SO (1000-1400 cm^{-1}) regions were observable.

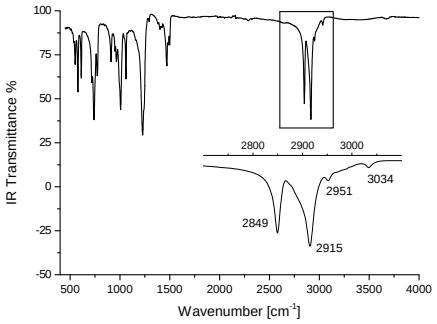

(a) Infrared spectrum of BTMS. A peak is visible at 3034 cm^{-1} in the expanded view of the CH region (2700-3100 cm^{-1}).

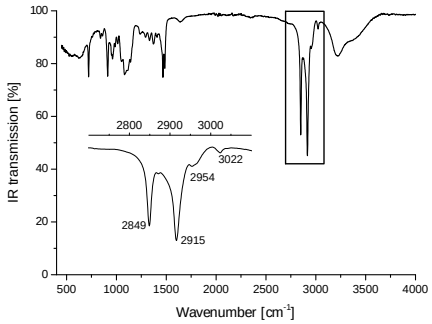

(b) Infrared spectrum of BTAC. A peak is visible at 3022 cm^{-1} in the expanded view of the CH region (2700-3100 cm^{-1}).

Figure 5.8: Single-reflection ATR infrared spectra of solid BTMS and BTAC.

In Figure 5.4 the 2945 cm^{-1} resonance appears as a dip due to destructive interference with OH resonances. Spectra obtained on D_2O do not display this destructive interference and are therefore clearer to assign and fit. Spectra of BTMS and BTAC at the air/D_2O interface are shown in Figure 5.5 (SSP), and Figure 5.6 (PPP). On the basis of these spectra, the resonance at 2945 cm^{-1} is assigned to the r^+_{FR}.

When comparing BTMS and BTAC, there are a few notable differences. Firstly, in Figure 5.5, a clear resonance is visible in the BTMS SSP spectrum at 2829 cm^{-1}, but is very weak (or not present) in BTAC. This is also visible in the SSP spectrum of CTAB [1], although the origin of this resonance was not addressed in that work. Secondly, the r resonances are stronger in the BTMS spectra than in the BTAC spectra. The r^+ resonance (SSP, Figure 5.5) and r^- resonance (PPP, Figure 5.6) show this difference very clearly, and the r^+_{FR} in Figure 5.5 is so weak as to be unresolved in the BTAC spectrum. The r^+/d^+ ratio is sensitive to the ordering of molecules, and when the monolayer of BTAC is slightly compressed, its spectrum shifts to look much more similar to the uncompressed BTMS monolayer, as shown in Figure 5.9. This indicates that the differences between the two spectra are due to a difference in conformational order of the two freshly prepared films.

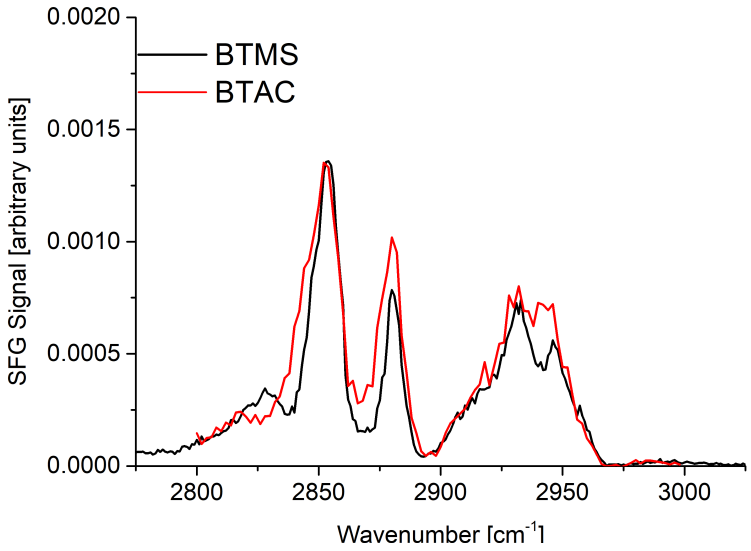

Figure 5.9: SFG in the SSP polarisation spectra of BTMS (black) without compression and BTAC (red) after slight compression, cast onto D_2O. The SFG spectra of the compressed monolayer is time-dependent. In order to capture the spectrum as quickly as possible, the BTAC spectrum was obtained with 100 acquisitions per wavenumber step, and is therefore noisier than the BTMS spectrum (200 wavenumbers per step). Spectra normalised to the d^+ resonance at 2852 cm^{-1}.

5.3 Effect of monolayer compression on the sum-frequency spectra of behenyltrimethyl surfactants

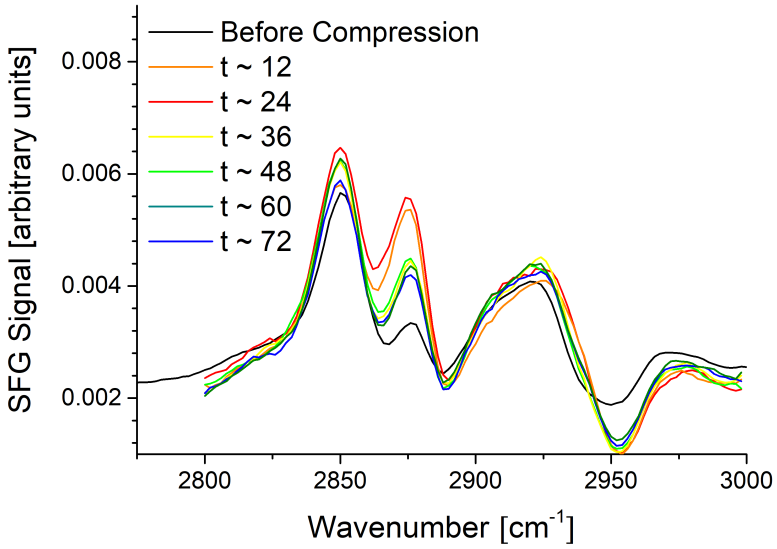

Figure 5.10: Successive SFG spectra recorded in the SSP polarisation at approximately 12 min intervals following compression of a BTMS films at the air/H_2O interface. 10 µl of 4.2 mM chloroform solution was deposited onto the H_2O surface and compressed to half the original area. These spectra have been smoothed (5-point adjacent averaging).

Compressing a monolayer film consisting of a surfactant with a single aliphatic chain is expected to increase its packing density and reduce the number of gauche defects in the chain, i.e. increase its conformational order. Consequently, a decrease in the intensities of the methylene d resonances (d^+ at 28503 cm^{-1}, and d^- at 2924 cm^{-1}) is expected on compression. Furthermore, the tilt angle of the tail with respect to the surface normal should decrease. In the SSP polarisation, only one component of the second-order susceptibility (χ_{yyz}) contributes to the SFG intensity, which means that only vibrational modes with components of their transition moment parallel to the surface normal can contribute to the spectrum. The decrease in tilt angle should lead to an increase in the intensity of the r^+ resonance (at 2878 cm^{-1}) of the terminal methyl group of the chain. The increased density of molecules due to the compression will also increase the overall

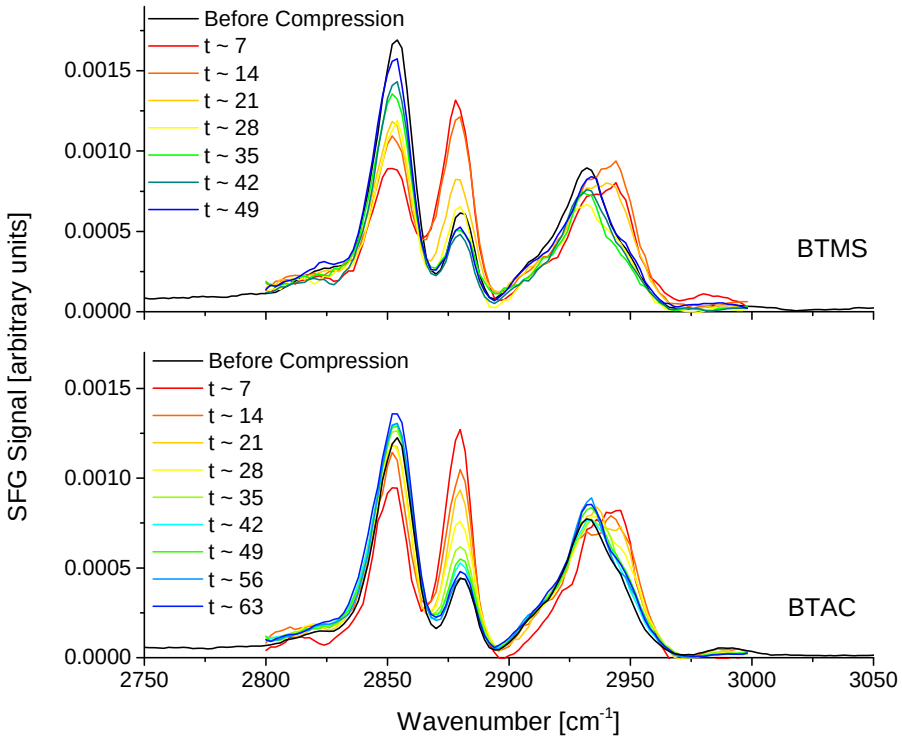

Figure 5.11: Successive SFG spectra recorded in the SSP polarisation at approximately 7 min intervals following compression of a BTMS films at the air/D_2O interface. 10 µl of 4.2 mM chloroform solution was deposited onto the D_2O surface and compressed to half the original area. These spectra have been smoothed (5-point adjacent averaging).

SFG intensity. In order to monitor the conformational order and packing density of the surfactant chains as a function of time, successive spectra were recorded following film compression. SFG spectra of BTMS at the air/H_2O interface before and after compression of the film to 50% of the original area are shown in Figure 5.10. Sequential spectra were recorded as the film relaxed - each new spectrum began immediately after completion of the previous spectrum, taking 12 minutes to acquire. As shown by the π-t behaviour in Figure 5.2, the compressed film is unstable, and relaxes to a lower equilibrium surface pressure. This change in lateral pressure is accompanied by the corresponding changes in the number of gauche defects and tilt angle changes as just described, and the changes in the d and r resonances reflect this - at lower surface pressure in the later scans, more gauche defects and larger tilt angles result in larger d resonances and smaller r resonances.

Although the resonance at 3025 cm^{-1} attributed to the methyl C-H stretch of the head group was definitely present, its low signal-to-noise ratio made it difficult to make temporal measurements of the same kind as for the r^+ and d^+ peaks of the aliphatic chain. However, to a good approximation- its intensity and position remained constant with time, suggesting that its orientation is independent of surface concentration. This is similar to results observed with sodium dodecyl sulfate (SDS) as the surfactant concentration changed [7].

To remove the interference caused by water resonances in the C-H region, and thereby obtain clearer spectra, analogous spectra of BTMS and BTAC were recorded at the air/D_2O interface. There are no significantly labile H positions in BTMS and BTAC, and no H-D exchange was observed during these experiments. The SSP spectra of these experiments are shown in Figure 5.11. These spectra were taken with fewer acquisitions in order to obtain a higher time resolution - in this case, each spectrum took 7 minutes to acquire rather than 12 minutes. This means that the first scan reaches 2880 cm^{-1} approximately 170 seconds after compression, as opposed to 300 seconds. Consequently, the first spectrum after compression (red trace of Figure 5.11) shows a greater SFG intensity at the r^+ band centre at 2878 cm^{-1} than at the d^+ band centre at 2852 cm^{-1}, in contrast to Figure 5.10. The change in the resonance at 2946 cm^{-1} is clearer without the H_2O resonances and it follows a similar time dependence to the r^+ resonances, confirming its assignment to the r^+_{FR} mode, the Fermi resonance of the r^+ mode at 2880 cm^{-1}.

From the changing r^+/d^+ ratios observed in the above spectra, the basic idea of what occurs in the monolayer is fairly clear - at the equilibrium pressure, a significant number of gauche defects are present, as indicated by the low r^+/d^+ ratio of the monolayer before compression. It is especially clear for the spectra taken on D_2O (Figure 5.11). Upon compression, the number of gauche defects is greatly reduced, as can be seen by the large increase in the r^+/d^+ ratio of the successive spectra. This is intuitive - the higher lateral pressure in the monolayer induces chains to straighten out so as to reduce their molecular area. Immediately following compression, the monolayer lateral pressure begins to reduce as shown by the π-t isotherms in Figure 5.2, and the return to the previous structure, including gauche defects, is clearly represented by the r^+/d^+ ratio. Film instability and slow-collapse at pressures below that at which the film fractures are well documented [8, 9].

5.4 Behenyltrimethyl surfactants at the air/glass interface

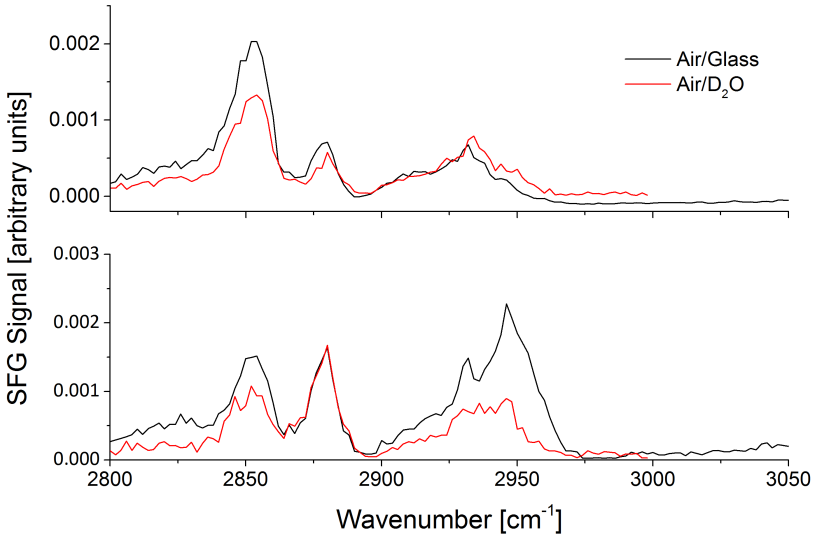

Figure 5.12: SFG spectra in the SSP polarisation of BTMS cast onto glass (black) from H_2O without compression (top) and with compression (bottom). Equivalent spectra of BTMS on D_2O (without and with compression) are overlaid in red.

The relaxation mechanism behind this slow-collapse cannot be deduced from the SFG spectra alone. To investigate it further, BTMS was cast onto glass slides immediately following and an hour after compression of the monolayer on water. Figures 5.12 (SSP) and 5.13 (PPP) show the C-H region of the SFG spectra of these films, along with spectra of films at the air/D_2O interface under the same conditions overlaid for comparison. The air/glass spectra are qualitatively similar to the analogous spectra at the air/D_2O interface, especially in terms of the r^+/d^+ ratios.

The air/glass monolayers are in fact quite stable, and the spectra do not change significantly on the timescle of a few hours (no samples were kept overnight). This is probably because the BTMS has a positively charged headgroup, so depositing the film onto a negatively charged surface such as glass produces a relatively stable system, long-lived enough to potentially obtain AFM images. Therefore, films were cast onto freshly cleaved mica (which has a very low surface roughness and similar charge to glass)

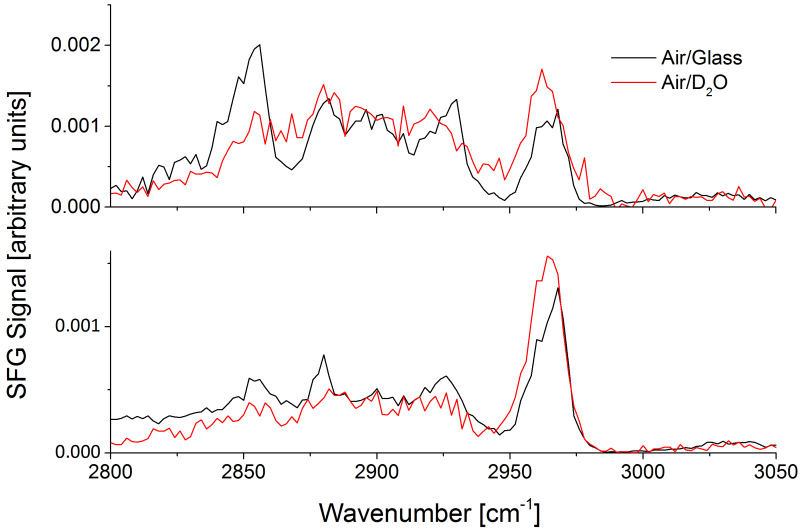

Figure 5.13: SFG spectra in the PPP polarisation of BTMS cast onto glass (black) from H_2O without compression (top) and with compression (bottom). Equivalent spectra of BTMS on D_2O (without and with compression) are overlaid in red.

in the same manner as for the glass/air interface, and AFM images and associated height profiles are shown in Figures 5.14 to 5.17. When the BTMS was deposited onto the mica immediately after being compressed on the water surface (Figure 5.14), there are many islands which are approximately 0.7 nm above the surrounding surfactant monolayer, which corresponds to the baseline in the height profile of the AFM images (Figure 5.14). Within some of these islands, are peak regions that are 2.5 to 3.5 nm above the islands. When the surfactants were allowed to relax on the trough surface before LB deposition (Figure 5.16), the islands are still 0.7 nm high , but each has a larger surface area and they are fewer in number. The peaks are now larger, rising 4 nm above the surrounding island, with less variation in the peak heights (Figure 5.17). The fully extended chain length of BTMS is roughly 2.5 nm. Therefore, the 0.7 nm difference between islands and surrounding material is interpreted as a change in tilt angle and/or packing density of the BTMS monolayer rather than another layer of BTMS. It is highly unlikely that BTMS is arranged with the charged headgroup pointing upwards due to the lack of stabilising interactions that exist when the headgroup is pointing downwards. Therefore, the peaks that rise above the islands are interpreted as a bilayer atop the monolayer. The peaks

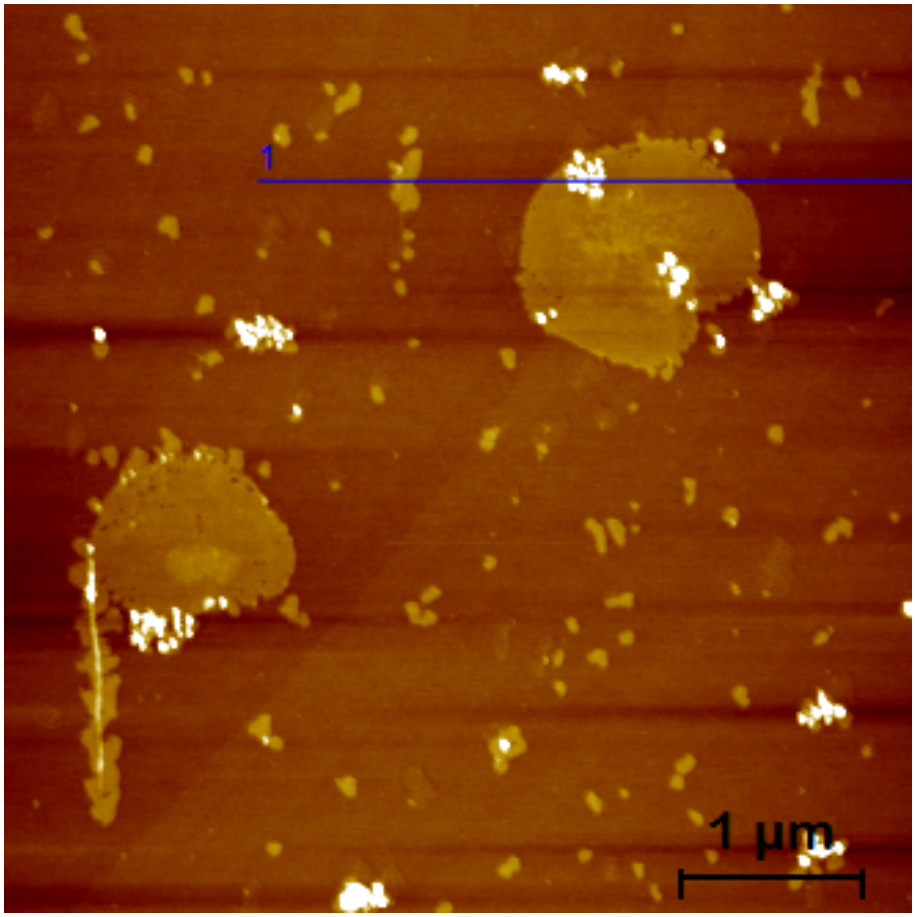

Figure 5.14: AFM image of BTMS cast onto mica immediately following compression. The blue line shows the position of the cross section used below in Figure 5.15.

rise 4 nm rather than a full 5 nm due to some tilting from the surface normal and/or gauche defects in their structure.

The AFM images of the unrelaxed film immediately after compression also show larger variability in the height of the multilayer phases - evidence that the multilayer regions are growing at this stage. Histogram plots of the total volume sum of BTMS in these multilayer regions increases as time passes following compression, as shown in Figures 5.18 and 5.19, and the AFM images show that a relatively small number of regions of multilayers grow at the expense of the others. The fact that multilayer regions can nucleate and then grow or shrink implies that under the conditions used here, the monolayer is in equilibrium with a multilayer phase, and the drop in surface pressure after compression represents an overall growth of these multilayer regions. This type of relaxation has

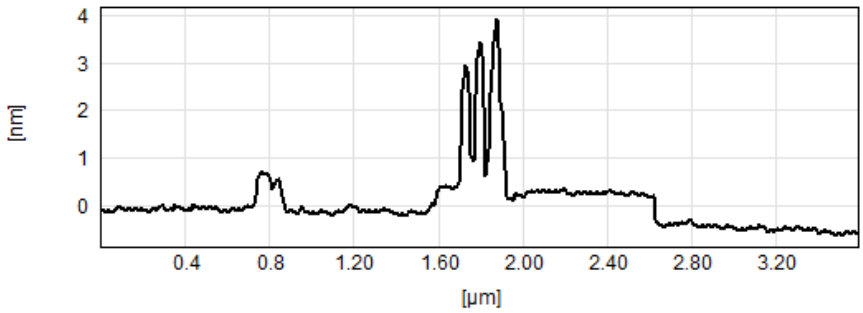

Figure 5.15: Cross section of surface heights of BTMS cast onto mica immediately following compression. The baseline of the trace corresponds to the top of the monolayer on glass. The 0.7 nm rise at 0.8 µm and from 1.60 to 2.60 µm are the regions referred to as plateaux in the text. Three of the peaks described in the text are visible within the plateau region between 1.60 and 2.00 µm.

been observed before and is referred to as a slow-collapse mechanism, whereby islands of multilayer phases nucleate and grow, and in this way reduce the lateral pressure of the monolayer [8, 10, 11].

The reason why SFG spectra fail to detect these multilayer phases is due to the symmetry of structures with an even number of layers - sum-frequency light from one layer is cancelled out by light with the opposite phase from the layer above. The SFG spectra therefore provide only very specific information about the molecular organisation of the BTMS in the surrounding monolayers. While it is possible that the bottom or top layer of the multilayer structure may also contribute, they represent only a fraction of the total area illuminated by the laser spot on the surface and, because the SFG intensity is proportional to the square of the number density of molecules, an even smaller fraction of the output SFG intensity.

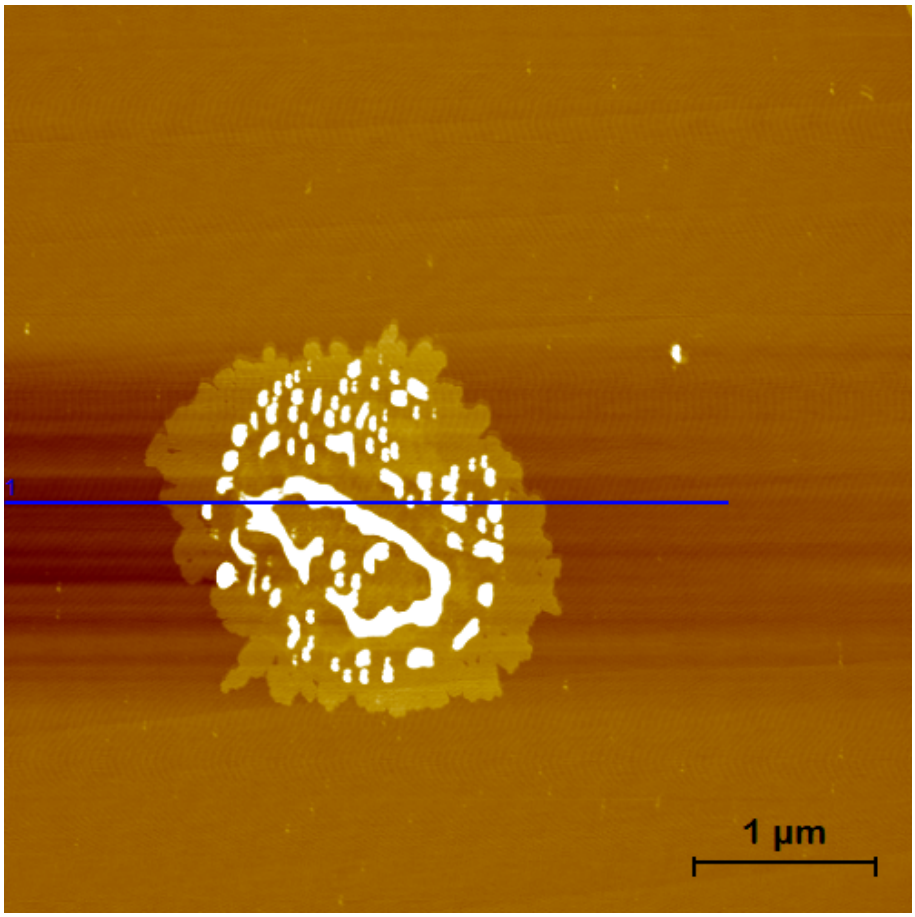

Figure 5.16: AFM image of BTMS cast onto mica 1 hour after compression. The blue line shows the position of the cross section used below in Figure 5.17

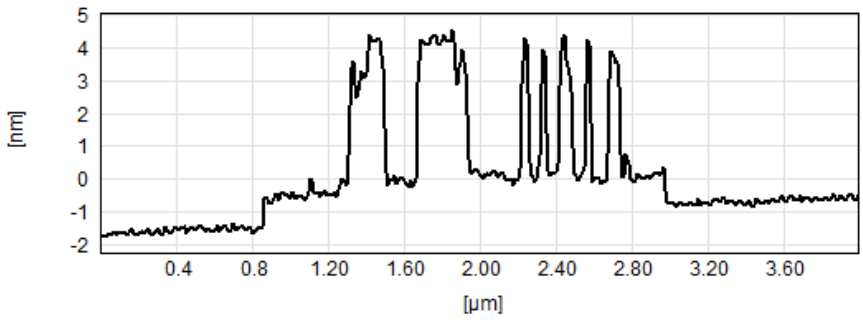

Figure 5.17: Cross section of surface heights of BTMS cast onto mica 1 hour after compression. The plateau region ranges from 0.9 to 2.9 µm, with a multitude of peaks atop this in the range.

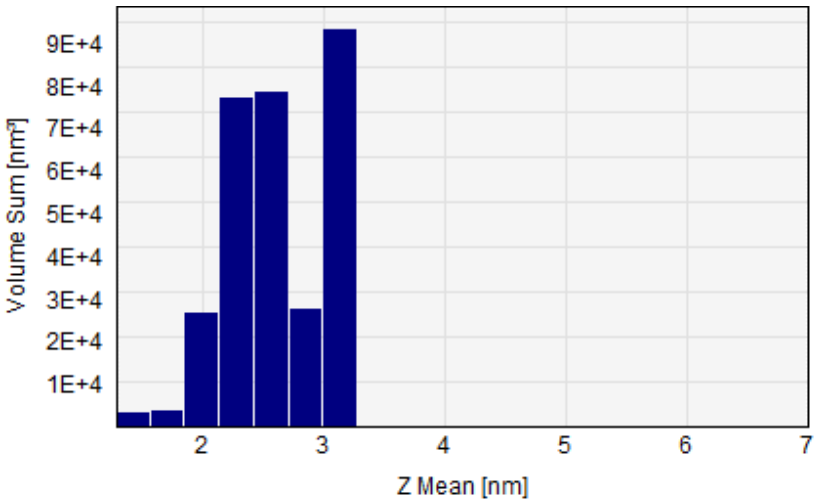

Figure 5.18: Histogram plot of the volume sum of material at each Z value observed in the AFM images (shown in Figure 5.14). Here, BTMS was cast onto the mica immediately following compression, and there is a relatively small amount of material with Z values greater than 0, which corresponds to the monolayer height.

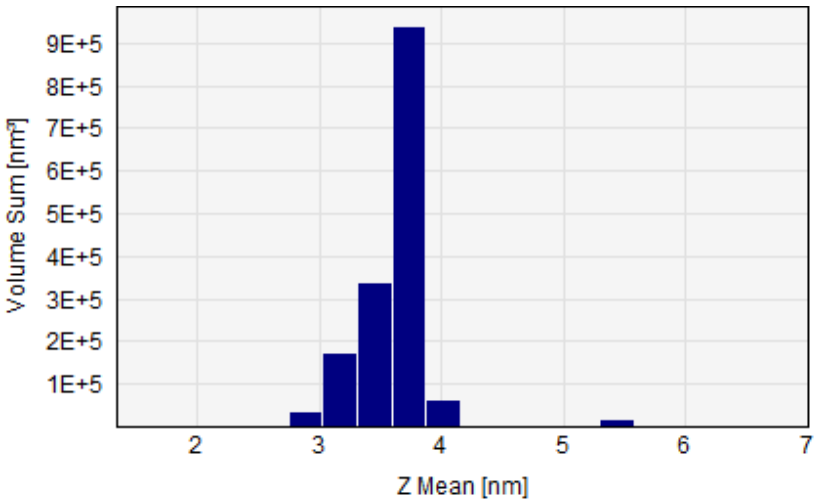

Figure 5.19: Histogram plot of the volume sum of material at each Z value observed in the AFM images (shown in Figure 5.16). Here, BTMS was cast onto the mica 1 hour after compression, and there is now a much larger amount of material with Z values greater than 0, indicating a greater amount of material in multilayer phases. Note that the volume sum scale is 10 times the scale of the previous figure.

5.5 Interpretation of time-dependent sum-frequency intensities

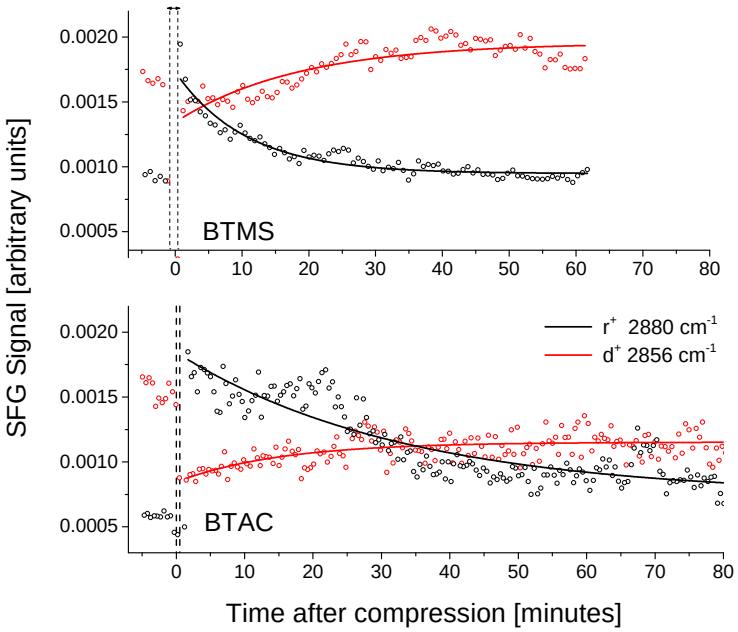

Figure 5.20: SFG intensities in the SSP polarisation of the methyl r^+ (black) and methylene d^+ (red) resonances of BTMS (top) and BTAC (bottom) before and after being compressed to 30mN/m.

In order to gain higher time resolution of the r^+ and d^+ resonances, the SFG intensities at specific wavenumbers were monitored over time. The current setup is limited to SFG intensities acquired at two different wavenumbers simultaneously (due to the design of the software that runs the laser). This allows for data points to be acquired more rapidly after compression of the monolayer. Quantitative analysis of the shape of these lines is complicated by the multiple factors affecting their intensity. Both signals will weaken as the film relaxes and the number density of molecules in the monolayer illuminated by the laser beam decreases (for instance, this may be the reason that the growth of the d^+ intensity is slower and less pronounced than the decrease in r^+ intensity). Additionally, the SFG response of the methyl and methylene groups vary with their respective tilt angles to the surface normal [5, 12] and the relationship between their average tilt angles will change as the number of gauche defects increases.

Overlaid on the SSP data in Figure 5.20 are exponential decay curves described by the function

$$I_{SF}(t) = I_{SF,0}\ e^{-t/\tau} + I_{SF}(\infty) \tag{5.1}$$

where $I_{SF}(t)$ and $I_{SF}(\infty)$ are the SFG intensities at time t and ∞ respectively, $I_{SF,0}$ is the difference between those two at ($t = 0$), and τ is the time period of the signal decay. For the d^+ resonances, $I_{SF,0}$becomes negative to produce an exponential decay curve of an increasing form. The values of the fitted parameters are shown in table 5.1.

Table 5.1: Fitted parameters for the BTMS and BTAC r^+/d^+ time dependence curves.

		τ (minutes)	$I_{SF,0}$ (arbitrary units)	$I_{SF}(\infty)$ (arbitrary units)
BTMS	r^+	10.6	7.8E-4	9.5E-4
	d^+	18.4	-6.1E-4	2.0E-3
BTAC	r^+	33.0	1.1E-3	7.4E-4
	d^+	15.1	-3.1E-4	1.2E-3

The two surfactants show significantly different time dependences in their SFG response, especially for their r^+ resonances, as shown by the time periods τ of their signal decay. The r^+ intensity decreases due to orientational averaging of the SFG light arising from increasingly disordered methyl groups, and also due to the increasing molecular area of the monolayer (and therefore the reduced number of molecules under the laser spot). These factors also affect SFG light arising from methylene groups (d resonances); however-the d^+ intensity increases due to the increasing number of gauche defects appearing as the monolayer disorder increases.

As an alternative to acquiring just the intensities at two wavenumbers, the successive spectra of BTAC and BTMS compressions (Figure 5.11) were fitted, and the peak areas of the r^+ and d^+ resonances are shown in Figure 5.21. By inspection of the graph, it is clear that the BTAC and BTMS time dependences now match each other much more closely than was observed in Figure 5.20.

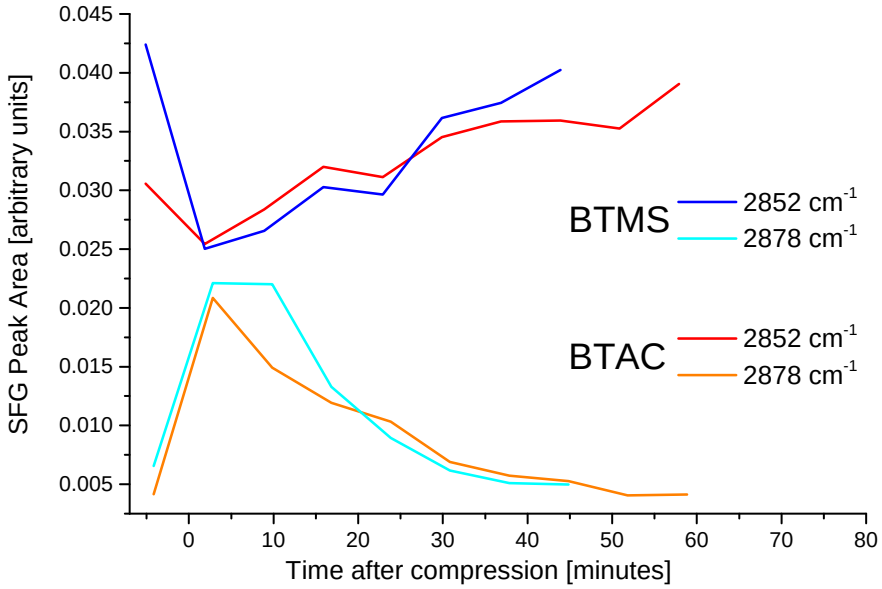

Figure 5.21: Fitted SFG peak areas of the r^+ (2878 cm^{-1}) and d^+ (2852 cm^{-1}) resonances of BTAC (red) and BTMS (blue) compressions shown in Figure 5.11, overlaid for easy comparison.

These differences highlight the problems arising from monitoring just the SFG intensity at specific wavenumbers. The increased time resolution comes at a cost - detailed peak information, such as peak areas/height/width and the intensity of resonances at other wavenumbers, are sacrificed. The SFG intensity obtained from this experiment is not equivalent to the peak height nor is it proportional to the peak area or the resonant susceptibility. The SFG intensity at a specific wavenumber will not only depend on the resonance centred there, but will be affected by adjacent peaks whose area overlaps at that wavenumber. The peak widths of resonances tend to become wider as the monolayer is more disordered, meaning that the extent to which adjacent resonances affect the SFG intensity at a peak centre changes as the experiment progresses. Fitting complete spectra allows us to deconvolute overlapping peaks; however, this is not possible when acquiring only the SFG intensities, since the peak width is not known.

The r^+/d^+ ratio can be used as an indication of monolayer ordering. Using the values from the time-dependent SFG intensities and from the fitted peak areas, and plotting this ratio against time, gives Figure 5.22. Again, we can see the difference in the SFG data arising from the different methods. The fitted peak areas show that the r^+/d^+ ratios of the two surfactants have a similar time dependence. In contrast, the time-dependent

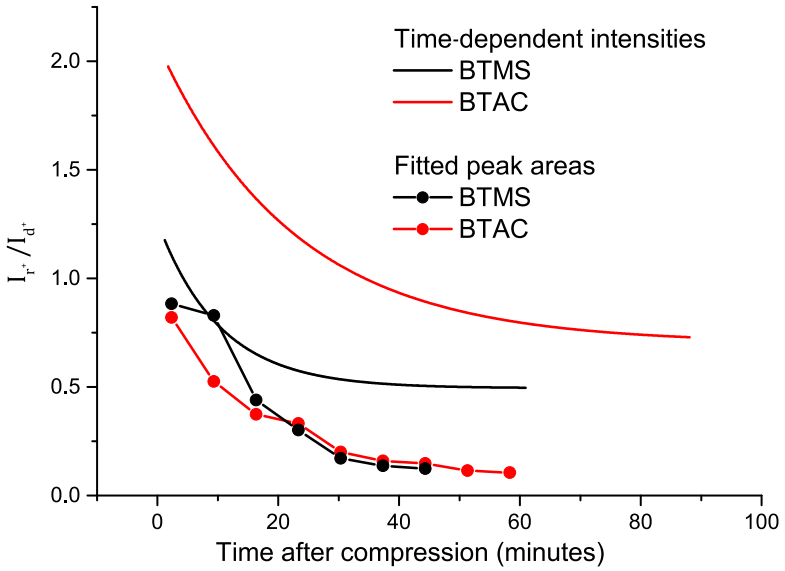

Figure 5.22: r^+/d^+ ratios of the r^+ and d^+ resonances of BTMS (black) and BTAC (red) monolayers relaxing following compression. Note that these plots are not off-set, but appear so because the time-dependent intensities are derived from peak height, as opposed to peak areas - the different peak shapes result in the offset appearance.

SFG intensities show that r^+/d^+ ratio of BTAC reduces more slowly than that of BTMS. The surface pressure plots in Figure 5.2 show the opposite trend than what would be expected from the time-dependent SFG intensity plot - that is the surface pressure initially drops more quickly for BTAC than for BTMS. The opposing trends between the time-dependent SFG intensities and the surface pressure can be dismissed on the basis of the issues discussed. Therefore, in Figure 5.23 only the fitted area r^+/d^+ ratios have been overlaid onto an expanded view of the surface pressure against time plot from Figure 5.2.

While the r^+/d^+ ratio and the surface pressure both drop during monolayer relaxation, the r^+/d^+ ratio does not relate directly to the surface pressure. It is more closely linked to molecular area and tilt angle, which determines the room available for gauche defects. The surface pressure of a monolayer does depend on the molecular area, but different monolayers with the same molecular area can have different surface pressures due to differing intermolecular repulsive forces. The only difference between BTMS and BTAC are their counterions, the methyl sulfate and chloride ions for BTMS and BTAC

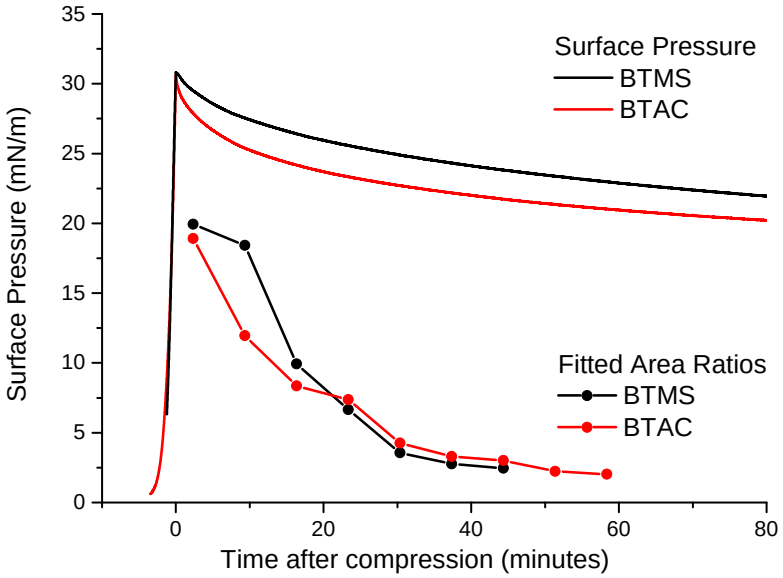

Figure 5.23: An expanded view of the surface pressure plot against time, with r^+/d^+ ratios of BTMS (black) and BTAC (red) monolayers overlaid for easy comparison Note also the change in timescale from hours in Figure 5.2 to minutes here.

respectively. Therefore, the difference in surface pressure behaviour is most likely due the different counterions.

The effect of counterions on the aggregation number of quaternary ammonium surfactants in solution has been studied previously [13]. The authors noted that the size of the counterions tested did not match the trend of their ability to stabilise the micelle, but their position in the Hofmeister series (or lyotropic series) did give an indication of their relative ability. The mechanistic origin of the Hofmeister series is complex and not fully understood [14]. Earlier theories were based on the disruption of the bulk water structure and the formation of a hydration shell [15]. More recent models focus on direct interaction of the ion with the macromolecules in question [16] (often proteins, but this also applies to micelles and surfactants at interfaces). An in-depth review of the Hofmeister series is beyond the scope of this document; however, it was found that counterions stabilised the micelles in the order (best to worst) $NO_3^- > Br^- > CH_3SO_4^- > Cl^- \gg OH^-$ [13]. Methyl sulfate ions were more efficient at stabilising the positive charge of the surfactant, and therefore gave larger aggregation numbers than chloride ions. It is simple to rationalise the end point of the π-t isotherms in Figure 5.2 - the greater

stabilisation provided by the methyl sulfate ions results in a lower final surface pressure, either by reducing headgroup-headgroup repulsion or by increasing the stability of the multilayer phases that form as the monolayer relaxes to its equilibrium pressure.

The BTMS surface pressure remains higher than for BTAC throughout the first 100 minutes of the relaxation, although the r^+/d^+ ratios indicate that the molecular areas should be quite similar. This indicates that the sulfate ion is initially less able to stabilise the repulsive headgroup-headgroup forces between the positively charged surfactants. Given that this is the opposite to the final equilibrium pressure, this initial difference might be a kinetic effect - the rate at which the multilayers are able to form is slower with the methyl sulfate counterion. This may be because the methyl sulfate ions are larger than the chloride ions (ionic radii of 0.258 nm to 0.18 nm, respectively) and therefore take longer to rearrange into the multilayer system.

References

[1] G. R. Bell, C. D. Bain, and R. N. Ward, "Sum-frequency vibrational spectroscopy of soluble surfactants at the air/water interface," *Journal of the Chemical Society, Faraday Transactions*, vol. 92, pp. 515–523, Jan. 1996.

[2] D. E. Gragson, B. M. McCarty, and G. L. Richmond, "Ordering of interfacial water molecules at the charged air/water interface observed by vibrational sum frequency generation," *Journal of the American Chemical Society*, vol. 119, pp. 6144–6152, July 1997.

[3] W. Sung, S. Seok, D. Kim, C. S. Tian, and Y. R. Shen, "Sum-frequency spectroscopic study of Langmuir monolayers of lipids having oppositely charged headgroups," *Langmuir*, vol. 26, pp. 18266–18272, Dec. 2010.

[4] A. Saha, H. P. Upadhyaya, A. Kumar, S. Choudhury, and P. D. Naik, "Sum-frequency generation spectroscopy of an adsorbed monolayer of mixed surfactants at an air–water interface," *The Journal of Physical Chemistry C*, vol. 118, pp. 3145–3155, Feb. 2014.

[5] R. Lu, W. Gan, B.-h. Wu, Z. Zhang, Y. Guo, and H.-F. Wang, "C-H stretching vibrations of methyl, methylene and methine groups at the vapor/alcohol (N = 1-8) interfaces," *The Journal of Physical Chemistry B*, vol. 109, pp. 14118–14129, July 2005.

[6] E. Tyrode, M. W. Rutland, and C. D. Bain, "Adsorption of CTAB on hydrophilic silica studied by linear and nonlinear optical spectroscopy," *Journal of the American Chemical Society*, vol. 130, pp. 17434–17445, Dec. 2008.

[7] C. M. Johnson and E. Tyrode, "Study of the adsorption of sodium dodecyl sulfate (SDS) at the air/water interface: targeting the sulfate headgroup using vibrational sum frequency spectroscopy," *Physical Chemistry Chemical Physics*, vol. 7, p. 2635, July 2005.

[8] R. D. Smith and J. C. Berg, "The collapse of surfactant monolayers at the air—water interface," *Journal of Colloid and Interface Science*, vol. 74, pp. 273–286, Mar. 1980.

[9] G. M. Bommarito, W. J. Foster, P. S. Pershan, and M. L. Schlossman, "A determination of the phase diagram of relaxed Langmuir monolayers of Behenic acid," *The Journal of Chemical Physics*, vol. 105, pp. 5265–5284, May 1996.

[10] C. Ybert, W. Lu, G. Möller, and C. M. Knobler, "Collapse of a monolayer by three mechanisms," *The Journal of Physical Chemistry B*, vol. 106, pp. 2004–2008, Feb. 2002.

[11] M. Weis, "Kinetics of slow collapse process: thermodynamic description of rate constants," *Applied Surface Science*, vol. 253, pp. 1469–1472, Nov. 2006.

[12] R. Lu, W. Gan, B.-h. Wu, H. Chen, and H.-F. Wang, "Vibrational polarization spectroscopy of CH stretching modes of the methylene group at the vapor/liquid interfaces with sum frequency generation," *The Journal of Physical Chemistry B*, vol. 108, pp. 7297–7306, June 2004.

[13] S. Berr, R. R. M. Jones, and J. S. Johnson, "Effect of counterion on the size and charge of alkyltrimethylammonium halide micelles as a function of chain length and concentration as determined by small-angle neutron scattering," *The Journal of Physical Chemistry*, vol. 96, pp. 5611–5614, June 1992.

[14] W. Kunz, P. Lo Nostro, and B. Ninham, "The present state of affairs with Hofmeister effects," *Current Opinion in Colloid & Interface Science*, vol. 9, pp. 1–18, Aug. 2004.

[15] K. D. Collins and M. W. Washabaugh, "The Hofmeister effect and the behavior of water at interfaces," *Quarterly Reviews of Biophysics*, vol. 18, pp. 323–422, Nov. 1985.

[16] Y. Zhang and P. S. Cremer, "Interactions between macromolecules and ions: the Hofmeister series," *Current Opinion in Chemical Biology*, vol. 10, pp. 658–663, Oct. 2006.

6. Using SFG to evaluate sparsely tethered membranes made by rapid solvent exchange and by Langmuir-Blodgett/ Langmuir-Schaefer deposition

In this chapter, we report the investigation of self-assembled monolayers (SAMs) consisting of tethers and spacers on gold substrates, the structure of a phospholipid monolayer formed onto this SAM by rapid solvent exchange (RSE) with DPPE, and the consecutive monolayer and bilayer formation by Langmuir-Blodgett (LB) and Langmuir-Schaefer (LS) deposition onto this SAM, as well as the structure of the SAM itself throughout these processes.

The T10 SAMs (described in detail in Section 1.3.1) contain aliphatic and aromatic CH and OH bonds. These can have SFG resonances which occur (approximately) in the regions 2800-3000 cm^{-1} (aliphatic CH stretches), 3000-3100 cm^{-1} (aromatic CH stretches), 3100-3400 cm^{-1} (OH stretches). It is the aliphatic CH stretches which can reveal the most structural information and the spectra shown will primarily be of this region, and also of the analogous aliphatic CD region, 2000-2300 cm^{-1}.

The spectra have been modelled with Lorentzian peaks to give the peak positions, and these have been assigned by comparison with the SFG spectra of similar molecules in the literature, or where these do not exist, by comparison with the IR and Raman spectra. The system being studied has many methyl and methylene groups which are orientated in multiple directions. Additionally, the system is not generally well-ordered, and the signal-to-noise ratio is therefore quite low. Finally, the non-resonant background introduces further ambiguities in the fitting [1]. As a result, spectral fitting is very difficult, and the modelled spectra are therefore used only as an initial approximation and as a guide to the eye. These limitations should not affect the conclusions that are presented here, as they are not made on the basis of detailed modelling of the spectra.

6.1 The initial T10 SAM

Spectra of the dry, uncoated T10 slides were taken first so as to give an indication of the ordering of the base SAMs. SAMs formed from asymmetric disulfides as used here are expected to be fairly disordered [2], because the short end, in this case the benzyl group, prevents the alkyl chains from packing closely, as they would for a thiol or symmetric disulfide.

In the CH region, the SSP spectrum (Figure 6.1a) shows three clear dips, modelled at 2884, 2921, and 2945 cm^{-1}, assigned to the r^+, the d^-, and the r^+_{FR} resonances respectively. The r resonances must arise from the phytanyl tethers, which are the only source of CH_3 groups. Although the glycol chains and spacers have CH_2 groups, the d^- resonance in the spectra at 2921 cm^{-1} also probably arises from the phytanyl group. This assignment is made on the basis of a smaller resonance at 2908 cm^{-1} which has also been modelled. This would normally be assigned to a d^+_{FR} resonance; however, this is not possible given the absence of a d^+ resonance. The d^- resonance of 1,2 ethylene glycol has previously been reported at 2900 cm^{-1} [3], and therefore the peak at 2908 cm^{-1} has been assigned to the antisymmetric stretch of the methylene groups in the glycol chain. This leaves the phytanyl tether as the only source for the d^- resonance at 2921 cm^{-1}.

The PPP spectrum (Figure 6.1b) shows the same resonances as the SSP (at 2883, 2905, 2921 and 2946 cm^{-1}), as well as two more at 2853 and 2973 cm^{-1}, which are assigned to the d^+ and r^- resonances of the phytanyl tether. In both spectra, all the signals appear as dips as the SFG resonances arising from these tethers interfere destructively with the non-resonant signal of the gold substrates. Therefore, the net polar orientation of the methyl and methylene vibrational modes must be pointing away from the surface (as explained in Section 2.2.2).

Normally, the relatively intense r and weak d resonances would be indicative of a conformationally well-ordered monolayer. However, the phytanyl tethers are unusual in that they have five methyl groups, and many methylene groups are replaced by the ether moieties, and hence the r^+/d^+ ratios cannot be used in the same way as for the surfactants of the hair conditioner models, which are straight-chain alkanes. The signal-to-noise ratio is much lower than would normally be seen from a well-packed and ordered monolayer. Overall, these spectra indicate that the phytanyl tethers do not

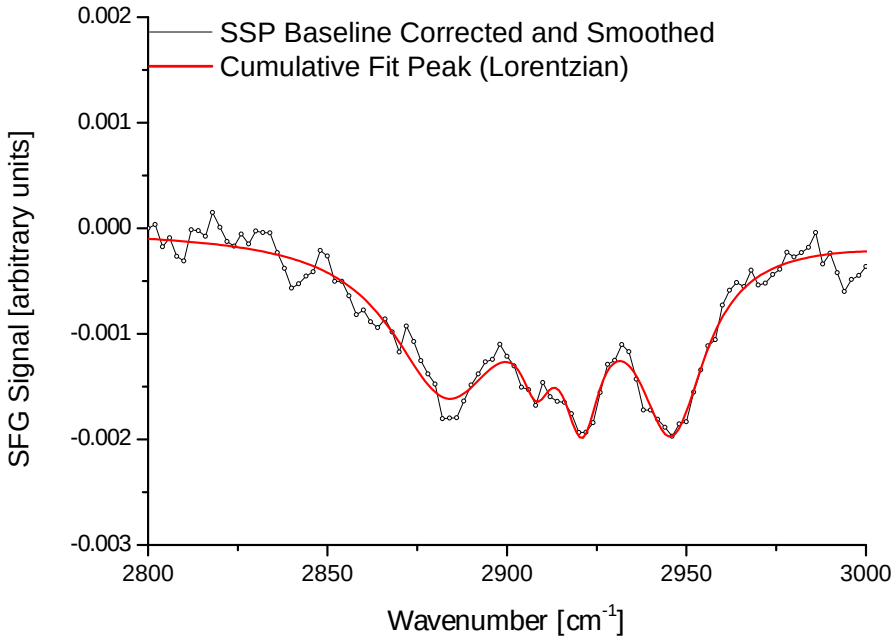

(a) SSP polarisation. Assigned: r^+ at 2884 cm^{-1}, d^- at 2921 cm^{-1}, r^+_{FR} at 2945 cm^{-1}; d^- of glycol at 2908 cm^{-1}

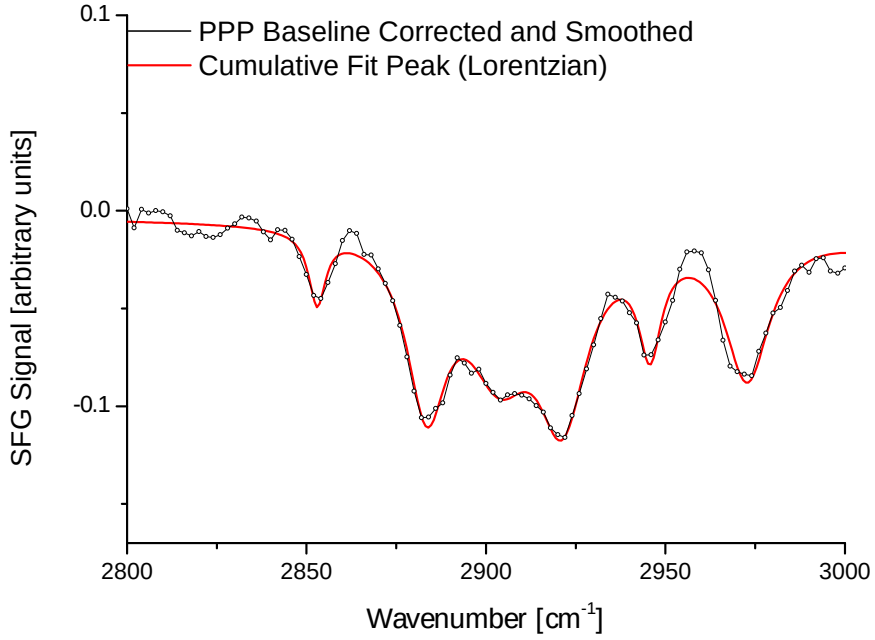

(b) PPP polarisation. Assigned: d^+ at 2853 cm^{-1}, r^+ at 2883 cm^{-1}, d^- at 2921 cm^{-1}, r^+_{FR} at 2946 cm^{-1}, r^- at 2973 cm^{-1}; d^- of glycol at 2905 cm^{-1}

Figure 6.1: Sum-frequency spectra in the CH region (2800-3000 cm^{-1}) of the fresh T10 slides in air.

form a well-ordered monolayer. This is not unexpected: the tether-to-spacer ratio is 1:9, which means that only one in ten of the disulfide molecules that form the SAM will carry a phytanyl group.

The r^- resonances only appear in the PPP spectra, and the corresponding dipole moment must therefore be close to the xy plane. The dipole moment of the r^- resonance is perpendicular to the methyl group, and we can conclude that the methyl groups point along the z axis. This is supported by the appearance of the r^+ resonance in the SSP spectra. The d^+ resonance also only appears in the PPP polarisation, indicating that the methylene groups point mostly in the xy plane. Since the d^- resonance appears in the SSP spectra, the antisymmetric methylene stretching mode must have some component along the z axis - a possible configuration is shown in Figure 6.2. These observations are consistent with a model in which the phytanyl tethers lie flat above the surface, with their CH_3 groups pointing into the air, away from the hydrophilic environment of the OH headgroups of the spacer (Figure 6.3).

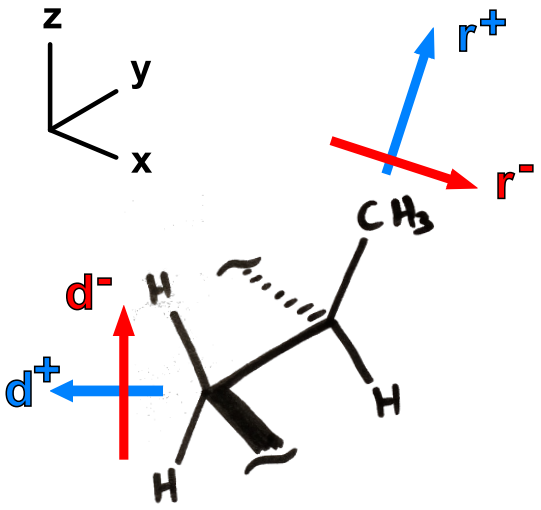

Figure 6.2: A segment of phytanyl tether, showing how the r and d resonances might be oriented relative to the substrate, (where the z axis represents the surface normal). For the methylene groups, the d^+ resonance is mostly in the xy plane, and the d^- resonance points along the z axis. For the methyl groups, the r^- resonance is mostly in the xy plane, and the r^+ resonance points along the z axis.

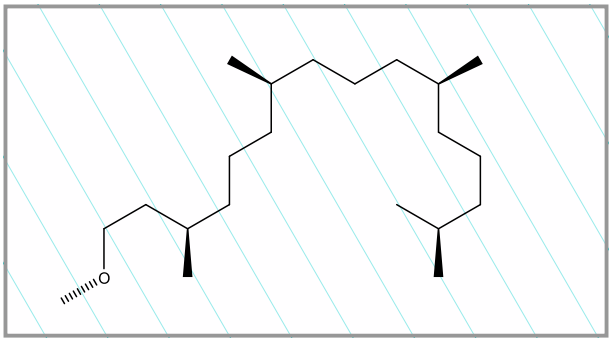

Figure 6.3: The phytanyl tether, lying flat above the surface, viewed from above (along the z axis). The blue lines lie in the xy plane and represent the hydrophilic environment of the glycol chain and alcohol headgroups of the spacer. The methyl groups are drawn pointing upwards into the air, so that their r^+ modes point upwards, and their r^- modes lie mostly in the plane of the surface.

Spectra of the same system are shown in Figure 6.4 for the range 2800-3400 cm^{-1}. As well as the alkyl CH peaks described above, peaks can be seen arising from the benzyl group of the disulfide molecules, and from the OH group of the spacers. The aromatic peaks in the SSP polarisation indicate that the benzyl group does not lie completely flat on the surface. The OH peaks are strong in the PPP spectra, and do not show above the noise in the SSP - this is evidence for H bonding between the alcohol groups of the spacer molecules, which would cause the OH bonds to lie largely in the xy plane. Although the glycol chain of the phytanyl tether presents alternative H bond acceptors, it appears that the neighbouring OH groups are preferred.

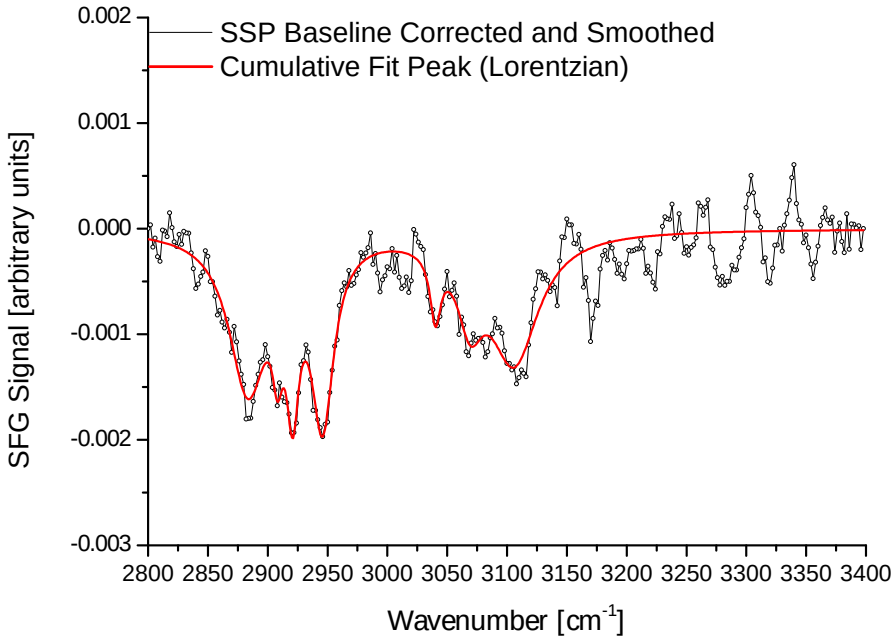

(a) SSP polarisation. Assigned r^+ at 2884 cm^{-1}, d^- at 2921 cm^{-1}, r^+_{FR} at 2945 cm^{-1}; d^- of glycol at 2908 cm^{-1}; Aromatic CH stretches at 3040 cm^{-1}, 3071 cm^{-1}, 3105 cm^{-1}

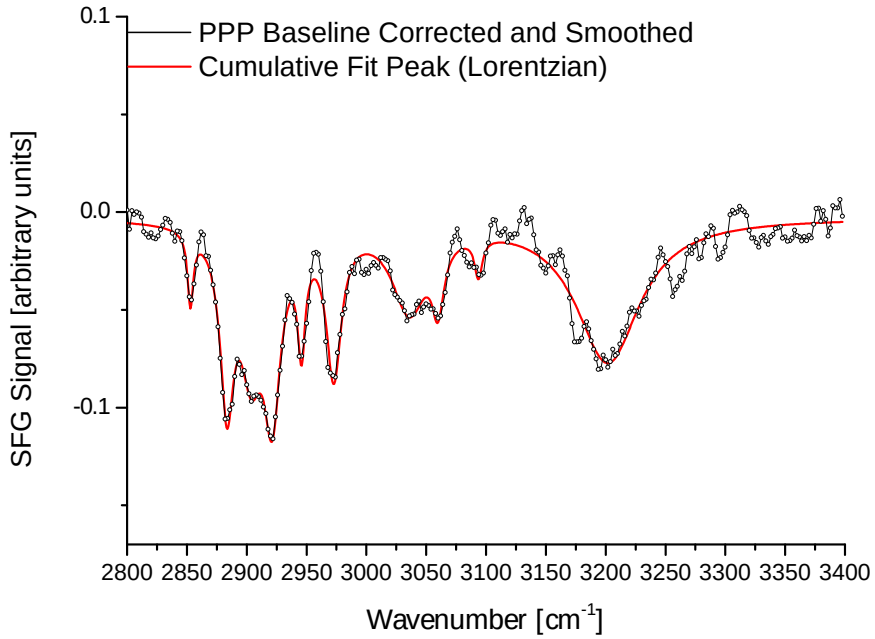

(b) PPP polarisation. Assigned: d^+ at 2853 cm^{-1}, r^+ at 2883 cm^{-1}, d^- at 2921 cm^{-1}, r^+_{FR} at 2946 cm^{-1}, r^- at 2973 cm^{-1}; d^- of glycol at 2905 cm^{-1}; Aromatic CH stretches at 3036 cm^{-1}, 3059 cm^{-1}, 3094 cm^{-1}. The broad peak centred on 3200 cm^{-1} is assigned to OH bonds of the spacers

Figure 6.4: Sum-frequency spectra in the aliphatic CH (2800-3000 cm^{-1}) and aromatic CH (3000-3100 cm^{-1}) regions, and part of the OH region (3000-3800 cm^{-1}) of the fresh T10 slides in air. The CH region is shown in an expanded view in the previous spectra. (Figure 6.1)

6.2 The T10 SAM after rapid solvent exchange (RSE)

RSE is a commonly employed method that produces a bilayer under water with the tethers incoorporated into the phospholipid membrane [4–6]. Unfortunately, due to the symmetry of the bilayer, it is SFG inactive. However, the bilayer is not stable in air, and rearranges into a mixture of monolayers and multilayers, which are SFG active. Figure 6.5 shows the spectra in the CH region of the resulting T10 SAM in air, after RSE with d-DPPE. The CH resonances arise from the T10 SAM, as in section 6.1. The spectra are very different compared to those of the T10 SAM before RSE. In the SSP (Figure 6.5a), the d resonances are not visible above the noise, and the r^- resonance has appeared at 2960 cm^{-1}. In the PPP (Figure 6.5b), the d^+ resonance has disappeared, but the d^- resonance has not. The r^- resonance also remains, but has changed from a dip into a peak.

These observations point to a change in orientation of the tether. The appearance of the r^- in the SSP, and its phase change in the PPP, suggest that the orientation of dipole moment change of the r^- is no longer close to the xy plane; therefore the methyl group, being perpendicular to the direction of the r^- dipole moment, is now probably orientated close to parallel to the substrate in the xy plane. The disappearance of the d^- resonances in the SSP indicate that both the d^+ and d^- modes now lie in the xy plane. It could also be that the reduction in the d resonances indicate a reduction in symmetry-breaking gauche defects. Within the noise, these spectra point to a tether that has a small tilt angle from vertical (Figure 6.6). This is compatible with the idea that the tethers are now incorporated into the lipid monolayer.

Spectra of the CD region (Figure 6.7) show resonances that must arise entirely from the d-DPPE. In the SSP, four peaks have been modelled, assigned to the r^+ and r^+_{FR}, the d^+, and the r^-. The PPP spectrum is more complex; as well as the r^+, r^+_{FR}, d^+, r^- seen in the SSP, the d^+_{FR}, and d^- are also visible. A peak has also been modelled at 2275 cm^{-1}. It has previously been seen in the spectra of d-DPPE (see the middle spectrum of figure 5 in reference [7]), but was not assigned. A speculative suggestion is that it may arise from the methylene next to the carboxylic acid.

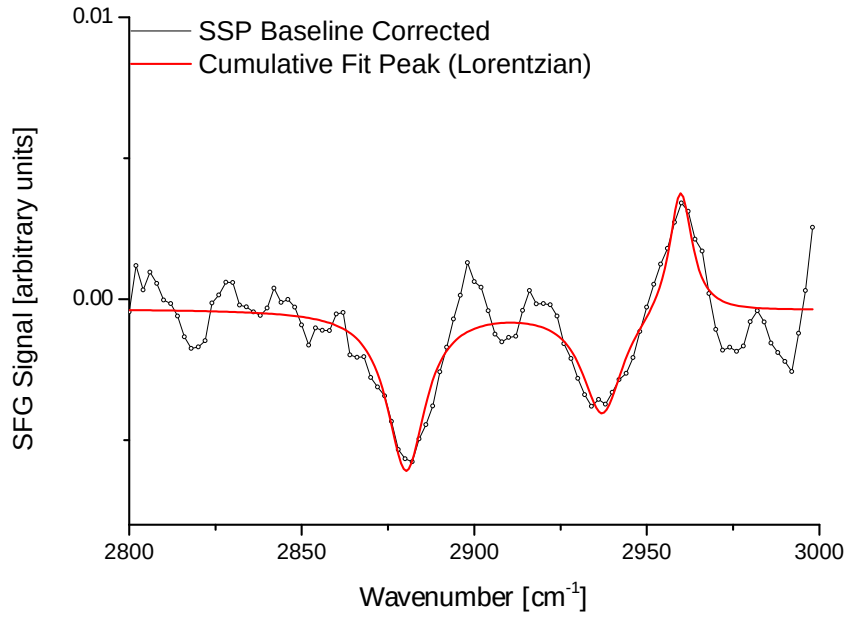

(a) SSP polarisation. Assigned: r^+ at 2880 cm^{-1}, r^+_{FR} at 2937 cm^{-1}, r^- at 2960 cm^{-1}

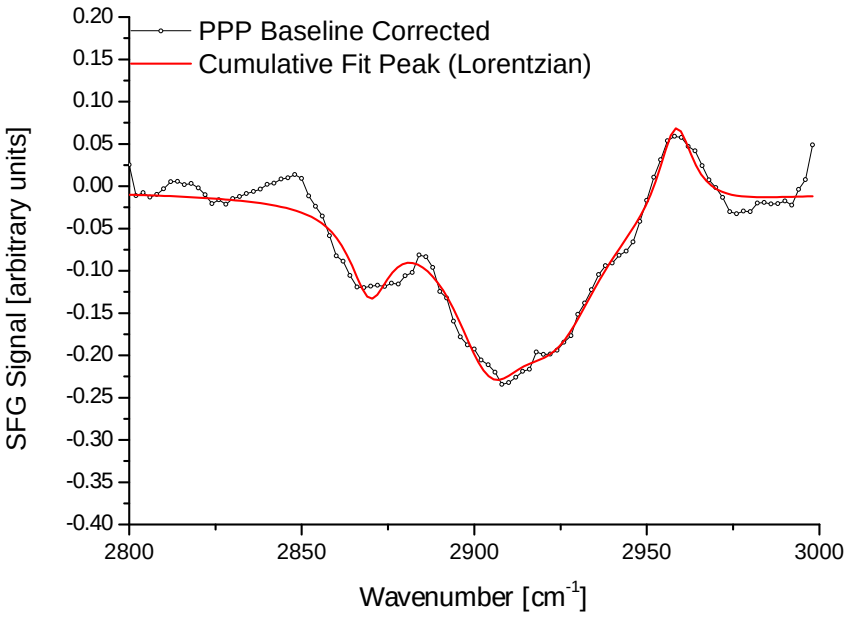

(b) PPP polarisation. Assigned: r^+ at 2870 cm^{-1}, d^- at 2923 cm^{-1}, r^- at 2958 cm^{-1}, d^- of glycol at 2904 cm^{-1}

Figure 6.5: Sum-frequency spectra in the CH region of the T10 slides after RSE with deuterated DPPE, taken in air. The expected structure after RSE is that a proximal leaflet of dDPPC has formed on the substrate, with the protonated phytanyl tethers incorporated. Signals in these spectra must arise from the protonated tethers and spacers, and not from the deuterated phospholipid.

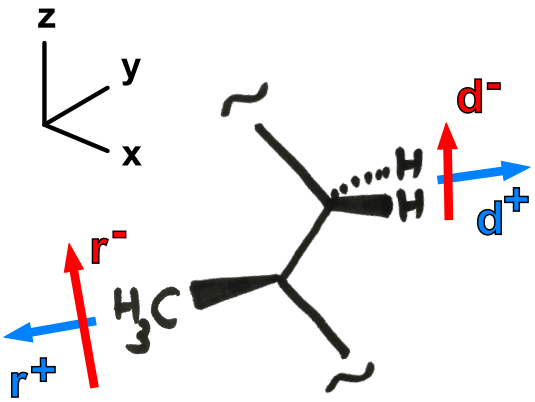

Figure 6.6: A segment of phytanyl tether, showing how the r and d resonances are oriented after RSE. The substrate lies in the xy plane, and the tether is drawn with only a small tilt from the z axis. The r^+, d^+, and d^- all vibrate mostly in the xy plane. The r^- is able to vibrate along the z axis as well the xy plane.

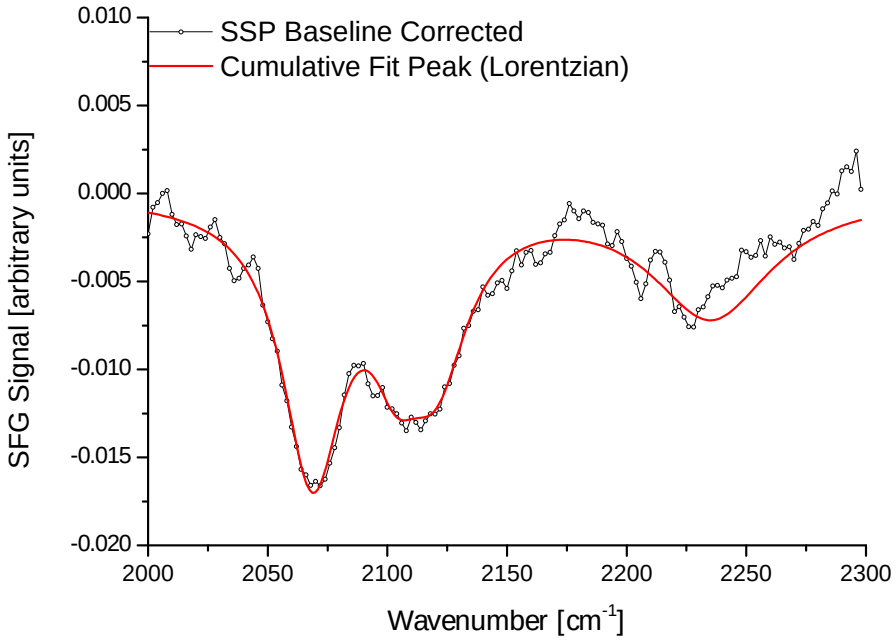

(a) SSP polarisation. Assigned: r^+ at 2073 cm^{-1}, d^+ at 2095 cm^{-1}, r^+_{FR} at 2115 cm^{-1} r^- at 2224 cm^{-1}

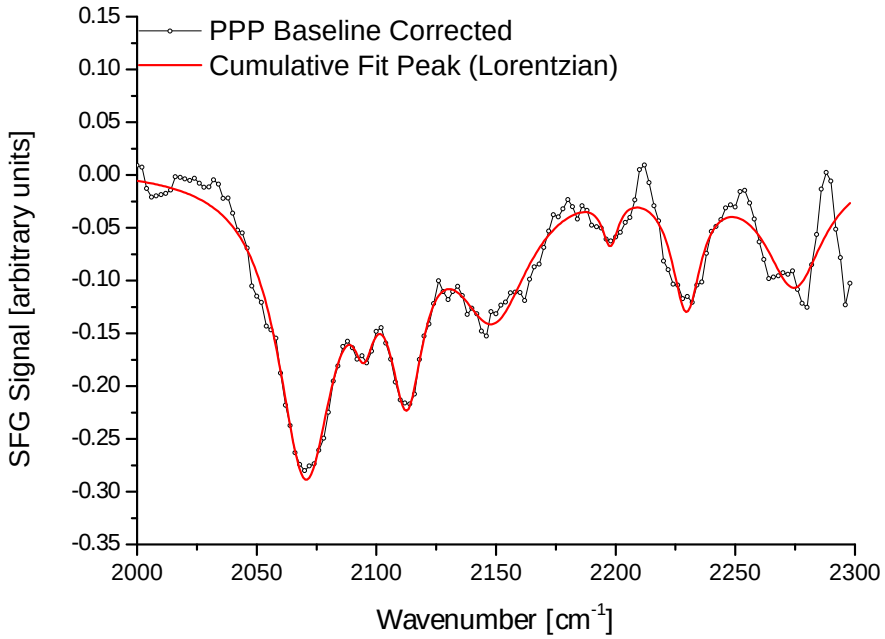

(b) PPP polarisation. Assigned: r^+ at 2071 cm^{-1}, d^+ at 2094 cm^{-1}, r^+_{FR} at 2115 cm^{-1}, d^+_{FR} at 2148 cm^{-1}, d^- at 2194 cm^{-1}, r^- at 2227 cm^{-1}, methylene next to carboxylic acid at 2275 cm^{-1}.

Figure 6.7: Sum-frequency spectra in the CD region of the T10 slides after RSE with deuterated DPPE, taken in air. The expected structure after RSE is that a proximal leaflet of dDPPC has formed on the substrate, with the protonated phytanyl tethers incorporated. Signals in these spectra must arise from the deuterated phospholipid.

6.3 The T10 SAM after Langmuir-Blodgett (LB) deposition of the deuterated DPPE proximal leaflet

The RSE process produces an isotopically symmetric bilayer under water. A bilayer that is not isotopically substituted is SFG inactive. Therefore, LB deposition, followed by Langmuir-Schaefer (LS) deposition, is used to produce a bilayer containing protonated phospholipids in one leaflet, and deuterated in the other.

However, it is not necessarily a safe assumption that the tethers should be incorporated into the membrane following LB deposition. Therefore, an initial monolayer of deuterated DPPE was produced by LB deposition on a T10 slide to test this assumption. As in section Sections 6.1 and 6.2, signals in the CH region can only be from the tethers or spacers of the T10 SAM. Spectra of the CH region (Figure 6.8) are unlike those produced after RSE (Figure 6.5). The SSP spectrum (Figure 6.8a) shows just one extremely weak, broad signal, at 2994 cm^{-1} which is unassigned. The PPP spectrum (Figure 6.8b) shows an r^{+} resonance and a weak r^{+}_{FR} resonance, as well as a peak at 2983 cm^{-1}, which may be the r^{-} resonance, although 2983 cm^{-1} is higher than observed previously in this system. It may also be the same resonance as that seen in the SSP, and would be unassigned in this case.

Spectra of the CD region (Figure 6.9), show signals which arise from the LB-deposited dDPPE. Both the SSP and the PPP spectra show only r resonances, typical of a well-packed, well-ordered monolayer. These spectra indicate a monolayer of a higher quality than that produced by RSE (Figure 6.7). This is partly due to the multilayer nature of the RSE membrane, and partly due to the fact that the monolayer is formed under compression during LB deposition. The difference in the spectra might also be because the tethers are not incorporated into the monolayer produced by LB deposition, as supported by the appearance of the CH spectra (Figure 6.8), and therefore do not disrupt the packing of the monolayer. If the monolayer is not tethered, as appears to be the case here, then LB/LS deposition is not a suitable method for producing tethered bilayers of this kind.

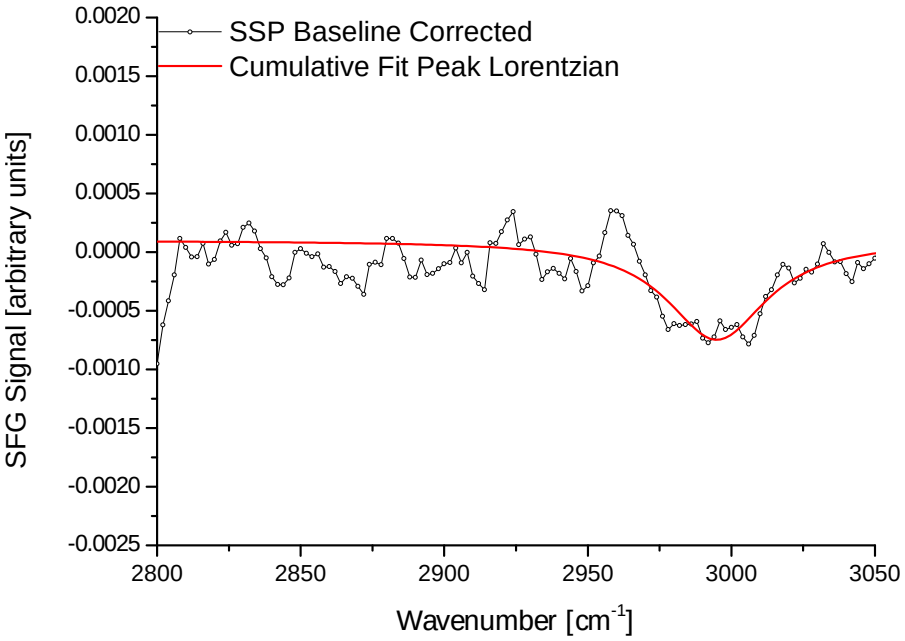

(a) SSP polarisation. Unassigned dip at 2994 cm^{-1}

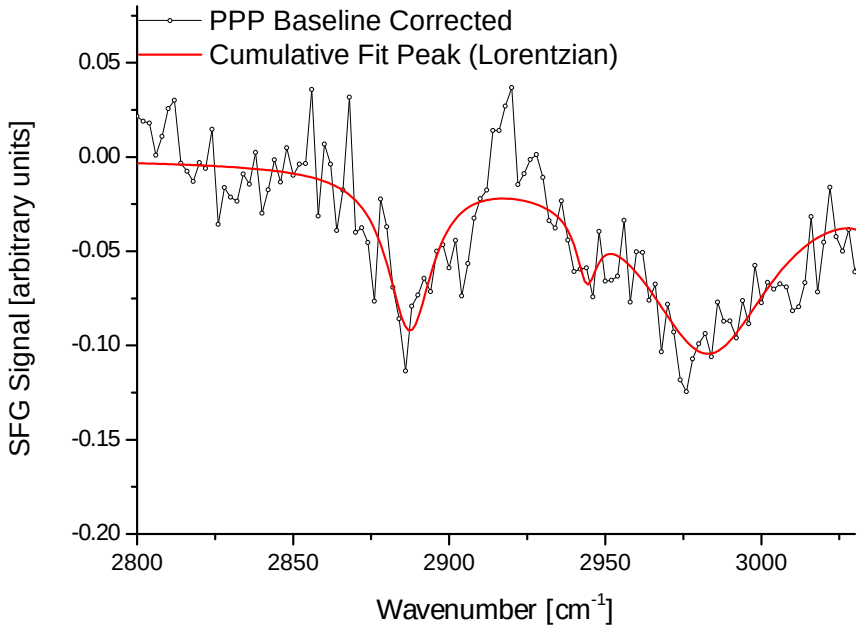

(b) PPP polarisation. Assigned: r^+ at 2884 cm^{-1}, r^+_{FR} 2944 cm^{-1}, unassigned at 2983 cm^{-1}

Figure 6.8: Sum-frequency spectra in the CH region of the T10 slides after LB deposition with deuterated DPPE, taken in air. A proximal leaflet of dDPPC has been deposited onto the substrate, although the tethers may not be incorporated into the monolayer. Signals in these spectra must arise from the protonated tethers and spacers, and not from the deuterated phospholipid.

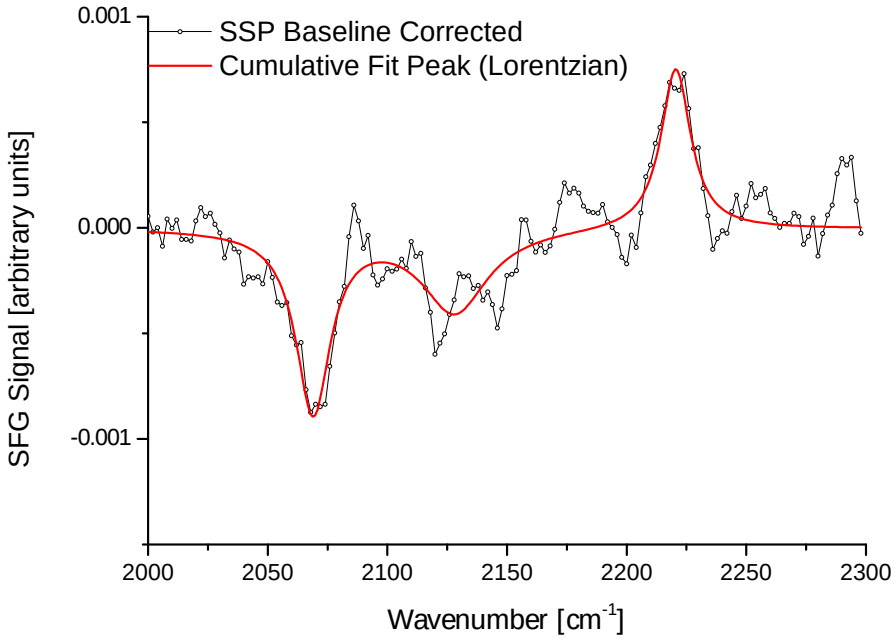

(a) SSP polarisation. Assigned: r^+ at 2069 cm^{-1}, r^+_{FR} at 2128 cm^{-1}, r^- at 2221 cm^{-1}

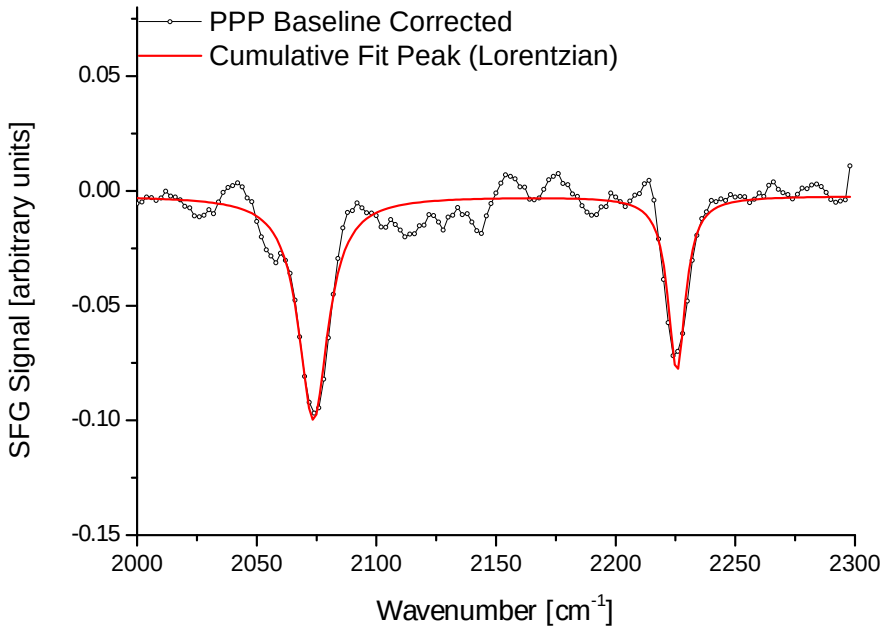

(b) PPP polarisation. Assigned: r^+ at 2074 cm^{-1}, r^- at 2225 cm^{-1}

Figure 6.9: Sum-frequency spectra in the CD region of the T10 slides after LB deposition with deuterated DPPE, taken in air. A proximal leaflet of dDPPC has been deposited onto the substrate, although the tethers may not be incorporated into the monolayer. Signals in these spectra must arise from the deuterated phospholipid.

6.4 The T10 SAM after LB deposition of the protonated DPPE proximal leaflet

An isotopically asymmetric bilayer was produced via LB deposition with protonated DPPE, followed by LS deposition with deuterated DPPE. Therefore, the proximal leaflet is made with protonated DPPE, and the distal leaflet is made with deuterated DPPE. This sample was characterised immediately after LB deposition (i.e. protonated DPPE deposited onto the protonated tethers), and these spectra are shown in this section. Spectra after LS deposition (i.e. protonated tethers, protonated proximal leaflet, deuterated distal leaflet) are shown in the next section.

Figure 6.10 shows the CH region of the spectra of the slide immediately after LB deposition with protonated DPPE. The spectra display strong methyl resonances, indicating a very well-packed monolayer, very similar to the previous spectra seen arising from the LB deposition of the d-DPPE (Figure 6.9). However, no resonances that were seen in the CH spectra from the deuterated LB deposition (Figure 6.8), which arose from the phytanyl tether, are seen here. Since it is highly unlikely that the tethers would act differently to isotopically substituted DPPE, this is probably because the more intense signal from the monolayer swamps the signal from the tethers.

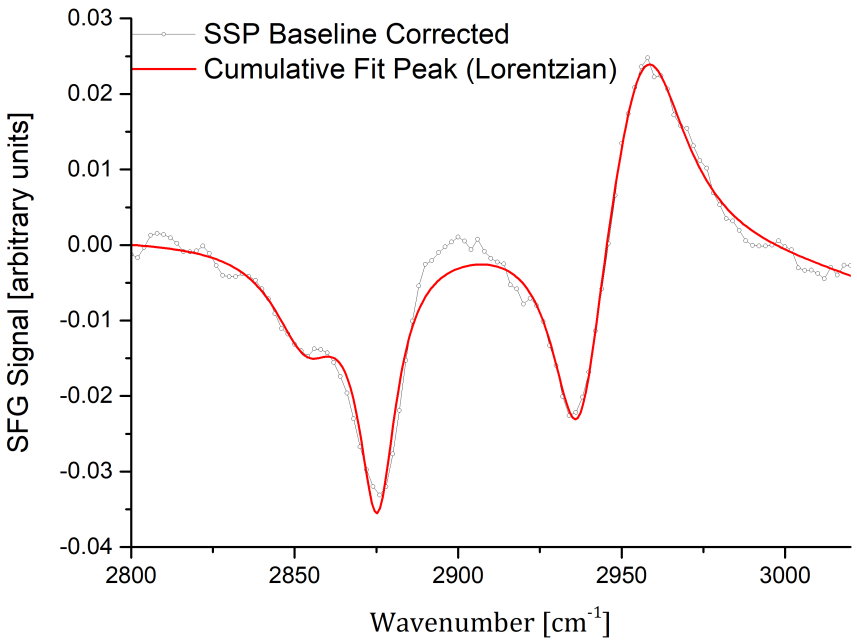

(a) SSP polarisation. Assigned: d^+ at 2855 cm^{-1}, r^+ at 2878 cm^{-1}, r^+_{FR} at 2944 cm^{-1}, r^- at 2965 cm^{-1}

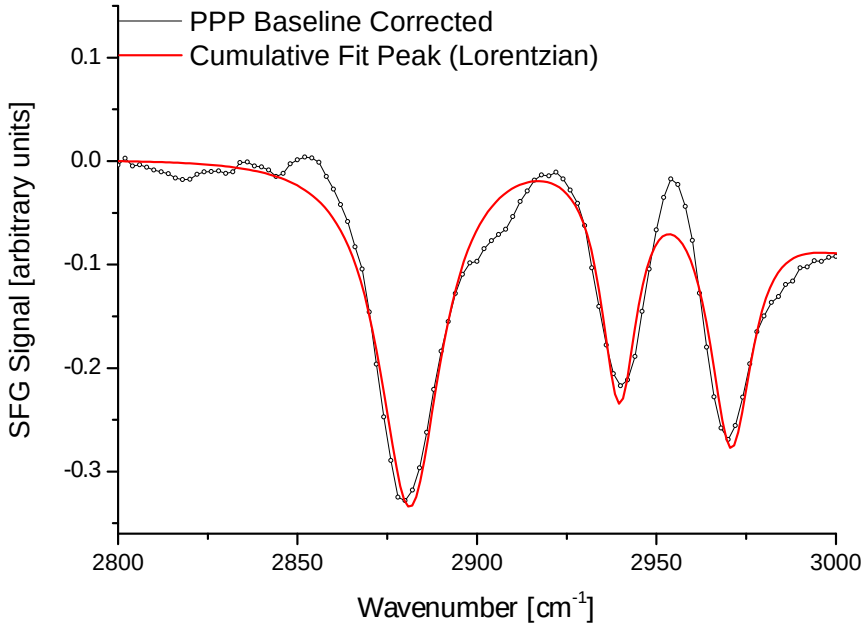

(b) PPP polarisation. Assigned: r^+ at 2880 cm^{-1}, r^+_{FR} at 2942 cm^{-1}, r^- at 2968 cm^{-1}

Figure 6.10: Sum-frequency spectra in the CH region of the T10 slides after LB deposition with protonated DPPE, taken in air. A proximal leaflet of protonated DPPC has been deposited onto the substrate, but the tethers may not be incorporated into the monolayer. Signals in these spectra may arise from the tethers and spacers as well as the phospholipid. The signals from the phospholipid are much more intense and likely to swamp any signals that might arise from the tethers.

6.5 The T10 SAM after Langmuir-Schaefer (LS) deposition of the deuterated DPPE distal leaflet

Finally, a monolayer of deuterated DPPE was LS deposited onto the proximal protonated DPPE deposited onto the substrate in the previous section, and spectra were taken of the isotopically distinguished bilayer under water using the liquid cell (described in Section 3.3). The spectra of the CD region of the resulting bilayer are shown in Figure 6.11. The signals of these spectra arise from the deuterated phospholipids of the distal leaflet. They are slightly more complicated than the previous spectra of the monolayer of d-DPPE on its own, where it was the proximal leaflet (Figure 6.9). The peaks that were observed in Figure 6.9 have undergone a phase reversal. This is as expected, since the phospholipids of the distal leaflet are orientated in the opposite direction to those in the proximal leaflet.

Apart from the change of phase, in the SSP a new weak dip is observed at 2092 cm^{-1}, which is assigned to the d^+ mode. In the PPP, new resonances are observed at 2093, 2159, 2191, and 2248 cm^{-1}. The first three are assigned to the d^+, d^+_{FR}, d^- resonances, respectively, and the last is not assigned, though it may arise from the methylene group next to the carbonyl. These new peaks are all methylene resonances, and indicate that the distal leaflet is not as well-ordered as the proximal leaflet.

Figure 6.12 shows the CH region of the PPP spectrum after the complete bilayer had been formed. These signals arise from the proximal DPPE layer. The same methyl resonances are visible as were visible before the LS deposition (Figure 6.9), but are now reduced in intensity. This exemplifies the problem of flip-flop between the isotopically substituted leaflets. Eventually, they mix completely, and the signals from the distal and proximal leaflets cancel each other out. This process occurs on the order of hours after the LS deposition is completed. Additionally, a small shoulder at 2860 cm^{-1}, and a peak at 2915 cm^{-1} are now visible, assigned to the d^+ and d^- resonances, respectively. These indicate that the bilayer membrane ordering reduces over time.

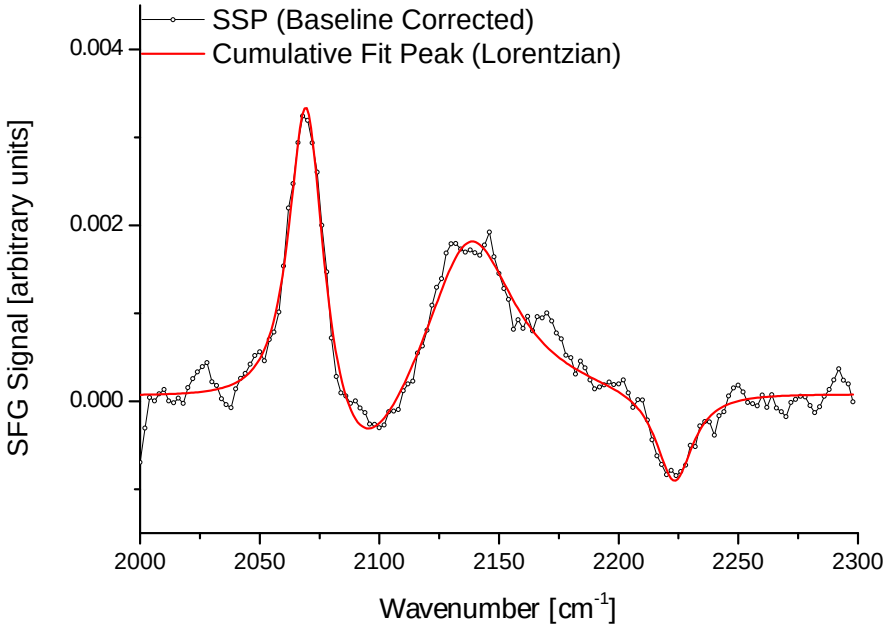

(a) SSP polarisation. Assigned: r^+ at 2068 cm^{-1}, d^+ at 2093 cm^{-1}, r^+_{FR} at 2137 cm^{-1}, r^- at 2222 cm^{-1}

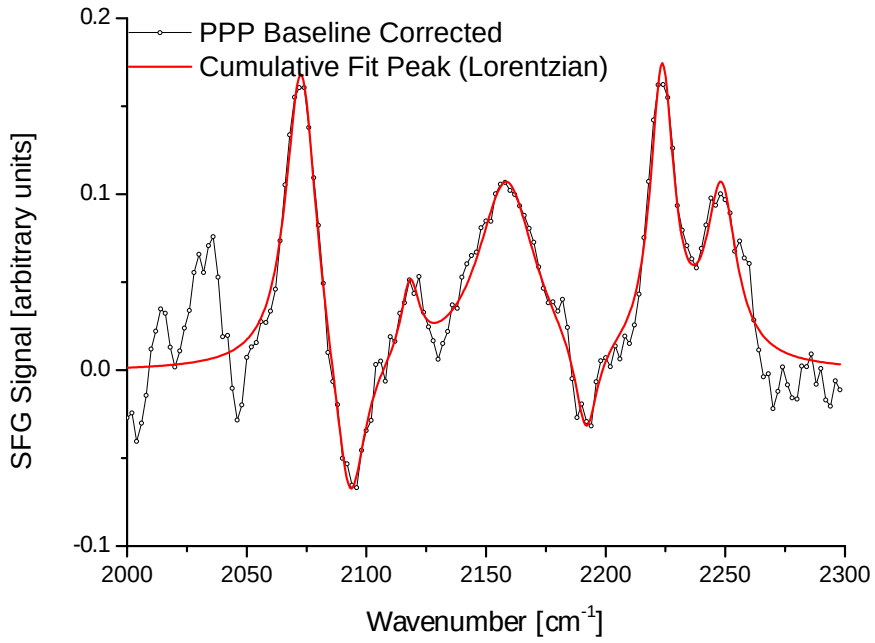

(b) PPP polarisation. Assigned: r^+ at 2073 cm^{-1}, d^+ at 2093 cm^{-1}, r^+_{FR} at 2118 cm^{-1}, d^+_{FR} at 2159 cm^{-1}, d^- at 2192 cm^{-1}, r^- at 2224 cm^{-1}, unassigned at 2248 cm^{-1},

Figure 6.11: Sum-frequency spectra in the CD region of the T10 slides after LB deposition with protonated DPPE, followed by LS deposition with deuterated DPPE, taken under water. A protonated proximal leaflet and deuterated distal leaflet enables SFG spectra of the otherwise symmetric bilayer. Signals in these spectra must arise from the deuterated phospholipids of the distal leaflet.

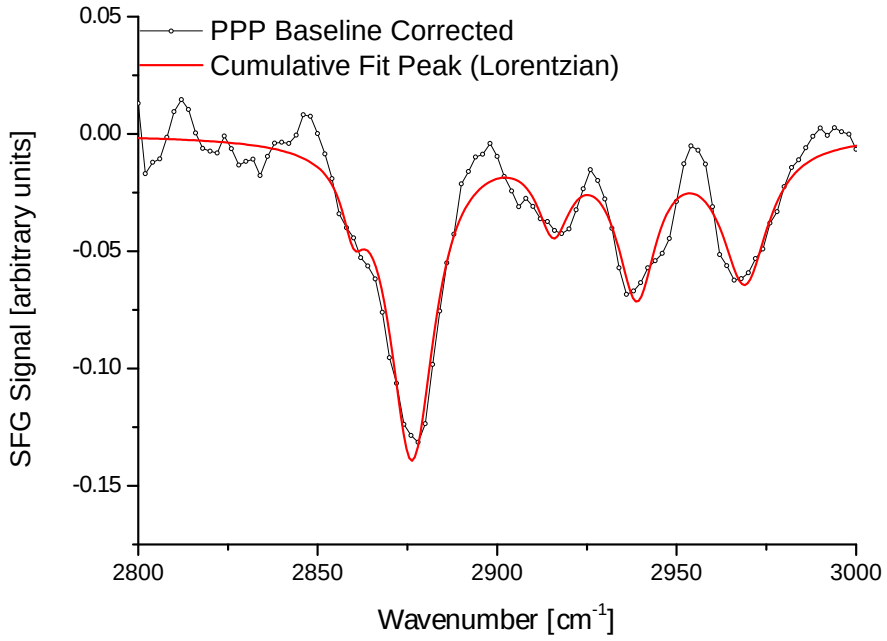

(a) PPP polarisation. Assigned: d^+ at 2856 cm^{-1}, r^+ at 2880 cm^{-1}, d^- at 2915 cm^{-1}, r^+_{FR} at 2942 cm^{-1}, r^- at 2968 cm^{-1}

Figure 6.12: Sum-frequency spectrum in the CH region of the T10 slides after LB deposition with protonated DPPE, followed by LS deposition with deuterated DPPE, taken under water. Signals in this spectrum must arise from the protonated phospholipids of the proximal leaflet.

As well as characterising the T10 SAM in various states of membrane completion, these results may inform future experimental design. SFG was used to confirm that RSE does produce a phospholipid membrane with tethers incorporated as expected, and also showed that LB deposition did not. Since LB deposition did not produce a membrane with incorporated tethers, LB/LS deposition is not a suitable method for producing tethered isotopically asymmetric bilayer membranes of this type. If an asymmetric bilayer of this type is required, as is the case for study by SFG, another method must be found. Additionally, asymmetric bilayers produced by LB/LS deposition underwent flip flop that resulted in fully mixed proximal/distal leaflets, and zero SFG resonances, on the order of hours after formation. Therefore, bilayers formed in this way are not suitable for very long experiments, such as those conducted with membrane-penetrating lipopetide surfactin and a phospholipid monolayer at the air/water interface in Chapter 8. If a bilayer for studying a longer timescale experiment is required, then another type may be more suitable, such as the hybrid bilayer or the fully tethered bilayer, as described in Section 1.3.

References

[1] B. Busson and A. Tadjeddine, "Non-uniqueness of parameters extracted from resonant second-order nonlinear optical spectroscopies," *The Journal of Physical Chemistry C*, vol. 113, pp. 21895–21902, Dec. 2009.

[2] E. B. Troughton, C. D. Bain, G. M. Whitesides, R. G. Nuzzo, D. L. Allara, and M. D. Porter, "Monolayer films prepared by the spontaneous self-assembly of symmetrical and unsymmetrical dialkyl sulfides from solution onto gold substrates: structure, properties, and reactivity of constituent functional groups," *Langmuir*, vol. 4, pp. 365–385, Mar. 1988.

[3] R. Lu, W. Gan, B.-h. Wu, H. Chen, and H.-F. Wang, "Vibrational polarization spectroscopy of CH stretching modes of the methylene group at the vapor/liquid interfaces with sum frequency generation," *The Journal of Physical Chemistry B*, vol. 108, pp. 7297–7306, June 2004.

[4] R. Budvytyte, M. Mickevicius, D. J. Vanderah, F. Heinrich, and G. Valincius, "Modification of tethered bilayers by phospholipid exchange with vesicles," *Langmuir*, vol. 29, pp. 4320–4327, Apr. 2013.

[5] S. Shenoy, R. Moldovan, J. Fitzpatrick, D. J. Vanderah, M. Deserno, and M. Lösche, "In-plane homogeneity and lipid dynamics in tethered bilayer lipid membranes (tBLMs)," *Soft Matter*, vol. 6, p. 1263, Jan. 2010.

[6] D. J. McGillivray, G. Valincius, D. J. Vanderah, W. Febo-Ayala, J. T. Woodward, F. Heinrich, J. J. Kasianowicz, and M. Lösche, "Molecular-scale structural and functional characterization of sparsely tethered bilayer lipid membranes.," *Biointerphases*, vol. 2, pp. 21–33, Mar. 2007.

[7] M. T. L. Casford, A. Ge, P. J. N. Kett, S. Ye, and P. B. Davies, "The structure of lipid bilayers adsorbed on activated carboxy-terminated monolayers investigated by sum frequency generation spectroscopy," *The Journal of Physical Chemistry B*, vol. 118, pp. 3335–3345, Mar. 2014.

7. SFG spectroscopy of surfactin at the air/water interface

Surfactin is a cyclic lipopeptide and powerful biosurfactant produced by various strains of the bacterium Bacillus Subtilis. It has been shown to have antiviral, antibacterial, anti-fungal, anti-mycoplasma and haemolytic properties [1, 2]. Surfactin's various biological properties are considered to arise from its interactions with the phospholipid bilayer of cell membranes. It is known to form pores in the cell membrane, and even completely solubilise the membrane when present above its critical micelle concentration.

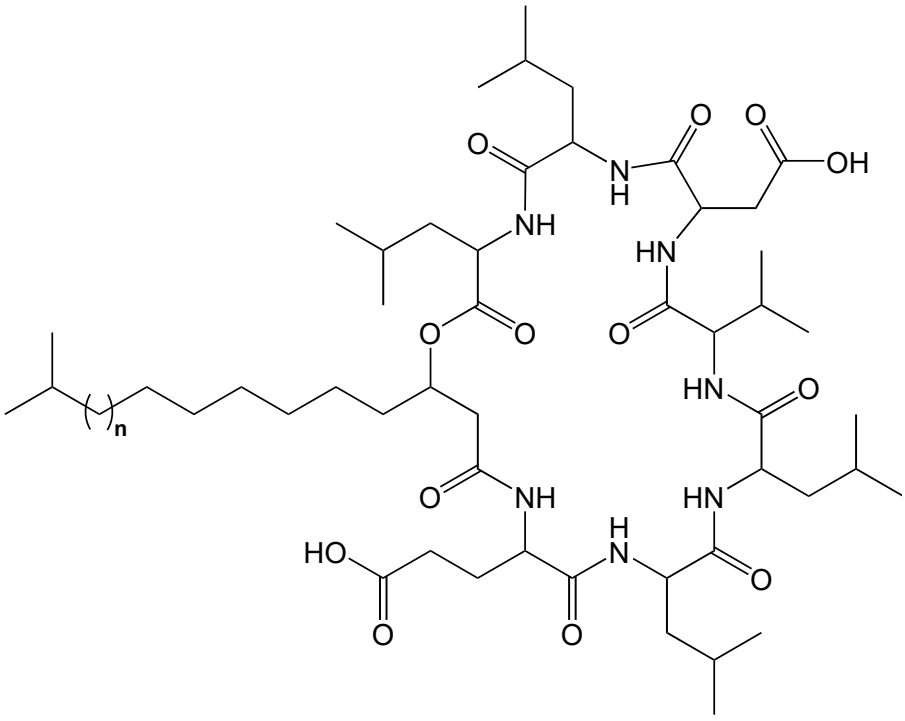

Figure 7.1: The chemical structure(s) of surfactin A (n=1), surfactin B (n=2) and surfactin C (n=3), as produced by Bacillus Subtilis.

The biological properties of surfactin are extremely useful. The biosurfactant is a non-specific antibacterial which acts by destroying the cell membrane, and is therefore unlikely to produce resistant strains, which are increasingly becoming a concern for

conventional antibacterials. Unfortunately, the non-specificity of surfactin extends to red blood cells, and this toxicity precludes its use directly. However, an understanding of the mechanism by which surfactin penetrates the cell membrane is potentially very valuable. In order to study this mechanism with SFG, a firm grasp of the structure of surfactin is required.

As a first step then, surfactin at the air/water interface was investigated by SFG using a variety of conditions and polarisations. Because surfactin is a relatively large molecule with multiple alkyl moeties, selectively deuterated analogues of surfactin were also used. This enables assignment of C-H signals that would otherwise be ambiguous. Sum-frequency spectra presented in this chapter include SFG signals arising from C-H bonds (2800-3000 cm^{-1}), and signals from the O-H bonds of water (above 3000 cm^{-1}). Signals in the region 2000-2300 cm^{-1} arise from the C-D bonds of deuterated molecules, and in the region 2300-2800 cm^{-1} arise from D_2O. Finally, signals in the region 1500-1800 cm^{-1} are typical of carbonyl bonds - the acid and amide groups of surfactin.

7.1 Surfactin in pure water

Figure 7.2 shows the SFG spectra of a surfactin solution well above the CMC, at neutral pH in the C-H and O-H stretching regions in SSP and PPP polarisations. Under these conditions, surfactin should form a monolayer at the air/water interface. This assumption is revisited towards the end of this section - it is supported by the data in Figure 7.5. There are clear C-H and O-H peaks in both the PPP and SSP spectra. In the SSP spectrum, the water resonances interfere with the C-H resonances and significantly alter their relative intensities.

Figure 7.3 shows the SFG spectra of a surfactin solution in D_2O under the same conditions in the C-H (2800-3000 cm^{-1}) and C=O (1500-1800 cm^{-1}) regions. D_2O resonances appear in the 2000-2300 cm^{-1} region (not shown), and the subphase resonances no longer interfere with those of surfactin. As a result, the fitting and assignment of the C-H features to well-characterised methyl stretching modes is straightforward: r^+ 2875 cm^{-1}; r^+_{FR} 2944 cm^{-1}; r^- 2966 cm^{-1}. Weak methylene resonances were detected at 2852 cm^{-1} (d^+) and 2922 cm^{-1} (d^-). In the C=O region of the SSP spectrum, amide I and carbonyl stretching resonances appeared with fitted positions of 1669 cm^{-1} and 1741 cm^{-1}, respectively. The hydrogen atoms on the alpha carbons (next to the carbonyl group) are potentially labile, and may undergo H-D exchange in D_2O. No evidence was seen for this in the SFG spectra. Either these C-H bonds do not contribute significantly to the spectra, or there was no significant H-D exchange.

From the molecular structure of surfactin, the only possible origin of methyl C-H resonances are the six isopropyl groups. These are found in the alkyl tail, the four leucine residues and the single valine residue of the ring. When compared to a "standard" surfactant, with a hydrophilic head-group and hydrophobic tail, the default assumption would be that SFG signals arise from the tail. In either case, just as for other surfactants, this would require organisation of isopropyl groups such that a component of their overall dipole is along the surface normal for SFG signals to appear in the SSP polarisation. Given the large size of the surfactin ring, it must be significantly tilted in order for the tails to pack close enough for a significant SFG signal. However, previous literature on the surface structure of surfactin indicates that the plane of the ring should lie parallel to the surface (at least in the case of the uncompressed monolayer here) [3–5].

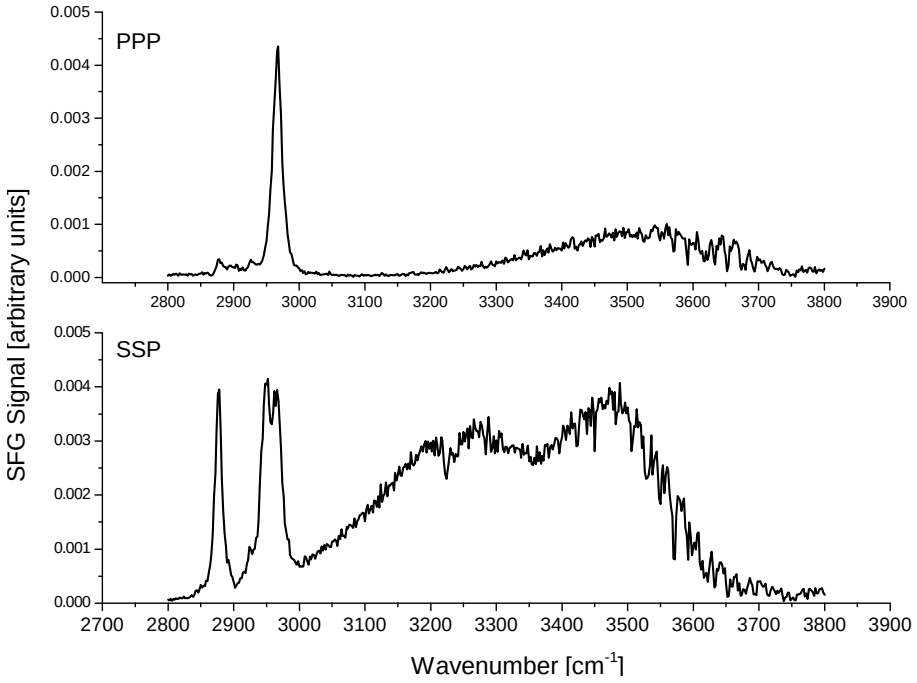

Figure 7.2: PPP (top) and SSP (bottom) spectra of surfactin in H_2O

To deduce conclusively the source of the SFG resonances, surfactin with deuterated leucine residues was prepared by growing a culture of bacillus subtillis with a feed of d_9-leucine (see section 3.9 for details). The surfactin produced from this experiment is referred to as d-Leu surfactin. The CD and CH spectra of the resulting partially deuterated surfactin is shown in Figure 7.4. Strong CD resonances and barely detectable CH resonances are observed. The CD resonances appear with fitted positions: 2039 cm^{-1} (d^+); 2136 cm^{-1} (r^+_{FR}); 2213 cm^{-1} (d^-); 2224 cm^{-1} (r^-). The two antisymmetric resonances are present in the SSP and PPP polarisations, whereas the symmetric resonances are absent, or very weak in the PPP polarisation. Weak symmetric resonances in the PPP polarisation are expected from the SFG selection rules [6].

Analysis of the d-Leu surfactin (available in section 3.9) showed that all of the leucine residues of the ring were successfully deuterated. However, it also showed that the bacterium utilized some d_9-leucine to produce the fatty tail, and hence some deuteratation was incorporated into the end of the fatty tail. Roughly 40-50% of the tail groups were deuterated in this manner. Despite the incorporation of the deuterated leucine into the fatty tail, the absence of strong C-H resonances provides unambiguous evidence that the strong methyl C-H resonances in the spectra of protonated surfactin are not from the isopropyl terminal group of the lipid chain but from the isopropyl groups of the

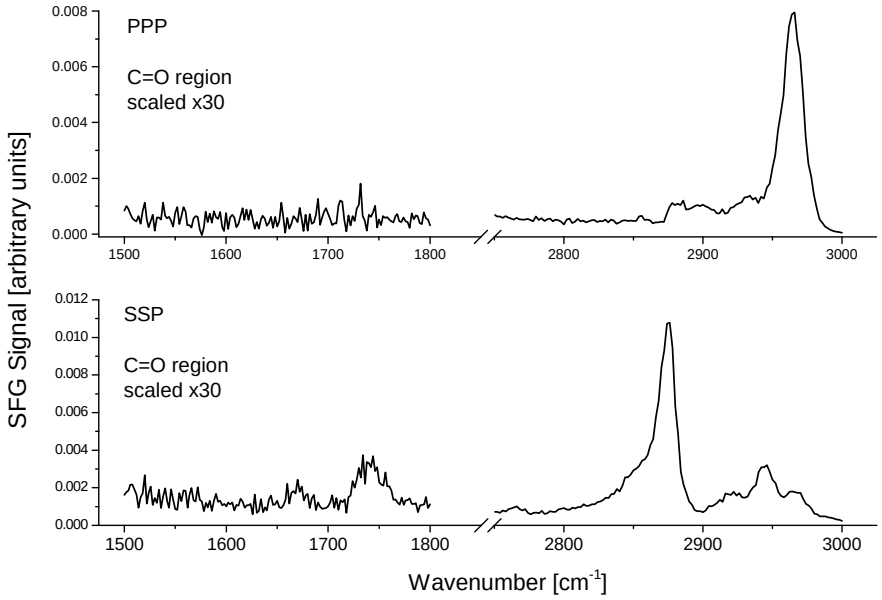

Figure 7.3: PPP (top) and SSP (bottom) spectra of surfactin in H_2O (C=O region, 1500-1800 cm^{-1}) and in D_2O (C-H region, 2800-3000 cm^{-1}). Spectra in the C=O region have been scaled by 30 times for clarity.

leucine components. If the fatty tail contributed significantly to the C-D resonances, analogous bands should be seen in the C-H region, especially because the infrared laser power output, and therefore the sensitivity and SFG signal intensity, is much higher in the C-H region than the C-D region. This is not observed, and the deuteration of the tail is therefore not troublesome. The weak C-H resonances in Figure 7.4 are assigned as: 2855 cm^{-1} (d^+); 2917 cm^{-1} (either d^- or methine); 2945 cm^{-1} (r^-). These may be either from the single valine component of the ring, or from the protonated fatty acid tail, or both. The profile of the r^- resonance appearing as two out-of-phase components may be due to destructive interference between resonances arising from methyl groups with different tilt angles, and may indicate that the signals arise from both of these isopropyl groups [7].

The fact that no strong SSP CH signals arise from the lipid tail of the d-Leu surfactin means that either the lipid chains have no dipole component perpendicular to the surface, or are so highly disordered that they only give rise to weak d resonances, associated with gauche defects in aliphatic chains. Furthermore, the absence of a significant PPP C-H

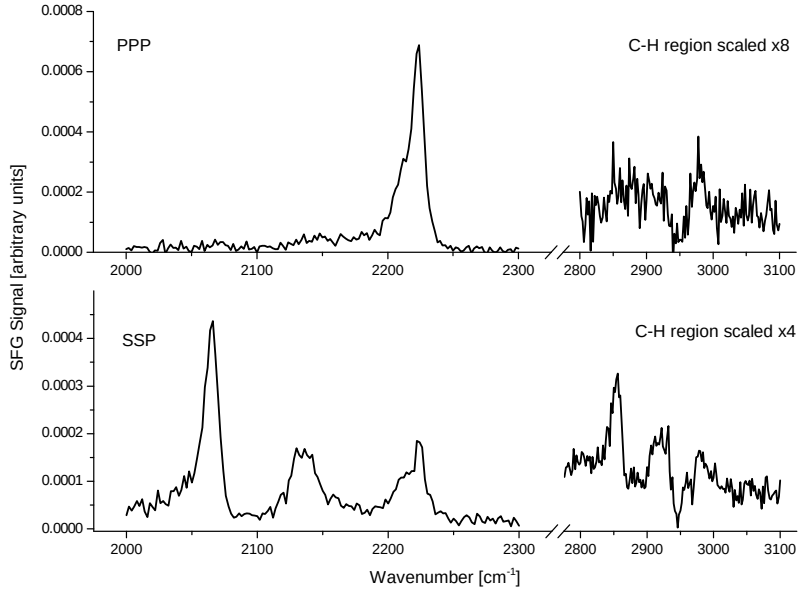

Figure 7.4: PPP and SSP spectra of surfactin comprising deuterated Leucine groups (d_9-Leucine) on H_2O (CD region) and on D_2O (CH region). The CD spectra represent 300 acquisitions, whereas the CH spectra are the average of 4 experiments of 400 acquisitions each.

spectrum indicates that, if the chains lie parallel to the plane of the interface, they have no net polarisation which is expected if the surfactin molecules are isotropically oriented in the x-y plane. This precludes the stacked-ring structure (proposed by Maget-Dana and Ptak [3]) because it is difficult to envisage a complete lack of net orientation if the rings were tilted and stacked in some way. Consequently, the most likely orientation of the ring itself is in the surface plane. These spectra therefore support those previous studies of surfactin on water [4, 5], which concluded that the peptide ring is largely coplanar with the interface, with the fatty acid tail lying atop the ring. This maximises the interaction of the fatty acid chain with the hydrophobic valine and leucine residues of the ring [8].

Figure 7.5 shows the changes in the spectrum of surfactin on D_2O as the bulk concentration is increased up to 10×CMC. Spectra of solutions at and above the CMC were identical. At concentrations of 0.0875×CMC and above, the point at which the spectra could be meaningfully fitted, there was no change in the intensity ratios of the C-H resonances. Therefore, the tilt angle and structure of the surfactin molecules are not sensitive to its concentration. The spectra of leucine and isopropanol change markedly

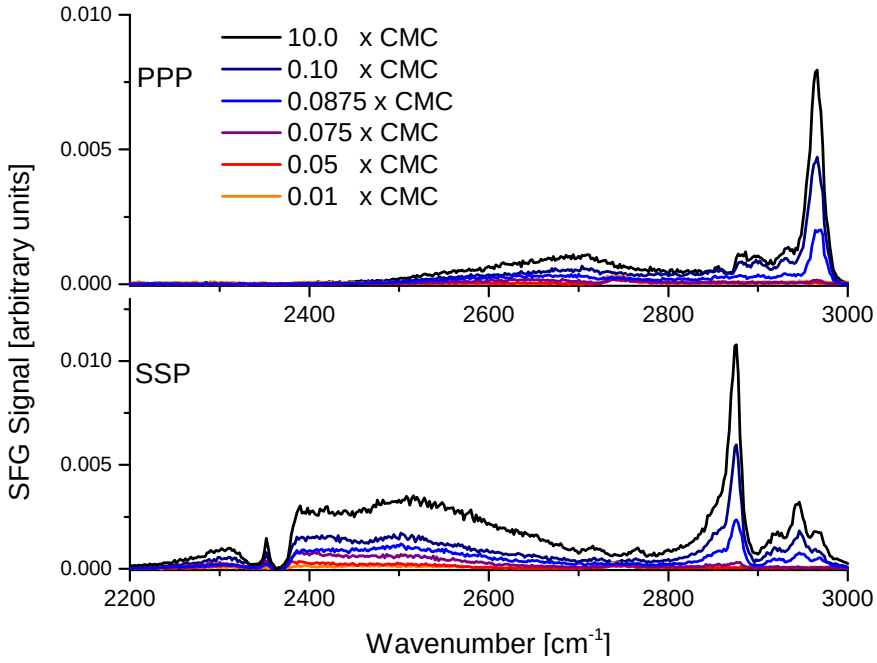

Figure 7.5: SSP and PPP spectra of surfactin solutions of various concentrations (expressed as multiples of the CMC) in D_2O. The wavenumbers scanned cover the O-D and C-H regions.

with higher concentration due to increased packing density and resulting reduction of their tilt angle [9, 10]. In contrast, the spectra observed here do not change with concentration. Given that the surfactin C-H resonances arise primarily from the leucine, this indicates that intra-molecular interactions dominate the structure and tilt angle of the leucine residues.

As mentioned previously in this section, only a monolayer can be present in the range of surface coverage and bulk concentrations used here. Though multi-layering of surfactin has been observed previously [11], this would strongly affect the SFG response, which is highly sensitive to the symmetry of the interface, and therefore to the degree of multi-layering. [12]. Some previous propositions for the structure of surfactin can be ruled out on the basis of the CH and CD spectra presented here. The dimerisation of the surfactin molecules in which lipid chains of the pair align with each other, proposed by Ishigami et al [13], results in vertical lipid chains at higher surface coverages. This would give rise to methylene and methyl resonances that change with concentration, as found for aliphatic single-chain surfactants like dodecanol, which is not observed here. If lipid tails were interacting with leucine residues of neighbouring surfactin molecules,

as proposed by Fernández at al [4], some change in the signals arising from the leucine residues should be apparent at different molecular areas, as their orientation changes to accommodate the tail group of another surfactin molecule at higher surface coverages.

7.2 Effect of pH on the structure of surfactin

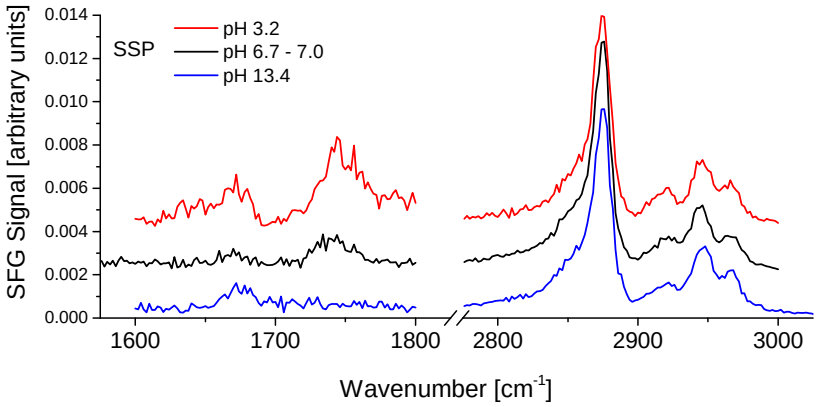

Figure 7.6: SSP spectra in the C-O and C-H regions of surfactin on D_2O at different pH values.

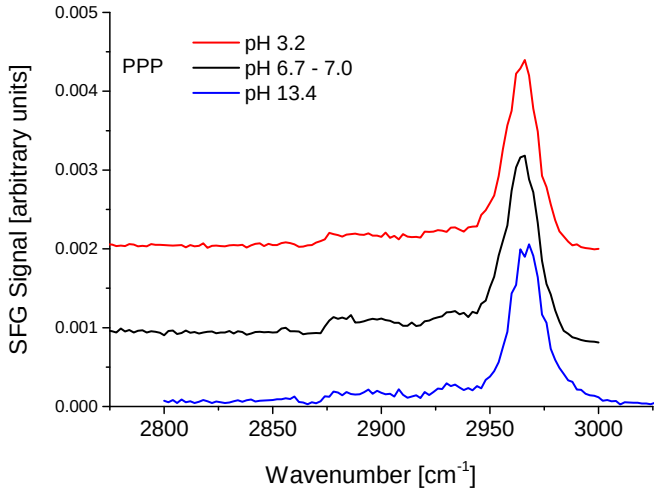

Figure 7.7: PPP spectra in the C-H regions of surfactin on D_2O at different pH values.

Figure 7.6 shows the SSP spectra of surfactin in the C-O and C-H region under different pH conditions. The spectra in the C-H region remain constant with change in pH. The

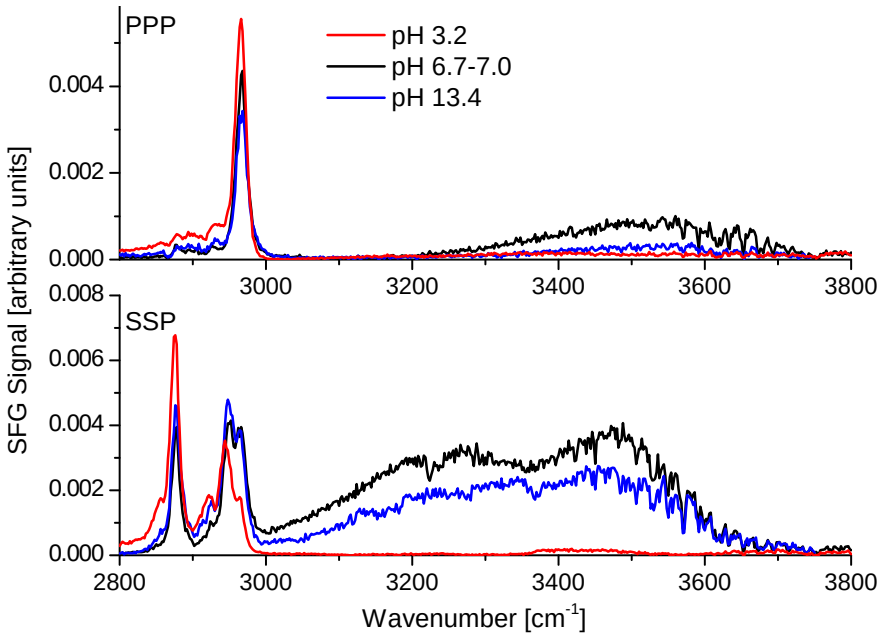

Figure 7.8: PPP and SSP spectra in the C-H and O-H regions of surfactin on H_2O at different pH values.

resonance at 1741 cm^{-1} is visible under acid conditions, weaker in neutral conditions, and disappears in alkali conditions. This resonance is assigned to the C=O bond of the un-dissociated carboxylic acid of the glutamate and aspartate residues. Although weak acids, such as the carboxylic acid present, should be almost completely dissociated at pH 7, the pH at the interface is substantially lower than the bulk phase due to the influence of surface charge. This effect is well understood - the density of charged groups at interfaces can give rise to an interfacial potential that results in an ionic concentration that is different from the bulk value [14]. In the case of negatively charged acid groups, the negative interfacial charge results in a greater concentration of H^+ at the interface, so that the surface pH is lower than the bulk pH [15, 16]. In this case, the surface pH must be similar to the pK_a of the acid group so that a proportion of the acid groups at the surface must be un-dissociated, giving rise to the 1741 cm^{-1} resonance visible in Figure 7.6. The resonance at 1670 cm^{-1} is weak but visible under all pH conditions, and is assigned to the amide I resonance (the C=O bond of the peptide bonds in the ring). The amide I band at 1670 cm^{-1} is usually assigned to β-turn structures [17]. However, the low signal-to-noise ratio (partly due to low infrared laser power in this region) prevented a quantitative analysis of changes in the peptide resonances at different pH values.

Given that the CH spectra do not change at all with changing pH, the changes in the C=O spectra must be due to localised changes of these bonds. While the changes at 1741 cm^{-1} can be explained entirely by protonation state, the amide groups remain uncharged at all bulk and surface pH conditions used here (based on the pKa values of a typical amide group and its conjugate acid, which are >20 and <0 respectively). Changing SFG intensity of the amide I band with pH has been noted previously [18], following a similar pattern of intensity with pH (highest with acid, weakest at neutral, and in between with alkali). They concluded that this change was due to reduced ordering and multilayering of the protein (bovine serum albumin). We can rule out multilayering based on the CH spectra. The changes in the intensity of the amide I resonances are therefore due to changes in the orientation of the amide bonds - the direction of the C=O bond of the amide changes to be closer to or further from being parallel to the surface normal. This change in orientation is probably small, as a large change in C=O bond orientation would also change the orientation of the leucine residues, and therefore change the CH spectra. It might be tentatively explained by the presence of OH^- and H_3O^+ at low and high pH respectively, which may induce some change in orientation of the carbonyl bond.

The effect of pH on the water resonances of a surfactin solution is shown in Figure 7.8. Surfactin is negatively charged at high pH due to the carboxylate groups of the glutamate and aspartate residues. At a neutral bulk pH, the surface carboxylic acid groups exist as a mixture of COO^- and COOH groups, as described previously. Charged surfactants are known to induce ordering of water molecules at the interface, resulting in strong SFG resonances [19], explaining the strong OH bands at bulk pH 7.0 and 13.4. Under acidic conditions, surfactin is uncharged, and consequently there is no strong electrostatic field which would induce a net orientation of the water molecules, and the OH resonances vanish or weaken significantly.

Overall, the effect of pH on the structure of surfactin is limited. Any change in orientation must be small, and from the results shown here, is most obvious in the acid groups (as a result of changing protonation state), and to a lesser extent in the amide bonds. This is in agreement with previous neutron reflectivity results [20]. Although a larger pH range was used here, based on the pKa of the functional groups of surfactin, the protonation state should be similar, and therefore it is reasonable to compare the results. Shen and co-workers found that, although the hydrophobicity of surfactin changes with pH (again mostly via the COOH groups, changing their extension into the water), the overall structure of surfactin remains as a compact ball-like structure.

7.3 Effect of Ca^{2+} on the structure of surfactin

Surfactin is known to associate strongly with divalent cations, especially Ca^{2+}, putatively via the two acid groups of the ring [2, 3, 20, 21]. This neutralisation of the acid groups might induce structural changes in the ring. To explore this possibility, SFG spectra of surfactin in a 1:1 mol solution with $CaCl_2$ was recorded in the C-H and C=O regions, and this was repeated for acidic and basic conditions. Figure 7.10 shows the SSP spectra of surfactin/$CaCl_2$ solution overlaid onto the equivalent surfactin water spectrum. The most notable difference is the reduction in water bands from 3000-3800 cm^{-1}, evidence for at least partial neutralisation of the surfactin by the Ca^{2+} ions.

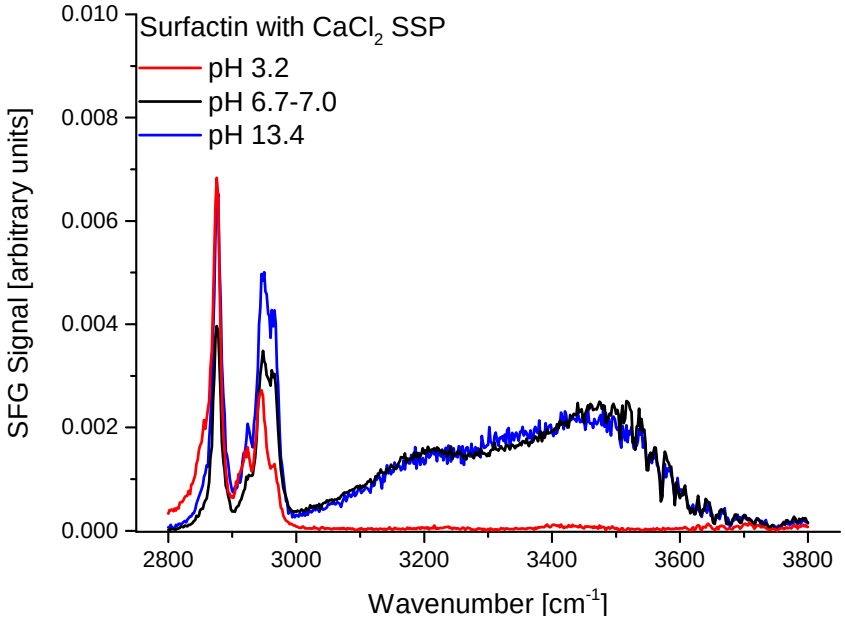

Figure 7.9: SSP spectra in the C-H region of surfactin with $CaCl_2$(aq) in a 1:1 mole ratio at different pH values.

Multiple previous studies of surfactin and Ca^{2+} have shown that this neutralisation is complete at a 1:1 mole concentration [2, 3, 20, 22]. The residual water bands are therefore somewhat puzzling when compared to the low pH spectra of surfactin/water solutions (Figure 7.8). In both cases, surfactin should be fully neutralised, and the spectra of the low pH surfactin solutions show almost no signal in the 3000-3800 cm^{-1} range, explained by the lack of charge that would induce the water ordering and structure at the interface. Since there must be some overall orientation of the water, the spectra of the surfactin/$CaCl_2$ solutions indicate that order-inducing hydrogen bonding must still be

present between the H_2O and the neutralised surfactin/Ca^{2+} complex. Indeed, neutron reflectivity studies have shown that even a small reduction in pH (down to pH 6.5 in their case) increased the hydrophobicity of the two acid groups more than the addition Ca^{2+}, as measured by the separation of the acid groups from the Gibbs water interface [20].

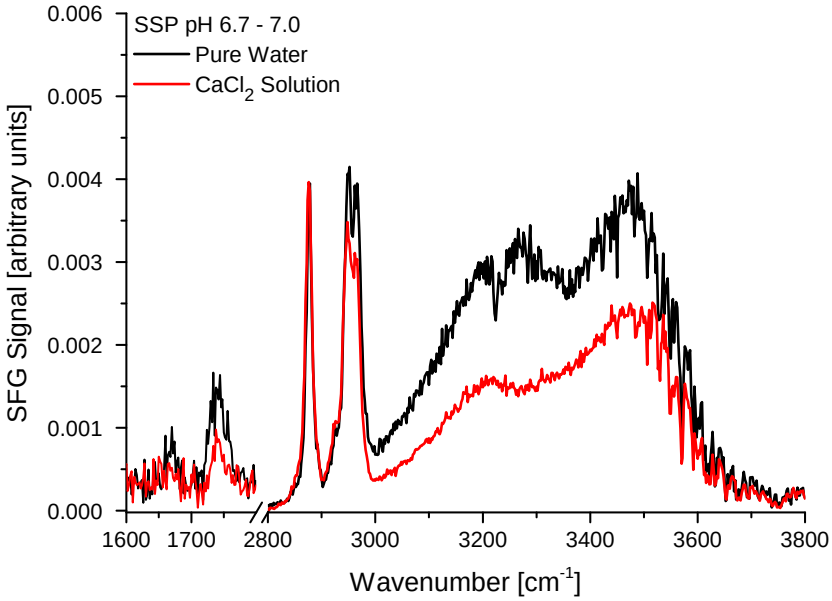

Figure 7.10: SSP spectra in the C-O, C-H and O-H regions of surfactin solutions with or without $CaCl_2$ at pH 6.7-7.0.

A similar reduction of O-H bands is seen in the spectra of the high-pH surfactin/Ca^{2+} solution (Figure 7.11), and the same reasoning can be applied - previously un-associated carboxylate groups are now complexed with Ca^{2+}, and the neutralised surfactin has a weaker ordering effect on the water molecules.

The O-H bands of the low pH surfactin/Ca^{2+} solution (Figure 7.12) are broad and weak, and do not appear to be strongly affected by the addition of Ca^{2+}. This makes intuitive sense, since surfactin at low pH should already be fully neutralised, and should not form a strong association to Ca^{2+}.

Turning now to the C=O region of the spectra - in neutral conditions, the band at 1741 cm^{-1} has reduced in intensity. This could indicate that the number of un-dissociated carboxylic acid groups has decreased. This is reasonable since the association of Ca^{2+} with carboxylate groups should shift the equilibrium (on the basis of Le Chatelier's Principle) and reduce the number of protonated carboxylic acids. Another explanation based on the orientation of the carboxylic acids is also possible - the structure of the

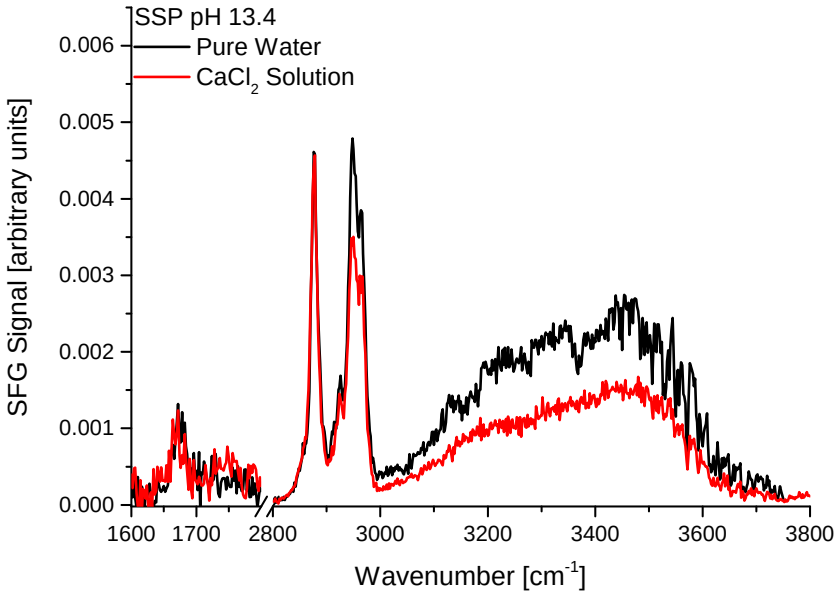

Figure 7.11: SSP spectra in the C-O, C-H and O-H regions of surfactin solutions with or without $CaCl_2$ at pH 13.4.

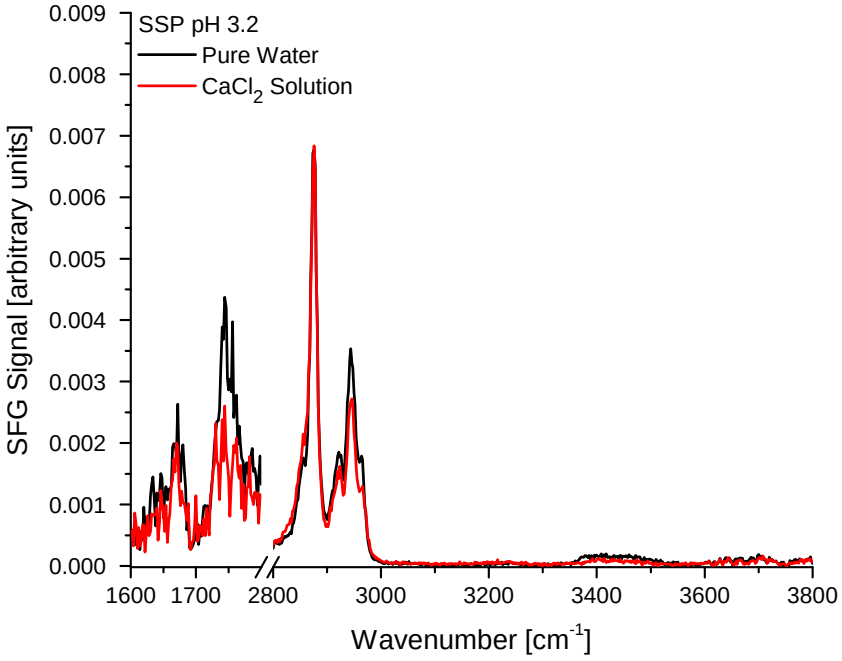

Figure 7.12: SSP spectra in the C-O, C-H and O-H regions of surfactin solutions with or without $CaCl_2$ at pH 3.2.

surfactin-calcium complex proposed in the literature involves the Ca^{2+} ion bridging the two carboxylate groups, so that surfactin acts as a bidentate ligand [22, 23]. If this is the

case, the binding of Ca^{2+} would be expected to induce a change in orientation of the carboxylic acid groups, and therefore affect their SFG resonance. The extent to which either of these two situations explains the reduction in intensity is difficult to quantify. At 1669 cm^{-1}, the already extremely weak amide I band seems to weaken or disappear upon addition of the Ca^{2+}, possibly indicating some change in orientation of the peptide bonds of the ring, although this level of variation is within the noise levels (again, due to the low infrared power available).

The corresponding alkali spectrum (Figure 7.11) appears to show an extremely weak peak at 1741 cm^{-1}. It is entirely implausible that protonated acid groups exist at a bulk pH of 13.4, and therefore this 'peak' is considered to be the result of the low signal-to-noise ratio in this region. There is no change in the amide I band at 1669 cm^{-1}, indicating that the neutralisation of the carboxylate groups does not cause any reorientation of the ring peptide bonds. Given that there are no significant changes in the C=O region, it appears that the structure of the ring of surfactin does not change when forming this complex. Unfortunately, since no signal arising from the deprotonated carboxylic acid groups could be found, it is impossible to tell if these groups have changed in orientation when binding to Ca^{2+}.

The acid spectra (Figure 7.12) show a reduction in the intensity of the 1741 cm^{-1} resonance. As for the neutral-pH case, Ca^{2+} appears to be interacting with the carboxylic acid groups, despite their reduced affinity for the cation in low-pH conditions. The amide I band at 1669 cm^{-1} does not appear to change with the addition of Ca^{2+}. As for the alkali spectra, this implies that the ring structure does not change significantly upon addition of Ca^{2+}.

Similar to the effect of pH, the addition of Ca^{2+} does not cause significant changes in the overall structure of surfactin. Any structural rearrangement is largely limited to the charged groups of surfactin, the carboxylates of the glutamate and aspartate residues, which are considered to be the binding points for the divalent cations [2, 3, 20–22]. This is still the case for Ca^{2+} added at low pH, indicating that the uncharged acid residues continue to be the primary binding point for Ca^{2+}. The lack of change in C-H resonance ratios again indicates that the overall orientation and compact ball-like structure remain unaffected by the presence of Ca^{2+} ions, in agreement with previous neutron reflectivity results and most of the results of MD simulations [4, 20].

References

[1] H. Heerklotz and J. Seelig, "Detergent-like action of the antibiotic peptide surfactin on lipid membranes," *Biophysical Journal*, vol. 81, pp. 1547–1554, Sept. 2001.

[2] L. Thimon, F. Peypoux, and G. Michel, "Interactions of surfactin, a biosurfactant from Bacillus subtilis, with inorganic cations," *Biotechnology Letters*, vol. 14, pp. 713–718, Nov. 1992.

[3] R. Maget-Dana and M. Ptak, "Interfacial properties of surfactin," *Journal of Colloid and Interface Science*, vol. 153, pp. 285–291, Oct. 1992.

[4] J. Iglesias-Fernández, L. Darré, A. Kohlmeyer, R. K. Thomas, H.-H. Shen, and C. Domene, "Surfactin at the water/air interface and in solution," *Langmuir*, vol. 31, pp. 11097–11104, Oct. 2015.

[5] H.-H. Shen, R. K. Thomas, J. Penfold, and G. Fragneto, "Destruction and solubilization of supported phospholipid bilayers on silica by the biosurfactant surfactin," *Langmuir*, vol. 26, pp. 7334–7342, May 2010.

[6] H.-F. Wang, W. Gan, R. Lu, Y. Rao, and B.-H. Wu, "Quantitative spectral and orientational analysis in surface sum frequency generation vibrational spectroscopy (SFG-VS)," *International Reviews in Physical Chemistry*, vol. 24, pp. 191–256, Apr. 2005.

[7] P. Kett, M. Casford, and P. Davies, "Effect of multiple group orientations on sum frequency generation spectra," *Molecular Physics*, vol. 111, pp. 175–187, Sept. 2012.

[8] H.-Z. Gang, J.-F. Liu, and B.-Z. Mu, "Molecular dynamics study of surfactin monolayer at the air/water interface," *The Journal of Physical Chemistry B*, vol. 115, pp. 12770–12777, Nov. 2011.

[9] R. Lu, W. Gan, B.-h. Wu, Z. Zhang, Y. Guo, and H.-F. Wang, "C-H stretching vibrations of methyl, methylene and methine groups at the vapor/alcohol (N = 1-8) interfaces," *The Journal of Physical Chemistry B*, vol. 109, pp. 14118–14129, July 2005.

[10] S. Kataoka and P. S. Cremer, "Probing molecular structure at interfaces for comparison with bulk solution behavior: water/2-propanol mixtures monitored by vibrational sum frequency spectroscopy," *Journal of the American Chemical Society*, vol. 128, pp. 5516–5522, Apr. 2006.

[11] C.-S. Song, R.-Q. Ye, and B.-Z. Mu, "Molecular behavior of a microbial lipopeptide monolayer at the air–water interface," *Colloids and Surfaces A: Physicochemical and Engineering Aspects*, vol. 302, pp. 82–87, July 2007.

[12] J. Holman, P. B. Davies, T. Nishida, S. Ye, and D. J. Neivandt, "Sum frequency generation from langmuir-blodgett multilayer films on metal and dielectric substrates," *Journal of Physical Chemistry B*, vol. 109, pp. 18723–18732, Sept. 2005.

[13] Y. Ishigami, M. Osman, H. Nakahara, Y. Sano, R. Ishiguro, and M. Matsumoto, "Significance of β-sheet formation for micellization and surface adsorption of surfactin," *Colloids and Surfaces B: Biointerfaces*, vol. 4, pp. 341–348, July 1995.

[14] G. S. Hartley and J. W. Roe, "Ionic concentrations at interfaces," *Transactions of the Faraday Society*, vol. 35, p. 101, Aug. 1940.

[15] X.-D. Xiao, V. Vogel, and Y. Shen, "Probing the proton excess at interfaces by second harmonic generation," *Chemical Physics Letters*, vol. 163, pp. 555–559, Nov. 1989.

[16] K. P. Fears, S. E. Creager, and R. A. Latour, "Determination of the surface pK of carboxylic- and amine-terminated alkanethiols using surface plasmon resonance spectroscopy," *Langmuir*, vol. 24, pp. 837–843, Jan. 2008.

[17] E. C. Y. Yan, Z. Wang, and L. Fu, "Proteins at interfaces probed by chiral vibrational sum frequency generation spectroscopy," *The Journal of Physical Chemistry B*, vol. 119, pp. 2769–2785, Feb. 2015.

[18] K. Engelhardt, A. Rumpel, J. Walter, J. Dombrowski, U. Kulozik, B. Braunschweig, and W. Peukert, "Protein adsorption at the electrified air-water interface: Implications on foam stability," *Langmuir*, vol. 28, pp. 7780–7787, May 2012.

[19] D. E. Gragson, B. M. McCarty, and G. L. Richmond, "Ordering of interfacial water molecules at the charged air/water interface observed by vibrational sum frequency generation," *Journal of the American Chemical Society*, vol. 119, pp. 6144–6152, July 1997.

[20] H.-H. Shen, T.-W. Lin, R. K. Thomas, D. J. F. Taylor, and J. Penfold, "Surfactin structures at interfaces and in solution: The effect of pH and cations," *The Journal of Physical Chemistry B*, vol. 115, pp. 4427–4435, Apr. 2011.

[21] A. Grau, J. C. Gómez Fernández, F. Peypoux, and A. Ortiz, "A study on the interactions of surfactin with phospholipid vesicles," *Biochimica et Biophysica Acta (BBA) - Biomembranes*, vol. 1418, pp. 307–319, May 1999.

[22] E. Vass, F. Besson, Z. Majer, L. Volpon, and M. Hollósi, "Ca^{2+}-induced changes of surfactin conformation: A FTIR and circular dichroism study," *Biochemical and Biophysical Research Communications*, vol. 282, pp. 361–367, Mar. 2001.

[23] J.-M. Bonmatin, M. Genest, H. Labbé, and M. Ptak, "Solution three-dimensional structure of surfactin: A cyclic lipopeptide studied by ^{1}H-NMR, distance geometry, and molecular dynamics," *Biopolymers*, vol. 34, pp. 975–986, July 1994.

8. Interaction of surfactin with phospholipid monolayers studied in real time by SFG

In this chapter, we will present the SFG spectra of a phospholipid monolayer spread on the air/water interface at a defined pressure before and after the injection of surfactin into the subphase. Resonances from both the phospholipid and the surfactin are observed, and are differentiated by use of deuterated materials. In addition to molecular structural information on both components derived from SFG spectroscopy, the surface pressure at the air/water interface was monitored simultaneously providing context to the SFG data. Specific spectral features and the surface pressure were monitored in real time for periods up to 8 hours. All real-time spectra presented here are in the SSP polarisation.

In this chapter, dipalmitoylphosphocholine (DPPC) and its deuterated analogue were used instead of the dipalmitoylphosphoethanolamine (DPPE) that was used previously in Chapter 6. In fact, DPPE was used initially, and the interaction as probed by SFG appeared to be very similar. However, the experiment reached the endpoint much more slowly with DPPE, which caused practical issues. Using DPPC, an entire experiment (including casting and solvent evaporation, monolayer compression and relaxation, laser alignment, obtaining the initial and final SSP and PPP spectra in the CH and CD regions, as well as the time-dependent SFG experiment - see Section 3.10 for details) could be completed within one day and before evaporation of the water subphase became a significant issue for the laser alignment.

8.1 Interaction as probed by SFG

Figure 8.1 presents the results of a representative experiment involving dDPPC and surfactin, showing the surface pressure of the monolayer, and the r^+ SFG resonances in the SSP polarisation, of the deuterated lipid and the protonated surfactin plotted against time. The dDPPC was cast onto the surface from chloroform, and the solvent

was allowed to evaporate for at least 20 minutes. After compression of the phospholipid monolayer, the system was allowed to reach equilibrium (normally around 30 minutes).

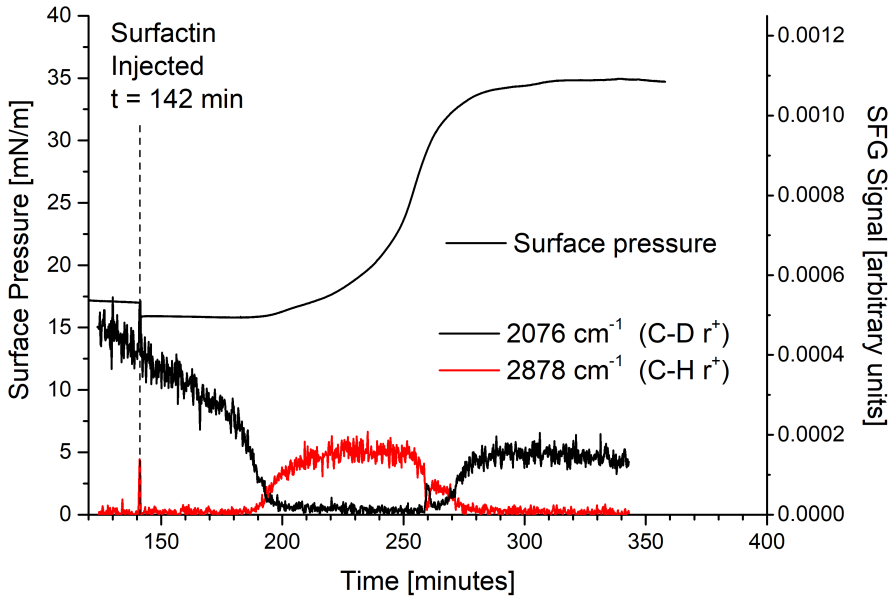

Figure 8.1: Plot of surface pressure and SFG intensity (r^+ in the SSP polarisation) of the dDPPC phospholipid monolayer and surfactin against time. 25 μl of surfactin solution (giving a concentration equal to 0.05×CMC in the trough) was injected into the subphase at 142 minutes, as indicated on the plot. The black SFG trace represents the SFG intensity of the r^+ resonance of the deuterated phosphoplipid, dDPPC, and the red SFG trace represents the SFG intensity of the r^+ resonance of the protonated surfactin.

Before the injection of surfactin, only CD resonances arising from the dDPPC were observed, and the surface pressure did not change over time. The surface pressure of the phospholipid monolayer after surfactin was injected into the subphase did not change for approximately 60-70 minutes, at which point it began to increase. Simultaneously, the SFG intensity arising from the CD bonds of dDPPC methyl groups began to decrease. Approximately 20-30 minutes later, CH resonances arising from methyl groups of the surfactin were detected. The CD signals continued to decrease, and the CH signals increase, reaching their minimum/maximum at the same time as the surface pressure increase had reached its inflexion point. The surface pressure continues to increase until its plateau (120-140 minutes after injection of surfactin), at which point the r^+ CD intensity began to recover, and the r^+ CH intensity of surfactin began to decrease again.

The extent to which the signals return to their original state, the time taken for the surface pressure to reach its final value, and that value itself, depend upon the initial conditions used, but are also subject to considerable run-to-run variation. However, when the appropriate amount of surfactin is injected (in this case 3×10^{-6}M or 0.05×CMC), this overall pattern, in which the resonances arising from surfactin appear and then subside, and the resonances arising from the phospholipid monolayer are diminished and then recover, alongside the changing surface pressure, occurs very consistently.

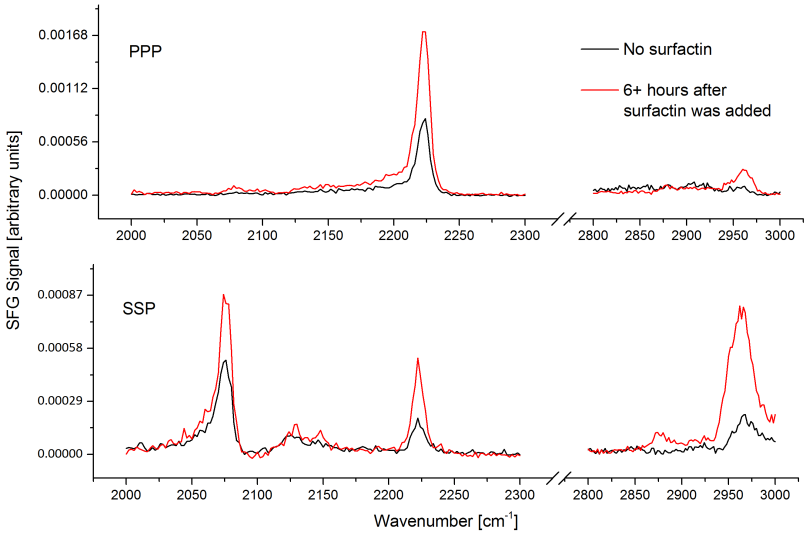

Figure 8.2: The "before" (black) and "after" (red) spectra of the CD (2000-2300 cm^{-1}) and CH (2800-3000 cm^{-1}) regions of the dDPPC and surfactin system, taken just before injection of the surfactin into the subphase, and after 400 minutes (the end of the time-dependent SFG results). As expected, before surfactin is added only resonances arising from the phospholipid are visible. In the SSP polarisation, they are assigned to the r^+ at 2074 cm^{-1}, the r^+_{FR} at 2136 cm^{-1}, and the r^- at 2220 cm^{-1}. Also visible is a resonance at 2965 cm^{-1}, probably from the single C-H bond in the dDPPC (this resonance is discussed further at the start of Section 8.2). Afterwards, resonances from the phospholipid and very weak resonances from the surfactin are visible (the r^+ in the SSP at 2878 cm^{-1}).

.

As well as monitoring the r^+ resonances of the CD and CH methyl groups, full spectra of the CH and CD regions were obtained before injection and after the surface pressure and SFG intensities had reached equilibrium. These are shown in Figure 8.2. Initially, only resonances arising from the phospholipid are observed, assigned to the r^+ (2072 cm^{-1} in the SSP), r^+_{FR} (2136 cm^{-1} in the SSP), and r^- (2222 cm^{-1} in the SSP and PPP). One further resonance in the CH region is observable at 2965 cm^{-1}, and this arises from a single CH bond of the tertiary carbon in the dDPPC. Afterwards, these resonances are still present. Additionally, a weak resonance from surfactin is now observed. It is assigned to the r^+ stretch (2878 cm^{-1} in the SSP). Surfactin may also contribute to the resonance at 2965 cm^{-1}. The extent to which the CD resonances are preserved, and the CH resonances rise, depends greatly on the amount of surfactin injected and also exhibited significant run-to-run variation. Usually CH resonances attributable to surfactin would not be visible at all in the final spectra.

By referencing surface-pressure - area isotherms of the dDPPC and DPPC phospholipids (shown in Figure 8.3), the surface phase of the phospholipid during the experiments can be deduced. With the exception of one low-pressure experiment (shown later in Figure 8.18), the initial pressure of dDPPC was always above 15 mN/m, and therefore in the liquid-condensed (LC) phase. This was done for two reasons. Firstly, biological cell membranes usually have a surface pressure of around 30 mN/m [1], and therefore the LC phase is the most relevant to investigate. Secondly, above 15 mN/m both dDPPC and DPPC are definitely in the same phase, whereas low surface pressures might result in different phases for each monolayer as seen in the isotherms of Figure 8.3, which would complicate comparisons between experiments.

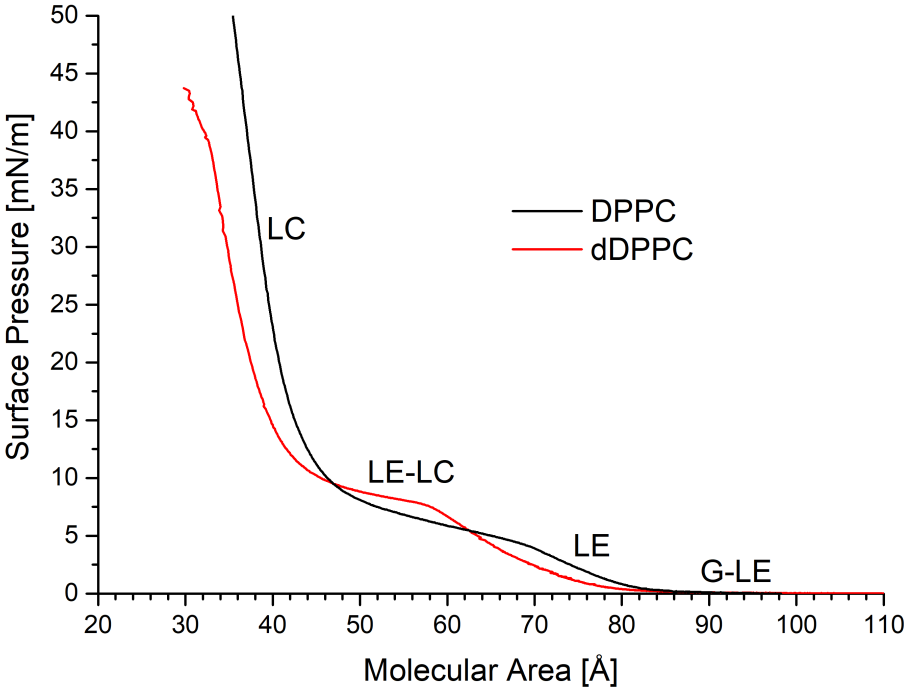

Figure 8.3: Surface-pressure - area isotherms of the DPPC and dDPPC phospholipids used in these experiments. Marked on the isotherms are the phases of the two phospholipids - liquid condensed (LC), liquid expanded (LE), gaseous (G) and their coexisting regions (LE-LC and G-LE).

8.2 Time dependence of the SFG spectra

It was mentioned in Chapter 5 that monitoring a single wavenumber over time provides excellent time resolution but unfortunately results in the loss of a great deal of spectral information. To investigate further the change in structure that occurs in the monolayer and surfactin, the same experiments were repeated while acquiring scans of the whole CH or CD region. The resulting set of spectra are shown below. Figure 8.4 shows the CH region of an experiment using dDPPC and protonated surfactin. Therefore, the CH signals arise largely from the surfactin, with the exception of a resonance at 2965 cm^{-1}. This arises from the lone C-H bond of the tertiary carbon in the otherwise fully deuterated dDPPC, and appears when the monolayer is very well ordered. Surfactin also shows a resonance at this wavenumber (see Chapter 7); however, it is usually smaller than the resonance at 2878 cm^{-1}. In fact, the resonance at 2965 cm^{-1} changes from being

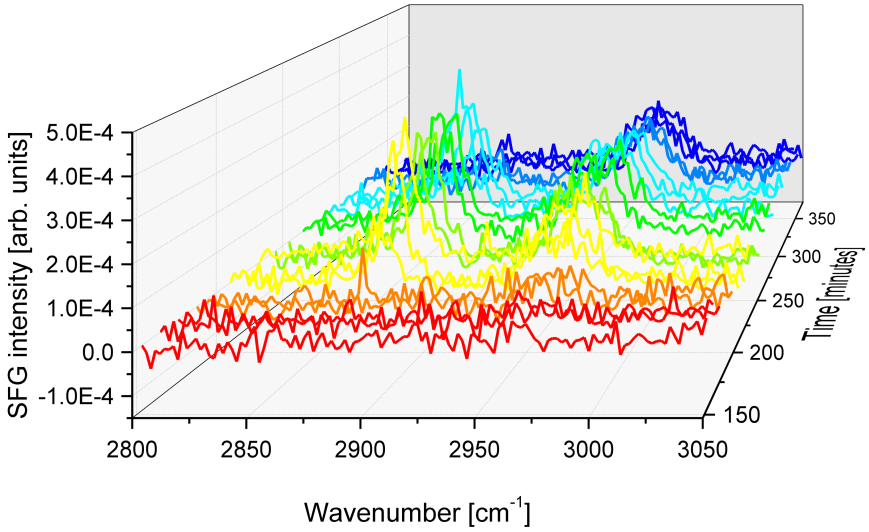

Figure 8.4: SFG spectra in the SSP polarisation of the CH (2800-3000 cm^{-1}) region acquired during the interaction of surfactin and deuterated phospholipid. The assigned peaks are the r^+, r^+_{FR}, and r^- at 2874 cm^{-1}, 2951 cm^{-1}, and 2966 cm^{-1}, respectively. The associated surface pressure and fitted peak areas are shown in Figure 8.5, and the associated before and after spectra showing the dDPPC signals in the CD region, as well as PPP spectra are shown in Figure 8.6.

mostly surfactin contributions during the middle part of the experiment to mostly dDPPC contributions at the end. This is validated later on when d-leucine surfactin was used in combination with protonated phospholipid (Figure 8.8), where there the analogous CD resonance at 2220 cm^{-1} is not visible at the end of the experiment.

The spectra show r^+, r^+_{FR}, and r^- intensities rising and then decreasing over time, mostly in the same way as seen in the previous time-dependent SFG intensity data. The exception is that the r^- intensity does not reduce to zero - it is very likely that the phospholipid contributes to this intensity, given that it is also seen when the pure phospholipid is highly compressed (this resonance is visible in the "before" spectra in Figure 8.2). By and large, these spectra appear very similar to the spectra of surfactin on water (Section 7.1, Figure 7.2), suggesting that no major changes in the structure of surfactin has taken place during its interaction with the phospholipid monolayer.

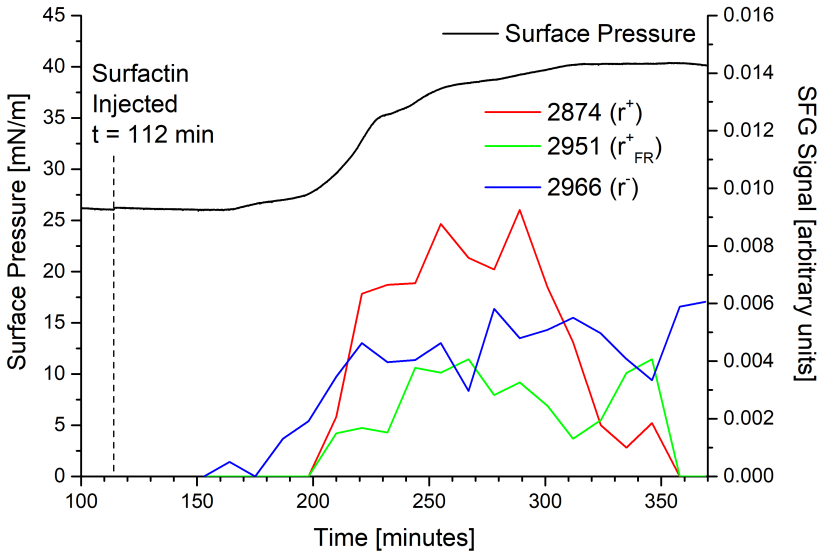

Figure 8.5: The surface pressure and fitted peak areas of the CH resonances plotted against time, extracted from the data in Figure 8.4, where the full spectra of the same system are shown.

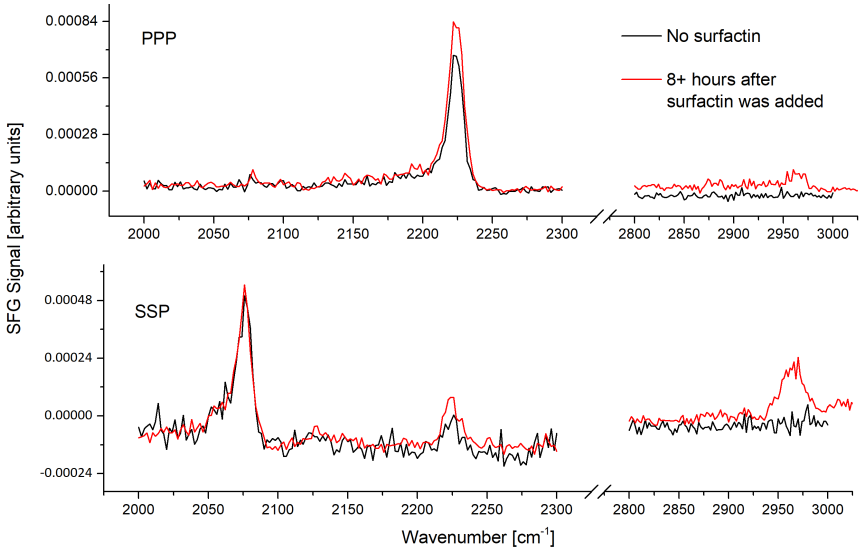

Figure 8.6: The "before" and "after" spectra of the CD and CH regions of the dDPPC and surfactin system, taken just before injection of the surfactin into the subphase, and after 380 minutes. The initial surface pressure was 26 mN/m and the final surface pressure was 42 mN/m. The surface pressure against time, and fitted peak amplitudes of the CH region throughout the experiment are shown in Figure 8.5. Assigned r^+ 2072 cm^{-1}; r^+_{FR} 2136 cm^{-1}; r^- 2220 cm^{-1}; tertiary CH at 2965 cm^{-1}.

The previous waterfall plot (Figure 8.4) showed the CH region of a protonated surfactin - deuterated phospholipid system. Figure 8.7 shows the corresponding phospholipid resonances in the CD region of a similar experiment (both the CH and CD regions could not be acquired at the same time, due to the large reduction in time resolution and/or spectral resolution that would occur). As before, it is clear that the SFG resonances arising from the phospholipid are reduced and then recover during the experiment. It is important to note that there is no evidence for d resonances at any point in these spectra. This is difficult to reconcile with the idea that the monolayer is becoming disordered, which would normally be the explanation for the reduction in the SFG intensity. If the whole monolayer gradually becomes disordered, as indicated by the time behaviour of the r^+ resonances of the DPPC, one would expect to see d resonances appearing as gauche defects formed in the monolayer (as shown in Figure 2.8).

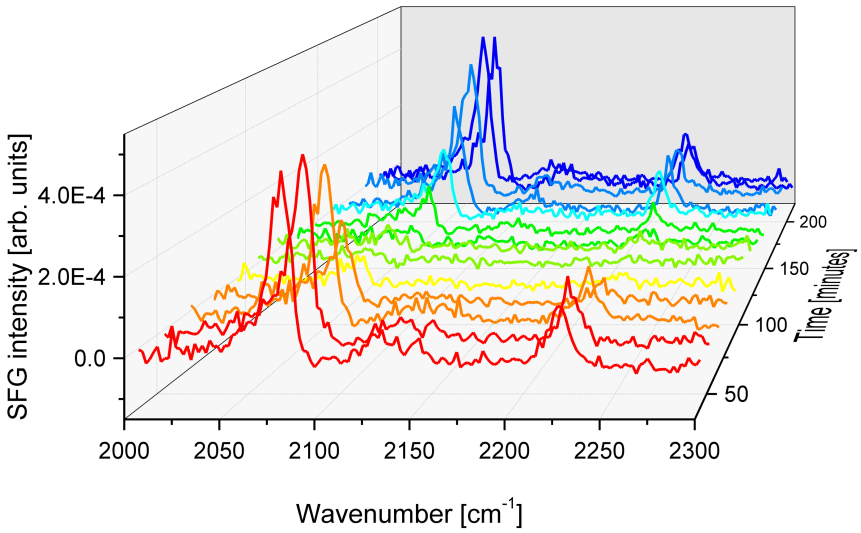

Figure 8.7: SFG spectra of the CD (2000-2300 cm^{-1}) region acquired during the interaction of protonated surfactin and deuterated phospholipid. These spectra show only the resonances arising from the phospholipid as the surfactin interacts with the monolayer. The r^+ (2072 cm^{-1}), r^+_{FR} (2136 cm^{-1}), and r^- (2222 cm^{-1}) are all observable at the start and end, but not during the middle part of the experiment. Additionally, no d resonances are observable (which would normally be at 2095-2100 cm^{-1} for the d^+, and around 2200 cm^{-1} for the d^-) in the CD region.

In addition to experiments using deuterated phospholipid and protonated surfactin, experiments were conducted using d-Leu surfactin (described in Chapter 7) and protonated phospholipid. Figure 8.8 shows the repeated scans of the CD region of such an experiment. Now the CD region shows signals arising from the deuterated leucine groups of the surfactin, and possibly also from the 40-50% of d_9 deuterated tail groups in the surfactin. (This is a result of *Bacillus Subtilis'* use of the deuterated leucine as a starter molecule for the fatty acid, as mentioned in Section 7.1 - see Section 3.9 for details.) Again, these look very similar to the spectra of the same d-leu surfactin on its own on water (Figure 7.4), varying only in intensity as the experiment progresses.

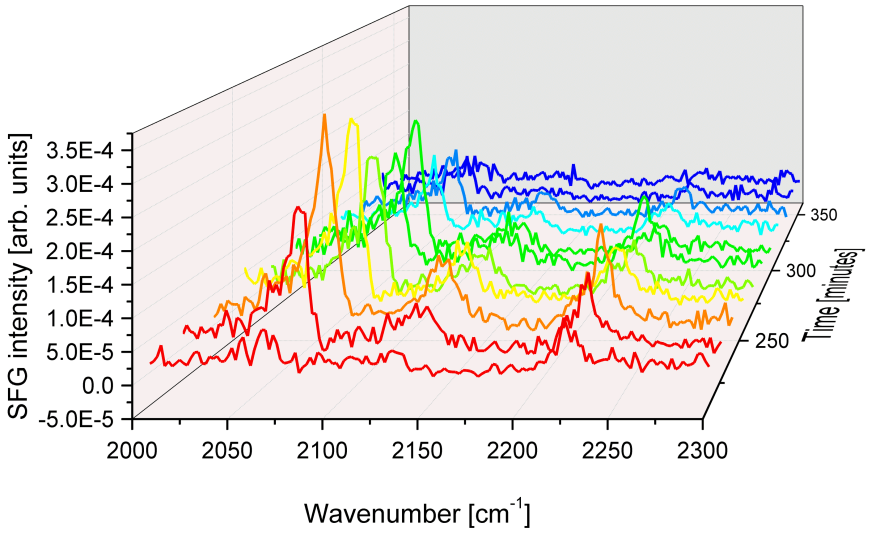

Figure 8.8: SFG spectra of the CD (2000-23000 cm^{-1}) region acquired during the interaction of d-leu surfactin and protonated phospholipid. All the resonances arise from the surfactin leucine groups. No CD resonances are observable at the start or the end of the experiment, and are only visible during the middle part the experiment in the same way that the CH resonances are observed in the previous protonated surfactin experiments. The resonances are assigned: r^+ 2072 cm^{-1}; r^+_{FR} 2136 cm^{-1}; r^- 2220 cm^{-1}.

The CH region scans of a repeated experiment (Figure 8.9) shows the intensity arising from the DPPC monolayers, and potentially any CH resonances that might arise from the CH bonds in the tail or ring of the d-leu surfactin. The spectra show r^+, r^+_{FR}, and r^- resonances, with very little evidence for d resonances. As described previously, the

intensity is reduced and then recovers as the experiment progresses. During the period when resonances arising from the lipid are suppressed, and those from surfactin would be visible, there are no detectable CH resonances in the spectra. We can have confidence that the SFG resonances arising from surfactin are entirely from the leucine groups - there are no observable contributions from the tail or ring CH bonds in the SFG spectrum of surfactin in this experiment.

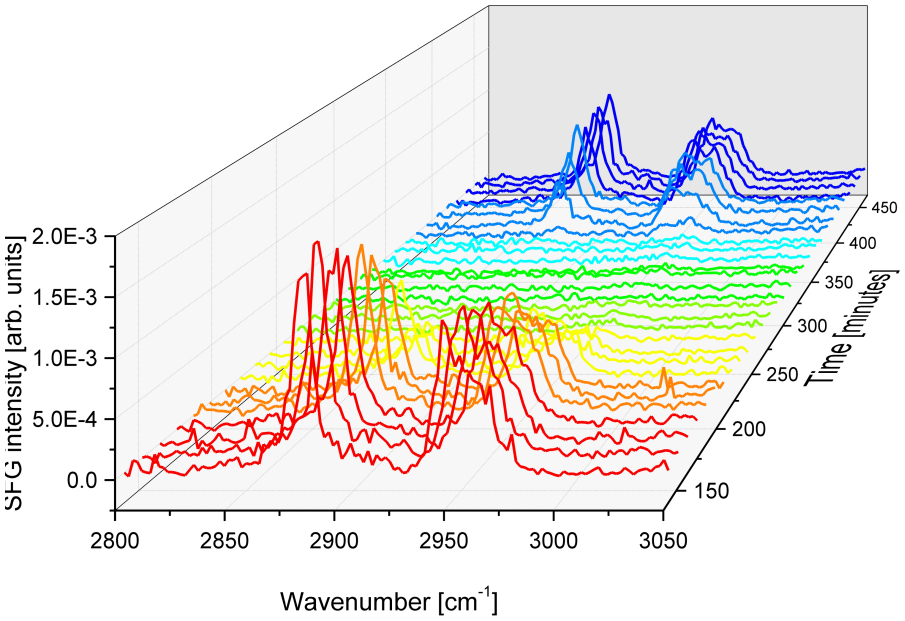

Figure 8.9: SFG spectra of the CH (2800-3000 cm^{-1}) region acquired during the interaction of d-leu surfactin and protonated phospholipid. The resonances are assigned: r^+ 2878 cm^{-1}; r^+_{FR} 2946 cm^{-1}; r^- 2966 cm^{-1}. As seen in the CD spectra of the deuterated phospholipid experiment (Figure 8.7), the resonances are only visible at the start and end of the experiments, and there is no evidence for d resonances. d resonances would typically be observed at around 2850 cm^{-1} for the d^+ and 2920-2925 cm^{-1} for the d^-.

The final easily accessible region of the spectrum is 3000-3800 cm^{-1}, which covers the OH stretches of water. A waterfall plot of the whole 2800-3800 cm^{-1} region is shown in Figure 8.10, and fitted values of the observed resonances are shown in Figure 8.11. The changes in CH resonances arising from surfactin are the same as in Figure 8.4. The changes in OH resonances are difficult to see in the waterfall plot, both due to the noise levels of the spectra and also due to the broad nature of the water resonances. However, the fitted values show a clear trend in OH resonance intensity - simultaneously with the

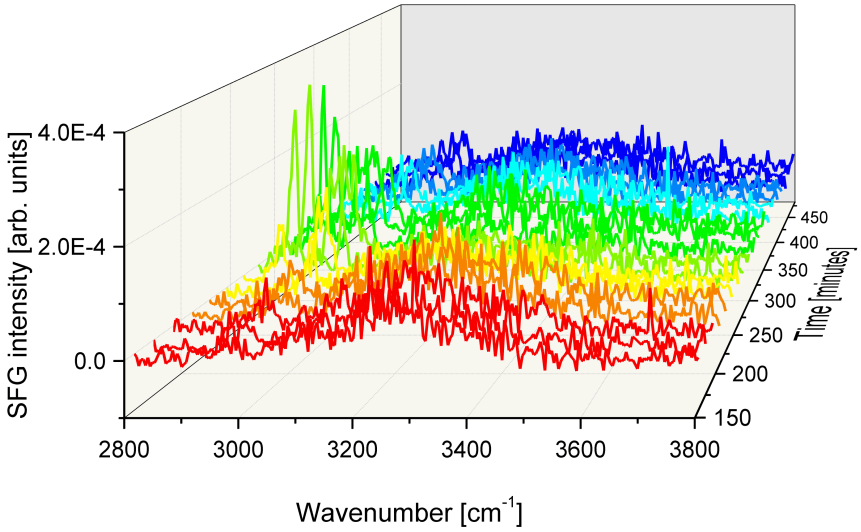

Figure 8.10: SFG spectra of the CH and OH (2800-3800 cm^{-1}) region acquired during the interaction of protonated surfactin and deuterated phospholipid. These spectra show resonances arising from the OH bonds of water (in the region 3000-3800 cm^{-1}) as surfactin interacts with the monolayer, as well as the CH region (2800-3000 cm^{-1}). Resonances from surfactin (r^+ 2874 cm^{-1}; r^+_{FR} 2951 cm^{-1}; r^- 2966 cm^{-1}) are not observable at the start and end, only during the middle part of the experiment. In this expanded range, OH signals are now also visible, centred at 3113, 3238, and 3477 cm^{-1}. Changes are difficult to see due to their broad nature. Refer to Figure 8.11 for fitted areas of the water peaks.

rise in surfactin resonances, those from the OH bonds decrease. Additionally, once the CH signals decrease again, the OH resonances recover. The negatively charged surfactin may have a disordering effect on the water bonds, which are normally aligned to the positive charge presented by the amide group of the zwitterionic phospholipid. This would explain the decrease in the OH resonances observed in Figure 8.11. An alternative explanation would be that where surfactin has adsorbed to the monolayer, OH bonds, which normally point away from the positively charged interface presented by the phospholpid, now point upwards towards the negatively charged interface presented by the surfactin. SFG resonances arising from these regions cancel with SFG resonances arising from regions of the monolayer where no surfactin is present, reducing the observed intensity of OH resonances.

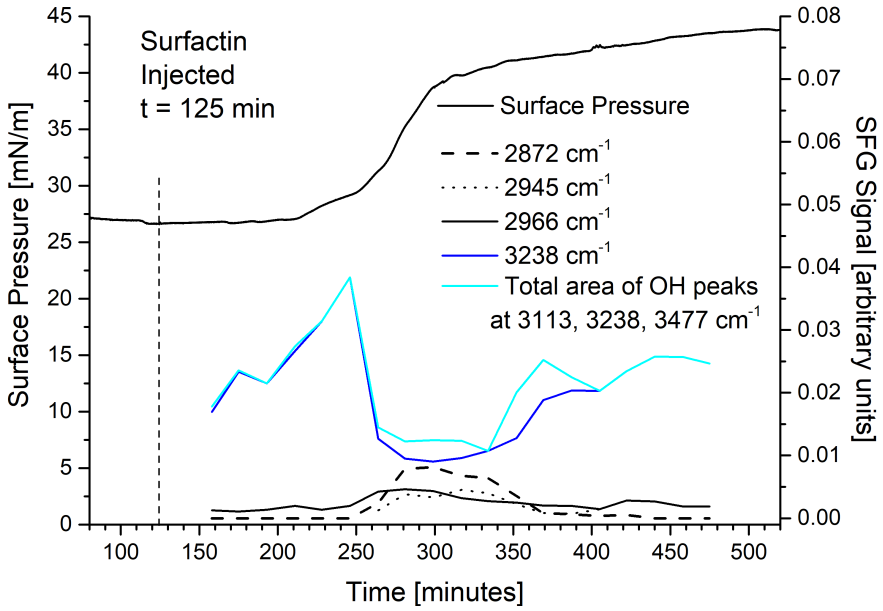

Figure 8.11: The surface pressure and fitted peak areas of the CH and OH resonances plotted against time, extracted from the data in Figure 8.10, where the full spectra of the same system are shown. The OH peaks are fitted at 3113 cm^{-1}, 3238 cm^{-1}, and 3477 cm^{-1}, with the largest contribution coming from the peak at 3238 cm^{-1}. In fact, the resonances arising from water are complex in nature and difficult to fit correctly without the use of phase-sensitive detection. In-depth phase analysis of the OH peaks is beyond the scope of this document, and beyond the capabilities of the scanning picosecond SFG spectrometer used here, since phase-sensitive detection is orders of magnitude slower in acquiring a spectrum.

8.3 Reflection absorption infrared spectroscopy

A general result in SFG spectroscopy is that when a monolayer containing long aliphatic chains becomes disordered, r resonances decrease in intensity and d resonances appear as gauche defects are formed. However, throughout the interaction with surfactin, no SFG d resonances arising from the phospholipid were observed, despite the complete suppression of r resonances during the middle stages of the experiment. A superficial conclusion would be that the monolayer is removed from the surface rather than becoming disordered, but this seems unlikely, given that afterwards the phospholipid would have to return to the interface and form a well-ordered monolayer to give rise to the "after" phospholipid spectra.

To investigate this further, Reflection Absorption Infrared Spectroscopy (RAIRS) was conducted on the same system. Unlike SFG, RAIRS probes CH vibrational modes regardless of their orientation on the surface. CH signals arising from the DPPC were observed throughout the experiment, as shown in Figure 8.12. They are visible as the yellow and orange regions denoting the wavenumbers where RAIRS reflectance was the lowest, at 2851 cm^{-1} and 2920 cm^{-1}, due to absorption by the d^+ and d^- vibrational modes, respectively. Also observed in Figure 8.12, but much more weakly than the d bands, is a dip at 3002 cm^{-1}. This is tentatively assigned to the tertiary CH bond of the phospholipid. Two of the scans used to produce the contour plot, taken from 88 and 285 minutes, are shown in Figure 8.13. Based on these RAIRS data, it was concluded unambiguously that the lipid remains at the interface throughout the whole of its interaction with surfactin.

Interestingly, RAIRS was not able to detect any vibrational bands arising from surfactin at the interface. Neither CD bands from d-leu surfactin nor CH bands from protonated surfactin were observed, regardless of surfactin concentration, and not even when surfactin was cast onto a pure water surface from chloroform and allowed to spread, or when solid surfactin was added to the surface. The molecular area of surfactin at the surface for a solution above the CMC is roughly 147 Å [2]. In the range of surface pressures used here, the molecular area of DPPC is roughly 40-50 Å(Figure 8.3). A molecule of surfactin has 16 CH_2 groups, (3 of which are adjacent to a carbonyl and are therefore expected to be shifted up in wavenumber slightly from 2920 cm^{-1}), compared to 34 for DPPC (of which 6 are adjacent to electronegative groups and should also be blue shifted). Therefore, a monolayer of DPPC has approximately 6-7 times more CH_2 groups

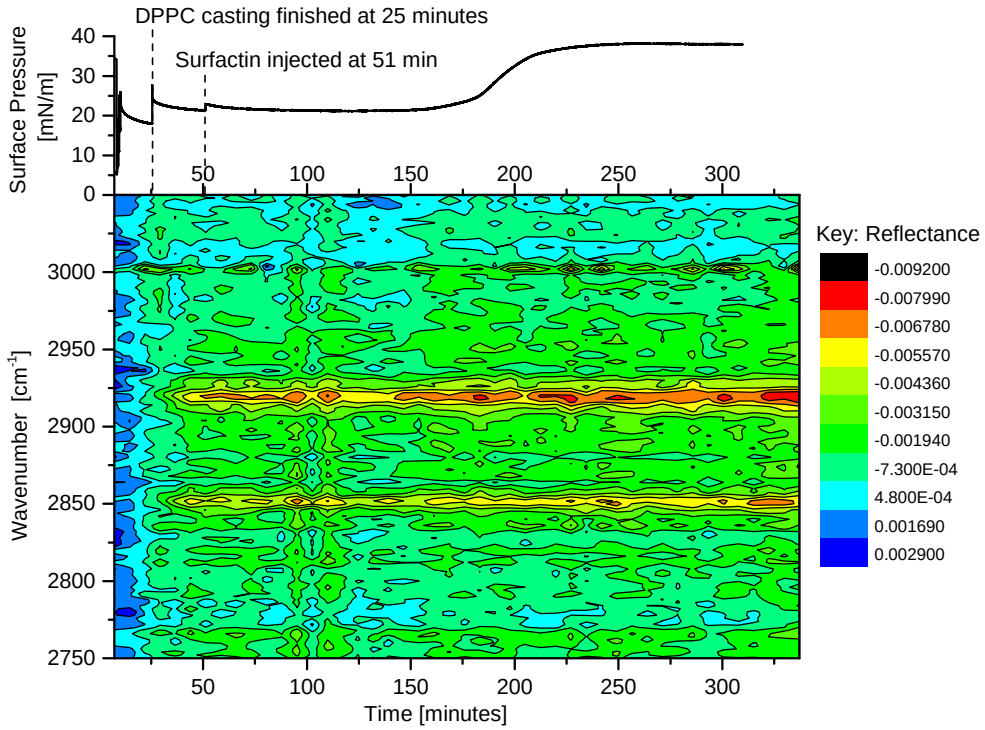

Figure 8.12: A contour plot showing RAIRS reflectance data acquired during the interaction of d-leu surfactin and DPPC. The surface pressure associated with the experiment is shown at the top of the diagram, with the DPPC casting and surfactin injection events as labelled. The d^+ and d^- resonances arising from the phospholipid were observed at 2851 cm^{-1} and 2920 cm^{-1} respectively, and appear as orange regions on the contour plot. No dips attributable to surfactin were detected. This is discussed further in the text.

per unit area at the water surface compared to surfactin. According to the Beer-Lambert law, absorbances would also be 6 times weaker. This would not be above the level of noise observed in Figure 8.13.

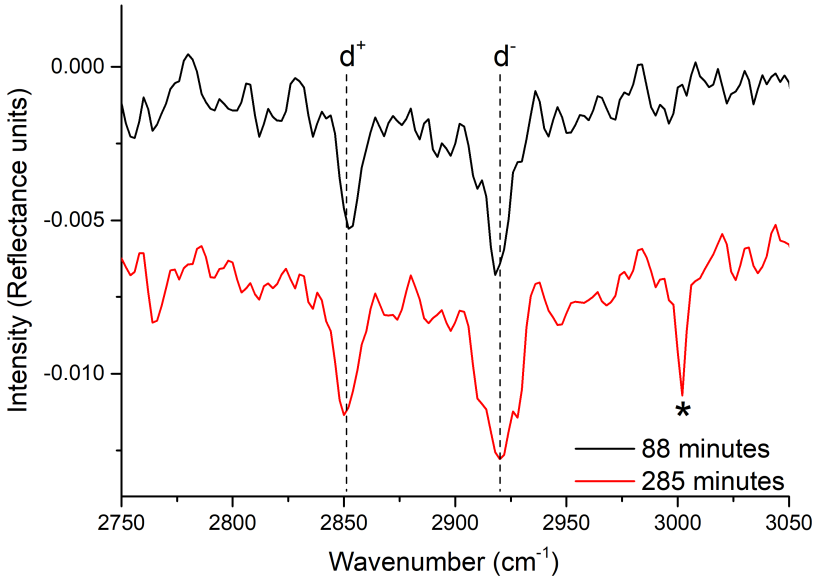

Figure 8.13: Two of the sequential RAIRS spectra recorded in order to produce the contour plot in Figure 8.12, offset for clarity. The d^+ and d^- bands have been assigned at 2851 cm^{-1} and 2920 cm^{-1} on the plot. An additional peak is visible at 3002 cm^{-1}, indicated by the * in the 285 minute scan. This is probably from the tertiary C-H bond. (In the contour plot, it is visible before the other DPPC bands appear, as a similar bond exists in the chloroform used to cast the DPPC.)

8.4 Mechanistic considerations

It is possible to arrive at a plausible explanation of the SFG, RAIRS, and surface pressure results. With regards to the RAIRS data, we must conclude that the lipid remains at the surface throughout the experiment. A compatible potential mechanistic interpretation is as follows. Surfactin molecules arrive at the interface and adsorb to the phospholipid monolayer, probably due to electrostatic interaction of the positively charged tertiary amide of the DPPC and the negatively charged surfactin. This causes disordering of the monolayer in the immediate vicinity of the surfactin. This region of monolayer is now so disordered that no SFG signal arises from it. Because the amount of surfactin arriving at the surface at any one moment is relatively small, there is no observation of the d resonances that would usually arise from a monolayer that is changing uniformly from well ordered to disordered. As the amount of surfactin at the interface increases, the ratio of disordered to ordered monolayer increases, and therefore the SFG resonances

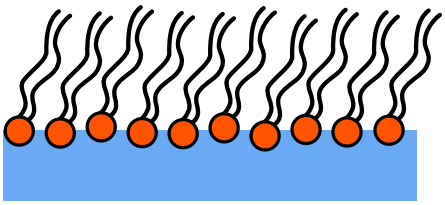

(a) The phospholipid monolayer before the surfactin is injected. It forms a close packed and therefore well-ordered monolayer at the interface, with very few gauche defects.

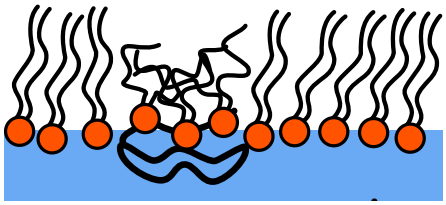

(b) Approximately 60-80 minutes after the injection of 0.05×CMC of surfactin, the surfactin arrives at the surface and begins adsorbing to the monolayer, probably by electrostatic interaction. Phospholipids that interact with the surfactin rapidly become disordered.

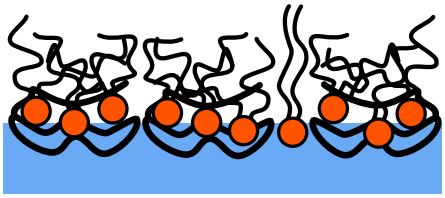

(c) Surfactin continues to adsorb to the phospholipid monolayer until almost all of the monolayer is very disordered.

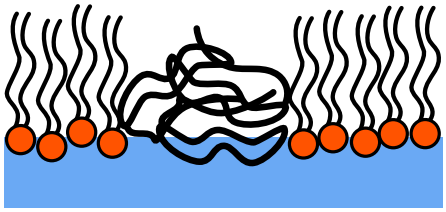

(d) Surfactin itself now aggregates at the interface. The surface area occupied by surfactin is reduced, giving room for the phospholipid to reoccupy the air/water interface and thereby form ordered monolayers once again.

Figure 8.14: Diagrams showing a mechanism compatible with the data presented in this chapter.

from the phospholipid decrease. The arrival of surfactin at the interface also explains the increase in surface pressure and surfactin resonances. The SFG data shows that, after the monolayer is fully disordered, it recovers after a certain amount of time. Simultaneously with this, the surfactin resonances disappear. The increased surface pressure indicates that there must be more material at the interface than at the start of the experiment, and therefore it seems highly unlikely that the surfactin leaves the interface after having been adsorbed to the monolayer. The recovery of the monolayer ordering is probably due to aggregation of surfactin at the interface, causing it to occupy a smaller area and creating room for the phospholipid to reform as an ordered monolayer. In this final state, the aggregated surfactin is either too disordered, or organised in a pairwise or in another symmetric fashion. Any centrosymmetric arrangement, or any arrangement with no

net polarisation in the z direction (since the aggregates will be orientated isotropically in the x-y plane) will be SFG inactive. This entire process is shown diagrammatically in Figure 8.14. Aggregation occurs when the DPPC-DPPC and surfactin-surfactin interactions are favoured over surfactin-DPPC interactions. Although one would expect that the double negative charge of surfactin at neutral pH would make aggregation unfavourable, at the interface the local pH is reduced compared to the bulk [3–5], so that the acid groups are not doubly dissociated at the interface, as discussed in Section 7.2. This reduces the charge repulsion that might otherwise make aggregation unfavourable.

8.5 Effect of surfactin concentration on interface composition

Surfactin is known to solubilise bilayer membranes when above the CMC [6] (which is equal to 6×10^{-6} M [2]). The accepted mechanism by which it does this is to adsorb to the phospholipid, incorporate into the membrane, and then form mixed phospholipid-surfactin micelles, removing the membrane from the interface [7, 8]. In the previous section, surfactin was injected into the subphase at a concentration of $0.05 \times$ CMC, and the SFG signals arising from the surfactin appear, increase to a maximum, and then fall again, while corresponding signals from the phospholipid decrease and then recover. The experimental data for the same experiment with a greater concentration of surfactin is shown in Figures 8.15 and 8.16. When injected into the subphase at a concentration of $0.2 \times$ CMC, the first step occurs as before - signals from surfactin appear and signals from the phospholipid decrease, but this does not reverse as the surface pressure reaches its maximum. Whereas previously SFG signals arising from both surfactin and phospholipid were observed at the surface, in this case only surfactin was detectable - there was no evidence of CD signals in the "after" spectra that would be attributable to the dDPPC phospholipid. One explanation is that the surfactin entirely and permanently displaces the phospholipid monolayer at the surface, even at concentrations well below the CMC. Another possibility is that after aggregating at the interface as in Figure 8.14d, the remaining phospholipid monolayer is disordered by the excess of surfactin. Further aggregation would increase the surface pressure beyond what surfactin is capable of, i.e there is no "free space" left for the phospholipid to occupy, and the final situation appears as Figure 8.17.

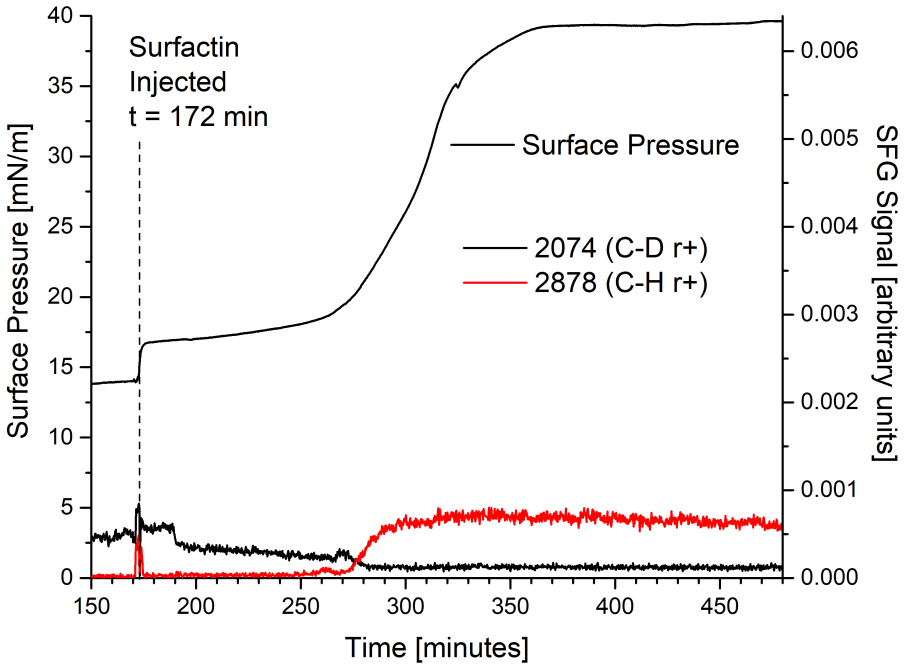

Figure 8.15: Plot of surface pressure and SFG intensity of the phospholipid monolayer and surfactin against time. In this case, 100 μl of surfactin was injected into the subphase (0.2× the CMC) at 172 minutes as indicated on the plot. The black SFG trace represents the SFG intensity of the r^+ resonance of the deuterated phospholipid, dDPPC, and the red SFG trace represents the SFG intensity of the r^+ of the protonated surfactin.

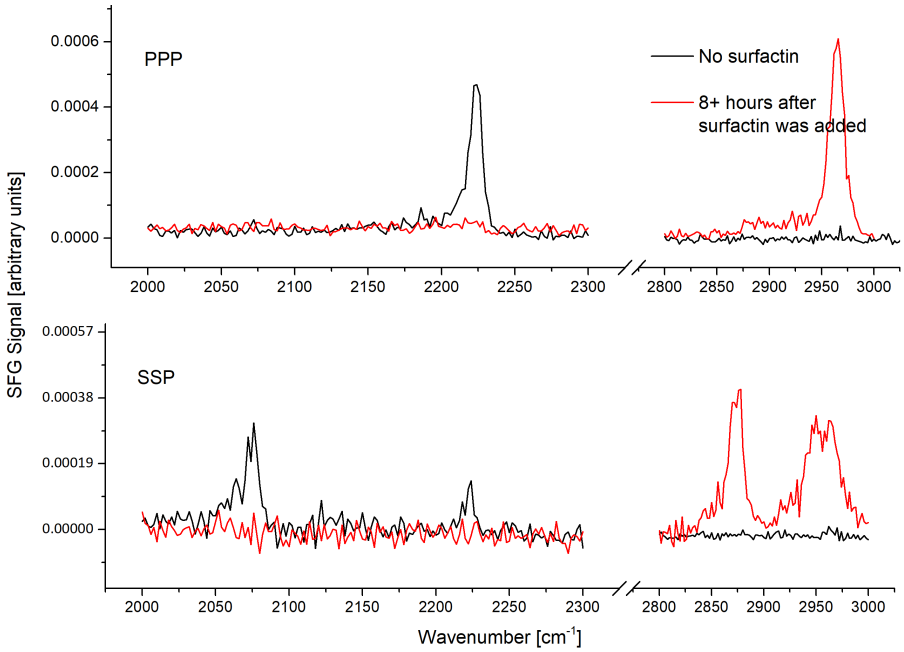

Figure 8.16: The "before" and "after" spectra of the CD (2000-2300 cm^{-1}) and CH (2800-3000 cm^{-1}) regions of the dDPPC and surfactin system, taken just before injection of the surfactin into the subphase, and after 400 minutes (the end of the time-dependent SFG results). As expected, before surfactin is added, only resonances arising from the phospholipid are visible - the CD resonances and the 2966 cm^{-1} resonance in the CH region. Afterwards, resonances from the phospholipid are no longer present, and CH resonances that are attributable to surfactin are visible, at 2878 cm^{-1} in the SSP and 2966 cm^{-1} in the PPP (which is probably not from the phospholipid, given the lack of resonances in the CD region).

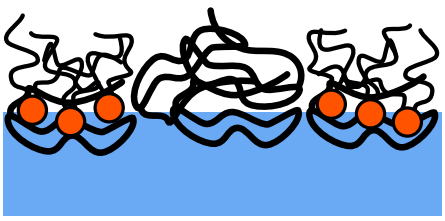

Figure 8.17: Postulated state of surfactin/phospholipid system at the end of the excess surfactin experiment.

8.6 Effect of initial surface pressure

The lateral pressure of the lipid bilayer membrane is known to have a strong effect on the uptake of molecules into the membrane and into the cell [9], and can affect the structure and function of embedded proteins [10]. For this reason, the effect of the phospholipid's initial surface pressure on the behaviour of surfactin was investigated. Figures 8.18 and 8.19 show the results when low and high initial surface pressures are used. The time between injection of surfactin and the initial rise in surface pressure and the initial change in SFG intensities does not alter significantly. Additionally, the time taken for the surface pressure to reach its plateau, and the time taken for the surfactin signals to begin changing towards their final equilibrium intensities, did not vary systematically with pressure.

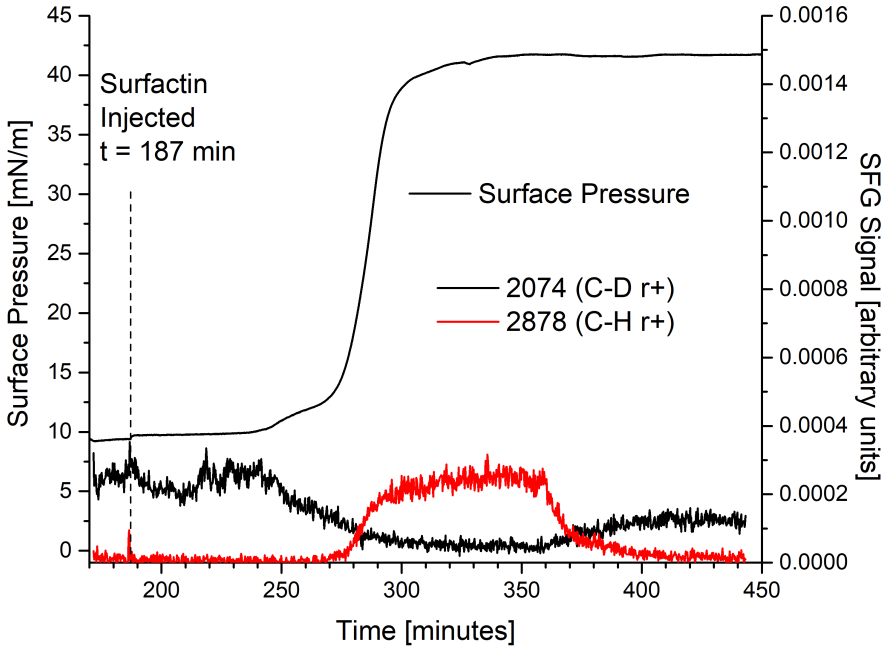

Figure 8.18: Plot of surface pressure and SFG intensity against time. In this case, the intial surface pressure of the phospholipid was 10 mN/m. Note that this is the only experiment where the dDPPC was not in the liquid condensed phase - here it begins in the liquid condensed - liquid expanded coexistence region, although this does not seem to have affected the rate of increase of surfactin signal intensity.

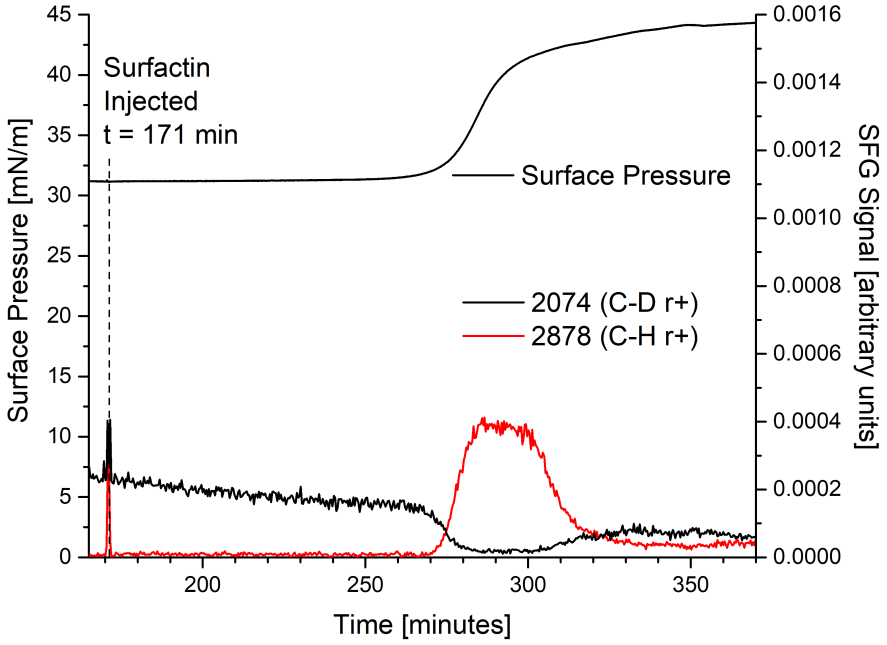

Figure 8.19: Plot of surface pressure and SFG intensity against time. In this case, the intial surface pressure of the phospholipid was 32 mN/m.

One would expect that the penetration of surfactin would be slowed by a high lateral pressure in the monolayer, and be faster for a lower lateral pressure. Since this does not seem to be the case, the surfactin penetration step is not rate-limiting. This could be because diffusion through the subphase and adsorption to the interface is fairly slow, and compared to this the penetration step occurs relatively quickly after the arrival of surfactin to the surface. This is a reasonable explanation, but when made on the basis of the data in Figures 8.18 and 8.19, it must be a tentative conclusion due to considerable run-to-run variation. However, this idea does fit nicely with the explanation for the lack of d resonances described earlier - that, at any one moment, the population of surfactin undergoing the penetration step is too small for d resonances to be observed.

8.7 Effect of low pH of the subphase

Surfactin is negatively charged at neutral pH. At low pH, the carboxylate groups are neutralised, and the effect of this on its interaction with the phospholipid monolayer is shown in Figure 8.20. This figure shows the data from an experiment similar to that

shown in Figure 8.1, except, in this case, the subphase was adjusted to pH 3.4 by addition of hydrochloric acid. In this case, the rise of the surfactin resonances and the dip in

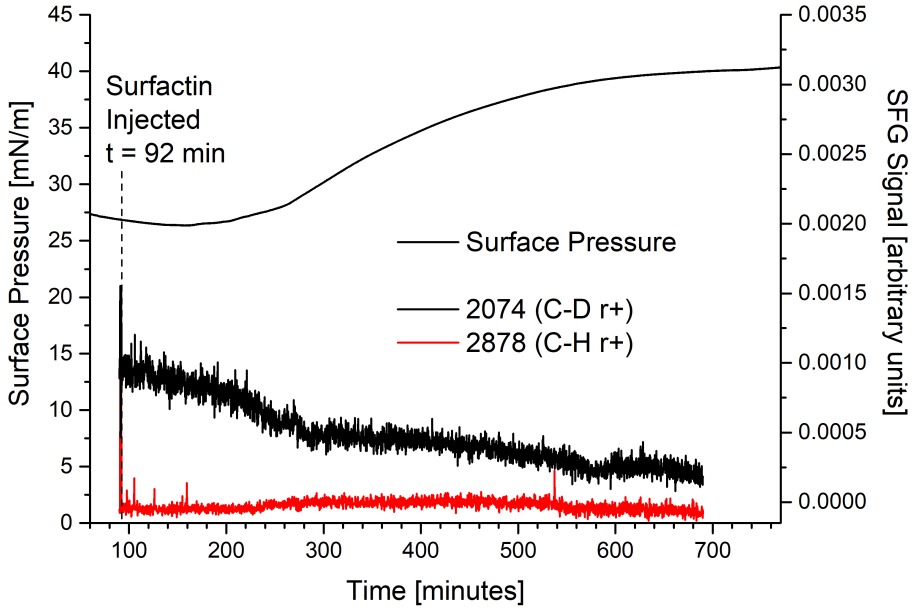

Figure 8.20: Plot of surface pressure and SFG intensity against time under acidic conditions (pH 3.4). The decrease in phospholipid resonances and the increase in surfactin resonances are now much less pronounced than in previous experiments.

the phospholipid resonances is much more subdued than previously, indeed almost unnoticeable. The time for surfactin resonances to appear took much longer (around 140 minutes), and remained detectable for a much longer time, around 300 minutes. The change in surface pressure is also more gradual, but still reaches 40 mN/m. (It should be noted that this experiment took a very long time, and the overall lowering of intensity as the experiment progresses may be due to evaporation/laser drift, reducing the overlap of the infrared and visible lasers, resulting in lower laser output power due to experimental issues rather than a decreasing number density of phospholipid on the surface.) There is a smaller increase in surfactin resonances, and a smaller decrease in lipid resonances when compared to the initial experiments at a higher pH, and this period lasts for a longer time. This can be explained by a slower build up of surfactin. The aggregation occurs quickly compared to this, preventing a large build-up of the surfactin beneath the phospholipid monolayer as shown in Figure 8.22. The only change is the low pH and the presence of chloride ions. Therefore, the change in behaviour can only be due

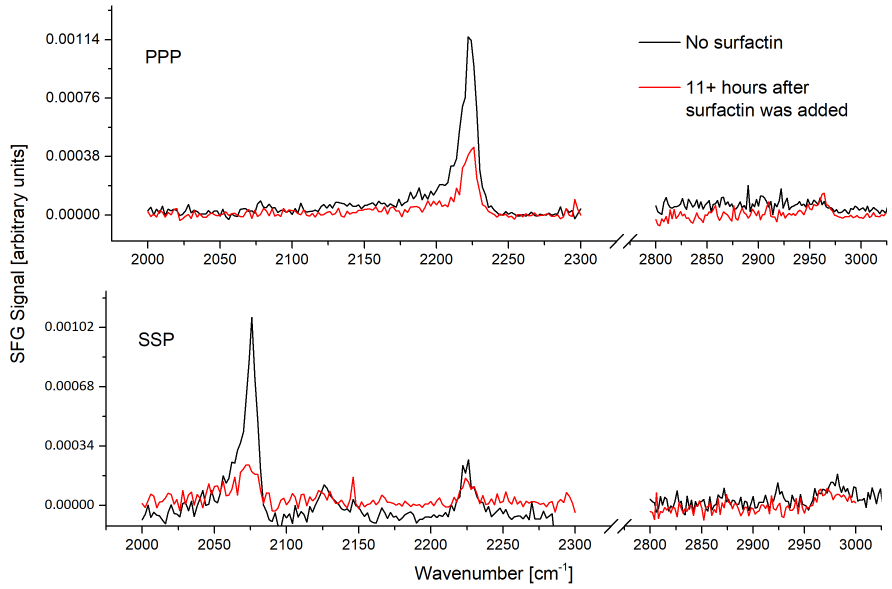

Figure 8.21: The "before" and "after" spectra of the CD and CH regions of the dDPPC and surfactin system under acidic conditions (pH 3.4), taken just before injection of the surfactin into the subphase, and after 600 minutes (the end of the time-dependent SFG results)

to these two differences. It seems likely that the uncharged surfactin has a reduced affinity for adsorbing to the interface - that is, the electrostatic interaction plays an important role in the interaction of surfactin with the phospholipid monolayer, which is zwitterionic with a positively charged amine group which would interact favourably with the negatively charged surfactin. The neutralisation of the surfactin may also increase the rate of aggregation of the surfactin, since there is no longer any charge-charge repulsion between the uncharged surfactin molecules.

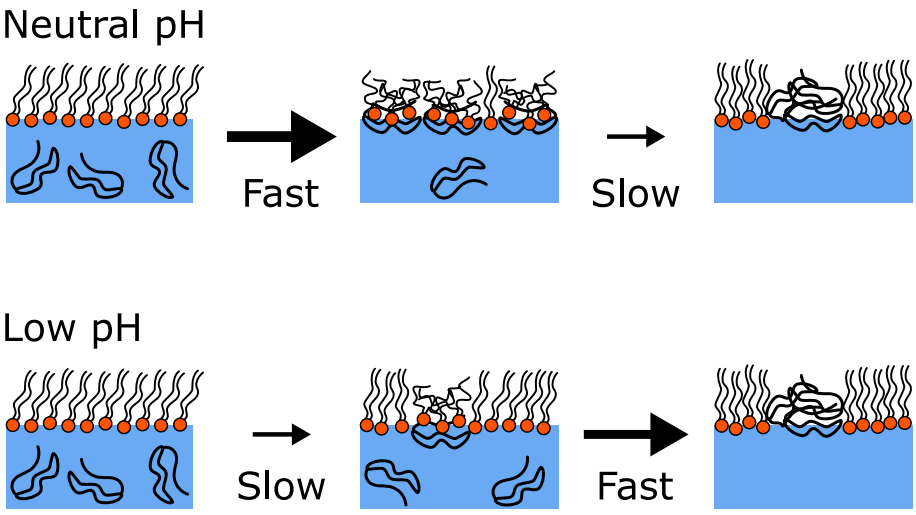

Figure 8.22: A diagram showing the relative speed of the adsorption and aggregation steps at neutral and low pH. At neutral pH, the adsorption step is relatively fast, and the aggregation step is slow. Therefore, a build-up of adsorbed surfactin is observed, leading to the strong surfactin signals and weak phospholipid signals in the SFG spectra. In the case of the low pH, the aggregation of the surfactin occurs about as quickly as the surfactin adsorbs, so that no build-up of adsorbed surfactin beneath the monolayer is observed.

References

[1] P. A. Janmey and P. K. Kinnunen, "Biophysical properties of lipids and dynamic membranes," *Trends in Cell Biology*, vol. 16, pp. 538–546, Oct. 2006.

[2] H.-H. Shen, R. K. Thomas, C.-y. Chen, R. C. Darton, S. C. Baker, and J. Penfold, "Aggregation of the naturally occurring lipopeptide, surfactin, at interfaces and in solution: an unusual type of surfactant?," *Langmuir*, vol. 25, pp. 4211–4218, Apr. 2009.

[3] G. S. Hartley and J. W. Roe, "Ionic concentrations at interfaces," *Transactions of the Faraday Society*, vol. 35, p. 101, Aug. 1940.

[4] K. P. Fears, S. E. Creager, and R. A. Latour, "Determination of the surface pK of carboxylic- and amine-terminated alkanethiols using surface plasmon resonance spectroscopy," *Langmuir*, vol. 24, pp. 837–843, Jan. 2008.

[5] X.-D. Xiao, V. Vogel, and Y. Shen, "Probing the proton excess at interfaces by second harmonic generation," *Chemical Physics Letters*, vol. 163, pp. 555–559, Nov. 1989.

[6] H.-H. Shen, R. K. Thomas, J. Penfold, and G. Fragneto, "Destruction and solubilization of supported phospholipid bilayers on silica by the biosurfactant surfactin," *Langmuir*, vol. 26, pp. 7334–7342, May 2010.

[7] M. Deleu, O. Bouffioux, H. Razafindralambo, M. Paquot, C. Hbid, P. Thonart, P. Jacques, and R. Brasseur, "Interaction of surfactin with membranes: a computational approach," *Langmuir*, vol. 19, pp. 3377–3385, Apr. 2003.

[8] H.-H. Shen, R. K. Thomas, and P. Taylor, "The location of the biosurfactant surfactin in phospholipid bilayers supported on silica using neutron reflectometry," *Langmuir*, vol. 26, pp. 320–327, Jan. 2010.

[9] C. Rauch, "On the relationship between drug's size, cell membrane mechanical properties and high levels of multi drug resistance: A comparison to published data," *European Biophysics Journal*, vol. 38, pp. 537–546, Dec. 2009.

[10] R. S. Cantor, "Lateral pressures in cell membranes: A mechanism for modulation of protein function," *The Journal of Physical Chemistry B*, vol. 101, pp. 1723–1725, Mar. 1997.

9. Conclusions & further work

9.1 Binary surfactant system

Molecular-level insight of the monolayer ordering of model hair conditioner samples on glass was obtained using SFG. The effect of temperature, self-assembly conditions, and sample preparation on the monolayer order was also investigated. It was found that the temperature dependence of the monolayer ordering was itself dependent on both the self-assembly conditions and the sample preparation.

For the "Unilever" model, the monolayer was assembled more densely at low solution temperatures, and monolayers assembled at low temperatures were not strongly affected by heating on the SFG sample stage. Monolayers assembled from solution at higher temperatures were not as densely packed onto the glass substrate, and subsequently were affected to a greater extent by heating on the SFG stage. In contrast, the density of the monolayer formed from the "RR63" and "RR80" model (which were prepared differently to the "Unilever" model) was found to be mostly unaffected by the solution temperature. Regardless of the solution temperature, the monolayer ordering was strongly affected by the temperature of the SFG sample stage.

The effect of including $CaCO_3$ in the solution for self-assembly was extremely small. This is probably due to the very low solubility, and therefore concentration, of $CaCO_3$ in water. To examine better the effects of ionic strength, a more soluble ion should be chosen, although this may be less relevant to the real-world use of hair conditioner.

Further investigation into these effects should focus on the composition of the monolayer formed from each of these models, in order to understand the differences in deposition behaviour, and how the composition of the deposited monolayer is affected by the preparation method and the solution temperature. One option is selective deuteration, so that the alkyl tails of BTAC and CetOH may be distinguished by SFG. Other methods of characterising the monolayer would also be useful. Ellipsometry would reveal the thickness of the deposited monolayer, and give an indication of the tilt angle, to hopefully corroborate the molecular-ordering information revealed by the SFG spectra.

9.2 Cell membrane models

The SFG spectra of the T10 SAM and adsorbed phospholipids reported here are preliminary; these systems are much more complicated to manipulate experimentally and to interpret spectroscopically. However, the SFG spectra of the T10 SAMs gave some indication as to their structure in air - the tethers must be quite disordered, the methyl groups must point upwards, and the methylene groups must be orientated such that the hydrogen atoms lie on a line close to vertical. A structure consistent with the data has been suggested - the tethers have many gauche defects and a large tilt angle, lying close to the plane occupied by the alcohol headgroups of the spacers.

RSE was used as a reliable method to produce a membrane in which the tethers were incorporated, and again, the spectra were used to speculate on the orientation and structure of the now incorporated tethers. The spectra of the tethers produced by RSE were then compared to the spectra of the tethers after LB deposition with d-DPPE, which did not look the same. These spectra indicate that the tethers are not incorporated after LB deposition, at least not initially.

An isotopically distinguished bilayer was produced by consecutive LB and LS deposition. The spectra showed that the polar orientations of the proximal and distal layers are in opposite directions, as expected, and that the membranes formed this way were well ordered, with few gauche defects. However, there was no evidence for signals arising from the tethers that would indicate their incorporation into the bilayer. They also demonstrated that flip-flop, the exchange of DPPE in the proximal leaflet with d-DPPE in the distal leaflet, causes a decrease in signal intensity on the order of hours after LS deposition has taken place. This process could be monitored by time-dependent SFG, to investigate the rate of flip-flop in the tethered membrane system.

Future work with isotopically distinguished bilayers would probably require the LB/LS methodology to be employed. Therefore, some method for ensuring the incorporation of the tethers is required. Perhaps, by heating the slide after LB deposition, the tethers might become incorporated. If this does occur, it might be possible to monitor the enthalpy of this process by calorimetry, confirming their incorporation and revealing some information about the thermodynamics of the tether-lipid interaction. Otherwise, exposing the bilayer produced by RSE to air, as done in this report, will cause a rearrangement of the

bilayer, to produce a surface with coexisting monolayer and odd-numbered multilayers. Before LS deposition atop this, the extent of multilayering would need to be examined, so that the potential disruption to the completed bilayer might be understood. Therefore, it would be useful to examine the surface after RSE and exposure to air by AFM. If the extent of multilayering is minimal, it may be reasonable to produce an isotopically distinguished bilayer by using LS deposition after forming the initial monolayer by RSE and exposure to air.

9.3 Behenyltrimethylammonium surfactants at the air/water and air/glass interfaces

In this work, we have monitored the relaxation of two long-chain insoluble cationic surfactants in a Langmuir monolayer below their fracture collapse pressure. SFG was employed to monitor the molecular structure of the surfactant in the monolayer phase, surface pressure measurements provided macroscopic information about the behaviour of the monolayer, and AFM was used to observe the multilayer structures of the films at the onset and at the end of the collapse process and provided valuable context for the molecular information provided by SFG. This type of relaxation follows a slow collapse mechanism, whereby islands of multilayer phases nucleate and grow, reducing the lateral pressure of the monolayer [1–3]. The AFM images imply that nucleation happens quickly.

The spectra taken during the collapse process showed that the cationic surfactant orders upon compression (as expected [4]), but that the relationship of the molecular structure to the surface pressure is not necessarily simple - the surface pressure took a longer time (greater than 10 h) to reach equilibrium than the SFG intensities (approximately 2 h). Although a weak SFG signal made temporal measurement difficult, the SFG response and position of the headgroup remained constant throughout compression and relaxation. This is in agreement with previous SFG studies of the headgroup of a negatively charged surfactant, sodium dodecylsulfate [5].

Differences between the two surfactants in their sum-frequency and surface pressure data are attributed to the counterion binding energies [6]. The data showed that the better shielded surfactant has a lower equilibrium spreading pressure, and a more ordered

monolayer - the methyl sulfate counterion of BTMS was better at shielding the positive charge of the headgroups. However, immediately after compression, the higher surface pressure for BTMS suggested that the methyl sulfate counterion was less able to stabilise the system. This is probably a kinetic effect - the rate at which the multilayers form is slower, so that initially the surface pressure drops more slowly. This may be because the methyl sulfate ions are larger than the chloride ions, and therefore take longer to rearrange into the multilayer system.

The reduced ordering of the monolayer phase, as shown by the SFG spectra, is associated with growth of the multilayer phases observed in the AFM images. The AFM images also showed a greater number of multilayer sites at the onset of the slow collapse of the film than was observed at the end. This also implies that either the formation of the multilayer phase is reversible, such that one multilayer phase grows at the expense of others, or that the multilayer phases are mobile enough that they can combine on the water surface during the relaxation process. The SFG spectra of BTMS recorded on glass are similar to those recorded at the air/water interface, and it is reasonable to conclude that this validates the assumption that LB deposition can be used to capture the state of the film. SFG was found to be a useful method for following the order and packing density of the monolayer as it changed over time, and combining it with other techniques, such as surface pressure measurement and AFM imaging, provided valuable context to the interpretation of the spectra.

9.4 SFG spectroscopy of surfactin and phospholipids at the air/water interface

The SFG data have revealed two key findings about the orientation and structure of surfactin on water surfaces. Firstly, by using surfactin with perdeuterated leucine groups, we have shown that the lipid chain lies in the surface plane and not along the surface normal, since the leucine groups are responsible for almost all the SFG resonances arising from surfactin. Secondly, the constant intensity ratios of the methyl resonances of the leucine groups as the surfactin concentration increases indicates that the orientation of the leucine residues, and therefore of the peptide ring itself, does not change. This is most satisfactorily explained by the ring lying horizontally on the interface with the lipid chain atop this, also lying in the plane of the interface. In this configuration, the

lipid tail can interact with the hydrophobic residues of the ring. This precludes structural inferences arising from surface tension measurements by Maget-Dana and Ptak [7] and Ishigami et al [8], and some conclusions regarding intermolecular interaction of surfactin arising from the MD studies of Iglesias-Fernández et al [9]. Small changes in amide I and carbonyl resonances with pH and not in the ratios of the C-H resonances suggest small realignments of these groups along the surface normal as the pH changes, without changing the overall orientation of the peptide ring. Similarly, Ca_2^+ did not cause significant changes to the overall structure of surfactin, despite being known to bind strongly to the acid groups of the ring [7, 10–13]. This is generally in agreement with previous neutron reflectivity (NR) studies [10] and most aspects of molecular dynamics (MD) calculations [9].

Having become familiar with the structure and behaviour of surfactin as studied by SFG, the interaction of surfactin with a phospholipid monolayer was investigated in real-time by SFG and surface pressure measurements at the air/water interface. By the use of selectively deuterated materials (both deuterated phospholipid and surfactin with deuterated leucine residues), the characteristic behaviour of the interaction of surfactin with the phospholipid monolayer was identified. Initially, only phospholipid resonances are observed. As the surface pressure of the monolayer begins to rise, SFG resonances from surfactin were detected, and the increasing intensity of these resonances coincides with the suppression of SFG resonances arising from the phospholipid. As the surface pressure of the monolayer begins to plateau, the resonances arising from surfactin all but disappear, and those arising from the phospholipid recover.

The SFG spectra of surfactin recorded during the penetration steps were very similar to spectra of surfactin alone at the air/water interface, and the use of surfactin with deuterated leucine residues showed that it is these residues that are responsible for the SFG resonances of surfactin throughout the interaction with the phospholipid. These observations lead to the conclusion that the majority of the surfactin remains in a similar arrangement as previously, with the tail group folded over to interact with the hydrophobic residues of the ring. This is in agreement with previous NR studies of surfactin [14].

Although the appearance of SFG resonances arising from surfactin was accompanied by the disappearance of resonances from the phospholipid, RAIRS was used to conclusively show that the phospholipid monolayer remains at the air/water interface throughout the

phospholipid-surfactin interaction. A two-step mechanism for this interaction which accounted for the surface pressure, SFG, and RAIRS data was put forward - firstly, surfactin adsorbs to the phospholipid monolayer, disordering the phospholipid in contact with it. In the second step, the adsorbed surfactin aggregates, reducing the surface area occupied at the interface, and allowing the phospholipids to reform into an ordered monolayer at the interface.

Additionally, the effects of the initial surface pressure of the monolayer, the concentration of surfactin used, and the pH of the subphase were investigated. It was found that the surface pressure did not have a strong effect on the time-scale of the interaction. It is reasonable to assume that the lateral pressure would reduce the rate at which surfactin can penetrate the monolayer. If this assumption is true, the fact that the time-scale did not change indicates that the penetration step was not rate limiting in the surfactin-phospholipid interaction. When higher surfactin concentrations in the subphase were used, the experiment began as normal - as the surface pressure began to increase the surfactin resonances appeared, coinciding with the suppression of the phospholipid resonance. However, as the surface pressure began to plateau, the surfactin SFG resonances did not disappear and the phospholipid resonances did not recover as in previous experiments. The increased amount of surfactin at the interface prevents the phospholipid from reordering, and therefore the phospholipid SFG resonances do not recover. When the pH in the subphase was reduced, significant changes were seen in the surface pressure and SFG behaviour. The time for surfactin resonances to appear took much longer, and remained detectable for a much longer time, around 300 minutes. The change in surface pressure was also more gradual. These changes are explained by a slower rate of surfactin adsorption to the monolayer, and a faster rate of aggregation of surfactin once in the phospholipid monolayer.

In order to understand the mechanism in more detail, work utilising the nano-IR AFM technique is currently under way. The phospholipid-surfactin system experiment was begun as normal and then LB deposition was used to cast the phospholipid-surfactin monolayer onto mica at specific times after the surfactin was injected into the subphase. Casting the monolayer disrupts the experiment, and therefore each casting was taken from a fresh experiment. Figure 9.1 shows an SFG experiment with the surface pressure trace labelled at points to represent where LB deposition would have taken place.

There are some experimental challenges involved in the use of LB deposition to investigate the surfactin - lipid mechanism. The exact progress of the experiment before casting onto the mica is difficult to determine. This is because the LB deposition disrupts the surface pressure measurement, and the SFG sample stage does not have room for a full-sized trough with computer-controlled barriers and dipper needed for LB casting. Therefore, the experimental progress can only be judged from the current surface pressure without being able to see the record of the plateau surface pressure. Additionally, casting onto mica is likely to cause changes to the surfactin-phospholipid system. In Chapter 5, casting onto mica worked very well to capture the state of the monolayer at the air/water interface for investigation by AFM. However, the surfactants in that chapter were positively charged. Surfactin has a negative charge, and therefore it is not a safe assumption that the mica (which is negatively charged under neutral conditions) is the best surface for capturing the state of the monolayer in the same way as before. These effects, compounded with the high run-to-run variation of the experiment makes capturing the state of the phospholipid monolayer very difficult. However, even these preliminary data show the potential power of the AFM-IR technique. Height profiles of the AFM image combined with the IR mapping add a wealth of information and give valuable context to the SFG, RAIRS, and surface pressure data.

After using these techniques to fully characterise the surfactin-phospholipid monolayer interaction, the next logical step is to investigate the interaction of surfactin with a phospholipid bilayer. The simplest bilayer model is a simple solid-supported bilayer with no tethering, produced either by RSE or by LB/LS deposition. However the surfactin experiment takes a significant amount of time, especially at low pH. A more stable bilayer, such as a tethered bilayer membrane, might be required in order that the bilayer might last for the whole experiment. For isotopically distinct bilayers, lipid flip flop will pose a problem. In this case, a hybrid bilayer membrane may be more appropriate, since the self-assembled proximal leaflet will be chemically bound to the solid support.

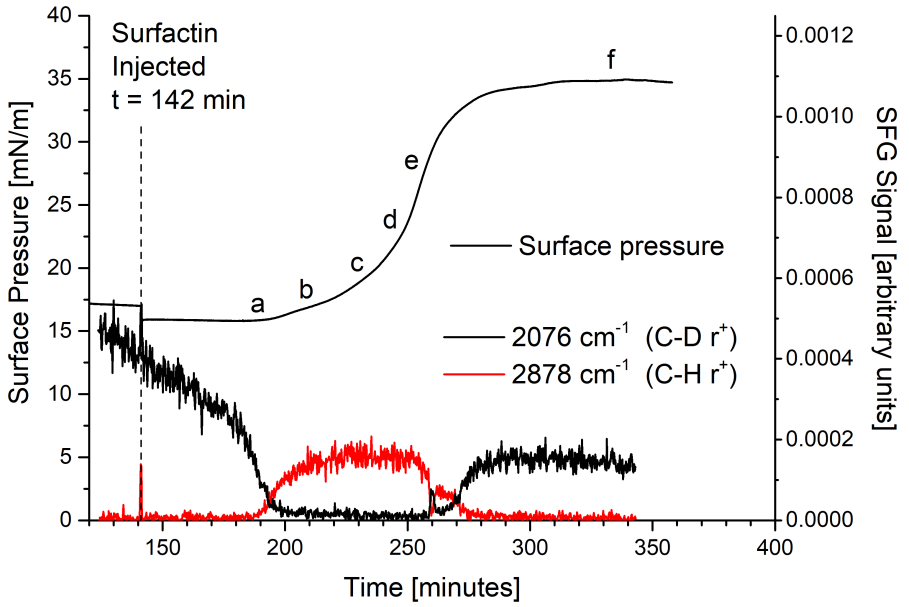

Figure 9.1: Plot of surface pressure and SFG intensity (r^+ in the SSP polarisation) of the dDPPC phospholipid monolayer and surfactin against time (reproduced from Figure 8.1). 25 μl of surfactin solution (giving a concentration equal to 0.05×CMC in the trough) was injected into the subphase at 142 minutes, as indicated on the plot. The black SFG trace represents the SFG intensity of the r^+ resonance of the deuterated phosphoplipid, dDPPC, and the red SFG trace represents the SFG intensity of the r^+ resonance of the protonated surfactin.

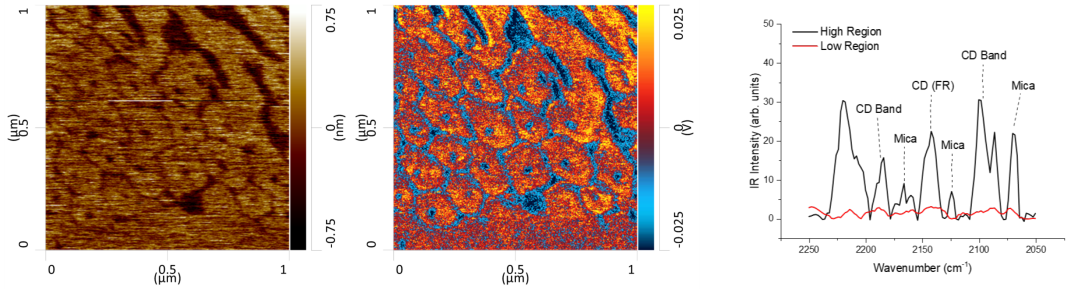

(a) Sample LB cast at a point corresponding to (a) on Figure 9.1. The AFM-IR mapping was done at 2200 cm^{-1}, which corresponds to the CD_2 antisymmetric stretch. The spectra are taken from specific regions of the image. The black spectra correspond to the higher regions of the height-mapping image, and the light regions of the IR intensity-mapping image. The red spectra are taken from the lower regions of the height-mapping image.

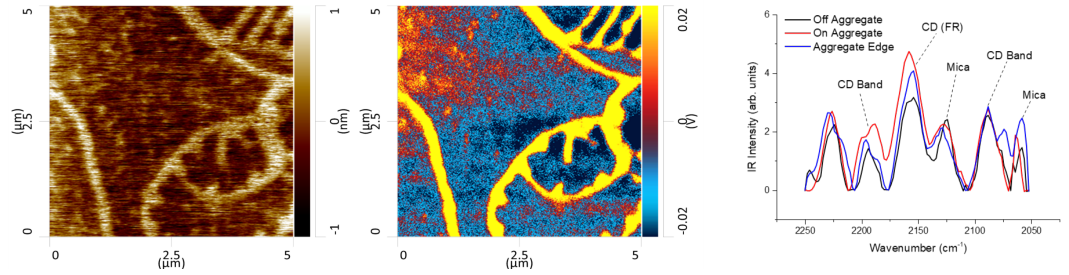

(b) Sample LB cast at a point corresponding to (b) on Figure 9.1. The AFM-IR mapping was done at 2200 cm^{-1}, which corresponds to the CD_2 antisymmetric stretch. The spectra are taken from specific regions of the image. Black spectra are from the low regions of the AFM height image, which are red/blue in the IR-mapping image, red spectra are from the high regions of the height-mapping image (bright yellow in the IR mapping), and blue spectra are from the boundary regions. Although the dDPPC has formed unusual domains with significant height variation, DPPC is visible throughout the surface.

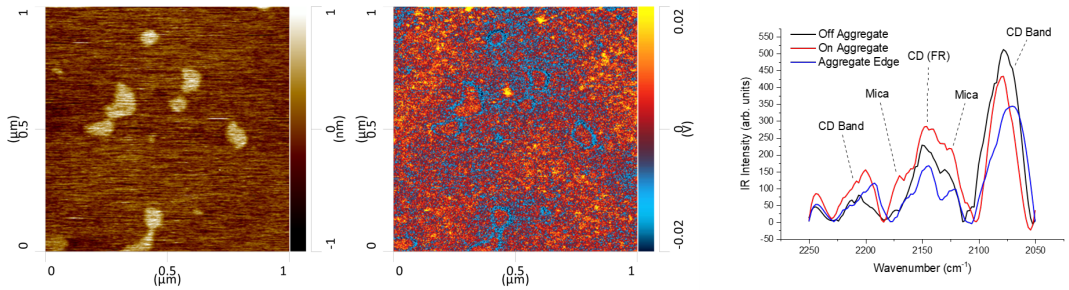

(c) Sample LB cast at a point corresponding to (c) on Figure 9.1. The AFM-IR mapping was done at 2142 cm^{-1}, which corresponds to the Fermi resonance of the CD_2 symmetric stretch. The spectra are taken from specific regions of the image. Black spectra are from low regions of the AFM-height image, red from high regions, and blue from the boundary regions. Again dDPPC signals are apparent all over the surface.

Figure 9.2: AFM images (left column), AFM-IR mappings of CD resonances (middle column), and IR spectra taken from specific regions of these images (right colum). AFM-IR data provided courtesy of A. Fellows.

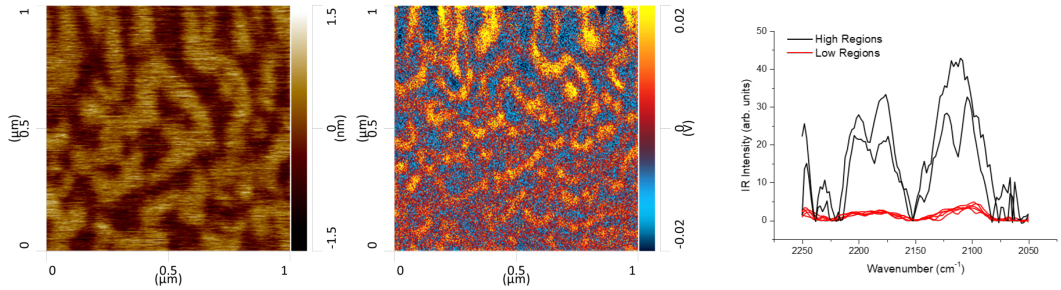

(d) Sample LB cast at a point corresponding to (d) on Figure 9.1. The AFM-IR mapping was done at 2100 cm^{-1}, which corresponds to the CD_2 symmetric stretch. The spectra are taken from specific regions of the image - black spectra correspond to higher regions of the AFM image, and red to the lower regions. It appears that there are now surfactin-rich regions (dark) which virtually exclude dDPPC.

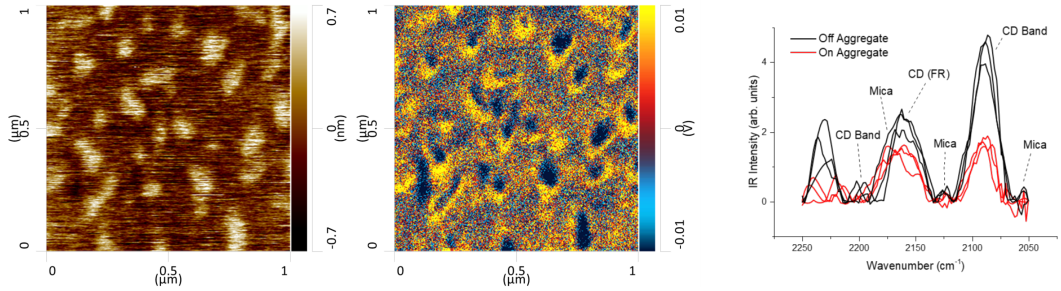

(e) Sample LB cast at a point corresponding to (e) on Figure 9.1. The AFM-IR mapping was done at 2142 cm^{-1}, which corresponds to the Fermi resonance of the CD_2 symmetric stretch. The black spectra are taken from the lower regions of the AFM-height image (lighter in the IR mapping image), and the red spectra are taken from the higher regions. Now there are surfactin-rich domains, which are higher than the surrounding dDPPC-rich region.

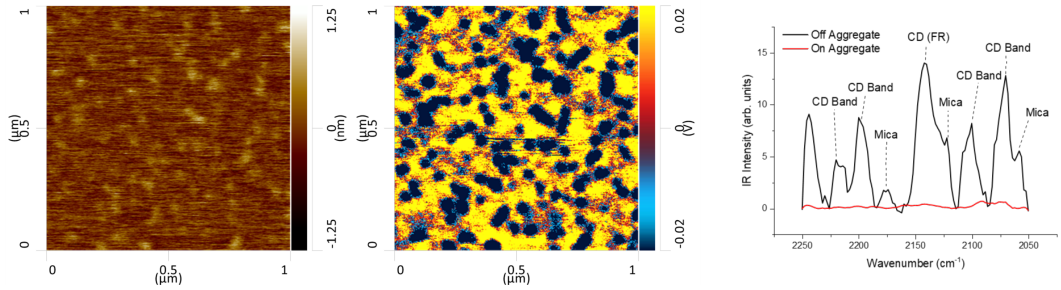

(f) Sample LB cast at a point corresponding to (f) on Figure 9.1. The AFM-IR mapping was done at 2200 cm^{-1}, corresponding to the CD_2 symmetric stretch. The black spectra correspond to the lower regions in the height-mapping image, and to the light regions in the IR-mapping image. The red spectra corresponds to the higher regions in the height-mapping image (darker regions of the IR mapping). These data show surfactin aggregates (or rather, aggregates where no DPPC is detectable) on the surface of the mica.

Figure 9.2 continued: AFM images (left column), AFM-IR mappings of CD resonances (middle column), and IR spectra taken from specific regions of these images (right column). Data provided courtesy of A. Fellows.

References

[1] R. D. Smith and J. C. Berg, "The collapse of surfactant monolayers at the air—water interface," *Journal of Colloid and Interface Science*, vol. 74, pp. 273–286, Mar. 1980.

[2] M. Weis, "Kinetics of slow collapse process: thermodynamic description of rate constants," *Applied Surface Science*, vol. 253, pp. 1469–1472, Nov. 2006.

[3] C. Ybert, W. Lu, G. Möller, and C. M. Knobler, "Collapse of a monolayer by three mechanisms," *The Journal of Physical Chemistry B*, vol. 106, pp. 2004–2008, Feb. 2002.

[4] G. R. Bell, C. D. Bain, and R. N. Ward, "Sum-frequency vibrational spectroscopy of soluble surfactants at the air/water interface," *Journal of the Chemical Society, Faraday Transactions*, vol. 92, pp. 515–523, Jan. 1996.

[5] C. M. Johnson and E. Tyrode, "Study of the adsorption of sodium dodecyl sulfate (SDS) at the air/water interface: targeting the sulfate headgroup using vibrational sum frequency spectroscopy," *Physical Chemistry Chemical Physics*, vol. 7, p. 2635, July 2005.

[6] S. Berr, R. R. M. Jones, and J. S. Johnson, "Effect of counterion on the size and charge of alkyltrimethylammonium halide micelles as a function of chain length and concentration as determined by small-angle neutron scattering," *The Journal of Physical Chemistry*, vol. 96, pp. 5611–5614, June 1992.

[7] R. Maget-Dana and M. Ptak, "Interfacial properties of surfactin," *Journal of Colloid and Interface Science*, vol. 153, pp. 285–291, Oct. 1992.

[8] Y. Ishigami, M. Osman, H. Nakahara, Y. Sano, R. Ishiguro, and M. Matsumoto, "Significance of β-sheet formation for micellization and surface adsorption of surfactin," *Colloids and Surfaces B: Biointerfaces*, vol. 4, pp. 341–348, July 1995.

[9] J. Iglesias-Fernández, L. Darré, A. Kohlmeyer, R. K. Thomas, H.-H. Shen, and C. Domene, "Surfactin at the water/air interface and in solution," *Langmuir*, vol. 31, pp. 11097–11104, Oct. 2015.

[10] H.-H. Shen, T.-W. Lin, R. K. Thomas, D. J. F. Taylor, and J. Penfold, "Surfactin structures at interfaces and in solution: The effect of pH and cations," *The Journal of Physical Chemistry B*, vol. 115, pp. 4427–4435, Apr. 2011.

[11] L. Thimon, F. Peypoux, and G. Michel, "Interactions of surfactin, a biosurfactant from Bacillus subtilis, with inorganic cations," *Biotechnology Letters*, vol. 14, pp. 713–718, Nov. 1992.

[12] A. Grau, J. C. Gómez Fernández, F. Peypoux, and A. Ortiz, "A study on the interactions of surfactin with phospholipid vesicles," *Biochimica et Biophysica Acta (BBA) - Biomembranes*, vol. 1418, pp. 307–319, May 1999.

[13] E. Vass, F. Besson, Z. Majer, L. Volpon, and M. Hollósi, "Ca^{2+}-induced changes of surfactin conformation: A FTIR and circular dichroism study," *Biochemical and Biophysical Research Communications*, vol. 282, pp. 361–367, Mar. 2001.

[14] H.-H. Shen, R. K. Thomas, J. Penfold, and G. Fragneto, "Destruction and solubilization of supported phospholipid bilayers on silica by the biosurfactant surfactin," *Langmuir*, vol. 26, pp. 7334–7342, May 2010.